Dissertation ETH Nr. 14248

Systematic Investigations on the Transition from Zintl Phases to Intermetallics

A dissertation submitted to the

Swiss Federal Institute of Technology Zürich

for the degree of

Doctor of Natural Sciences

presented by

Simone Zürcher

Dipl. Chem. ETH

born on 6th November 1972

from Thalwil (ZH), Switzerland

accepted on the recommendation of

Prof. Dr. R. Nesper, examiner

Prof. Dr. H. Grützmacher, co-examiner

Zürich, 2001

Ai miei Genitori e a Elisabetta

"Un altro uomo, dotato di spirito divino, ha detto che la sapienza è nascosta e che il luogo dell'intelligenza è lontano dagli occhi dei viventi. Se è così [...] allora, se il nostro desiderio non è vano, ciò che desideriamo è sapere di non sapere. Se potremo giungere a tanto, avremo raggiunto la dotta ignoranza. Nessun'altra dottrina più perfetta può sopraggiungere all'uomo (anche più diligente) oltre quella di scoprire di essere dottissimo nella sua propria ignoranza: e tanto più uno sarà dotto, quanto più si saprà ignorante."

Niccolò Cusano (1401-1464), "De docta ignorantia", 1440

"Another man said that the wisdom is hided and that the place of the intelligence is far from the eyes of human beings. If this is true then what we wish is to know to not know. If we achieve that, we would reach the learned ignorance. No other more perfect doctrine can occur to the man than that to discover to be learned in his own ignorance: and the more one will be learned, the more he will know he is ignorant."

Seite Leer /
Blank leaf

Seite Leer /
Blank leaf

Seite Leer
Blank leaf

Table of Contents

Abstract

The work presented here is a compilation of syntheses and characterizations of intermetallic phases formed between elements of the 13th group (the aluminum group), the 14th group (the silicon group), alkaline metals, and alkaline-earth metals. The primary aspect was to investigate the electronic properties of compounds formed by elements separated by the Zintl border, group 13 or triel and group 14 or tetrel elements, respectively. While the majority of the compounds of triels with more electropositive cations fall into the class of intermetallics, the corresponding tetrel compounds typically belong to the valence or Zintl phases.

The following new compounds were synthesized and structurally characterized: **α-** and **β-Li_5AlSi_2**, **$Li_{4+x}Al_{2-x}Si_2$** (x ~ 1), **α-** and **β-Li_5AlGe_2**, **$Li_{4+x}Al_{2-x}Ge_2$** (x ~ 1), **$Li_{4+x}Ga_{2-x}Si_2$** (x ~ 1), **α-Li_5GaGe_2**, **$Li_{4+x}Ga_{2-x}Ge_2$** (x ~ 1), **Li_5AlSn_2**, **$Li_xCaAl_{1-x}Si$** (x ~ 0.5), **$Li_xCaAl_{1-x}Ge$** (x ~ 0.5), **$Li_xSrAl_{1-x}Si$** (x = 0.5), **$Li_xSrAl_{1-x}Ge$** (x = 0.5), **$Li_{2+x}Sr_2Al_{6-x}Si_6$** (x ~ 2.8), **$Li_{3+x}Sr_5Al_{16-x}Si_{12}$** (x ~ 6.2), and **SrGaSi**.

Measurements of the thermal behaviour, magnetic properties, and electrical conductivity were performed on many of these compounds whenever possible. Quantum mechanical calculations, especially of density of states (DOS), band structures, and of the electron localization function (ELF), were used to investigate the electronic structure and the bonding characteristics of these phases.

Structures and structural relationship of the ternary compounds found in the Li/Tr/Tt systems were very intensively investigated. All the synthesized compounds have almost the same compositions Li_5TrTt_2. Three different structure types were found. The tetragonal α-Li_5TrTt_2 (Tr = Al, Ga; Tt = Si, Ge, Sn), which shows a cristobalite-like network built of the Tr-Tt elements; the cubic β-Li_5TrTt_2 (Tr = Al, Ga; Tt = Si, Ge), closely related to the tetragonal structure; and the hexagonal $Li_{4+x}Tr_{2-x}Tt_2$ (x ~ 1) (Tr = Al, Ga, Tt = Si, Ge), which is a coloured version of graphite with layer built of the tetrel element sites and triel/lithium mixed occupied positions while in addition lithium is

intercalated between the layers. These compounds show interesting phase relationships. In fact the last two structures can be described as **high temperature modifications** of the **α-Li_5TrTt_2 phase**. The phase transition between the α-Li_5TrTt_2 and β-Li_5TrTt_2 was investigated by difference thermal analysis (DTA) and high temperature X-ray powder diffraction experiments for the Al/Si, Al/Ge, Ga/Ge compounds. The hexagonal $Li_{4+x}Tr_{2-x}Tt_2$ phases can be described as the γ-modifications, because the composition is close to Li_5TrTt_2. This phase was very often found together with the α-Li_5TrTt_2 modifications. The hexagonal $Li_{4+x}Tr_{2-x}Tt_2$ phases exist within a phasewidth of, yet, unknown range. Interestingly the double nature semimetal/metal of the electronegative elements becomes evident by analysing the physical properties of the α- and the γ-phases: the first are semiconductors with the more or less expected exception of the tin compound, the second are all metals.

In all the newly discovered quaternary phases, interestingly, the aluminum atoms share always positions with lithium atoms in a more or less statistical way. In the quaternary Li/Sr/Al/Tt systems (Tt = Si, Ge) three new structure types were discovered. The first structure, $Li_xSrAl_{1-x}Tt$ (x = 0.5, Tt = Si, Ge), presents layer of the tetrel-Al/Li atoms and is isostructural and isoelectronic to the NaAlSi compound. The second compound $Li_{2+x}Sr_2Al_{6-x}Si_6$ (x ~ 2.8) crystallizes in a new structure type, which can be seen as an intermediate between the well known $BaAl_4$ structure and the first phase. The third phase $Li_{3+x}Sr_5Al_{16-x}Si_{12}$ (x ~ 6.2) presents an interesting zeolite-like network built of the silicon, aluminum and mixed occupied positions Al/Li. The channels are filled by strontium and lithium atoms. All these four new compounds are, as expected, metals.

In the quaternary Li/Ca/Al/Tt (Tt = Si,Ge) systems two new, isostructural, compounds were found. The $Li_xCaAl_{1-x}Tt$ ($0.4 < x < 0.6$, Tt = Si, Ge) phases although almost isoelectronic to the strontium compounds crystallize in another structure type. The phasewidth was determined. The silicon compound presents a superstructure, which was intensively investigated. However, also there remain some blocks where aluminum/lithium positions are mixed occupied. Also these new phases are metals.

The ternary phase SrGaSi crystallizes in the AlB_2 structure type, and, like recently discovered for other isostructural compounds, becomes superconducting at temperatures below 4.5 K. Therefore, the electronic structure was intensively studied. The planar Ga/Si layers are characterized by half filled π^*-states, the compound is therefore expected to be Pauli paramagnetic and a metal.

Riassunto

Il lavoro presentato in questa tesi è una collezione di sintesi di fasi intermetalliche formate dagli elementi del sistema periodica che giacciono lungo la cosiddetta linea di Zintl (gli elementi del 13° gruppo (il gruppo dell'alluminio) e del 14° (quello del silicio)), e dai metalli alcalini ed alcalino terrosi. In particolare sono state studiate le proprietà elettroniche dei suddetti composti: mentre la maggioranza dei composti tra elementi del 13° gruppo e cationi più elettropositivi appartengono alla classe dei composti intermetallici, quelli corrispondenti contenenti elementi del 14° gruppo sono fasi di Zintl.

I seguenti nuovi composti sono stati sintetizzati e caratterizzati strutturalmente: α- e β-**Li_5AlSi_2**, **$Li_{4+x}Al_{2-x}Si_2$** (x ~ 1), α- e β-**Li_5AlGe_2**, **$Li_{4+x}Al_{2-x}Ge_2$** (x ~ 1), **$Li_{4+x}Ga_{2-x}Si_2$** (x ~ 1), α-**Li_5GaGe_2**, **$Li_{4+x}Ga_{2-x}Ge_2$** (x ~ 1), **Li_5AlSn_2**, **$Li_xCaAl_{1-x}Si$** (x ~ 0.5), **$Li_xCaAl_{1-x}Ge$** (x ~ 0.5), **$Li_xSrAl_{1-x}Si$** (x = 0.5), **$Li_xSrAl_{1-x}Ge$** (x = 0.5), **$Li_{2+x}Sr_2Al_{6-x}Si_6$** (x ~ 2.8), **$Li_{3+x}Sr_5Al_{16-x}Si_{12}$** (x ~ 6.2), e **SrGaSi**.

Ove possibile sono state determinate la dipendenza delle proprietà fisiche dalla temperatura, così come la suscettività magnetica e la conducibilità elettrica. Lo studio della struttura elettronica e della natura dei legami è stato eseguito mediante calcoli quantomeccanici. In particolare sono state determinate la densità degli stati (DOS), la struttura di banda e la funzione di localizzazione elettronica (ELF).

Inoltre sono state studiate approfonditamente le strutture e le relazioni strutturali dei composti ternari osservati nei sistemi Li/Tr/Tt. I nuovi composti hanno circa la stessa composizione: Li_5TrTt_2. Tre diversi tipi di struttura sono stati identificati: la tetragonale α-Li_5TrTt_2 (Tr = Al, Ga; Tt = Si, Ge, Sn), caratterizzata da un reticolo formato dagli elementi del 13° e del 14° gruppo simile a quello della cristobalite; la cubica β-Li_5TrTt_2 (Tr = Al, Ga; Tt = Si, Ge), strettamente legata alla struttura tetragonale; l'esagonale $Li_{4+x}Tr_{2-x}Tt_2$ (x ~ 1) (Tr = Al, Ga, Tt = Si, Ge), che è una versione colorata della grafite con strati formati da elementi del 13°, 14° gruppo, e da litio. In questi strati metà delle

posizioni reticolari è occupata esclusivamente dagli elementi del 14° gruppo, le restanti posizioni sono statisticamente occupate dagli atomi del 13° gruppo o dal litio. Intercalati fra questi strati sono presenti altri atomi di litio. Questi composti presentano interessanti relazioni di fase: le due ultime strutture, infatti, sono delle fasi stabili ad alta temperatura. La transizione di fase tra α-Li_5TrTt_2 e β-Li_5TrTt_2 è stata studiata attraverso la diffrazione di raggi X su polveri (a differenti temperature) e l'analisi termica differenziale per i composti formati da Al/Si, Al/Ge e Ga/Ge. Le fasi esagonali $Li_{4+x}Tr_{2-x}Tt_2$ ($x \sim 1$) possono essere descritte come una modificazione γ poichè hanno una composizione molto simile alle altre due fasi e spesso coesistono con i composti α-Li_5TrTt_2. Le fasi esagonali $Li_{4+x}Tr_{2-x}Tt_2$ esistono in un intervallo di valori di x la cui ampiezza non è stata determinata. La doppia natura semimetallo/metallo degli elementi elettronegativi risulta evidente dall'analisi delle proprietà fisiche delle diverse fasi: le fasi α sono semiconduttrici, con la prevista eccezione del composto contenente stagno, le fasi γ sono tutte metalliche.

In tutte le nuove fasi quaternarie gli atomi di alluminio e quelli di litio condividono statisticamente le stesse posizioni reticolari. Nei sistemi quaternari Li/Sr/Al/Tt (Tt = Si, Ge) sono state scoperte tre nuove strutture. La prima struttura, quella del composto $Li_xSrAl_{1-x}Tt$ ($x = 0.5$, Tt = Si, Ge), presenta strati formati dagli elementi del 14° gruppo e da alluminio/litio ed è isostrutturale ed isoelettronica col composto NaAlSi. Il secondo composto, $Li_{2+x}Sr_2Al_{6-x}Si_6$ ($x \sim 2.8$), cristallizza in un nuovo tipo di struttura che può essere definita come un intermedia tra la struttura di $BaAl_4$ e quella di $Li_xSrAl_{1-x}Tt$. La terza fase, $Li_{3+x}Sr_5Al_{16-x}Si_{12}$ ($x \sim 6.2$), presenta invece un reticolo simile a quello delle zeoliti formato da silicio, alluminio e litio. Nei canali sono presenti atomi di stronzio e litio. Tutti questi composti sono, come previsto, metallici.

Nei sistemi quaternari Li/Ca/Al/Tt (Tt = Si, Ge) sono stati osservati due nuovi composti isostrutturali. Le fasi $Li_xCaAl_{1-x}Tt$ ($0.4 < x < 0.6$, Tt = Si, Ge), anche se isoelettroniche con i composti di stronzio, cristallizzano in una nuova struttura. L'intervallo di esistenza di queste fasi è stato determinato. La fase contenente silicio presenta una superstruttura che è stata investigata in dettaglio. Tuttavia, anche nella superstruttura, sussistono dei

blocchi dove le posizioni litio/alluminio sono occupate statisticamente. Anche questi ultimi due composti sono dei metalli.

La fase ternaria SrGaSi cristallizza secondo la struttura dell'AlB_2 e, come recentemente scoperto per altri composti isostrutturali, diventa un superconduttore a temperature inferiori a 4.5 K. Perciò la struttura elettronica è stata studiata con attenzione. I piani formati da atomi di gallio e silicio sono caratterizzati da stati π^* semioccupati, il composto è quindi metallico e con proprietà paramagnetiche (paramagnetismo di Pauli).

1. Introduction

1.1 Intermetallic Compounds

In the last 20 years, a large number of inorganic compounds has been synthesized and their study has given much information about structure property relationships in the field of semiconductor cluster or Zintl compounds. Nevertheless, we still know much less about structure and chemical bonding in Zintl phases and intermetallic compounds than in other classes of chemical compounds. Since the majority of the chemical elements are metals, the combinatorial potential for the syntheses of new compounds is huge, of which only a small part has been studied yet.

The chemical bonding in these structures is complex, but, to an increasing extent, it is becoming quantitatively determinable and therefore clearer [1-3]. Figure 1.1 gives an overview of the correlation between classes of chemical compounds, electron counts, and structural elements. Among the earliest systems to be understood electronically were the salt-like compounds, in which cationic and anionic components attain a complete octet or an 18-electron shell.

The Zintl phases, with their various anion frameworks, now form a large family of compounds whose electron structures mostly conform to the 8-N rule (see chapter 1.3). Borderline cases of Zintl phases, that is, those exhibiting "locally delocalised electrons" and not conforming to either the 8-N rule or the Zintl-Klemm concept, mark the transition to the intermetallic phases (marked in grey in Figure 1.1). This transition can be investigated by systematic chemical combination: in the last years a large number of new intermetallic phases located in the neighbourhood of the Zintl phases have been synthetised in this way.

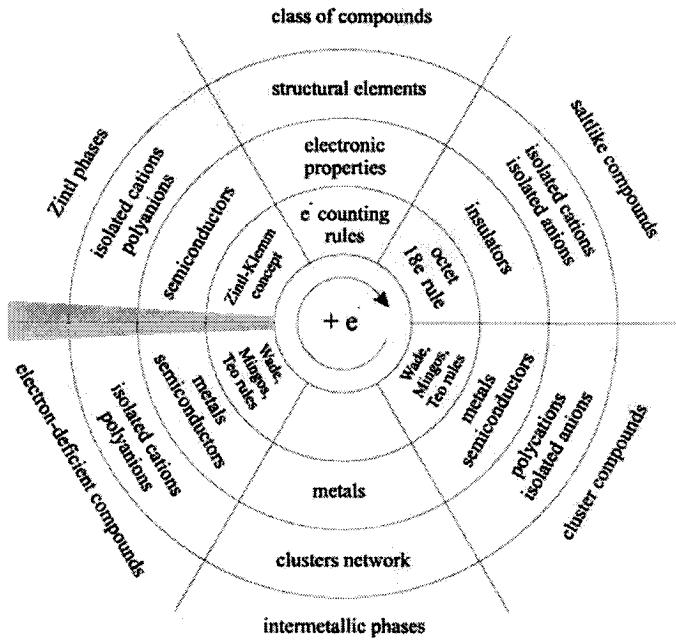

Figure 1.1: Relations between classes of chemical compounds through the comparison of structural elements, electronic properties, and electron-counting rules. The part investigated in this work is marked in grey.

The definition of the intermetallic compounds as a uniform family is not easy. The simplest definition would be that intermetallic phases are (1) compounds between metals and (2) metallic conductors. However, both definitions cannot really discriminate between Zintl phases and intermetallics. W.B. Pearson has distinguished five groups of intermetallic phases [4]:

1. Compounds with dense packing
2. Compounds in which the band-structure energy accounts for a large part of the total energy.
3. Compounds with framework structures. In these structures, all atoms form a common framework and they do not follow the valence and valence-electron-concentration rules.
4. Compounds with hybrid framework structures such as $BaAl_4$. These contain partial structures made up of one or more types of atoms, which depend in certain ways on the number of valence electrons.

5. Pearson named valence compounds, that is, compounds that follow the valence rules, as the fifth group. However, these have been better classified as Zintl phases.

In numerous investigations Burdett and Hoffmann investigated structure – electronic structure correlations by a diversity of projection methods based on Extended Hückel band structure calculations [2,5-18]. The essence of which was that there are hardly new bond types found in intermetallics but the multicenter cases are more frequent and polymer dependent states (bands) are in some cases not easily broken down to local bonding schemes. Still it had to be explained why intermetallics have a completely own structural chemistry. Quite recently, Nesper and Häussermann could show that bonding in intermetallics can be quantified based on electron localization calculations [19], one result of which is that the coexistence of a large variety of different bond types leads to their characteristic structures. In contrary to the Zintl-Klemm concept one might argue that the electron transfer of all valence electrons into basically semimetal centered states is not anymore true. However, this has still to be verified on a broader level.

1.2 The Zintl Border

One of the first classifications of chemical substances that students learn is to distinguish between metals and nonmetals. With respect to the chemical elements, many published periodic tables highlight this distinction with a bold-faced zigzag line as demarcation between metals lying to the left and nonmetals to the right. Of course, this is not strictly true. Closer examination of the elements near this line, usually known as the Zintl border, (see Table 1.1) shows that room temperature electrical conductivities, melting points, and Pauling electronegativities drop significantly from group 11 metals (Cu, Ag, Au) to group 12 metals (Zn, Cd, Hg).

Table 1.1: elements on the Zintl border, their structure types, Pauling electronegativities, electrical conductivities, and melting points.

Zintl Border

11	12	13	14	15	16
Element (Structure type)		**Al** (fcc)	**Si** (diam)	**P** (ortho)	
χ (Pauling electronegativities)		1.61	1.90	2.19	
σ [$10^6 \cdot \Omega^{-1} \cdot cm^{-1}$] (293 K)		0.377	$2.52 \cdot 10^{-12}$	10^{-17}	
Melting Point [°C]		660.4	1410	44.1	
Cu (fcc)	**Zn** (hcp)	**Ga** (ortho)	**Ge** (diam)	**As** (rhom)	**Se** (hex)
1.90	1.65	1.81	2.01	2.18	2.40
0.596	0.166	0.0678	$1.45 \cdot 10^{-8}$	0.0345	10^{-16}
1083	419.5	29.8	937.2	816 (28 atm)	217
Ag (fcc)	**Cd** (hcp)	**In** (tet)	**Sn** (tet)	**Sb** (rhom)	**Te** (hex)
1.93	1.69	1.78	1.96	2.05	2.10
0.630	0.138	0.116	0.0917 β-Sn	0.0288	$2 \cdot 10^{-6}$
961	320.8	156.6	232	630.7	452
Au (fcc)	**Hg** (rhom)	**Tl** (hcp)	**Pb** (fcc)	**Bi** (rhom)	**Po** (sc)
2.54	2.00	2.04	2.33	2.02	2.00
0.452	0.0104	0.0617	0.0481	0.00867	0.0219
1064	-38.9	303.5	327.4	271.4	254

Furthermore, the structures change from cubic closed packing (ccp) to highly distorted hexagonally close packed (hcp) variants (*c/a* ~ 1.85 in Zn and Cd instead of the ideally 1.63 for hcp), which indicates either some degree of directional bonding or large polarizabilities of these elements or both.

Thus Klemm has called the group 12 metals, as well as In, α-Tl, and β-Sn, metametals [20], some others named them metalloids. To the right of the metametals the semimetals and semiconductors are found, to the left the classical metals. This classification of Klemm is shown in Figure 1.2 where the metametals are grey coloured.

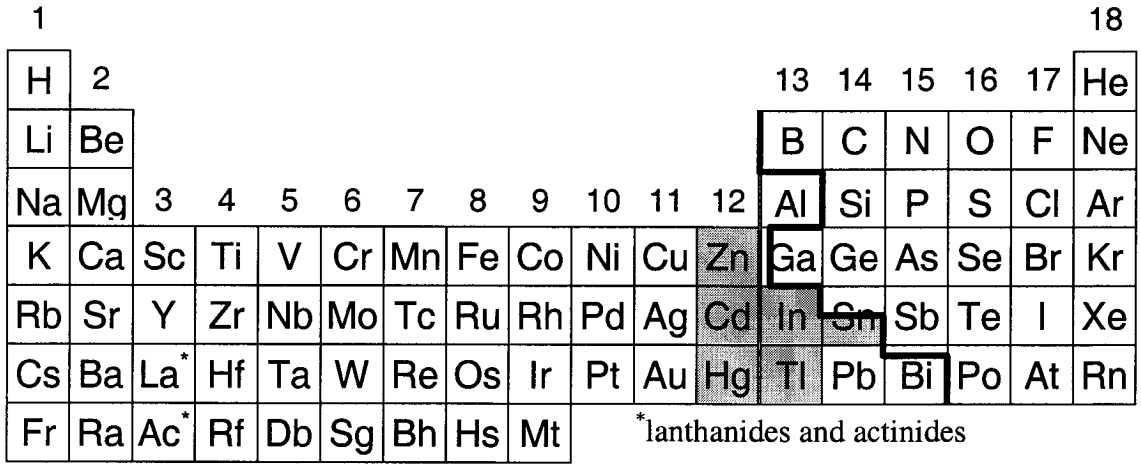

Figure 1.2: Periodic table of the elements showing the border between metals (left of double line) and metametals according to Zintl. The solid line is the dividing line between nonmetals and metals later given by Klemm [21]. Elements considered to be metametals group around this demarcation line and are marked in grey.

Elemental tin occupies the borderline position between semiconductors and metametals due to the occurrence of both α(grey)-Sn (diamond structure; semiconducting) and β(white)-Sn (tetragonal distortion of diamond; metallic). In fact, the β modification may be considered as a bordercase between semimetals and metametals. Furthermore, Al mostly resembles the normal metals, but, like all of the metametals, it becomes superconducting at temperatures below 10 K. Gallium behave in many compounds like a semimetal but melts at 28°C.

1.3 Zintl Phases

Eduard Zintl founded with his fundamental work [22-26] the basis for a fascinating class of compounds, the Zintl phases. Despite the great number of known representatives, the extent of the Zintl phases is not yet foreseeable [27]. Yet it is well accepted that nearly all structural and chemical trends observed in families of classical compounds are present and in addition, some novel features which have not hitherto been observed elsewhere [28-30].

Constituent of Zintl phases are typically metals and metametals. The Zintl phases are a bridge between the classical valence compounds (molecules, salts) and the metallic intermetallic phases. They are especially interesting because of their extraordinary structural variety. The metametal substructures can be build zero-, one-, two-, or three-dimensional polyanionic frameworks. The bonding structure of these frameworks can usually be described by combining the (8-N) rule with structural information and also with the help of empirical concepts which have been formulated in different ways by several authors (Mooser & Pearson [31], Parthé [32], Schäfer [33],Nesper & v. Schnering [34], Nesper [35]). In some though rare cases Zintl phases exhibit coexistence of cationic and anionic clusters [1,36,37].

1.3.1 The Zintl-Klemm Concept and the Zintl Phases

Mooser and Pearson [38] as well as Klemm and Busmann [39-41] found a correlation between the generalised (8-N) rule and the possible anionic substructure in normal valence compounds A_aX_x. The Zintl-Klemm-Busmann concept (ZKB or Zintl-Klemm concept) states [41]:

> *Formulated in extreme terms, the non-noble metal transfers electrons to the more noble component of the alloy, the "anion former". With the resulting outer electronic configuration an "anion partial lattice" is constructed whose atomic arrangement corresponds to the element having the same number of valence electrons.*

In the ensuing years a large number of new Zintl phases were discovered that also contain complex anions. On this base Schäfer and Eisenmann developed an extension of the definition of Zintl phases, going beyond the concept of isostructural relationship to structure of the elements with the same number of valence electrons [33].
Nesper proposed [35] that the Zintl phases show the characteristics of normal valence compounds, meaning:

- There is a well-defined relationship between the chemical structure of a Zintl phase and its electronic structure. For the majority of these compounds, short interatomic X-X contacts represent two-centre two-electron bonds, and the octet rule is satisfied for both components. Klemm proposed to view the charged $[X^{(a\cdot\alpha/x)-}]$ unit as a x or

pseudo-element [42] (or a set of pseud-atoms, if N_X is not an integral number), which exhibits a structure closely related to the isoelectronic element [21].

- Zintl phases are either semiconductors, or the incompletely occupied states at the Fermi level are centered on the anionic network. The difference between a semiconductor and an insulator is based empirically on the size of the band gap. The usual limit is taken at 2.0 eV.

- Zintl phases are usually diamagnetic, but may have paramagnetic centers, e.g. local radicals.

These three criteria are valid for all semiconducting valence compounds and thus do not differentiate Zintl phases from other classical semiconductors. Hence discrimination is difficult. One may insist on having oligo- or polyanionic units in Zintl phases to allow for a more accurate classification. In this case there are always regions of cation-anion interactions and others with predominantly covalent bonds. An important role is played by the electropositive components which do not simply provide electrons to the electronegative partners, but control the structure of the covalent network, playing some sort of templating effect. Recent investigations show that the concept is resilient even when compounds exhibit semimetallic or metallic properties as long as the preffered localisation of occupied states is kept as a criterion [30].

The Zintl-Klemm concept and its present extensions are quite useful for assessing structure and properties, but they do not provide unique information. Given the number of allotropes for many of the elements, Klemm's pseudoatom concept provides potential models, but of course it cannot precisely predict structures.

In addition to compounds with structures obeying the Zintl-Klemm concept, in the last 20 years, many unusual phases have been discovered with polyanionic substructures and chemical composition related to normal Zintl phases but with valence electron numbers that do not strictly follow the simple (8-N) rule.

Nesper and von Schnering have already pointed out [43,44], that concepts such as Wade's cluster rule, delocalised molecule orbitals, or partial multiple bonding may then be introduced to described the electronic structure of polyanionic substructures. The Zintl-Klemm concept can therefore be extended, but there should be a clear way of

distinguishing the valence states of the polyanionic species from those of the metals or cations.

There are low dimensional metals with conducting bands that are clearly localised on the anionic framework sites [28-30].

1.3.2 Extensions of the Zintl-Klemm Concept

The basis of these electron counting rules is the assumption of a complete electron transfer from the electronegative metal A to the metametals X:

$$A_aX_x \longrightarrow \left(A^{\alpha+}\right)_a\left(X^{(a\cdot\alpha/x)-}\right)_x$$

To fill up the valence shell in the case of the formula A_aX_x, the x atoms X need 8·x electrons:

$$a \cdot V_A + x \cdot V_x = 8 \cdot x = E$$

V_a: *Number of valence electrons of* A V_x: *Number of valence electrons of* X

E = *Number of valence electrons per formula unit*

If the number of electrons transferred is not sufficient to fill the valence shells of the X atoms, covalent bonds must form. It is also possible, if there is a surplus of valence electrons or if the anionic component cannot accept the maximum transferable charge that covalent bonds form between the A atoms (clusters, polycationic substructures), or non-bonding electrons remain on the A atoms (non-bonding electrons pairs). The equation given before then becomes:

$$E = \left(8 - N_x\right) \cdot x + (N_A + e_A) \cdot a$$

N_x: *Number of covalent bonds per atom* X

N_A: *ibidem per atom* A e_A: *Number of valence electrons remaining on atom* A

This equation represents a generalised (8-N) rule which may be further extended by taking into account a parent structures which is transformed into the Zintl compound by generating defects in the semimetal framework. Around the defects then lone electron

pairs are localized to saturize the resulting dangling bonds. This leads to a straight forward correlation between parent structure, structure of the Zintl phase and electron count. For example, the compound $A_aX_x\square_d$ containing d defects, is then a derivative of the parent structure A_aX_{x+d}. The electron counting equation can thus be formulated as [34]:

$$E = (8 - N_x)\cdot x + (N_A + e_A)\cdot a + N^*\cdot d$$

N^*: *takes into account that the defects are isolated or neighbouring (for isolated defects:* $N^* = N_x$, *e.g. each isolated defects breaks* N_x *bonds and lead to* N_x *lone electron pairs)*

It is usually assumed that the A atoms formally transfer all of their valence electrons to the X atoms. In this case, there can neither be bonds between A atoms nor non-bonding electrons centred on A. When $N_A = 0$ and $e_A = 0$ the equation reduces to:

$$E = (8 - N_X)\cdot x + N^*\cdot d$$

The electron transfer concept is strictly formal and has generated a great deal of misunderstanding. Nesper pointed out that the enormous success of this electron counting rule has nothing to do with the effective electron transfer, but with the prefered location and the number of the occupied orbitals [35]. If these are centred exclusively at X atom sites, a counting scheme based on the formal charge transfer concept is absolutely correct. Quite recently this has been beautifully supported by calculations of the electron localisation function (ELF) for a large number of Zintl phases [28-30].

Seite Leer /
Blank leaf

2. Experimental and Theoretical Part

2.1 Starting Materials and Syntheses

The starting materials used for the syntheses of this work are summarised in Table 2.1. Almost all manipulations were carried out in a dry box (Mbraun) under argon atmosphere.

Table 2.1: Starting materials used in the syntheses.

Element	*Form*	*Purity [%]*	*Source*	*m.p. [°C]*	*b.p. [°C]*
Lithium	rod	99.9	Alfa	181	1342
Magnesium	powder	>99.8	Fluka	649	1107
Calcium	chips	99.8	Johnson & Matthey	839	1484
Strontium	granules	99.9	Alfa	769	1384
Aluminum	powder	99	Johnson & Matthey	650	2520
Gallium	chips	99.9999	Alfa	30	2205
Silicon	powder	99.99	Alfa	1410	2355
Germanium	powder	99.99	Alfa	937	2830
Tin	powder	99.5	Aldrich	232	2270

All syntheses were carried out in welded steal, niobium or tantalum tubes (external diameter: 10-15 mm, wall width: 0.5 mm). The tubes were chosen between 20 and 70 mm in length. For syntheses below 1363 K the metal tubes were heated in an evacuated quartz tube. For syntheses above 1363 K a corundum tube under outer argon pressure (about 1.1 bar) was used.

None of the alkali and alkali earth metals forms binary alloys with niobium or tantalum [45,46]. However, niobium and tantalum form a variety of binary alloys with aluminum, gallium, silicon, germanium and tin [45,46]. The reactivity of the elements of groups 13

and 14 towards the tube materials is nevertheless much lower than with the alkaline, alkaline-earth metals. However, the best results, i.e. the most pure samples, were obtained using tantalum tubes with the exception of gallium where the use of niobium tubes has to be recommended.

The metal tubes were pressed together at one end with a vice and then sealed by arc melting in an argon plasma (ca. 400 mbar). The tubes were then filled with the educts in a dry box under argon atmosphere. The open side was closed using a pair of pliers and then sealed under argon.

The majority of the syntheses were performed according to the temperature program in Figure 2.1. The normal heating rate r_1 employed was between 200 and 300 K/h. The reaction time t_1, reaction temperature T_1, cooling rate r_e were different for each synthesis, cooling rate r_2, temperature T_2 and reaction time t_2 were not in each case applied. All these parameters are discussed in a more detailed way in the preparative parts of each chapter.

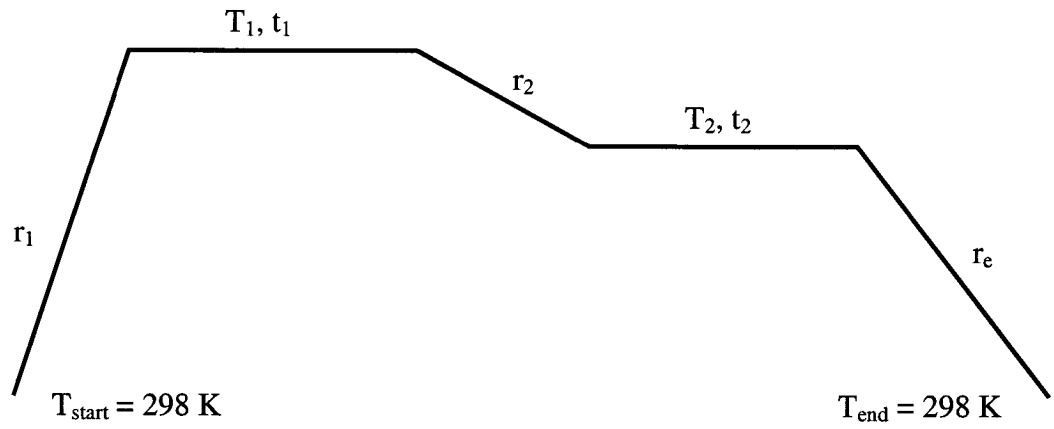

Figure 2.1: Typical temperature program for the chemical syntheses.

Often the syntheses were performed in two steps. After the first step the crucible was opened in the dry box and the product was ground in an agate mortar. The powder obtained was pressed to a pellet (diameter: 13 mm; thickness: ca. 1 mm) and used for subsequent syntheses. Specific deviations from this general preparative concept are discussed in the preparative part of each chapter.

The metal tubes were always opened in a dry box as the products are generally very sensitive to moisture and air.

2.2 Analyses and Data Processing

2.2.1 X-Ray Diffraction Analysis

2.2.1.1 Powder Diffraction Analysis

For the X-ray powder diffractometry analysis the samples were ground in a dry box using an agate mortar, then transferred into a glass capillary (Mark-Röhrchen, length = 80 mm, diameter = 0.1-0.5 mm). The capillaries were sealed in the dry box by welding with a red-hot platinum wire.

The powder diagrams were collected on a STOE powder diffractometer (STADI P2, germanium monochromator; $CuK_{\alpha 1}$ = 1.54056 Å; PDS detector with $2\Theta_{eff} \sim 40°$) using a Debye-Scherrer geometry. Calculations of theoretical powder diagrams, as well as data processing of the experimental powder diagrams were performed with the STOE program package. A background correction of the base line was applied to all measured powder diagrams.

The high temperature experiments were carried out using quartz instead of glas capillaries, these were then put into an oven (Anton Paar HTK1200) mounted on the same STOE powder diffractometer, were the diagrams were collected at different temperatures (up to 1200°C) using the PDS detector with $2\Theta_{eff} \sim 40°$. To avoid corrosion of the capillaries the oven was filled with nitrogen during the temperature treatments.

The powder diagrams used for the refinement of structures were collected using a small linear PDS detector with $2\Theta_{eff} = 7°$ (also Debye-Scherrer geometry) and a long exposition time (5 minutes/step; step width = 0.5°) to increase the quality of the diffraction data.

The refinement of structures using powder diffraction data was based on the Rietveld method and performed by the GSAS program [47].

The refinement technique used by this program is the least-squares method. As the minimisation problem is non linear the process is an iterative one. Table2.2 summarises the different definitions of the refinement parameters used in the GSAS program.

Table 2.2: Definition of the *R* value used in GSAS

Minimisation function	$M = \sum w(I_o - I_c)^2$
Reliability Factor	$R_p = \frac{\sum \lvert I_o - I_c \rvert}{\sum I_o}$
Weighted Reliability Factor	$wR_p = \sqrt{\frac{M}{\sum wI_o^2}}$
Goodness of fit	$\chi^2 = \frac{M}{(N_{obs} - N_{var})}$
"expected" wR_p	$wR_p = \frac{wR_p}{\sqrt{\chi^2}}$

2.2.1.2 Single Crystal Diffraction Analysis

Single crystals were selected in a dry box using a stereo microscope (M3Z, Wild), mounted on a 0.1 mm glass capillary with silicon grease, then inserted and sealed in a 0.3 mm glass capillary. Prior to using, the capillaries were heated to 200°C under vacuum (10^{-9} atmosphere) for about 6 h. Preliminary screening of the crystals was done on a Bürger precession camera.

The single-crystal measurements were performed on either a four-circle diffractometer STOE STADI 4 (graphite monochromator; MoK_α = 0.71073 Å), or a CCD-equipped diffractometer Siemens Platform CCD (graphite monochromator; MoK_α = 0.71073 Å). The cell parameters of the crystals measured on the CCD system diffractometer were redeterminated on the four-circle diffractometer. The data collection on the four-circle was performed with the program package of STOE (Lorenz and polarisation correction, Ψ-scan empirical absorption correction). For the data collection on the CCD system diffractometer the following programs were applied: SMART [48] for the data

collection, SAINT [48] for the data reduction and SADABS [49] for absorption corrections.

The following programs were used for the structure determination:

XPREP	unit cell reduction and determination of possible space groups according to the systematic absences and the internal R-value of the data [50]
SHELXS97	solution of crystal structures (direct methods, Patterson method) [51]
SHELXL97	refinement of crystal structures (full-matrix least-squares on F^2) [52]
PHASES	program package for the calculation and graphical representation of the electron density [53]
XPOW	simulation of powder diagrams based on the single-crystal data [50]
MISSYM	recognition and correction of misassigned space group symmetry according to the atomic coordinates [54]
STRUKTUR	structure model generation [55]
ORFFE	calculation of the atomic distances and angles [56]
ORTEP	graphical representation of crystals and molecular structures [57,58]
COLTURE	graphical representation of crystals and molecular structures [59]
CERIUS^2	graphical representation of crystals, molecular structures [60]

The definitions of the R-values, which are given for all structure refinements of single crystals, are given in the Table 2.3.

Table 2.3: Definition of the *R*-values

Reliability Factor	$R = \frac{\Sigma \left\| F_o \right\| - \left\| F_c \right\|}{\Sigma \left\| F_o \right\|}$
Weighted Reliability Factor	$wR = \sqrt{\frac{\Sigma w \cdot \left(F_o^2 - F_c^2\right)^2}{\Sigma w \cdot \left(F_o^2\right)^2}}$ $w = \frac{1}{\sigma^2\left(F_o^2\right) + (a \cdot P)^2 + b \cdot P}$ a,b = weight factors $P = \frac{F_o^2 (\geq 0) + 2 \cdot F_c^2}{3}$
Goodness of Fit	$GooF = \sqrt{\frac{\Sigma w \cdot \left(F_o^2 - F_c^2\right)^2}{n - p}}$ n: number of reflections p: number of parameters
Reliability Factor of collected Data	$R_{\text{int}} = \frac{\Sigma F_o^2 - \overline{F}_o^2}{\Sigma F_o^2}$

2.2.1.3 Superspace Description for Crystal Diffraction Analysis

The superspace description and superspace symmetry have been developed for incommensurately modulated structures. Presently, three kinds of incommensurate phases are known: incommensurately modulated structures, incommensurate intergrowth compounds and quasicrystals.

However, the superspace description and superspace symmetry can also be applied to structures with a commensurate modulation, where new, larger, basis vectors can be defined such that the 3-dimensional translation symmetry is restored.

A modulated structure can be considered as a perturbed periodic crystal, which has periodic distortions of the atomic position and/or the occupation probability of atoms from some basic structure. In general the distortion from the three-dimensional periodicity is periodic by itself.

A superspace group can be assigned to any structure for which the reflections can be divided into a subset of main reflections and a subset of satellite reflections. The simplest case is one-dimensional modulation. Then the diffraction vector **h** of each spot can be written with the unit vectors $\mathbf{a}^*$, $\mathbf{b}^*$, $\mathbf{c}^*$ in the reciprocal lattice of the basic structure and wave vector **q** of the modulation wave as

$$\mathrm{h} = h \cdot \mathrm{a}^* + k \cdot \mathrm{b}^* + l \cdot \mathrm{c}^* + m \cdot \mathrm{q}$$

where h,k,l,m are integers and the wave vector $\mathrm{q} = q_1 \cdot \mathrm{a}^* + q_2 \cdot \mathrm{b}^* + q_3 \cdot \mathrm{c}^*$; main reflections have $m = 0$.

The modulation wave is defined by modulation functions for the constituent atoms: each independent atom of the basic structure has its own independent modulation function. Displacive modulation and occupational probability are commonly encountered. The positions of the μth atom is given as the sum of its average position $\bar{\mathrm{r}}_\mu$ and a periodic function u_μ, which depends on the average position coordinates:

$$x_{\mu,i} = \bar{x}_{\mu,i} + u_{\mu,i}(\bar{x}_{\mu,4}) \;,\; \bar{x}_{\mu,4} = \mathrm{q} \cdot \bar{\mathrm{r}}_\mu + t$$

$$\bar{\mathrm{r}}_\mu = \left(\bar{x}_{\mu,1}, \bar{x}_{\mu,2}, \bar{x}_{\mu,3}\right)$$

The modulation wave is characterised by its modulation wave vector $q = (q_1, q_2, q_3)$.
The modulation function $u_{\mu,i}(\bar{x}_{\mu,4})$ is periodic with a period of 1:

$$u_{\mu,i} = A_{\mu,i} \cdot \sin(2\pi\bar{x}_{\mu,4}) + B_{\mu,i} \cdot \cos(2\pi\bar{x}_{\mu,4})$$

The occupation probability of the μth atom is then the sum of the average occupation probability $\overline{P}_\mu$ and a modulation function $p_\mu(\bar{x}_{\mu,4})$:

$$P_\mu = \overline{P}_\mu + p_\mu(\bar{x}_{\mu,4})$$

$$p_\mu = A_\mu \cdot \sin(2\pi\bar{x}_{\mu,4}) + B_\mu \cdot \cos(2\pi\bar{x}_{\mu,4})$$

In the formulae given t is a phase shift parameter which has, for commensurate modulated structures, a fixed value and for noncommensurate ones it is a variable.
The refinement of modulated structures was performed with the computing program JANA2000 [61].

2.2.2 Physical Analysis

2.2.2.1 DTA Analysis

The reaction temperatures were often selected according to thermal data measured by differential thermal ananlysis (DTA-TASC 414/2 system controller, DSC 404 high temperature oven; Netzsch). This method allows the determination of reaction temperatures, and melting or decomposition points. While the temperature in the DTA device is changed, the temperature difference between the sample and a reference probe is recorded. This difference arises because of endothermic or exothermic effects of the sample which are not present in the reference material. The amount of sample usually is of about 100-200 mg of ground material sealed under argon in a small niobium or tantalum crucible. The reference probes of Al_2O_3 are prepared in a similar way in open niobium or tantalum crucibles. The DTA experiments were performed under a constant pressure (ca. 1.1 bar) and flux (ca. 10 cm^3/min) of argon. In most cases two cycles of heating and cooling were performed.

2.2.2.2 Electrical Conductivity

The electrical conductivities were measured using tempered powder pellets (diameter: 6 mm, thickness: ca. 1 mm). A four-point contact method (with rhodium/iridium electrodes) was used: a constant current I was applied across two electrodes, while the potential across the two other electrodes was measured. The electrical resistance R can be calculated according to the Ohm's law $R = U/I$. According to this method the specific resistance ρ of the sample is only a function of the resistance R and the thickness d of the pellet. The specific electronic conductivity is the reciprocal value of the specific resistance. The measurements were performed in a dry box. The samples were cooled down to 11 K under vacuum using a two stage helium cryostat, and heated continuously to about 700 K under argon atmosphere.

In the case of metals the specific resistance at 0 K (ρ_{0K}) can be determined from the experimental data based on the temperature dependence of the electrical resistance:

$$\rho(T) = \rho_{0K} \cdot (1 + \alpha \cdot T)$$

For semiconductors the band gap can be calculated from the temperature dependence of the electrical resistance according to:

$$R = \frac{L}{A \cdot \kappa_0} \cdot e^{-\Delta E/2 \cdot kT}$$

L: length of the conductor [m] *A: section of the conductor [m^2]*

κ_0: specific electrical conductivity [S/m] *ΔE: band gab [eV]*

The band gap ΔE can be derived from a plot of $ln(R)$ or $ln(1/R)$ vs $1/T$, if a linear dependence is found. The values obtained must however be interpreted very carefully because of potential problems arising from the contacts, grain boundary effects, electrical corrosions, oxide films on the sample surfaces, or chemical reactions.

2.2.2.3 Magnetic Measurements

The magnetic measurements were performed on a SQUID magnetometer (MPMS 5S, Quantum Design) between 2 and 300 K in a constant magnetic field. The samples were finely ground and transferred into a small glass tube, which was mounted in the magnetometer in a small quartz tube. The diamagnetic contribution of the sample container was always subtracted.

The molar susceptibility χ_{mol} was calculated as follows:

$$\chi_{mol} = \frac{M \cdot m_{mol}}{H \cdot m} \text{ [cm}^3\text{/mol]}$$

M: magnetic moment [emu] *m: weight of the sample [g]*

H: magnetic field [G] *m_{mol}: molar weight of the sample [g/mol]*

Generally, the susceptibility is the sum of different contributions:

$$\chi_{mol} = \chi_{mol}^{para}(T) + \chi_{mol}^{TUP} + \chi_{mol}^{dia}$$

χ_{mol}: molar susceptibility

χ_{mol}^{para}: T-dependent paramagnetic contribution

χ_{mol}^{TUP}: T-independent paramagnetic contribution (Pauli paramagnetism)

χ_{mol}^{dia}: T-independent diamagnetic contribution

The total susceptibility is positive for paramagnetic and negative for diamagnetic substances. The susceptibilities of the different kinds of magnetic materials are distinguished by their different temperature dependences. Many paramagnetic substances obey the simple Curie law, especially at elevated temperatures.

According to this law the magnetic susceptibility is inversely proportional to the temperature:

$$\chi_{mol}^{para}(T) = \frac{C}{T}$$

C: Curie constant

The magnetic properties of materials are often conveniently expressed in terms of the magnetic moment, μ, since this is a parameter that may be directly related to the number of unpaired electrons present.

The relationship between χ and μ is:

$$\chi_{mol}^{para}(T) = \frac{N\mu^2}{3kT}$$

N: Avogadro's number *k: Boltzmann constant*

By comparing the two last equations we obtain:

$$C = \frac{N\mu^2}{3k}$$

and at any given temperature:

$$\mu = \sqrt{3k/N} \cdot \sqrt{\chi_{mol}^{para}(T) \cdot T} = 2.84\sqrt{\chi_{mol}^{para}(T) \cdot T}$$

Often, however, a better fit to the experimental data is provided by the Curie-Weiss law:

$$\chi_{mol}^{para}(T) = \frac{C}{T - \Theta}$$

Θ: Weiss constant

The Weiss constant is characteristic for each particular substance under consideration. By plotting the inverse of the molar susceptibility against the temperature, the constant *C* can be calculated from the slope of the linear function. This constant and the intercept with the y-axis are then used to calculate the Weiss constant Θ. The magnetic moment is then calculated as follows:

$$\mu = 2.84\sqrt{\chi_{mol}^{para}(T) \cdot (T - \Theta)}$$

A positive Θ indicates a net ferromagnetic coupling, and a negative one an antiferromagnetic interaction characteristic.

2.2.3 Theoretical Investigations

Theoretical investigations were performed using the LMTO method (Linear Muffin-Tin Orbital) [62-64] and the extended Hückel method. DOS (Density Of State), band structures and ELF (Electron Localisation Function) [28,29,65-68] were calculated using the density matrices obtained from both methods. For COOP (Crystal Orbital Overlap Population) calculations only the extended-Hückel method was used. Calculations and graphical representations were performed using the following programs:

TB-LMTO	Program package for LMTO calculations [69]
EHMACC	Extended-Hückel molecular and crystal calculations [70]
EHPC	Extended-Hückel property calculations [70]
GRAPA	Graphical representation of 2D-ELF distributions [71]
COLTURE	Graphical representation of crystal and molecular structures [59]

The scale used in the 2D-ELF pictures, the parameters used for all the calculations, and the Brillouin zones of the Bravais lattices used in the band structure calculations are given in the chapters A.2-A.4.

3. Ternary Systems

3.1 The Lithium/Triel/Tetrel Systems

3.1.1 The Lithium/Aluminum/Silicon System

Literature Results:

The LiAlSi phase was the first ternary compound found in this system more than 40 years ago [72,73]. In this compound the Al- and the Si-atoms forma zinc blende network, and the Li atoms occupy those octahedral holes next to the more electronegative silicon species (Fig.3.1) ($F4\bar{3}m$, a = 593.5 pm).

For a long time, no other ternary Li/Al/Si compound turned up in literature until 1992 when Pavlyuk and coworkers [74] were able to solve the structure of the new ternary $Li_{12}Al_3Si_4$ compound which crystallises in the space group $I\bar{4}3d$ (a = 1062 pm) and can be understood as a superstructure to the hardly understood $Cu_{15}Si_4$ type.

In contrast to the other tetrel (Tt) elements no lithium rich "Li_2TrTt" compounds (Tr = triel element, i.e. B-Tl) were observed in this ternary system.

This work:

During this work the three new ternary phases α-, β-Li_5AlSi_2 and $Li_{4+x}Al_{2-x}Si_2$ were isolated and crystallographically characterised. The first crystallises in a tetragonal space group and the two electronegative species build a distorted cristobalite network. The second is the high temperature modification and is cubic. The third crystallises in a hexagonal space group with the Li_2ZnSi structure type.

3.1.2 The Lithium/Aluminum/Germanium System

Literature Results:

The first compound found in this system was LiAlGe which is isostructural to LiAlSi,

(a = 597.7 pm) [72,73]. The existence of a cubic Li_2AlGe phase (a = 616(3) pm) was

postulated from data [75], but no refined structure could be provided. It seems to be a LiAlGe structure filled with lithium atoms.

This work:

During this work the three new ternary phases α-, β-Li_5AlGe_2 and $Li_{4+x}Al_{2-x}Ge_2$ (x ~ 1) were isolated and characterised. The first crystallises in a tetragonal space group and the two electronegative species build a distorted cristobalite network. The second is the high temperature modification and is cubic and could be the compound found by Bockelmann. The third crystallises in a hexagonal space group with the Li_2ZnSi structure type.

3.1.3 The Lithium/Gallium/Silicon System

Literature Results:

The first compound found in this system was the, to the LiAlSi isostructural, LiGaSi [72] (a = pm). Some other compounds were found in diffraction diagrams [75], but no refined structure could be provided. The reflections of a high temperature hexagonal phase (a = 413 pm, c = 667 pm) isostructural to the LiGaGe compound were found. Also two cubic F phases with the composition of $LiGaSi_x$ ($0.05 \leq x \leq 0.4$, and 615 pm $\geq a \geq$ 611 pm) and Li_2GaSi_x ($0.2 \leq x \leq 1$, and 622 pm $\geq a \geq$ 612 pm) were observed.

This work:

During this work the new ternary phase $Li_{4+x}Ga_{2-x}Si_2$ was isolated and characterised and crystallises with the Li_2ZnSi structure type.

3.1.4 The Lithium/Gallium/Germanium System

Literature Results:

In this system the first structure which was refined is the LiGaGe. This phase crystallises in the hexagonal space group $P6_3mc$ (a = 417 pm, c = 678 pm) [76]. In this compound the electronegative elements build up a wurtzite network and the lithium atoms occupy the octahedral holes (Fig.3.2).

Beside this compound four cubic F phases with the composition of $LiGaGe_x$ ($0 \leq x \leq 0.2$, and 619 pm $\geq a \geq$ 612 pm), Li_2GaGe_x ($x \sim 0.2$, and a = 626 pm), Li_2GaGe_x ($0.6 \leq x \leq 0.8$, and 615 pm $\geq a \geq$ 613 pm), and $Li_8Ga_5Ge_3$ (a = 613 pm) were observed [75,77]. In the cited article the existence of an hexagonal phase with cell parameters (a = 437 pm, c = 820 pm) very close to our new compound is postulated, however by a total different Li/Ga/Ge ratio: $Li_2GaGe_{0.4}$ vs $Li_{4+x}Ga_{2-x}Ge_2$ ($x \sim 1$).

This work:

During this work three new ternary phases α-, β-Li_5GaGe_2 and $Li_{4+x}Ga_{2-x}Ge_2$ were isolated and characterised. The first crystallises in a tetragonal space group and the two electronegative species build a distorted cristobalite network. The second is the high temperature modification and is cubic. The third crystallises in a hexagonal space group with the Li_2ZnSi structure type.

3.1.5 The Lithium/Gallium/Tin System

Literature Results:

In this system four compounds had already been discovered [78] two of which were also crystallographically characterised: LiGaSn (*Fd-3m*, a = 632.9 pm) with a disordered zinc blende arrangement of the Ga and Sn, the two hexagonal *P* phases $Li_3Ga_3Sn_2$ (a = 445.4 pm, c = 1090.0 pm) and $Li_5Ga_5Sn_3$ (a = 447 pm, c = 4220 pm), and Li_2Ga_2Sn (*P6₃/mmc*, a = 441.1 pm, c = 2164.5 pm) where the Ga/Sn atoms build a network which is a mixture between the zinc blende and the wurtzite structure.

3.1.6 The Lithium/Indium/Tetrel Systems

LiteratureResults:

In these three ternary systems four cubic *F* phases were discovered but the structure of none of them could be refined [75,79].

In the silicon system the two cubic phases Li_2InSi (a = 677 pm) and $Li_8In_5Si_3$ (a = 678 pm) were observed. In the germanium system the cubic LiInGe (a = 630 pm) and in the tin system the LiInSn (a = 667 pm) were observed.

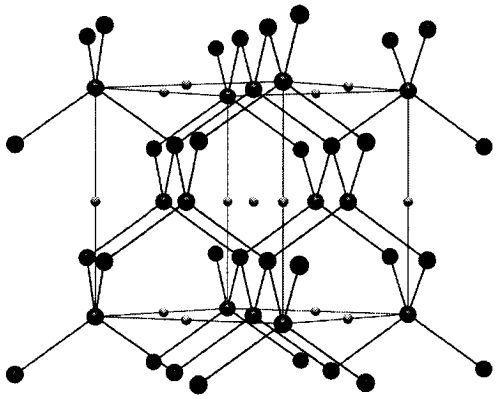

Figure 3.1: The LiAlSi structure
(Si black, Al grey, Li light grey)

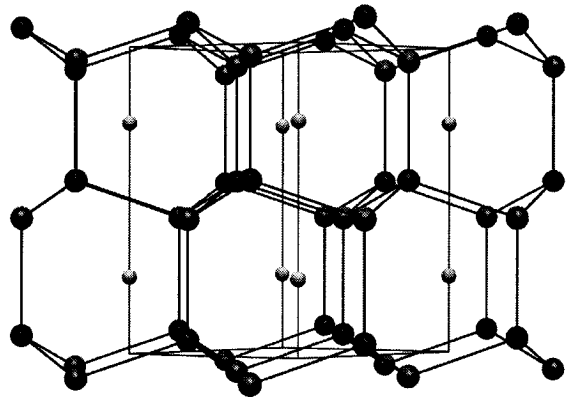

Figure 3.2: The LiGaGe Structure
(Ge black, Ga grey, Li light grey)

3.2 The Calcium/Triel/Tetrel Systems

3.2.1 The Calcium/Aluminum/Tetrel Systems

Literature Results:

In the ternary system Calcium/Aluminum/Silicon there are two known phases: the trigonal $CaAl_2Si_2$ ($P\bar{3}m1$; a = 413 pm, c = 714.5 pm) [80], and the orthorhombic $Ca_3Al_2Si_2$ (*Immm*; a = 400 pm, b = 1824 pm, c = 457.6 pm) [81]. In the first structure, a Zintl compound, (Fig. 3.3) two dimensional rafts of Ca^{2+} ions are separated by tightly bond $[Al_2Si_2]^{2-}$ layers, each atom in the layer is four-coordinate, but the coordination of the silicon is most unusual: a flipped tetrahedron or umbrella shape. The second compound shows one dimensional chains of hexagon of Al/Si separated by the Ca^{2+} ions.

In the ternary system Calcium/Aluminum/Germanium there are three known compounds. The first two are the isostructural to the Al/Si compounds: the trigonal $CaAl_2Ge_2$ ($P\bar{3}m1$; a = 416.7 pm, c = 721.1 pm) [80], and the orthorhombic $Ca_3Al_2Ge_2$ (*Immm*; a = 408 pm, b = 1854 pm, c = 458 pm) [82]. The third compound is the orthorhombic $Ca_3Al_2Ge_3$ (*Pnma*, a = 1139.5 pm, b = 434.7 pm, c = 1483.3 pm) [83].

3.2.2 The Calcium/Gallium/Tetrel Systems

Literature Results:

In the ternary system Calcium/Gallium/Silicon there is one known compound: the hexagonal CaGaSi phase (*P6/mmm*; a = 411.7 pm, c = 442.6 pm) [84]. This compound crystallises in the AlB_2 structure type and shows graphite-like layers of statistically disordered Ga/Si atoms. This phase is isostructural to the new compound we found in the ternary system Sr/Ga/Si.

In the ternary system Calcium/Gallium/Germanium there is also one known compound: the hexagonal CaGaGe phase (*P6$_3$/mmc*; a = 422.5 pm, c = 1731.5 pm) [84]. This compound (Fig.3.4) is almost isostructural to the CaGaSi phase but shows a fourfold superstructure along the c-axis, due to the ordering of the Ga/Ge atoms within the layers and to the waving of the layers.

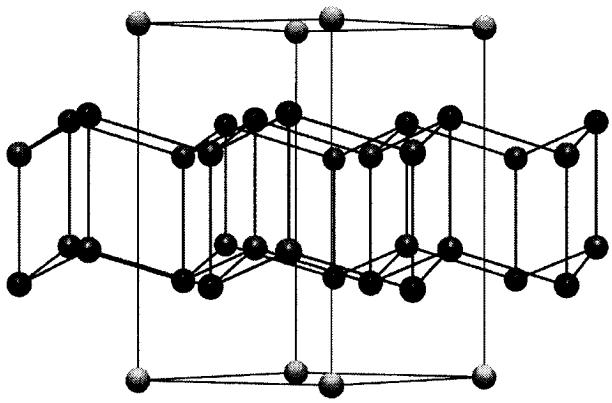

Figure 3.3: Structure of $CaAl_2Si_2$

(Ca light grey, Si black, Al grey)

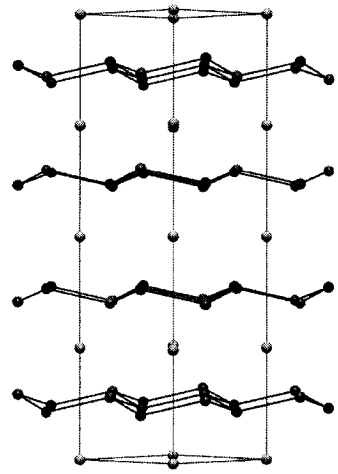

Figure 3.4: Structure of CaGaGe

(Ca light grey, Ge black, Ga grey)

3.3 The Strontium/Triel/Tetrel Systems

3.3.1 The Strontium/Aluminum/Tetrel Systems

Literature Results:

In the ternary system Strontium/Aluminum/Silicon there are four known compounds: the hexagonal SrAlSi phase (*P6/mmm*; a = 421.5 pm, c = 477 pm) [85], which crystallises in the AlB_2 structure type and is, therefore, isostructural to the CaGaSi phase; the trigonal $SrAl_2Si_2$ compound ($P\bar{3}m1$; a = 417.9 pm, c = 742.9 pm) [80] which is isostructural to the $CaAl_2Si_2$ compound (see Fig.3.3); the orthorhombic $Sr_3Al_2Si_2$ phase (*Immm*; a = 407 pm, b = 1899.1 pm, c = 482.5 pm) which is isostructural to the Ca compound; and the cubic $Sr_8Al_{16}Si_{30}$ ($Pm\bar{3}n$, a = 1047.67 pm) [86], which crystallises in the K_4Si_{23} structure type: a clathrate structure.

In the ternary system Strontium/Aluminum/Germanium there are two known structure in the literature: the $SrAl_2Ge_2$ phase ($P\bar{3}m1$; a = 422.5 pm, c = 744.8 pm) [80], and the $Sr_3Al_2Ge_2$ phase (*Immm*; a = 422 pm, b = 1921 pm, c = 486 pm) [82]. Both structure are isostructural with their silicon counterpart.

In the ternary system Strontium/Aluminum/Tin there is one known structure in the literature: the the $Sr_3Al_2Sn_2$ phase (*Immm*; a = 446.5 pm, b = 1979.5 pm, c = 494.4 pm) [87]. The structure is isostructural with its silicon counterpart.

3.3.2 The Strontium/Gallium/Tetrel Systems

Literature Results:

In the ternary system Strontium/Gallium/Silicon there was only one structure in the literature: the clathrate $Sr_8Ga_{16}Si_{30}$ ($Pm\bar{3}n$, a = 1045.95 pm) [86].

In the ternary system Strontium/Gallium/Germanium there are two published structures: the hexagonal SrGaGe ($P6_3/mmc$; a = 425 pm, c = 1863 pm) [84] which is isostructural with the Calcium phase (see Figure 3.4), and the clathrate compound $Sr_8Ga_{16}Ge_{30}$ ($Pm\bar{3}n$, a = 1073.43 pm) [86].

This work:

During this work a new phase was found: the hexagonal SrGaSi, which is isostructural with the CaGaSi compound and crystallises in the AlB_2 structure type.

4. Li_5TrTt_2 and $Li_{4+x}Tr_{2-x}Tt_2$ Phases

The ternary systems Li/Tr/Tt show a fairly uniform behaviour. For most of them there is a compound Li_5TrTt_2 which can occur in at least two modifications. New phases of the types α-Li_5TrTt_2 (Tr = Al, Ga; Tt = Si, Ge, and Sn), β-Li_5TrTt_2 (Tr = Al, Ga; Tt = Si, Ge), and $Li_{4+x}Tr_{2-x}Tt_2$ (Tr = Al, Ga; Tt = Si, Ge) were synthesized and their structures were determined.

4.1 The α-Li_5AlSi_2 Phase

In this work we succeeded in synthetising the new Zintl phase α-Li_5AlSi_2, which shows a novel 3D network of the electronegative atoms similar to that of cristobalite. The existence of a phase transition to a high temperature modification was also discovered. We could neither find literature data on this compound as well as on any other Zintl phase with this kind of network.

4.1.1 Synthesis

The compound was first successfully synthesized from a mixture of LiAlSi and $Li_{21}Si_5$, then also from the elements. The synthesis of pure-phase α-Li_5AlSi_2 appeared to be difficult: in almost all the synthesis the hexagonal $Li_{4+x}Al_{2-x}Si_2$ (x ~ 1) was also found among the products. This could be a sign of a possible phase transition between the two new phases, or of a peritectical decomposition of the cubic high temperature phase into the hexagonal one discussed later in this chapter.

Despite all, it was possible to synthezise a phase-pure compound. A stoichiometric mixture of the elements with small excess on Lithium (5% to compensate diffusion through the crucible) was heated at 625°C (t_1 = 8 hours, r_1 = 200°C/h, r_e = 25°C/h).

α-Li_5AlSi_2 forms grey-silver crystals with a metallic lustre. It is brittle like LiAlSi and also very air and moisture sensitive. By contact with water it reacts explosively like the Li_xSi, probably due to the formation of silanes SiH_x.

4.1.2 Crystal Structure

Crystals were difficult to find in the reaction product, moreover most of them were twins or intergrown species. Finally, very small crystals of good shape and quality were found and tested on a Bürger precession camera but, due to the small size of the crystals, the diffraction was to weak for the conventional four-circle STOE, the STOE IPDS, or the Siemens Platform CCD diffractometers.

Therefore a good set of crystal data was collected on a four-circle diffractometer using synchrotron radiation at DESY in Hamburg (HASYLAB synchrotron).

The Laue symmetry is *4/mmm* and the extinctions are consistent with the space group $I4_1/amd$ but no reasonable solution could be found in this space group.

The actual space group is in fact $I\bar{4}2d$: the *a*-glide plane extinctions arise from an *a*/2 pseudo translation in [100] direction (the *a* glide plane is fulfilled by Al1, Li1 and Li2 but it would translate Si1 into Li3). The structure was then solved in $I\bar{4}2d$ using direct methods. All atoms were anisotropically refined and the displacement parameters are all satisfactory.

The measurement parameters, the crystal data and parameters, the atomic coordinates, the anisotropic displacement parameters as well a selection of interatomic distances of the α-Li_5AlSi_2 structure are summarised in the Tab.4.1-4.

Table 4.1: Crystal data and parameters of the data collection for α-Li_5AlSi_2

Empirical formula	Li5AlSi2
Formula weight [g/mol]	117.86
Crystal size [mm]	0.04 x 0.04 x 0.04
Colour	silvery metallic lustre
Crystal system	tetragonal
Unit cell dimension [pm]	a = 617.0(2) pm; c = 1219.3(3) pm
Volume [pm^3]	$464(1)\cdot10^6$
Space group	$I\bar{4}2d$ (122)
Formula unit pro cell	4
ρ (calculated) [g/cm^3]	1.687
Absorption coefficient μ [mm^{-1}]	0.378
F (000)	224.0
Temperature [K]	298
Data collection	HASYLAB synchrotron, 4-circle diffractometer
Monochromator; Wavelength	flat Si(111) crystal; λ = 0.56000 Å
Scan parameters (steps; $\Delta\omega$; scan)	61; 0.020°; ω-θ - Scan
Theta range	$2° < 2\theta < 60°$
h(min), h(max); k(min), k(max); l(min), l(max)	-9, 9; -9, 9; 0, 18
Reflections collected	1717
Independent reflections	422; R(int) = 0.050
Independent reflections with $\|F\|^2 > 2\,\sigma(\|F\|^2)$	349
Absorption correction	Ψ-Scan
Refinement	SHELXL-97 (full matrix least-squares of F^2
Parameters	20
Restraints	0
Extinction coefficient	none
Maximal shift/esd	0.000
Mean shift/esd	0.000
Largest diff. peak and hole [electrons/$pm^3\cdot10^6$]	min = -0.31; max = 0.40
[a] wR for $\|F\|^2 > 2\,\sigma(\|F\|^2)$	0.0543
wR for all reflections	0.0578
[a] R for $\|F\|^2 > 2\,\sigma(\|F\|^2)$	0.0264
R for all reflections	0.0339
[a] Goodness of Fit (*GooF*) for all reflections	1.090

[a] the definitions are given in chapter 2.2, Table 2.3

Table 4.2: Wyckoff sites, atomic coordinates, and equivalent isotropic displacement parameters [pm^2] for α-Li_5AlSi_2

Atom	*Wyckoff site*	*x*	*y*	*z*	*U(iso)*
Si1	*8d*	0.2640(1)	1/4	1/8	81(2)
Al1	*4b*	0	0	1/2	117(6)
Li1	*4a*	0	0	0	220(20)
Li2	*8c*	0	0	0.2512(2)	110(20)
Li3	*8d*	0.7671(9)	1/4	1/8	440(30)

Table 4.3: Anisotropic displacement parameters [pm^2] for α-Li_5AlSi_2

Atoms	*U11*	*U22*	*U33*	*U23*	*U13*	*U12*
Si1	82(3)	84(3)	78(3)	8(1)	0	0
Al1	123(6)	*U11*	104(9)	0	0	0
Li1	220(20)	*U11*	200(20)	0	0	0
Li2	70(20)	150(30)	110(20)	0	0	10(10)
Li3	410(30)	510(30)	390(20)	130(20)	0	0

Table 4.4: Selected interatomic distances [pm] for α-Li_5AlSi_2

Al1	–Si1	261.19(9)	4x	Li1	–Li3	260.1(8)	4x	Li3	–Li1	260.1(8)	2x
	–Li3	272.3(9)	4x		–Si1	271.2(1)	4x		–Li2	261.0(8)	2x
	–Li2	303.4(3)	2x		–Li2	306.2(3)	2x		–Li2	271.5(9)	2x
	–Li2	308.49(3)	4x		–Li2	308.49(3)	4x		–Al1	272.3(9)	2x
									–Si1	305.12(6)	2x
Si1	–Li2	260.4(2)	2x	Li2	–Si1	260.4(2)	2x		–Si1	306.6(13)	1x
	–Al1	261.19(9)	2x		–Li3	261.0(8)	2x		–Si1	309.1(1)	2x
	–Li1	271.2(1)	2x		–Li3	271.5(9)	2x		–Si1	310.4(13)	1x
	–Li2	272.0(2)	2x		–Si1	272.0(2)	2x				
	–Li3	305.12(6)	2x		–Al1	303.4(3)	1x				
	–Li3	306.6(13)	1x		–Li1	306.3(3)	1x				
	–Li3	309.1(1)	2x		–Al1	308.49(3)	2x				
	–Li3	310.4(13)	1x		–Li1	308.49(3)	2x				

α-Li_5AlSi_2 crystallizes with a new ternary structure type (Fig.4.1). In this structure the anionic part $[AlSi_{4/2}]^{5-}$ sets up a 3 dimensional framework which is similar to the $SiO_{4/2}$ framework of cristobalite with aluminum on the silicon and silicon on the oxygen position.

The structure can be described by the formulation $(Li^+)_5\,{}^3_\infty[((4b)Al^-)((2b)Si^{2-})_{4/2}]$, which is in agreement with the Zintl-Klemm concept (chap.1). The expression (nb) means n-bonded species where a bond is assumed to be a twocenter-twoelectron bond. According to the Zintl-Klemm concept there is one four connected aluminum atom, isoelectronic to silicon, and one two connected silicon atom, isoelectronic to sulfur or oxygen. In an extreme but still conventional chemical view the compound may be called a lithium silicoaluminate in correspondence cristobalite as oxosilicate.

The network is only slightly distorted, the angles Si-Al-Si are only close to the tetrahedral angle of 109,5°. There are two different angles 109.91(2)° (4x) and 108.60(3)° (2x).

The distortion of the Si1 position from the ideal position is a consequence, of the steric lone pair activity at silicon which is enhanced by interactions with the cationic sublattice of lithium. In fact with the silicon lying on the ideal (1/4, 1/4, 1/8), the Si–Al bond distance would be 267 pm, which is probably too long, and a contraction of the cell parameters would lead to too short Li-Li distances.

The resulting Si–Al distance of 261.2 pm (Tab.4.4) in the anionic framework is slightly longer than that observed in the LiAlSi structure (256.8 pm) but still in the range of Si–Al covalent bonds.

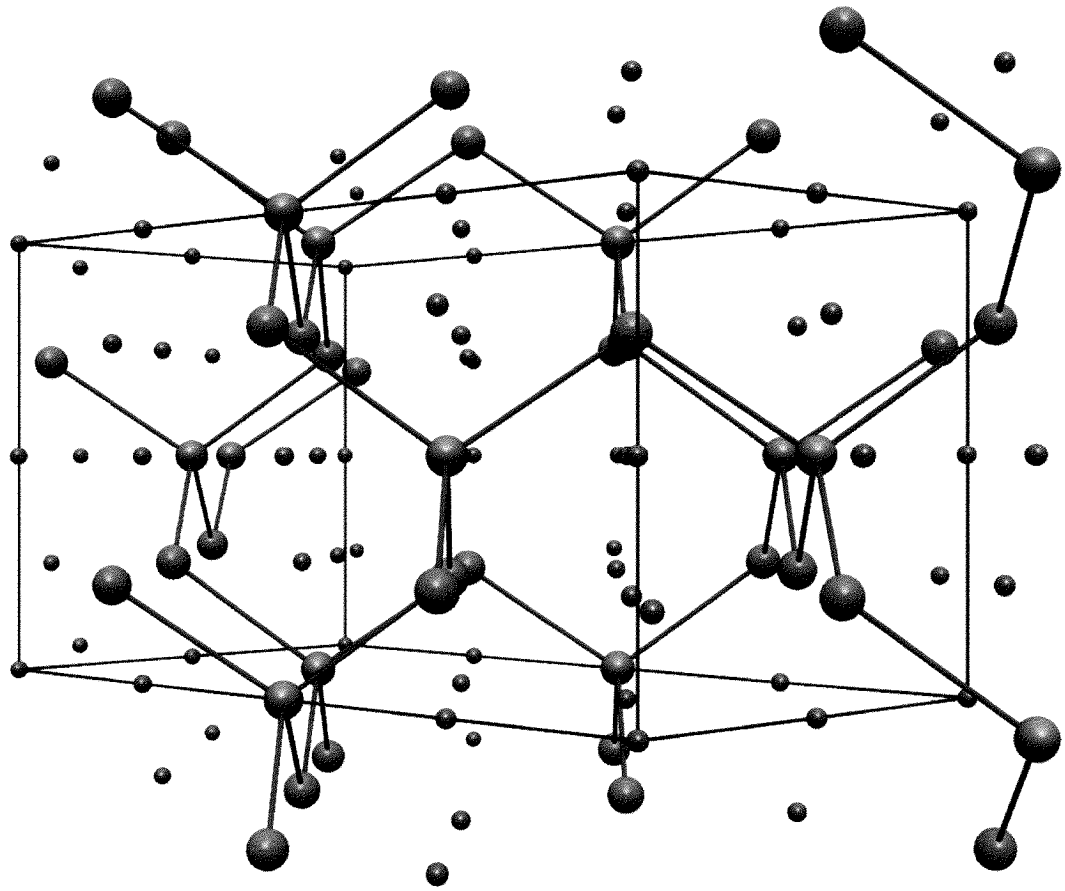

Figure 4.1: Structure of α-Li_5AlSi_2 (Si red spheres, Al green, Li grey)

The whole arrangement can also be seen as a distorted cubic closed packing (fcc) of the Li2 atoms with the octahedral holes occupied half by Al1 and half by Li1, the tetrahedral ones half by Si1 and half by Li3. In this respect, it is a coloured version of the Li_3Bi or the $FeAl_3$ type.

The Al1 atoms occupy half of the octahedral holes of the fcc arrangement of Li2 atoms and is therefore octahedrally coordinated by them (Fig.4.2 left), the Li3 atoms and the four covalently bonded Si1 atoms occupying each half of the tetrahedral holes build two tetrahedra around Al1.

It is important to note, that Al1 and Li1 positions together with the Si1 sites form a diamond network. This is of importance in order to understand the phase transition from this low temperature phase to the cubic high temperature modification β-Li_5AlSi_2, where these two independent crystallographic positions are merged to only one crystallographic site which is then exhibits mixed occupancy of the two atom types (cf. chapter 4.2).

The coordination of Si1 (Fig.4.2 right) is more complicated as it is surrounded by four Li2 atoms of the fcc arrangement building therefore a distorted tetrahedron, and by six Li3 atoms building a distorted octahedron. The two covalently bonded Al1 atoms arrange together with two Li1 atoms also to a distorted tetrahedron.

The resulting tetrahedron of Li2 around silicon is smaller than the tetrahedron of Li3 around the aluminum atoms, this is expected since the Zintl-Klemm description assigns a higher negative formal charge on the silicon, and is also understandable with the higher electronegativity of silicon.

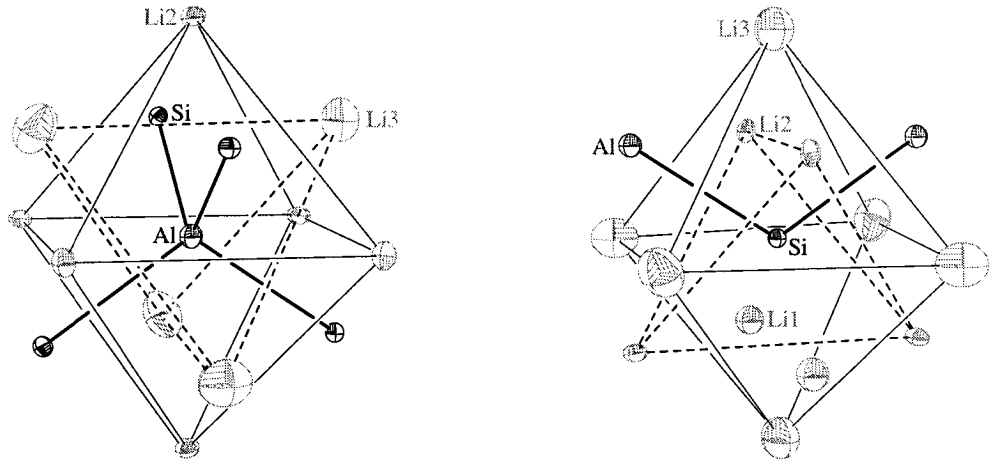

Figure 4.2: Coordination of Al (left) and Si (right) in α-Li_5AlSi_2

4.1.3 Physical Properties

The thermal properties of α-Li_5AlSi_2 were investigated on a pure phase sample. According to the DTA (Fig.4.3), as well as high temperature diffraction experiments, there is a first order phase transition at about 300°C to a cubic high temperature phase which was called β-Li_5AlSi_2 (cf. Chapter 4.2).

Another small reversible thermal effect was observed at the temperature of ~660°C. This effect could be due to another phase transition from the cubic β- to a γ-Li_5AlSi_2 phase, which is, probably, the hexagonal $Li_{4+x}Al_{2-x}Si_2$ (x ~ 1) phase (cf. Chapter 4.3). On the other hand this thermal effect could also be assigned to a peritectical decomposition of the tetragonal phase to the hexagonal phase and other binary compounds or one of the elements, since the composition of the hexagonal phase could not be accurately defined and likely there exists a phasewidth. Since in almost all the syntheses of the tetragonal α-Li_5AlSi_2 also the later phase was present it is hard to decide whether there is an incomplete transformation because of kinetic effects at the same stoichiometry or because of a slight change of stoichiometry.

At 820°C the melting temperature of the sample is found..

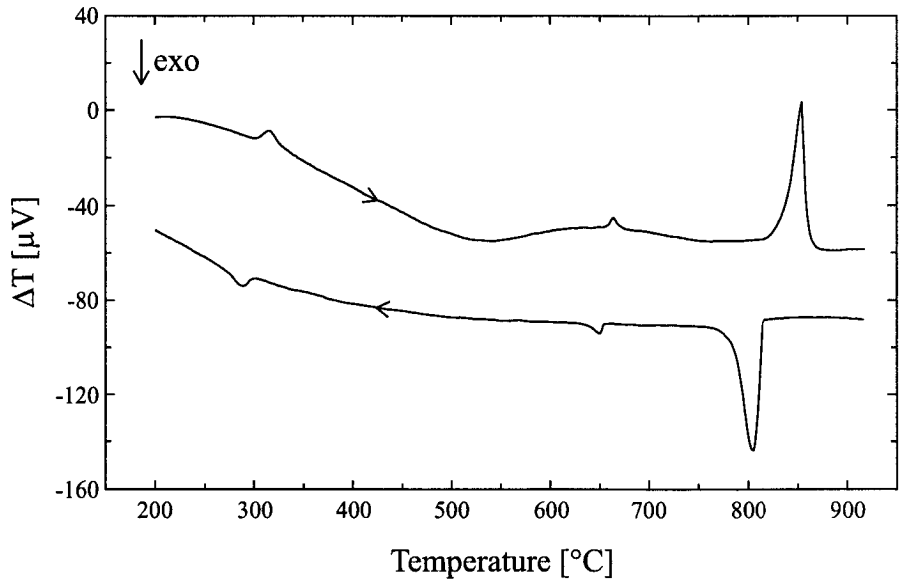

Figure 4.3: DTA of α-Li_5AlSi_2

Measurements of the conductivity were performed on pressed pellets (diameter = 6 mm; thickness = 0.75 mm), which were heated from one up to five days at 250°C.
However, the measurements turned out to be difficult cause grain boundary effects and contacts problems between pellets and electrodes, so the data turned out to contain large reproducibility errors.
Unfortunately no improvement of the quality of the pellets was possible since the tempering temperature had to be too low to prevent from the phase transition.

4.1.4 Theoretical Investigations

The bonding structure of α-Li_5AlSi_2 accords with the Zintl-Klemm concept. It is therefore expected that α-Li_5AlSi_2 would be a semiconductor like the typical Zintl phases and also like the LiAlSi phase[88]. The typical Zintl phases have low energy electronic states, centred on the anionic substructure, which are filled with electrons and empty high energy states that are centred on the cationic metal atoms.
In order to investigate the electronic properties and bonding structure of α-Li_5AlSi_2 we performed theoretical calculations using both EHMO and LMTO-methods (parameters: cf. Tab. A1 in Appendix).
As expected, the DOS calculated by the LMTO- as well as those by the EHMO-method shows a band gap at the electronic filling level (Fig.4.3 and Fig.4.4). The LMTO gap is small whereas that from the EHMO calculation is quite large. This effect is a general outcome for these two methods. Furthermore, it is enhanced due to the parameters of aluminum in the EHMO calculation, which are derived for the Al^{3+} cation more than for Al^- as in our case and thus the overlap integrals in the EHMO calculation are too small which is reflected by the small dispersion of the bands. In both cases the s- and p-block states are well separated in energy.

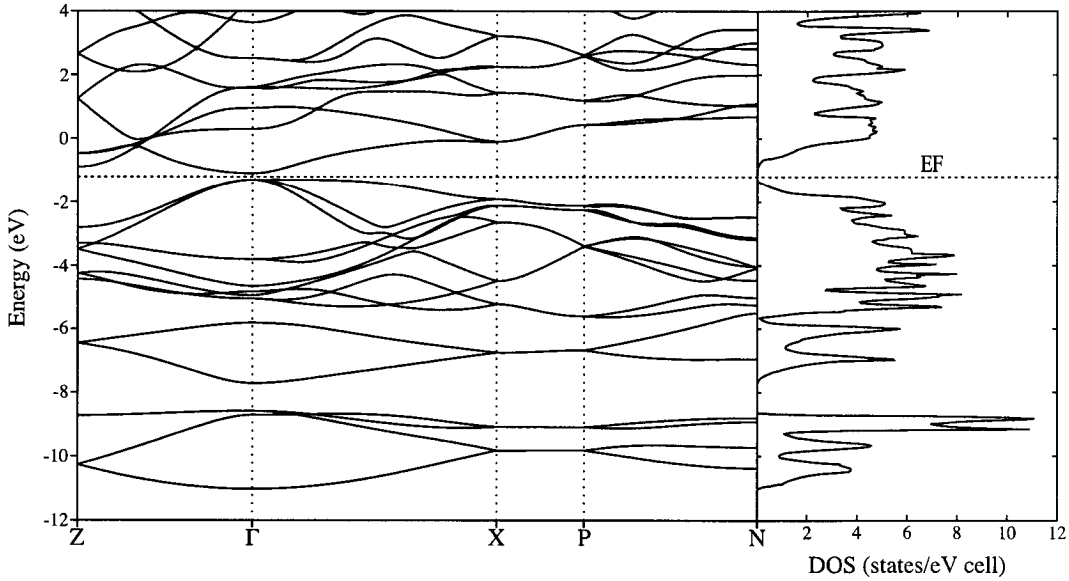

Figure 4.3: LMTO band structure and DOS of α-Li_5AlSi_2

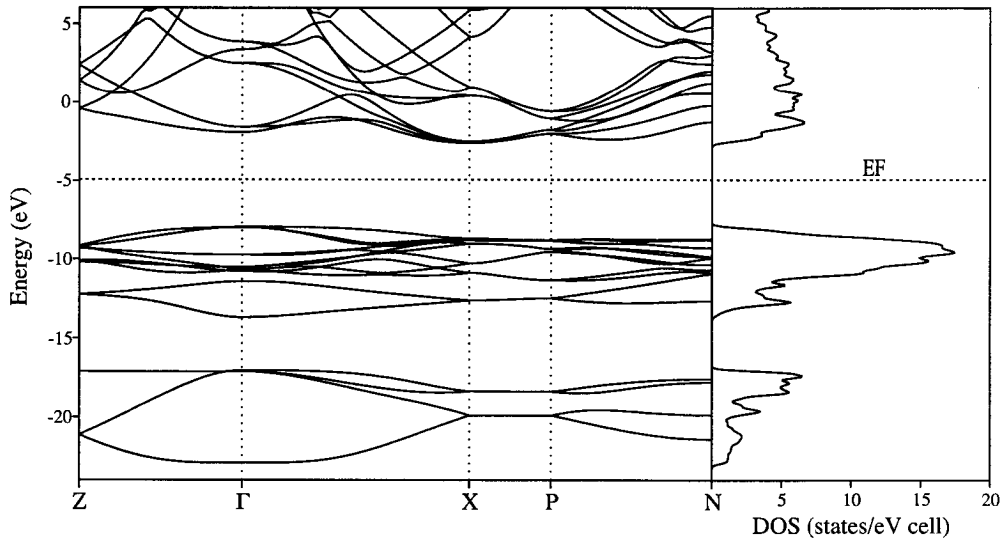

Figure 4.4: EHMO band structure and DOS of α-Li_5AlSi_2

In the Figure 4.5 the LMTO-ELF section along the cristobalite network of the α-Li_5AlSi_2 structure is shown. The ELF confirms the prevalent covalent character of the aluminum-silicon network, this is nicely shown by the high electron pair localisation between the two elements. Also the lone pair localised on the silicon pointing towards

the lithium atoms are nicely displayed in Figure 4.5 (bottom left and right), whereas the very low electron localisation between the lithium atoms and the two others centers is typical for ionic interactions. Furthermore, it is clear that silicon is the electron sink in these compounds as was already quantified in [89]. In addition, Figure 4.5 shows beautifully the change of the valence state distributions at silicon form polar covalency (second from left) over polar bonded plus lone pair (left/second from right) to a section of lone pair dominance. Note that these are just different section of one silicon center. All these results underline the typical Zintl phase character of the α-Li_5AlSi_2 structure and the counting concept of formal charges.

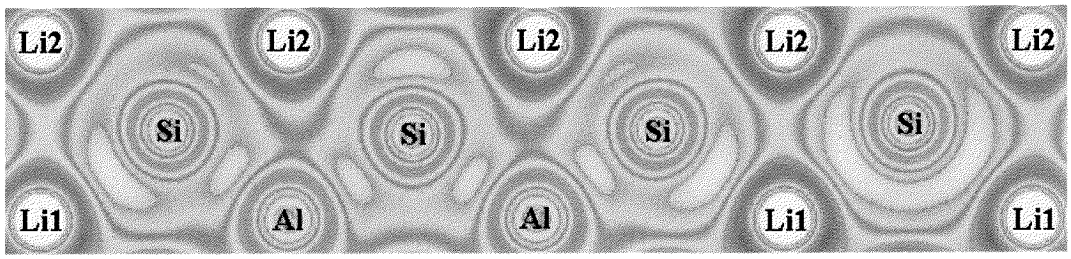

Figure 4.5: LMTO-ELF section along one part of the Al-Si network ($\bar{2}01$ plane)

4.2 The High Temperature β-Li_5AlSi_2 Phase

According to the DTA measurements (cf. Chapter 4.1.3), the tetragonal phase α-Li_5AlSi_2 undergoes a phase transition at the relatively low temperature of 300°C to the cubic high temperature modification β-Li_5AlSi_2. This phase transition was investigated by high temperature X-ray experiments.

4.2.1 Synthesis

An almost pure-phase β-Li_5AlSi_2 was obtained after synthesis from a stoichiometric mixture of the elements, with 5% excess on lithium to compensate the diffusion through the crucible walls during the reaction, heated at 625°C (t_1 = 4 hours, r_1 = 200°C/h). The reaction crucible was then quenched in order to avoid the phase transition to the low temperature phase α-Li_5AlSi_2.

4.2.2 Crystal Structure

Since the compound can only be obtained upon quenching the crystals found in the samples were all of very poor quality and no single crystal measurements could be carried out. However the obtained products were almost phase pure, therefore a Rietveld analysis of the powder diffraction could be performed (Fig.4.6), although the presence of some reflections, which could not be assigned to any known phases, strongly influenced the refinement of the structure.

For the refinement of the powder data the structure of the low temperature phase α-Li_5AlSi_2 was taken as the starting model. The Rietveld analysis was then carried out: it was possible to refine the cell parameters, the atomic position, the isotropic displacement factors (Tab.4.5-7) as well as the profile coefficients of the fitting curve.

However, as usual for Rietveld analysis, the refinement of all parameters at one time was not possible, the different parameters were then refined in different steps. The profile coefficients of the fitting curve (totally 8 coefficients were refined in different steps) turned out to be critical for a good refinement.

The occupancy of the mixed occupied M position was not refined. It was assumed that the position is equally occupied by lithium and aluminum (1:1), since this position results from the Al1 and Li1 positions of the tetragonal phase when the symmetry raises to cubic.

Table 4.5: Crystal data and parameters of the data collection for the β-Li_5AlSi_2

Empirical formula	Li5AlSi2
Formula weight [g/mol]	117.86
Crystal system	cubic
Unit cell dimension [pm]	a = 615.5(9) pm
Volume [pm^3]	$233(3)\cdot10^6$
Space group	$F\bar{4}3m$ (216)
Formula unit pro cell	2
ρ (calculated) [g/cm^3]	1.678
Absorption coefficient μ [mm^{-1}]	0.74
F (000)	112.0
Temperature [K]	298
Data collection	STOE STADI P2, PDS detector ($2\Theta_{eff}$ = 7°)
Monochromator; Wavelength	germanium; λ(CuKα) = 1.54056 Å
Scan parameters: step width; time/step	0.5°; 280 seconds
Theta range	20° < 2θ < 98°
Refinement	GSAS
Largest diff. peak and hole [electrons/$pm^3\cdot10^6$]	min = -0.71; max = 0.66
[a] wR_p	0.1365
[a] R_p	0.0930
[a] R_F	0.0817
[a] Goodness of Fit χ^2	2.00

[a] the definitions are given in chapter 2.2, Table 2.2

Table 4.6: Wyckoff sites, atomic coordinates, and equivalent isotropic displacement parameters [pm^2] for β-Li_5AlSi_2

Atom	*Wyckoff site*	*x*	*y*	*z*	*U(iso)*
Si1	4*c*	1/4	1/4	1/4	290(20)
M1	4*a*	0	0	0	260(20)
Li1	4*b*	1/2	1/2	1/2	260(20)
Li2	4*d*	3/4	3/4	3/4	820(50)

Table 4.7: Selected interatomic distances [pm] for β-Li_5AlSi_2

Si1	–M1	266.5(3)	4x	Li1	–Si1	266.5(3)	4x
	–Li1	266.5(3)	4x		–Li2	266.5(3)	4x
	–Li2	307.8(8)	6x		–M1	307.8(8)	6x
M1	–Si1	266.5(3)	4x	Li2	–M1	266.5(3)	4x
	–Li2	266.5(3)	4x		–Li1	266.5(3)	4x
	–Li1	307.8(8)	6x		–Si1	307.8(8)	6x

The quality of the Rietveld refinement is nicely displayed in the Figure 4.6, where the pink curve at the bottom represents the difference between the calculated data (blue line in the figure) and the measured reflection pattern (represented as red crosses).

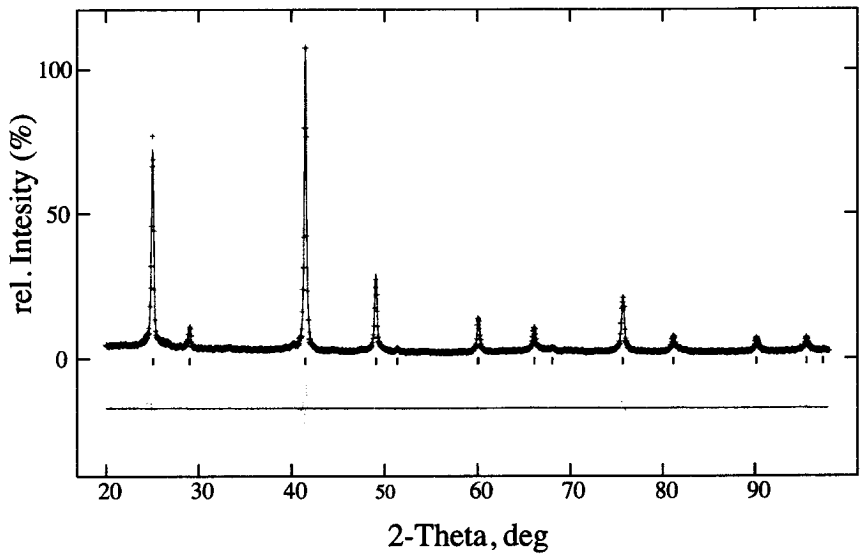

Figure 4.6: Rietveld Analysis of the high temperature modification β-Li_5AlSi_2

During the phase transition from the low to the high temperature structure the Al1 and Li1 positions of the low temperature phase mix on the M1 position, the c axis is stretched to $c' = 2a$, whereas the a axis is slightly compressed leading to a new cubic cell. This results in a small increase of the volume of about ~0.5% which is reasonable for a high temperature phase. Furthermore, it exemplifies that there is a volume part in the transition enthalpy, which is inline with a first order transition.

The mixing is the result of high mobility of the aluminum and the Li1 atoms of the low temperature phase. The consequence is that at temperature above 300°C the Al–Si bond are weak enough to permit this mobility.

The high isotropic temperature displacement observed for the Li2 atoms is indicative for a disordered position (Tab.4.6). A similar case occurs also for the low temperature phase (cf. Tab.4.3, Li3 position).

The structure of the high temperature modification β-Li_5AlSi_2 is shown in the Figure 4.7. The mixing of the Al1 and Li1 position of the low temperature phase becomes evident, the result is two interpenetrating zinc blende networks: one built of Si1-M1 and the other of Li1-Li2. In fact the M-Si network is isostructural to the Al-Si network of the LiAlSi structure (Fig.3.1), Li1 occupies the same position of Li in the cited structure, whereas the Li2 occupies the empty half of the tetrahedral holes of the fcc arrangement of Al in the LiAlSi structure.

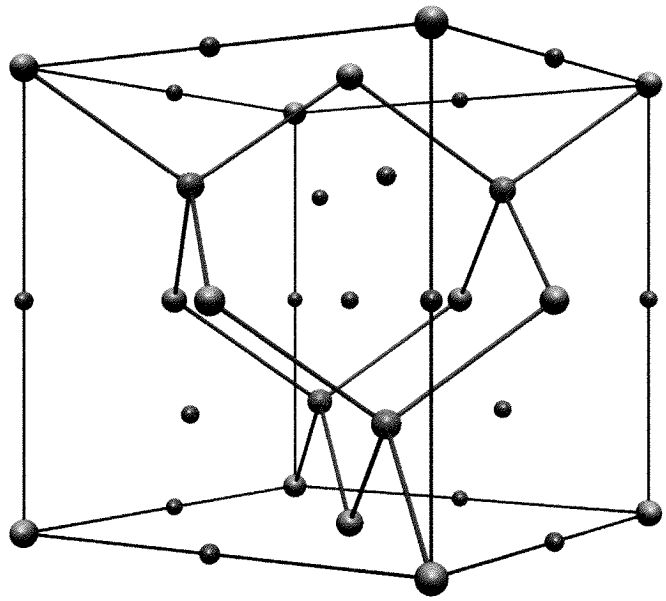

Figure 4.7: Structure of β-Li_5AlSi_2 (Si red spheres, M turquoise, Li grey)

The resulting Si–M distance (266.5 pm) is, as expected, an average of the Si1–Al1 (261.2 pm) and the Si1–Li1 (271.2 pm) distances in the low temperature phase (cf. Tab.4.4).

4.2.3 Physical Properties

In order to investigate the existence of a phase transition from the low temperature phase to the high temperature phase, X-ray powder diffraction experiments were carried out. The grounded sample was transferred to a glass capillary (0.3 mm), this was sealed and then inserted into one quartz capillary (0.5 mm), which was closed using wax in the glove box to avoid any contact with oxygen and moisture. The measurements were carried out by different temperatures (starting temperature 100°C, ending temperature 375°C, step 25°C, heat/cooling rate 50-100°C/h, holding time before the measurement 3-10 minutes, measurement time 5 minutes). Unfortunately, measurements at higher temperature were not possible because the capillaries corroded and broke. So the thermal effect at 625°C could structurally not be investigated.

In Figure 4.8 the resulting powder diffractograms from 250°C to 325°C and back to 250°C are shown. In the temperature range from 300 to 325°C the phase transition from the low temperature phase (tetragonal, the calculated position of the reflections is given in the figure) to the high temperature (cubic with c' ~ c/2) is evident. It is also completely reversible. The superstructure reflections belonging only to the tetragonal phase are marked by red arrows.

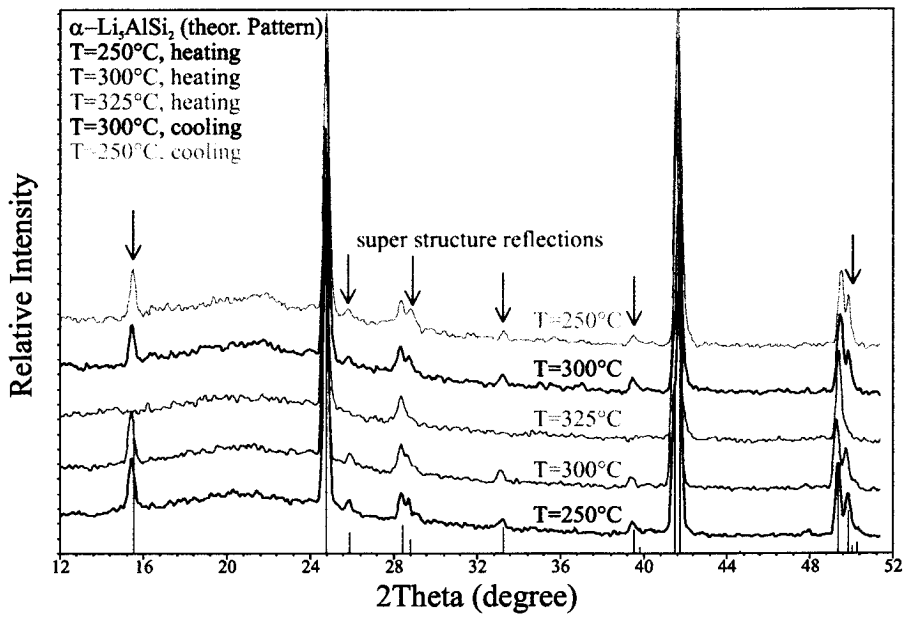

Figure 4.8: High temperature powder diagrams of the Li_5AlSi_2

4.3 The $Li_{4+x}Al_{2-x}Si_2$ Phase

The third novel phase $Li_{4+x}Al_{2-x}Si_2$ (x ~ 1) shows a new 2D network of the electronegative atoms and crystallizes in the Li_2ZnSi structure type. In no previous work could we find evidence of this new compound. Two different types of superstructures were observed. According to our observations there is a phasewidth of yet unknown range. This makes it difficult to decide, although probable, whether there is a direct phase relation between this phase and the Li_5TrTt_2 phases.

4.3.1 Synthesis

The compound was first successfully synthesized from a mixture of LiAlSi and $Li_{21}Si_5$, then also from the elements. The synthesis of pure-phase $Li_{4+x}Al_{2-x}Si_2$ appeared to be difficult: in almost all the syntheses a mixture of this phase and the tetragonal α-Li_5AlSi_2 was found. This is a sign of a possible phase transition between the two new phases, or of a peritectical decomposition of α-Li_5AlSi_2 into the hexagonal phase and other by products, however the stoichiometry difference is only very small.

The synthesis of an almost phase-pure compound was possible by heating a stoichiometric mixture of the elements with a small excess on Lithium (5% to compensate for diffusion through the crucible walls) at 950°C (t_1 = 8 hours, r_1 = 200°C/h, r_e = 25°C/h).

$Li_{4+x}Al_{2-x}Si_2$ forms grey-silver crystals with a metallic lustre. It is brittle like LiAlSi and also very air and moisture sensitive. By contact with water reacts explosively like the tetragonal phase probably due to the formation of SiH_n.

4.3.2 Crystal Structure

The quality of single crystals of $Li_{4+x}Al_{2-x}Si_2$ was tested on a Bürger precession camera and then the crystals data were collected on a four-circle diffractometer (STADI STOE 4). Three different measurements were carried out with three different crystals (Tab.4.8, 4.13, 4.26). In the first measurement superstructure reflections were overlooked, the reflection data were collected up to 2θ = 60° (Tab.4.8). The Laue symmetry of the reflections is *6/mmm* and the extinctions are consistent with the space groups $P6_3mc$, $P\bar{6}\,2c$, and $P6_3/mmc$. The structure was solved in $P6_3/mmc$ using direct methods.

All atoms were anisotropically refined and the displacement parameters are all satisfactory, but also indicate a light tendency of the Si/M-layer not to be planar, as indicated by the *U33* value of the M atom (Tab.4.10). The occupancy factor of Al/Li for the mixed M position was also refined (Tab.4.11).

Table 4.8: Crystal data and parameters of the data collection for $Li_{4+x}Al_{2-x}Si_2$, small cell, crystal 1

Empirical formula	Li4.92Al1.08Si2
Formula weight [g/mol]	119.46
Crystal size [mm]	0.12 x 0.20 x 0.20
Colour	silver metallic lustre
Crystal system	hexagonal
Unit cell dimension [pm]	a = 434.3(1); c = 814.9(2)
Volume [pm^3]	$133.1(1)\cdot10^6$
Space group	$P6_3/mmc$ (194)
Formula unit pro cell	1
ρ (calculated) [g/cm^3]	1.490
Absorption coefficient μ [mm^{-1}]	0.66
F (000)	56.8
Temperature [K]	298
Data collection	four-circle diffractometer STOE STADI4
Monochromator; Wavelength	graphite; λ(MoKα) = 0.71073 Å
Scan parameters (steps; Δω; scan)	45; 0.03; ω-θ - Scan
Theta range	$2° < 2\theta < 60°$
h(min), h(max); k(min), k(max); l(min), l(max)	-5, 5; -5, 5; -9, 9
Reflections collected	568
Independent reflections	62 ; R(int) = 0.0294
Independent reflections with $\|F\|^2 > 2\,\sigma(\|F\|^2)$	47
Absorption correction	Ψ-Scan
Refinement	SHELXL-97 (full-matrix least-squares of F^2)
Parameters	9
Restraints	0
Extinction coefficient	none
Maximal shift/esd	0.000
Mean shift/esd	0.000
Largest diff. peak and hole [electrons/$pm^3\cdot10^6$]	min = -0.221; max = 0.067
[a] wR for $\|F\|^2 > 2\,\sigma(\|F\|^2)$	0.0284
wR for all reflections	0.0303
[a] R for $\|F\|^2 > 2\,\sigma(\|F\|^2)$	0.0124
R for all reflections	0.0233
[a] Goodness of Fit (*GooF*) for all reflections	1.194

[a] the definitions are given in chapter 2.2, Table 2.3

Table 4.9: Wyckoff sites, atomic coordinates, and equivalent isotropic displacement parameters [pm^2] of $Li_{4+x}Al_{2-x}Si_2$, small cell, crystal 1

Atoms	*Wyckoff site*	*x*	*y*	*z*	*U(iso*
Si	2*c*	1/3	2/3	1/4	108(3)
M	2*b*	0	0	1/4	165(7)
Li	4*f*	1/3	2/3	0.5809(4)	251(10)

Table 4.10: Anisotropic displacement parameters [pm^2] for $Li_{4+x}Al_{2-x}Si_2$, small cell, crystal 1

Atoms	*U11*	*U22*	*U33*	*U23*	*U13*	*U12*
Si	109(3)	*U11*	106(4)	0	0	54(2)
M	91(9)	*U11*	313(13)	0	0	46(5)
Li	277(15)	*U11*	200(17)	0	0	14(1)

Table 4.11: Occupancy of the M position for $Li_{4+x}Al_{2-x}Si_2$, small cell, crystal 1

Position	*Aluminum*	*Lithium*
M	0.540(5)	0.460(5)

Table 4.12: Selected interatomic distances [pm] for $Li_{4+x}Al_{2-x}Si_2$, small cell, crystal 1

Li	–Si	269.7(3)	1x	Si	–M	250.75(3)	3x	M	–Si	250.75(3)	3x
	–Li	275.6(7)	1x		–Li	269.7(3)	2x		–Li	286.1(2)	6x
	–Li	283.3(3)	3x		–Li	286.1(2)	6x				
	–Si	286.1(2)	3x								
	–M	286.1(2)	3x								

$Li_{4+x}Al_{2-x}Si_2$ (x ~ 1) crystallizes with the Li_2ZnSi type (Fig.4.9). The structure presents hexagonal layers of M-Si atoms, these are stacked along the c-axis in the same way as in hexagonal graphite: with an ABAB succession, where the M atoms stack on top of each other along the c-direction. This mutual arrangement is an exact coloured version of hexagonal graphite. In between the M-Si layers there are two layers of trigonal arranged lithium atoms, these atoms build up a wurtzite network. This kind of arrangement of the cationic sub lattice in a graphite analogous anionic network was predicted in a recent PhD work which has shown that, partitioned by a periodic hyperbolic surface (PNS), hexagonal graphite and wurtzite networks (or hexagonal diamond) are the mutual empty spaces (Fig.4.10, [90]). In the above cited work the transition from hexagonal graphite to cubic diamond was fully described.

With an occupancy of Li:Al = 1:1 of the M position, the composition of the phase would be Li_5AlSi_2: the same found for the α- and β-Li_5AlSi_2. This would mean that this phase is the γ modification of the Li_5AlSi_2 compound. However, since the composition of this phase could not be exactly determined and since the existence of a phasewidth was observed (cf. Chapter 4.3.3), we believe this phase as a stoichiometrically ill defined high temperature modification of the ternary compound Li_5AlSi_2. At this point, a definition grey zone for the term modification is reached. The combined occurrence of α- and γ-phase can be rationalized by the structural difference of the two while α- and β-phase are much more related to each other

The Si–M distance found in the small cell (251 pm) are in the range of covalent Si–Al bonds but it is too short for Si–Li distances, this explain the somewhat larger *U33* value of the M position as split position Li/Al. The resulting mean displacement of 18pm is large enough to correct for a reasonable Li–Si contact distance. Therefore, a deeper analysis of this position was carried out: the residual electron density on the Fourier difference map around the M position clearly shows the existence of two split positions above and below it (Fig.4.11). These residual electron maxima lie on the special position 2*e* (0,0,0.18) and are likely under occupied by lithium, because the distance between them is only 114 pm. The resulting Si–Li distance is now 257 pm, which is still unusually short for lithium silicon distances. Unfortunately the refinement of this model with the split positions turned out to be impossible due to the high correlation between the Al and the resulting Li positions.

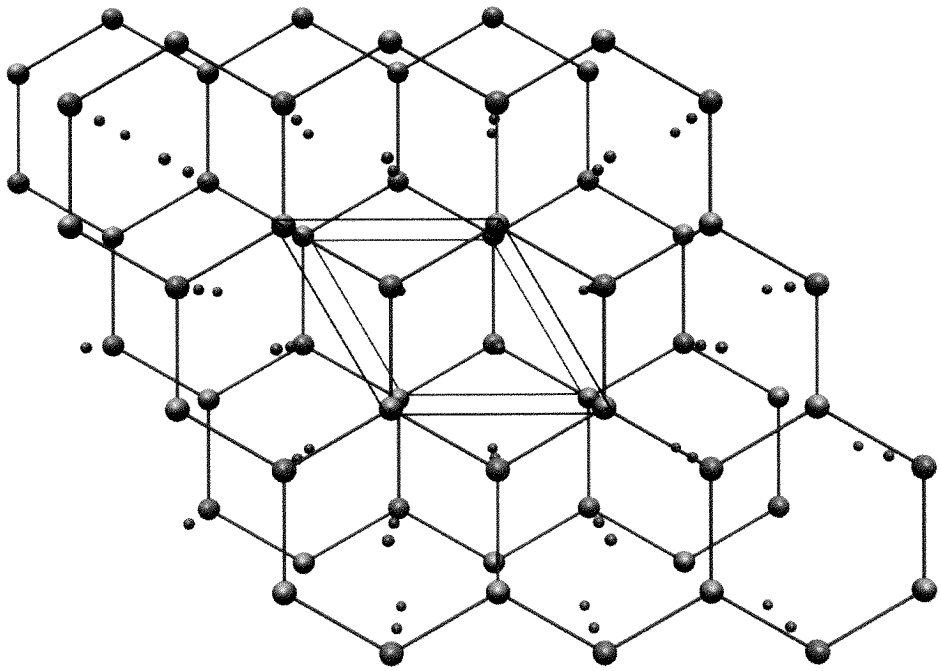

Figure 4.9: Structure of $Li_{4+x}Al_{2-x}Si_2$ (x ~ 1) (Si red spheres, M turquoise, Li grey)

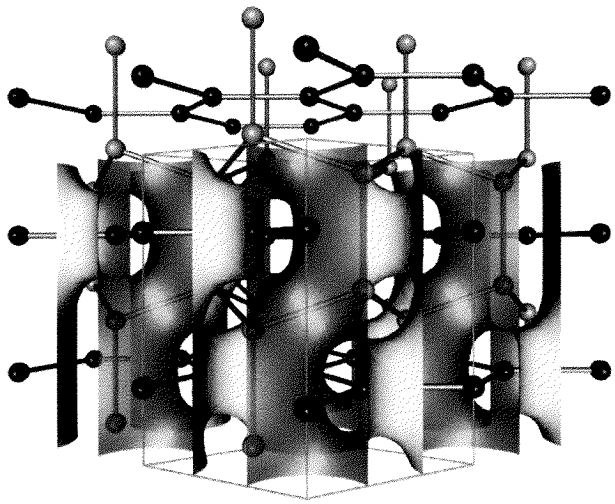

Figure 4.10: Trydimite surface generating two tunnel systems: one for a graphite-like network, the other for hexagonal diamond (wurtzite network) [90]

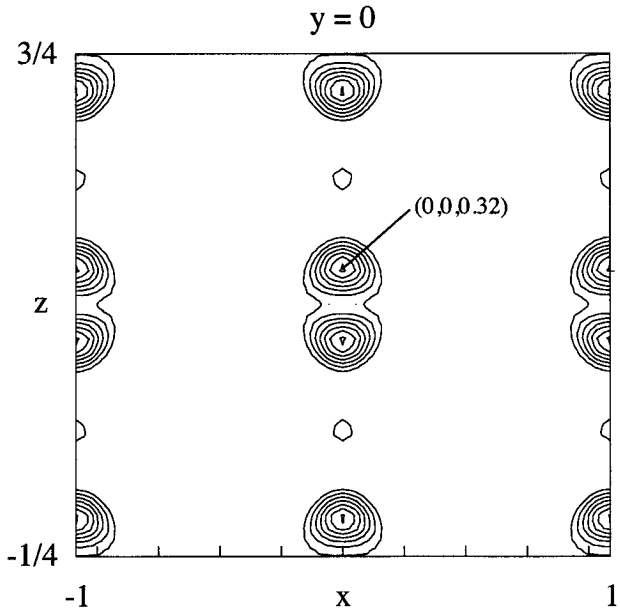

Figure 4.11: Difference Fourier Map around the M position

In the Figure 4.12 the coordination of the different atoms in the $Li_{4+x}Al_{2-x}Si_2$ structure are shown. The Si atoms lie in the middle of a trigonal prism of lithium capped on the top by lithium atoms and on the side by the M atoms (top left). The M atoms are also located in the middle of a trigonal prism of lithium atoms capped on the side by Si atoms (top right). The hexagonal diamond sub lattice of lithium atoms is also nicely shown.

The Li atoms lie in the middle of two distorted tetrahedra: one built of lithium, the other of silicon atoms. The M atoms build a trigonal prism around the Li position, but the lithium does not lie in the middle of it.

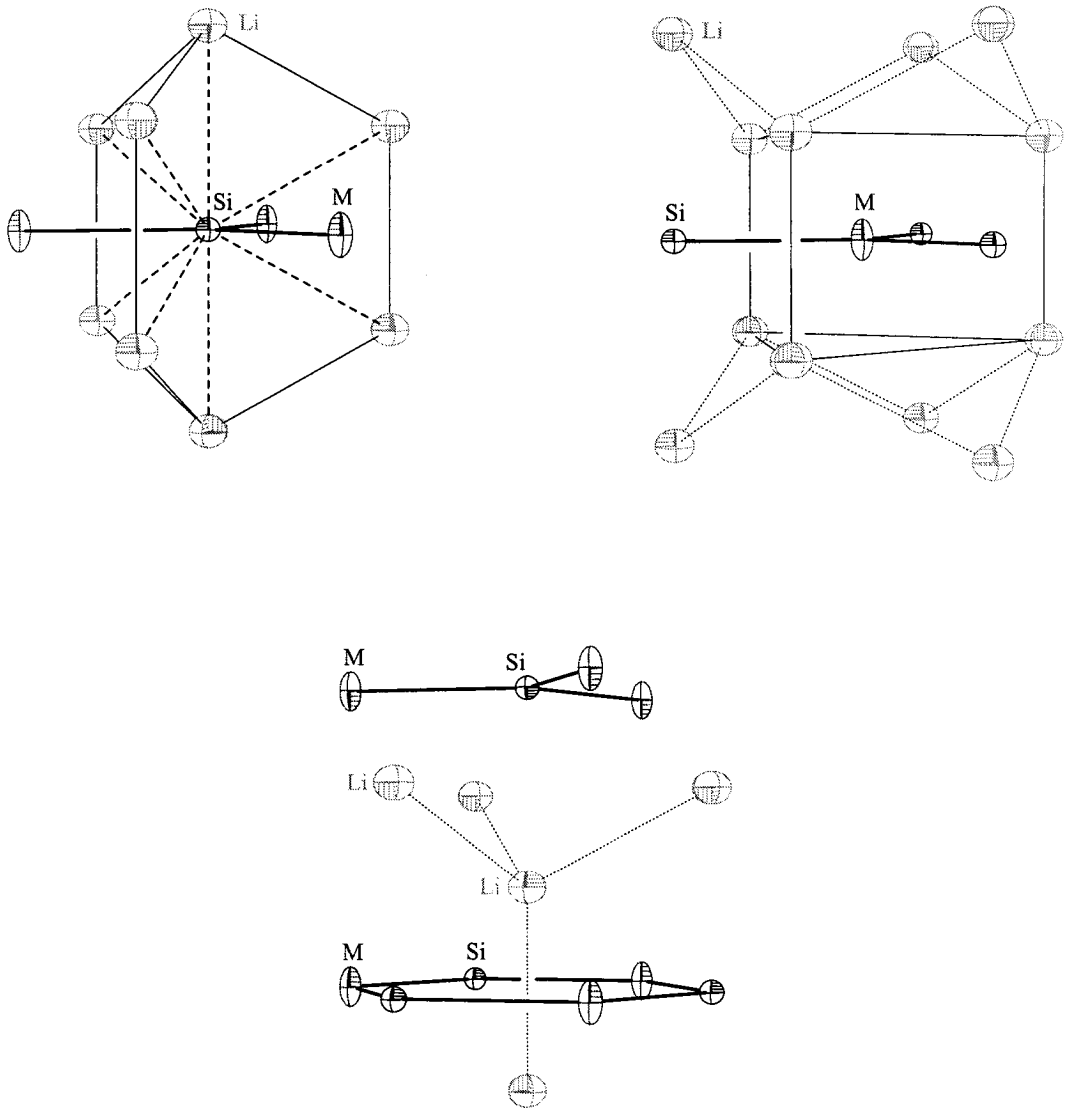

Figure 4.12: Coordination of Si (top left), M (top right) and Li (bottom) in $Li_{4+x}Al_{2-x}Si_2$

During the measurement of another crystal of this new phase superstructure reflections were observed and the corresponding data set measured (Tab.4.13). The super cell vectors a_x', and a_y' are given by the vector sum: $a_x' = a_x - a_y$, $a_y' = a_x + 2a_y$ (Fig.4.13). The resulting super cell contains three times the small cell.

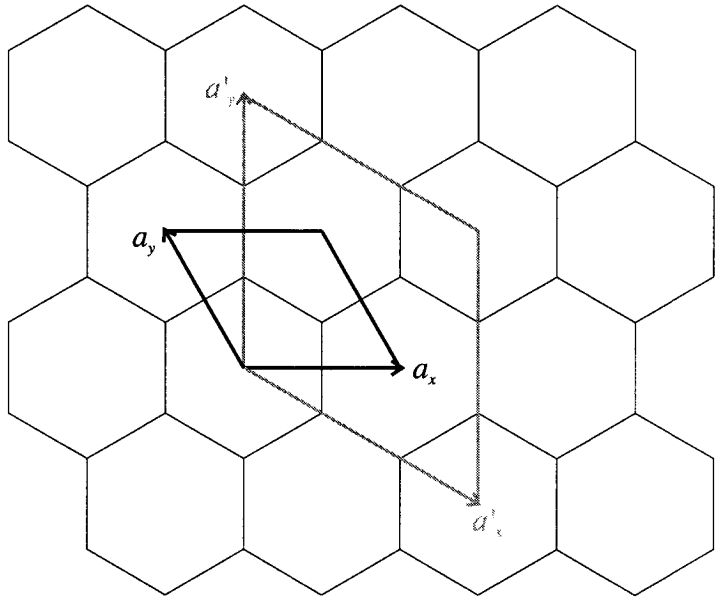

Figure 4.13: basis cell a = 435.1 pm (black), super cell a' = 753.5 pm (grey)

The reflection data were collected up to $2\theta = 60°$ (Tab.4.13). The Laue symmetry is *6/m* and the extinctions are consistent with the space groups $P6_3$, $P6_3/m$, $P6_322$. The structure was refined in the space group $P6_3/m$ (Tab.4.13) as well as in the space group $P6_3$. However, the difference between the two refinements was negligible, and therefore only the refinement in the higher symmetric space group was taken into account.

All atoms were anisotropically refined and the displacement parameters are all satisfactory, with the expected high value of *U33* for the M positions (Tab.4.15). The occupancy factors of the three mixed occupied M positions were also refined (Tab.4.16).

It is interesting to note the difference in the composition of the $Li_{4+x}Al_{2-x}Si_2$ compound between this crystal and the first measured. For the first crystal the refined x was equal to 0.92, in this second crystal it is larger than one (1.08). This change in the composition together with the observed change in the cell parameters (*a*-axis 0.2% longer, *c*-axis 0.4% shorter) is indicative for a phasewidth (cf. Chapter 4.3.3).

Table 4.13: Crystal data and parameters of the data collection for $Li_{4+x}Al_{2-x}Si_2$, big cell in $P6_3/m$, crystal 2

Empirical formula	Li5.08Al0.92Si2
Formula weight [g/mol]	116.26
Crystal size [mm]	0.12 x 0.12 x 0.08
Colour	silver metallic lustre
Crystal system	hexagonal
Unit cell dimension [pm]	a = 753.5(1); c = 811.8(2)
Volume [pm^3]	399.2(1)·10^6
Space group	$P6_3/m$ (176)
Formula unit pro cell	3
ρ (calculated) [g/cm^3]	1.451
Absorption coefficient μ [mm^{-1}]	0.633
F (000)	166
Temperature [K]	298
Data collection	four-circle diffractometer STOE STADI4
Monochromator; Wavelength	graphite; λ(MoKα) = 0.71073 Å
Scan parameters (steps; Δω; scan)	50; 0.03; ω-θ - Scan
Theta range	2° < 2θ < 60°
h(min), h(max); k(min), k(max); l(min), l(max)	-9, 9; -9, 9; -11, 11
Reflections collected	4522
Independent reflections	418; R(int) = 0.1779
Independent reflections with $\|F\|^2 > 2\,\sigma(\|F\|^2)$	142
Absorption correction	Ψ-Scan
Refinement	SHELXL-97 (full-matrix least-squares of F^2)
Parameters	25
Restraints	0
Extinction coefficient	none
Maximal shift/esd	0.000
Mean shift/esd	0.000
Largest diff. peak and hole [electrons/pm^3·10^6]	min = -0.506; max = 0.810
[a] wR for $\|F\|^2 > 2\,\sigma(\|F\|^2)$	0.0832
wR for all reflections	0.1144
[a] R for $\|F\|^2 > 2\,\sigma(\|F\|^2)$	0.0429
R for all reflections	0.1572
[a] Goodness of Fit (*GooF*) for all reflections	0.950

[a] the definitions are given in chapter 2.2, Table 2.3

Table 4.14: Wyckoff sites, atomic coordinates, and equivalent isotropic displacement parameters [pm^2] of $Li_{4+x}Al_{2-x}Si_2$, big cell in *P6₃/m*, crystal 2

Atoms	*Wyckoff site*	*x*	*y*	*z*	*U(iso)*
Si	6*h*	0.0090(3)	0.3378(3)	1/4	129(4)
M1	2*c*	1/3	2/3	1/4	139(13)
M2	2*a*	0	0	1/4	160(30)
M3	2*d*	2/3	1/3	1/4	320(70)
Li	12*i*	0.995(1)	0.665(1)	0.082(1)	251(11)

Table 4.15: Anisotropic displacement parameters [pm^2] of $Li_{4+x}Al_{2-x}Si_2$, big cell in *P6₃/m*, crystal 2

Atoms	*U11*	*U22*	*U33*	*U23*	*U13*	*U12*
Si	103(9)	113(8)	157(5)	0	0	45(7)
M1	107(15)	*U11*	200(30)	0	0	54(7)
M2	90(30)	*U11*	310(70)	0	0	45(16)
M3	70(50)	*U11*	810(190)	0	0	60(30)
Li	220(40)	320(40)	220(20)	70(40)	50(30)	140(40)

Table 4.16: Occupancies of the M positions for $Li_{4+x}Al_{2-x}Si_2$, big cell in *P6₃/m*, crystal 2

Position	*Aluminum*	*Lithium*
M1	0.80(2)	0.20(2)
M2	0.50(3)	0.50(3)
M3	0.07 (2)	0.93(2)

Table 4.17: Selected interatomic distances [pm] for $Li_{4+x}Al_{2-x}Si_2$, big cell in *P6₃/m*, crystal 2

Li	–Si	269.7(5)	1x	M1	–Si	246.1(2)	3x	Si	–M1	246.1(2)	1x
	–Li	272.4(9)	1x		–Li	288.6(7)	6x		–M2	251.2(2)	1x
	–M3	283.2(7)	1x						–M3	256.3(2)	1x
	–Si	283.8(8)	1x	M2	–Si	251.2(2)	3x		–Li	269.7(5)	2x
	–Li	284.1(9)	2x		–Li	285.4(9)	6x		–Li	283.8(8)	2x
	–Li	285.3(17)	1x						–Li	286.3(8)	2x
	–M2	285.4(9)	1x	M3	–Si	256.3(2)	3x		–Li	287.3(7)	2x
	–Si	286.3(8)	1x		–Li	283.2(7)	6x				
	–Si	287.3(7)	1x								
	–M1	288.6(7)	1x								

The anisotropic displacement parameters of the three different M positions found for the super cell (Tab.4.16) are of interest, because the different ratios Li:Al result, as expected, in different values of *U33*. The M1 position, which is an Al rich position, shows only a small anisotropy along the z direction.

The M2 position, which has a Li:Al ratio of about 1, shows a larger anisotropy along the *c* direction, about that found for the M site in the small cell. In analogy to the M position of the small cell, split positions, likely under occupied by lithium atoms, above and below the hexagonal network can be found in the difference Fourier map (Fig.4.14). The maxima lie on the special position 4*e* with coordinates (0,0,0.18), the resulting Si–Li(split) distance amounts now to 258 pm instead of 251 pm for the average M2–Si distance.

The M3 position is a lithium rich position and exhibits a large anisotropy along the z direction. The difference Fourier map (Fig.4.15) shows two split position above and below the M3 position. The maxima lie on the special position 4*f* (1/3,2/3,0.71), the resulting Si–Li(split) distance is now 258 pm, the same distance found for the lithium resulting from the M2 positions.

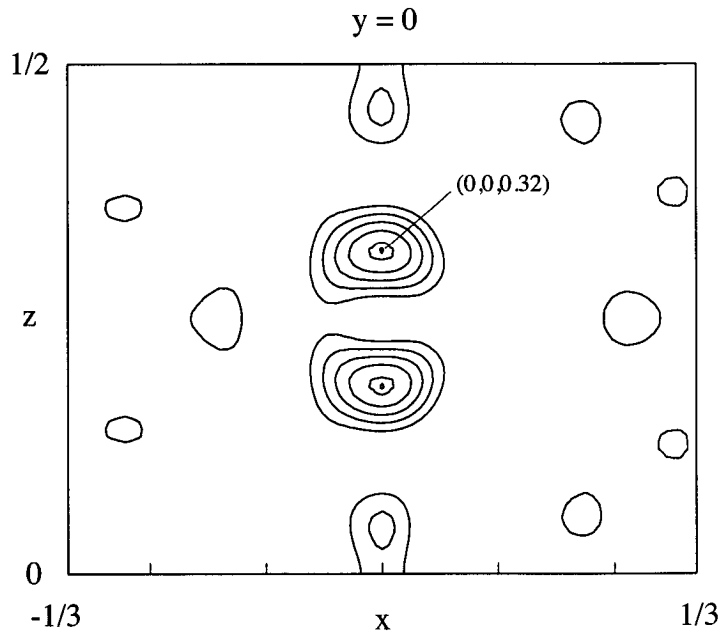

Figure 4.14: Difference Fourier Map around the M2 position

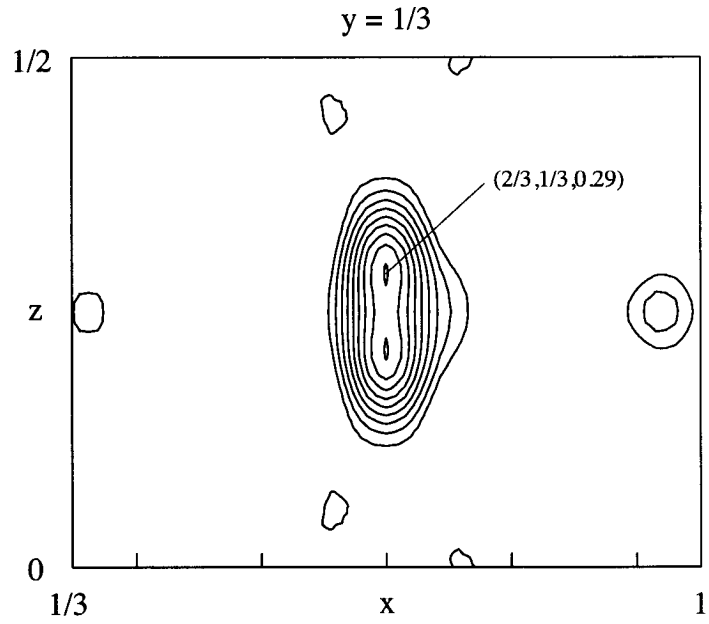

Figure 4.15: Difference Fourier Map around the M3 position

As expected the free refinement with these new split positions turned out to be impossible, because the correlation between the resulting Al and split Li positions was too high.

The presence of three different occupancies of the M positions is also evident in the silicon-M distances: the higher the aluminum content the shorter the silicon-M distance, and thus the Si–M1 distance is the shortest (246 pm), the Si–M2 with 251 pm is in the same range as that found in the small cell, the Si–M3 distance is the longest one (256 pm).

The structure refinement of the small cell was also carried out for the second crystal omitting the superstructure reflections (Tab.4.18-22). The composition of the phase is the same found for the super cell, differing, therefore, from the composition found in the first crystal. Another difference is observed in the cell parameters: the second crystal has a shorter *c*-axis (0.4%), but longer *a*-axis (0.2%), this can also be seen in the interatomic distances (Tab.4.22) (cf. Chapter 4.3.3).

Table 4.18: Crystal and refinement parameters for $Li_{4+x}Al_{2-x}Si_2$, small cell, crystal 2

Empirical formula	Li5.08Al0.92Si2
Formula weight [g/mol]	116.26
Crystal system	hexagonal
Unit cell dimension [pm]	a = 435.1(1); c = 811.8(2)
Volume [pm^3]	133.1(1)·10^6
Space group	$P6_3/mmc$ (194)
Formula unit pro cell	1
ρ (calculated) [g/cm^3]	1.451
Absorption coefficient μ [mm^{-1}]	0.633
F (000)	55
Independent reflections	96; R(int) = 0.0637
Independent reflections with $\|F\|^2 > 2\,\sigma(\|F\|^2)$	64
Refinement	SHELXL-97 (full-matrix least-squares of F^2)
Parameters	9
Restraints	0
Extinction coefficient	none
Maximal shift/esd	0.000
Mean shift/esd	0.000
Largest diff. peak and hole [electrons/pm^3·10^6]	min = -0.188; max = 0.461
[a] wR for $\|F\|^2 > 2\,\sigma(\|F\|^2)$	0.0563
wR for all reflections	0.0611
[a] R for $\|F\|^2 > 2\,\sigma(\|F\|^2)$	0.0227
R for all reflections	0.0446
[a] Goodness of Fit (*GooF*) for all reflections	1.019

[a] the definitions are given in chapter 2.2, Table 2.3

Table 4.19: Wyckoff sites, atomic coordinates, and equivalent isotropic displacement parameters [pm^2] of $Li_{4+x}Al_{2-x}Si_2$, small cell, crystal 2

Atoms	*Wyckoff site*	*x*	*y*	*z*	*U(iso)*
Si	2*c*	1/3	2/3	1/4	141(4)
M	2*b*	0	0	1/4	163(9)
Li	4*f*	1/3	2/3	0.0824(7)	251(12)

The *U33* value of the M position (Tab.4.20) shows the characteristic anisotropy along the *c* axis, signal of the presence of split positions, under occupied by lithium atoms. The refinement of these positions was also in this case impossible.

Table 4.20: Anisotropic displacement parameters [pm^2] for $Li_{4+x}Al_{2-x}Si_2$, small cell, crystal 2

Atoms	*U11*	*U22*	*U33*	*U23*	*U13*	*U12*
Si	134(5)	*U11*	153(6)	0	0	67(2)
M	85(11)	*U11*	320(20)	0	0	43(6)
Li	260(18)	*U11*	230(30)	0	0	14(1)

Table 4.21: Occupancy of the M position for $Li_{4+x}Al_{2-x}Si_2$, small cell, crystal 2

Position	*Aluminum*	*Lithium*
M	0.461(8)	0.539(8)

Table 4.22: Selected interatomic distances [pm] for $Li_{4+x}Al_{2-x}Si_2$, small cell, crystal 2

Li	–Si	269.8(5)	1x	Si	–M	251.18(3)	3x	M	–Si	251.18(5)	3x
	–Li	272.1(9)	1x		–Li	269.8(5)	2x		–Li	285.7(3)	6x
	–Li	284.6(5)	3x		–Li	285.7(3)	6x				
	–Si	285.7(3)	3x								
	–M	285.7(3)	3x								

With the aim to find crystals of better quality and therefore with ordered Al/Li positions another crystal was measured. In this crystal other superstructure reflections of the *a*-axis ($a' = 3a$) were observed (Fig.4.16) and measured, even if the quality of the crystal was not very good (cf. Tab.4.23, *R*(int)).

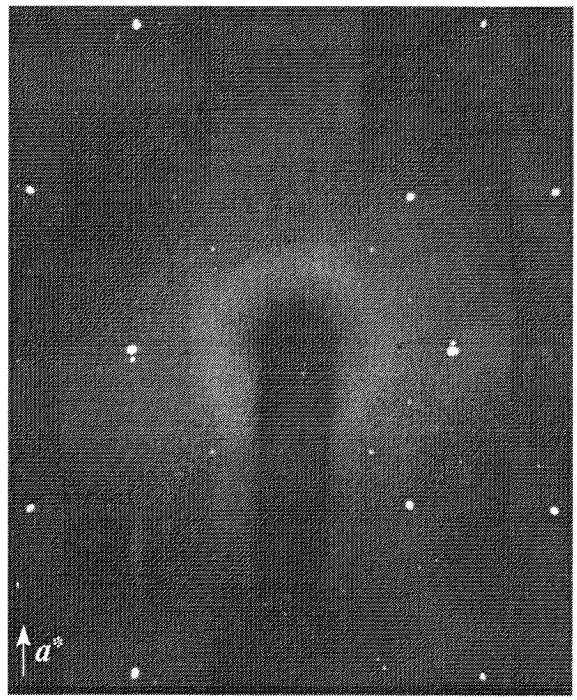

Figure 4.16: Reciprocal space section parallel to the a^*-axis showing the weak superstructure reflections

The reflection data were collected up to $2\theta = 60°$ (Tab.4.23), the Laue symmetry of these reflections is *6/m* and the extinctions are consistent with the space groups $P6_3$, $P6_3/m$, and $P6_322$. The structure was refined in the space group $P6_3/m$. However the correlation between the different Si, M and Li positions was very high and therefore the refinement did not lead to accurate values and was not very stable, this becomes evident by inspection of the isotropic displacement parameter of the M2 position (Tab.4.24). For that reason the anisotropic refinement of the atoms was not carried out.

An interesting result of the refinement of this superstructure is that of the resulting 18 mixed occupied positions in the small cell, six are fully occupied by aluminum, six fully by lithium, and only six show still mixed occupancy by lithium and aluminum atoms.

However, it must pointed out that due to the bad quality of the refinement this results must not be overestimated.

Table 4.23: Crystal data and parameters of the data collection for $Li_{4+x}Al_{2-x}Si_2$, super cell in $P6_3/m$, crystal 3

Empirical formula	Li5.05Al0.95Si2
Formula weight [g/mol]	116.77
Crystal size [mm]	0.08x0.08x0.04
Colour	silver metallic lustre
Crystal system	hexagonal
Unit cell dimension [pm]	a = 1304.6(2); c = 812.0(2)
Volume [pm^3]	$1196.8(3)\cdot10^6$
Space group	$P6_3/m$ (176)
Formula unit pro cell	9
ρ (calculated) [g/cm^3]	1.458
Absorption coefficient μ [mm^{-1}]	0.638
F (000)	499
Temperature [K]	298
Data collection	four-circle diffractometer STOE STADI4
Monochromator; Wavelength	graphite; λ(MoKα) = 0.71073 Å
Scan parameters (steps; Δω; scan)	40; 0.03; ω-θ - Scan
Theta range	$2° < 2\theta < 60°$
h(min), h(max); k(min), k(max); l(min), l(max)	-15, 15; -15, 15; -9, 9
Reflections collected	5654
Independent reflections	764 ; R(int) = 0.1501
Independent reflections with $\|F\|^2 > 2\,\sigma(\|F\|^2)$	161
Absorption correction	Ψ-Scan
Refinement	SHELXL-97 (full-matrix least-squares of F^2)
Parameters	34
Restraints	1
Extinction coefficient	none
Maximal shift/esd	0.031
Mean shift/esd	0.009
Largest diff. peak and hole [electrons/$pm^3\cdot10^6$]	min = -0.510; max = 1.258
[a] wR for $\|F\|^2 > 2\,\sigma(\|F\|^2)$	0.1655
wR for all reflections	0.2659
[a] R for $\|F\|^2 > 2\,\sigma(\|F\|^2)$	0.0687
R for all reflections	0.2302
[a] Goodness of Fit (*GooF*) for all reflections	0.975

[a] the definitions are given in chapter 2.2, Table 2.3

Table 4.24: Wyckoff sites, atomic coordinates, and equivalent isotropic displacement parameters [pm^2] of $Li_{4+x}Al_{2-x}Si_2$, super cell, crystal 3

Atoms	*Wyckoff site*	*x*	*y*	*z*	*U(iso)*
Si1	6*h*	0.5559(4)	0.7818(4)	1/4	119(15)
Si2	6*h*	0.8815(4)	0.1057(4)	1/4	143(15)
Si3	6*h*	0.5611(4)	0.1127(4)	1/4	154(16)
Al1	6*h*	0.6677(7)	0.0004(8)	1/4	261(8)
M1	2*a*	0	0	1/4	170(40)
M2	2*d*	2/3	1/3	1/4	60(40)
M3	2*c*	1/3	2/3	1/4	150(50)
Li1	6*h*	0.666(4)	0.668(2)	1/4	250(40)
Li2	12*i*	0.577(4)	0.784(2)	0.915(3)	180(50)
Li3	12*i*	0.886(4)	0.109(2)	0.926(4)	180(50)
Li4	12*i*	0.558(4)	0.114(2)	0.910(4)	230(60)

Table 4.25: Occupancies of the M positions for $Li_{4+x}Al_{2-x}Si_2$, super cell, crystal 3

Position	*Aluminum*	*Lithium*
M1	0.42(1)	0.58(1)
M2	0.41(1)	0.59(1)
M3	0.42(1)	0.58(1)

4.3.3 Physical Properties

For the three different crystals differences in the Li:Al ratios as well as differences in the *a*- and *c*-axis length were observed. Quite clearly this indicates that there exists a phasewidth for the $Li_{4+x}Al_{2-x}Si_2$ compound. Unfortunately the range of x could not be determined.

In the Figure 4.17 the axis lengths are displayed against the Li contents of the mixed occupied positions. The dependence of the *a*-axis against the Li:Al ratio is nicely displayed in the graphic, the higher the content of aluminum in the mixed occupied position the shorter the *a*-axis, which can be easily understood since this results in shorter Si–M distance. On the other hand the increase of lithium leads to a contraction of the *c* axis, which basically leaves the volume of the cell unchanged.

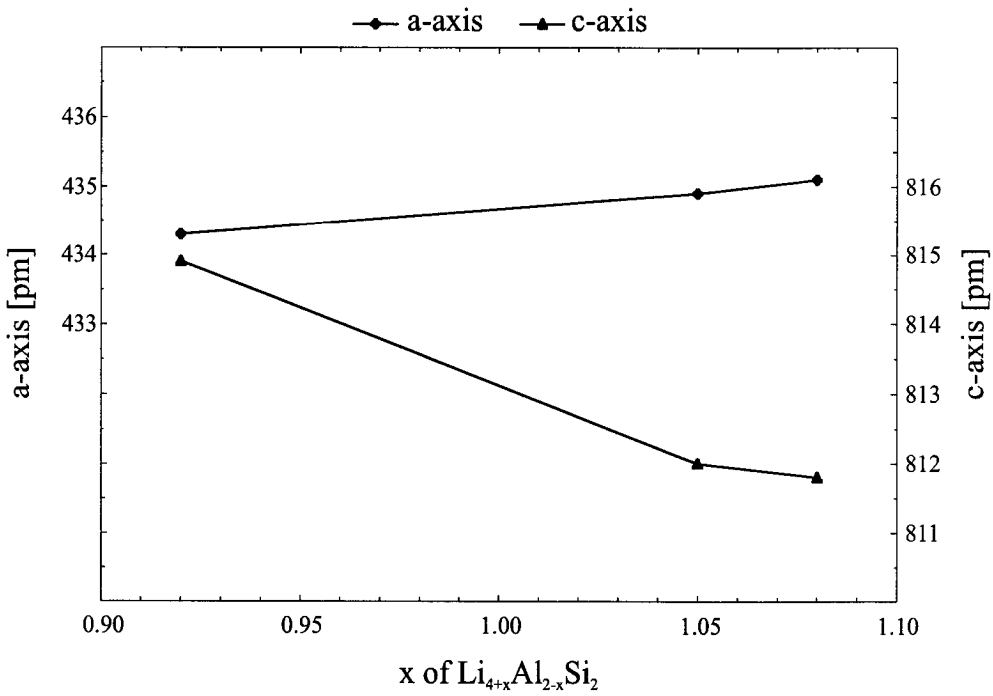

Figure 4.17: *a*- and *c*-axis length against Li contents of the three crystals of $Li_{4+x}Al_{2-x}Si_2$

4.3.4 Theoretical Investigations

The electronic properties of the $Li_{4+x}Al_{2-x}Si_2$ compound were investigated on the basis of theoretical calculations performed using the LMTO method. Since an ordered model has to be applied for the calculations and because there is one mixed occupied M position of multiplicity two in the small cell refinement a larger cell has to be applied. The structure model of the super cell with $a' = 3a$ (Tab.4.23-25) was used as starting model, because there already half of the M positions are ordered. The other six M atoms were arbitrary assigned to aluminum and lithium; the resulting model (Tab.4.26, Fig.4.18) has now the space group $P\bar{6}$.

Table 4.26: Atomic position in the $P\bar{6}$ (174) model used for LMTO calculations

Atoms	*Wyckoff site*	*x*	*y*	*z*
Si1	3*j*	0.1111	0.2222	0
Si2	3*j*	0.4444	0.2222	0
Si3	3*j*	0.1111	0.5556	0
Si4	3*k*	0.2222	0.1111	1/2
Si5	3*k*	0.2222	0.4444	1/2
Si6	3*k*	0.5556	0.4444	1/2
Al1	1*a*	0	0	0
Al2	1*d*	1/3	2/3	1/2
Al3	1*e*	2/3	1/3	0
Al4	3*j*	1/3	0	0
Al5	3*k*	1/3	1/3	1/2
Li1	1*b*	0	0	1/2
Li2	1*c*	1/3	2/3	0
Li3	1*f*	2/3	1/3	1/2
Li4	3*j*	1/3	1/3	0
Li5	3*k*	1/3	0	1/2
Li6	6*l*	0.1111	0.2222	0.3309
Li7	6*l*	0.4444	0.2222	0.3309
Li8	6*l*	0.1111	0.5556	0.3309
Li9	6*l*	0.2222	0.1111	0.8309
Li10	6*l*	0.2222	0.4444	0.8309
Li11	6*l*	0.5556	0.4444	0.8309

There are two different types of silicon now: one half of the silicon atoms are two bonded to aluminum, the other half has only one bond with the aluminum (Fig.4.18).
As a prerequisite, this model is valid in the frame of the Zintl-Klemm concept according to $(Li^+)_5((3b)Al^-)((2b)Si^-)((1b)Si^{3-})$ assuming π-contributions between the Al and the Si-2b. The occurance of π-bonds within the silicon-aluminum layers is highly probable since 1. the layers are planar in all the different crystal refinements, 2. the Al–Si distances are clearly shorter than for the tetrahedral phases, and 3. partial π-bonding has very frequently found in silicon based Zintl anions.

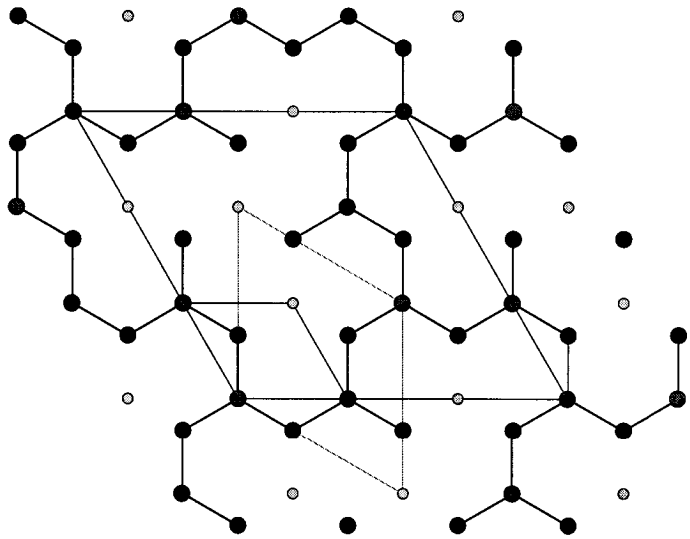

Figure 4.18: Model used for LMTO calculation (large cell); the small cell represents the experimental substructure, the light grey cell the experimental superstructure (Si black, Al grey, Li small light grey spheres)

In the Figure 4.19 the calculated LMTO-DOS of the $Li_{4+x}Al_{2-x}Si_2$ model is displayed. The resulting DOS the metallic character of the compound is evident due to incomplete occupation of the planar π-system.

The metallic character of the phase would also explain the existence of a phasewidth.

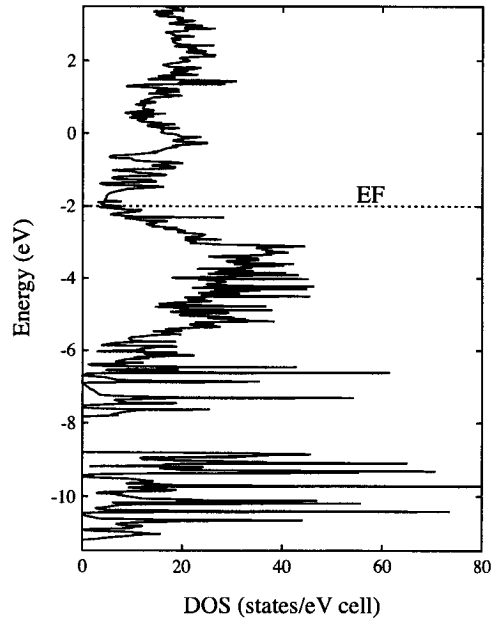

Figure 4.19: LMTO-DOS of the model of the $Li_{4+x}Al_{2-x}Si_2$

4.4 The α-Li_5AlGe_2 Phase

Here synthesis and characterization of the new Zintl phase α-Li_5AlGe_2 are described. It is isostructural to the α-Li_5AlSi_2 phase, i.e. which exhibits also the 3D network of the Al and Si related to cristobalite. Just like for the silicide a phase transition to a high temperature modification, the cubic β-Li_5AlSi_2 phase, was observed and investigated.

4.4.1 Synthesis

The compound was successfully synthesized from the elements, however the synthesis of pure-phase α-Li_5AlGe_2 appeared to be difficult, because in almost all cases the hexagonal γ-phase $Li_{4+x}Al_{2-x}Ge_2$ (x ~ 1) was the main product. As already discussed for the related silicides this is quite likely due to kinetic effects which interestingly seem to more pronounced for the germanide. However, synthesis of phase pure products was achieved by heating a stoichiometric mixture of the elements with small excess on lithium (5% to compensate diffusion through the crucible) and on aluminum (also 5%) at 700°C (t_1 = 8 hours, r_1 = 200°C/h, r_e = 25°C/h).

α-Li_5AlGe_2 forms grey-silver crystals with a light violet metallic lustre. It is brittle like α-Li_5AlSi_2 and also air and moisture sensitive. By contact with water reacts leaving a yellow-orange powder, which according to the colour should be GeO_2. The decomposition products have a pungent smell.

4.4.2 Crystal Structure

Even if it was possible to obtain almost phase pure crystalline compound, the quality of the crystals was very poor. Attempts to achieve larger crystals of better quality were all unsuccessful. This strongly supports the assumption of a kinetically hindered phase transition of the hexagonal high temperature phase. Thanks to the good quality of the powder diffraction data a Rietveld analysis was carried out (Fig.4.20). The product contains also a small amount (~7%) of $Li_{14}Ge_6$ ($R\bar{3}m$; a = 449.4 pm, b = 1843.9 pm, [91]) which was also included in the structure refinement.

For the refinement of the powder data, the structure of α-Li_5AlSi_2 was used as the starting model. The Rietveld analysis was then carried out successfully by refining the

phase fraction of the two phases (α-Li_5AlGe_2 and $Li_{14}Ge_6$), the cell parameters, the atomic positions, the isotropic displacement factors (Tab.4.23-25) as well as the profile coefficients of the fitting curves. However, as usual for Rietveld analyses, the refinement of all parameters at one time was not possible, the different parameters were then refined stepwise. The profile coefficients of the fitting curve (totally 17 coefficients were refined iteratively) turned out to be critical for a good refinement.

Problems arose from the refinement of the atomic as well as the displacement parameters of Li3. The position of this atom was therefore determined by difference Fourier analysis (Fig.4.21), but could not be optimised and its displacement parameter refined to an unusually large value (Tab.4.24). The consequence is that all distances between Li3 and other atoms are not very accurate. These difficulties with the refinement of the parameters of the lithium position were also present in the refinement of the silicon phase (cf. Tab.4.3).

Table 4.27: Crystal data and parameters of the data collection for α-Li_5AlGe_2

Empirical formula	Li5AlGe2
Formula weight [g/mol]	206.87
Crystal system	tetragonal
Unit cell dimension [pm]	a = 621.5(3) pm; c = 1229.8(5) pm
Volume [pm^3]	$475(1)\cdot10^6$
Space group	$I\bar{4}2d$ (122)
Formula unit pro cell	4
ρ (calculated) [g/cm^3]	2.893
Absorption coefficient μ [mm^{-1}]	6.624
F (000)	224.0
Temperature [K]	298
Data collection	STOE STADI P2, PDS detector ($2\Theta_{eff}$ = 7°)
Monochromator; Wavelength	germanium; λ(CuKα) = 1.54056 Å
Scan parameters: step width; time/step	0.5°; 280 seconds
Theta range	$14° < 2\theta < 91°$
Refinement	GSAS
Largest diff. peak and hole [electrons/$pm^3\cdot10^6$]	min = -0.69; max = 0.63
[a] wR_p	0.0802
[a] R_p	0.0588
[a] R_F	0.0467
[a] Goodness of Fit χ^2	2.00

[a] the definitions are given in chapter 2.2, Table 2.2

Table 4.28: Wyckoff sites, atomic coordinates, and equivalent isotropic displacement parameters [pm^2] for α-Li_5AlGe_2

Atom	*Wyckoff site*	*x*	*y*	*z*	*U(iso)*
Ge1	*8d*	0.2561(2)	1/4	1/8	74(2)
Al1	*4b*	0	0	1/2	90(20)
Li1	*4a*	0	0	0	120(30)
Li2	*8c*	0	0	0.248(2)	120(30)
Li3	*8d*	0.755	1/4	1/8	510(50)

Table 4.29: Selected interatomic distances [pm] for α-Li_5AlGe_2

Al1	–Ge1	265.8(1)	4x	Li1	–Li3	266(1)	4x	Li3	–Li2	265(1)	2x
	–Li3	270(1)	4x		–Ge1	270.3(1)	4x		–Li1	266(1)	2x
	–Li2	310.6(1)	2x		–Li2	305(2)	2x		–Al1	270(1)	2x
	–Li2	311(3)	4x		–Li2	310.6(1)	4x		–Li2	271(1)	2x
									–Ge1	307(1)	2x
Ge1	–Al1	265.8(1)	2x	Li2	–Li3	265(1)	2x		–Ge1	310(2)	1x
	–Li2	267.2(8)	2x		–Ge1	267.2(8)	2x		–Ge1	311(1)	2x
	–Li2	268.9(8)	2x		–Ge1	268.9(8)	2x		–Ge1	311(2)	1x
	–Li1	270.3(1)	2x		–Li3	271(1)	2x				
	–Li3	307(1)	2x		–Li1	305(2)	1x				
	–Li3	310(2)	1x		–Al1	310(2)	1x				
	–Li3	311(1)	2x		–Li1	310.6(1)	2x				
	–Li3	311(2)	1x		–Al1	310.6(1)	2x				

The good quality of the Rietveld refinement is nicely displayed by the graphic representation (Fig.4.20), where the pink curve at the bottom represents the difference

between the calculated (blue line in the figure) and the measured reflection pattern (represented as red crosses in the figure).

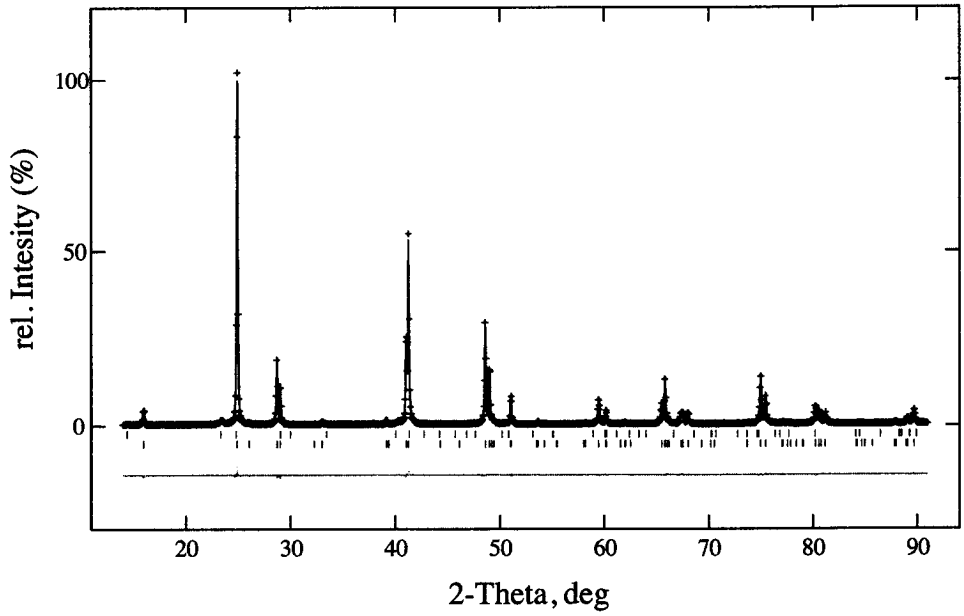

Figure 4.20: Rietveld Analysis of the α-Li_5AlGe_2 structure

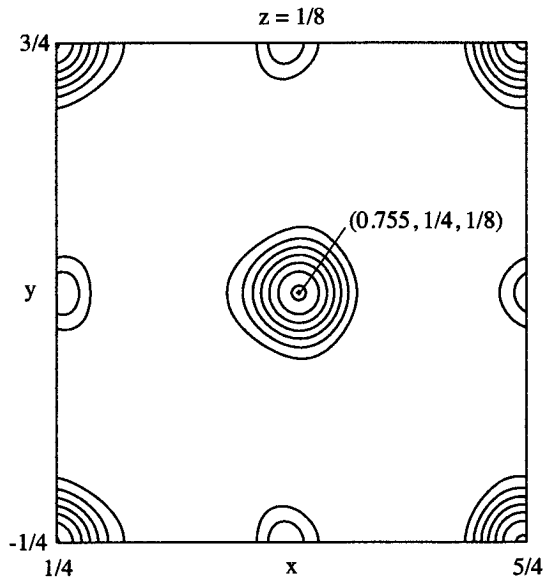

Figure 4.21: Difference Fourier Map around the Li3 position

α-Li_5AlGe_2 crystallizes in the new structure type already found for α-Li_5AlSi_2 (Fig.4.22). The structure can be described by the formulation $(Li^+)_5\,{}^3_\infty[(Al^-)(Ge^{2-})_{4/2}]$,

in agreement with the Zintl-Klemm concept (chap.1). According to the Zintl-Klemm concept there is one four connected aluminum atom isoelectronic to silicon and one two connected germanium atoms isoelectronic to selenium.

The angles Ge-Al-Ge are very close to the tetrahedral angle with 109.5(2)° (4x) and 109.4(3)° (2x), and the deviations are much smaller than in the silicide.

The Ge–Al distance of 265.8 pm (Tab.4.29) in the anionic framework is slightly longer than that observed for the LiAlGe structure (259.3 pm) but still in the range of Ge–Al covalent bonds (255-266 pm).

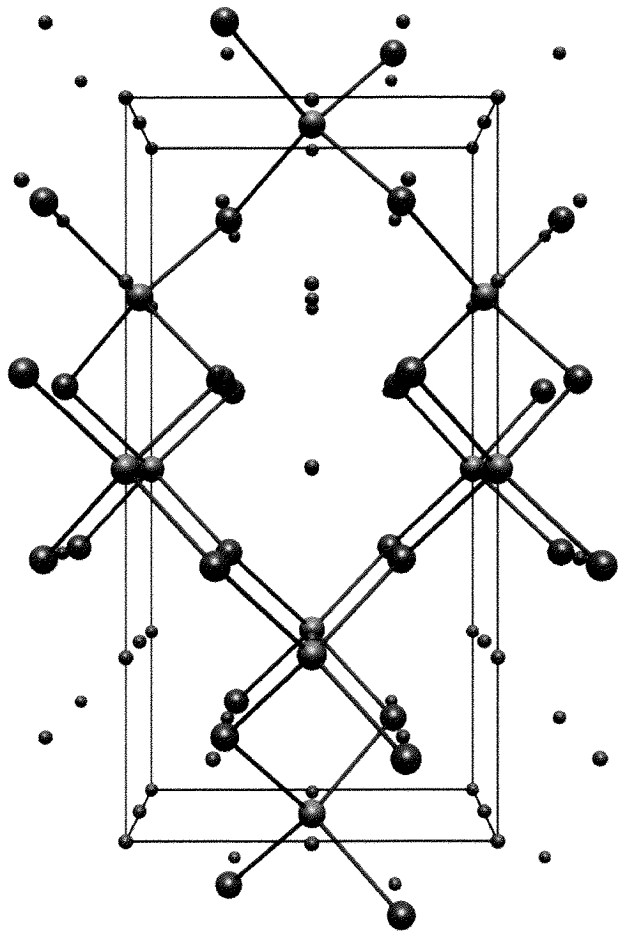

Figure 4.22: Structure of α-Li_5AlGe_2 (Ge violet spheres, Al green, Li grey)

The α-Li_5AlGe_2 compound crystallizes with the α-Li_5AlSi_2 structure type and therefore most of the structural considerations for α-Li_5AlSi_2 are also valid for the α-Li_5AlGe_2 phase. Compared to the silicon phase the basic cell of the germanium compound is, as

expected, larger. The *a*-axis is about 0.7% and the *c*-axis 0.9% longer, resulting in an increase of the volume of about 2.4%.

4.4.3 Physical Properties

The thermal properties of α-Li_5AlGe_2 have thoroughly been investigated, since the existence of a higher temperature phase of the analogous silicon compound was known (cf. Ch. 4.1-2). In fact, according to the DTA (Fig.4.23), as well as high temperature diffraction experiments, the expected first order phase transition the cubic high temperature phase β-Li_5AlGe_2 (cf. Chapter 4.5), was observed at 285°C.

Like for the silicide a second reversible thermal effect was observed at about 735°C. This effect is, probably, the phase transition between the cubic β- and the γ-Li_5AlGe_2 phase, which again is the hexagonal $Li_{4+x}Al_{2-x}Ge_2$ (x ~ 1) phase (cf. Chapter 4.6). On the other hand this thermal effect could also be assigned to a peritectical decomposition of the cubic phase to the hexagonal phase and other binary compounds or one of the elements.

The endothermic effect at about 890°C is the congruent melting point of the hexagonal phase which is then the dominating species in the sample at that temperature.

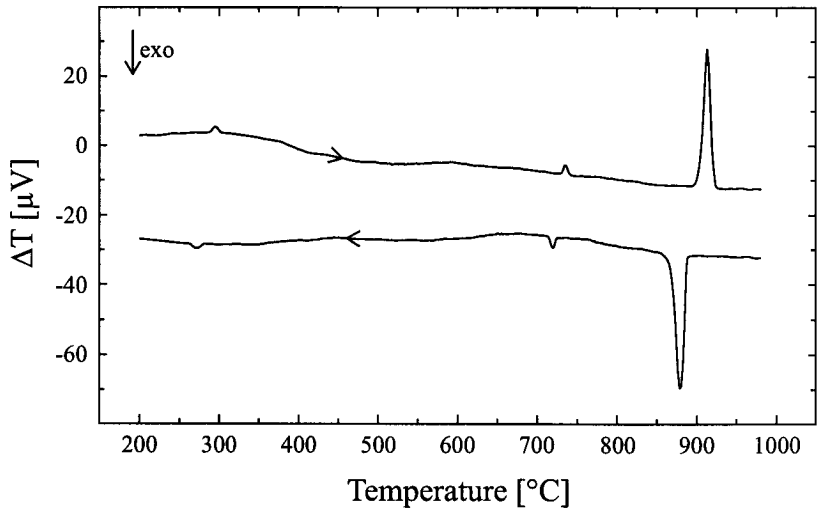

Figure 4.23: DTA of α-Li_5AlGe_2

Measurements of the conductivity were also performed on pellets (diameter = 6 mm; thickness = 0.75 mm), which were heated from one up to five days at 250°C. Again, the same grain boundary and contacts problems occurred as for the silicide and lead to unreliable results. Unfortunately no improvement of the quality of the pellets was possible since the allowed tempering temperature was even lower and the kinetics slower than in the silicon case.

4.4.4 Theoretical Investigations

The bonding structure of α-Li_5AlGe_2 accords with the Zintl-Klemm concept. It is therefore expected that α-Li_5AlGe_2 would be a semiconductor like the typical Zintl phases and also like the LiAlGe phase. In order to investigate the electronic properties and bonding structure of α-Li_5AlGe_2 we performed theoretical calculations using LMTO-methods.

As expected the DOS calculated by the LMTO-method shows a band gap at the Fermi level, though very small (Fig.4.24).

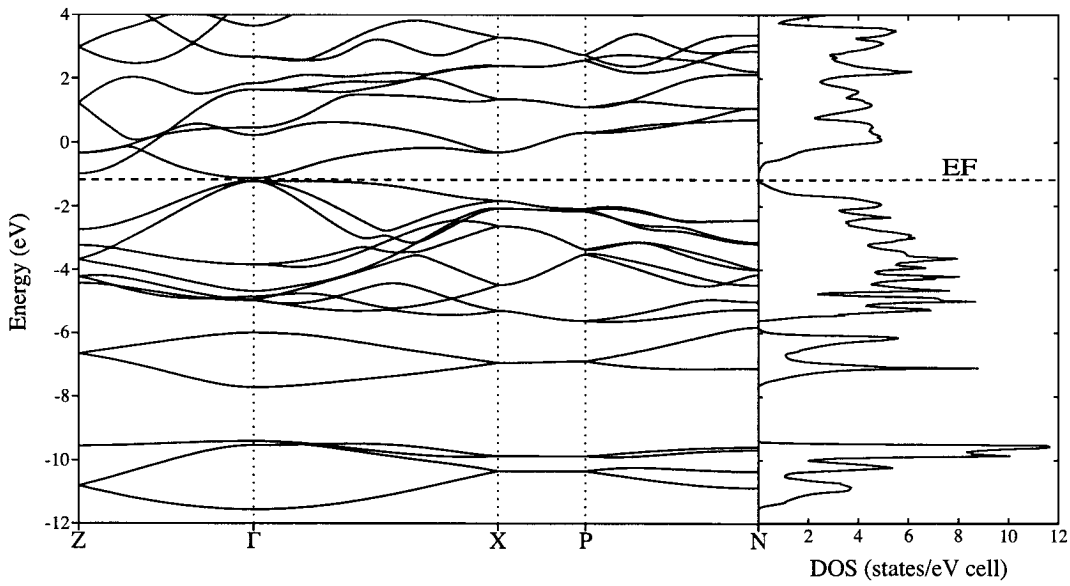

Figure 4.24: LMTO-Band structure and DOS of α-Li_5AlGe_2

In the Figure 4.25 an LMTO-ELF section of the α-Li_5AlGe_2 structure is shown. The ELF confirms the prevalent covalent character of the aluminum-germanium network, this is nicely shown by the high electron pair localisation between the two elements. Also the lone pair localised on the germanium pointing towards the lithium atoms are clearly seen in the figure (bottom left and right). There is very low electron localisation between lithium atoms and the two others species which is typical for ionic interactions. All these remarks underline the typical Zintl phase character of the α-Li_5AlGe_2 structure.

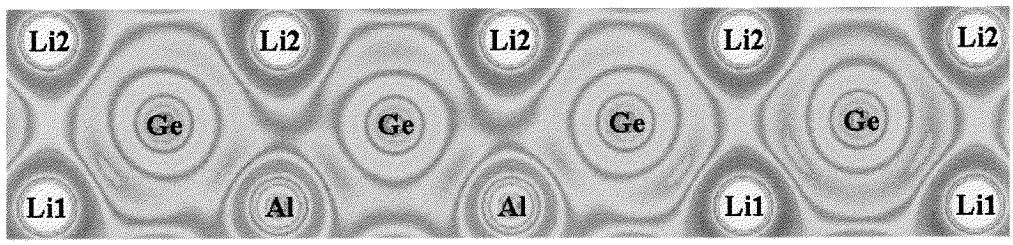

Figure 4.25: LMTO-ELF section along one part of the Al-Ge network ($\bar{2}01$ plane)

4.5 The High Temperature β-Li_5AlGe_2 Phase

According to the DTA measurements (cf. Chapter 4.4.3), the tetragonal phase α-Li_5AlGe_2, like its silicon analogue, undergoes a phase transition at the relatively low temperature of 285°C to the cubic high temperature modification β-Li_5AlGe_2. The structure of this new phase was characterized and the phase transition was investigated by high temperature X-ray experiments.

4.5.1 Synthesis

An almost pure-phase β-Li_5AlGe_2 was obtained after synthesis from a stoichiometric mixture of the elements, with 5% excess on lithium to compensate the diffusion through the crucible walls during the reaction, heated at 625°C (t_1 = 4 hours, r_1 = 200°C/h). The reaction crucible was then quenched in order to avoid the phase transition to the low temperature phase α-Li_5AlGe_2.

4.5.2 Crystal Structure

Since the compound was obtained upon quenching, the crystals found in the samples were mainly of poor quality. However, it was possible to find and isolate a single crystal, which was measured on a Siemens Platform diffractometer. All data were collected up to 2θ = 60°. For reasons of precision the lattice parameters were redetermined on the four-circle diffractometer and taken for the structure refinement. The Laue symmetry is $m\bar{3}m$ and the extinctions are consistent with the space groups $F23$, $Fm\bar{3}$, $F432$, $F4\bar{3}m$, and $Fm\bar{3}m$. The structure was refined in $F4\bar{3}m$. The structure of the β-Li_5AlSi_2 was taken as starting model for the refinement, which turned out to be difficult as the crystal was of poor quality (cf. R(int) Tab.4.30).

Measurement parameters, crystal data and parameters, atomic coordinates, occupation of the M-positions as well a selection of interatomic distances of the β-Li_5AlGe_2 structure are summarised in the Tables 4.30-33.

The occupancy factors of Al/Li for the mixed M positions were refined (Tab.4.32) and show very high standard deviation due to the bad quality of the crystal and the small

number of independent reflections used in the refinement. The obtained composition $Li_{4.96}Al_{1.04}Ge_2$ is identical with that of the low temperature phase in the range of the standard deviations.

Table 4.30: Crystal data and parameters of the data collection for β-Li_5AlGe_2

Empirical formula	Li5AlGe2
Formula weight [g/mol]	206.86
Crystal size [mm]	0.06 x 0.08 x 0.10
Colour	grey metallic lustre
Crystal system	cubic
Unit cell dimension [pm]	a = 620.5(3)
Volume [pm^3]	$238.9(2)\cdot10^6$
Space group	$F\bar{4}3m$ (216)
Formula unit pro cell	2
ρ (calculated) [g/cm^3]	2.876
Absorption coefficient μ [mm^{-1}]	12.559
F (000)	184
Temperature [K]	298
Data collection	Siemens Platform CCD
Monochromator; Wavelength	Graphite; λ(MoKα) = 0.71073 Å
Detector distance; Collection method	d = 30 mm; Hemisphere ω-Scan
Δω; Irradiation time	Δω = 0.20°; t = 30 sec
Theta range	$2° < 2\theta < 60°$
h(min), h(max); k(min), k(max); l(min), l(max)	-6, 6; -6, 6; -6, 6
Reflections collected	436
Independent reflections	30 ; R(int) = 0.1083
Independent reflections with $\|F\|^2 > 2\,\sigma(\|F\|^2)$	30
Absorption correction	empirical (SADABS)
Refinement	SHELXL-97 (full-matrix least-squares of F^2)
Parameters	7
Restraints	0
Extinction coefficient	none
Maximal shift/esd	0.000
Mean shift/esd	0.000
Largest diff. peak and hole [electrons/$pm^3\cdot10^6$]	min = -0.139; max = 0.244
[a] wR for $\|F\|^2 > 2\,\sigma(\|F\|^2)$	0.0265
wR for all reflections	0.0265
[a] R for $\|F\|^2 > 2\,\sigma(\|F\|^2)$	0.0144
R for all reflections	0.0144
[a] Goodness of Fit (*GooF*) for all reflections	1.140

[a] the definitions are given in chapter 2.2, Table 2.3

Table 4.31: Wyckoff sites, atomic coordinates, and equivalent isotropic displacement parameters [pm^2] for β-Li_5AlGe_2

Atom	*Wyckoff site*	*x*	*y*	*z*	*U(iso)*
Ge1	4*c*	1/4	1/4	1/4	163(9)
M1	4*a*	0	0	0	110(40)
M2	4*b*	1/2	1/2	1/2	240(50)
Li1	4*d*	3/4	3/4	3/4	380(70)

Table 4.32: Occupancy of the M position for β-Li_5AlGe_2

Position	*Aluminum*	*Lithium*
M1	0.4(1)	0.6(1)
M2	0.12(8)	0.88(8)

Table 4.33: Selected interatomic distances [pm] for β-Li_5AlGe_2

Ge1	–M1	268.7(1)	4x	M2	–Ge1	268.7(1)	4x
	–M2	268.7(1)	4x		–Li1	268.7(1)	4x
	–Li1	310.2(2)	6x		–M1	310.2(2)	6x
M1	–Ge1	268.7(1)	4x	Li2	–M1	268.7(1)	4x
	–Li1	268.7(1)	4x		–M2	268.7(1)	4x
	–M2	310.2(2)	6x		–Ge1	310.2(2)	6x

During the phase transition from the low to the high temperature phase the Al1, Li1 and Li2 positions of the low temperature phase mix resulting in the M1 and M2 position, the *c* axis is stretched to *c*' = 2*a*, whereas the *a* axis remain almost unchanged leading to a new cubic cell. This results in a small increase of the volume of about ~0.8%.

Presumably the rearrangements are due to mobility of the Al, the Li1 and the Li2 atoms of the low temperature phase. This is in contrast to the silicon compound where the Li2 position still remains full occupied by lithium. Although, the refinement of the silicon compound performed on powder data and therefore is less accurate than may allow for a similar situation, different site preferences due to different phono couplings are reasonable for silicides and germanides. Obviously, at temperature above 300°C the Al-Ge bonds are weak enough to permit such a mobility.

The structure of the high temperature modification β-Li_5AlGe_2 is shown in the Figure 4.26. The mixing of the Al1, Li1 and Li2 sites of the low temperature phase becomes evident. The results is a pseudo-fcc arrangement of the M1 atoms, with the M2 atoms occupying the octahedral holes, and one half of the tetrahedral holes are occupied by the germanium atoms, the other half by the Li1 atoms (Fig4.26).

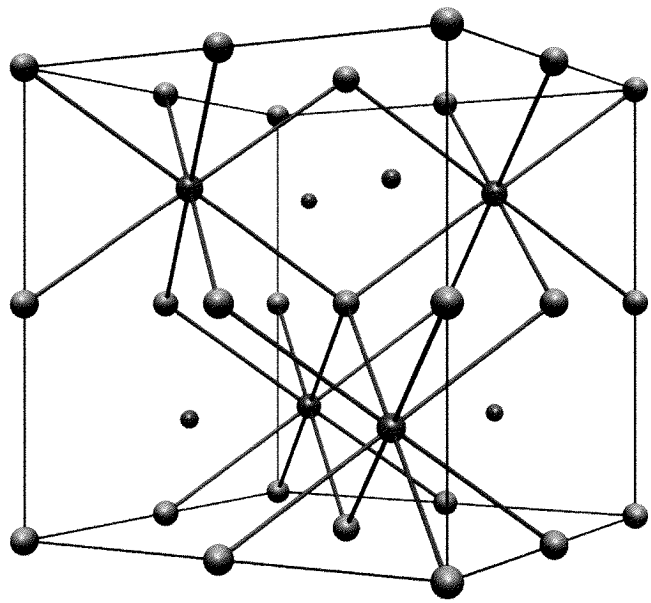

Figure 4.26: Structure β-Li_5AlGe_2 (Ge violet spheres, M turquoise, Li grey)

The resulting Ge–M distances (268.7 pm) are, as expected, an average of the Ge1–Al1 (265.8 pm), the Ge1–Li1 (270.3 pm) and the Ge1–Li2 (267.2 and 268.9 pm) distances in the low temperature phase (cf. Tab.4.29).

4.5.3 Physical Properties

In order to investigate the existence of a phase transition from the low temperature phase to the high temperature phase, X-ray powder diffraction experiments were carried out. The grounded sample was transferred to a glass capillary (0.3 mm), this was sealed and then inserted into one quartz capillary (0.5 mm), which was closed using wax in the glove box to avoid any contact with oxygen and moisture.

The measurements were carried out at different temperatures (starting temperature 100°C, end temperature 375°C, step 25°C, heat/cooling rate 50-100°C/h, holding time before the measurement 3-10 minutes, measurement time 5 minutes). In Figure 4.27 the resulting powder diffractions from 250°C to 325°C and back to 250°C are shown. In the temperature from 300 to 325°C the phase transition from the low temperature phase (tetragonal, the calculated position of the reflections is given in the figure) to the high temperature (cubic with c' ~ c/2) is evident. It is completely reversible. The super structure reflections belonging only to the tetragonal phase are marked by red arrows.

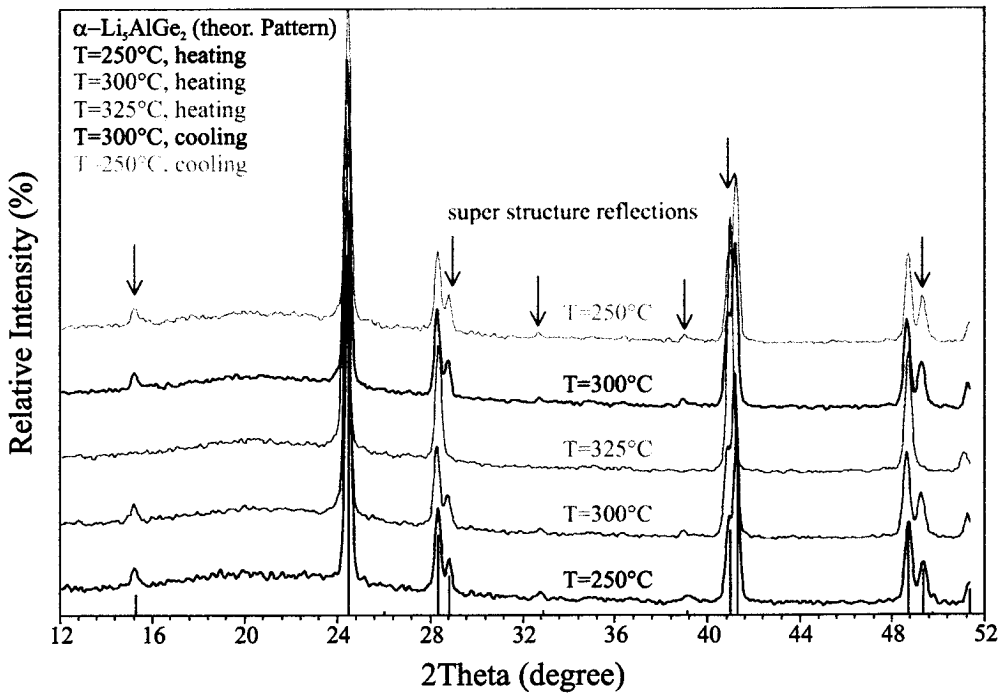

Figure 4.27: High temperature powder diagrams of the Li_5AlGe_2

4.6 The $Li_{4+x}Al_{2-x}Ge_2$ Phase

In this part synthesis and characterization of the new phase $Li_{4+x}Al_{2-x}Ge_2$ ($x \sim 1$) is described. As the isotypic silicide it exhibits new form of a graphite like 2D network of the triel-tetrel element. Unfortunately, no superstructure was found during X-ray single crystal measurements, but only indicated by powder XRD.

4.6.1 Synthesis

The compound was successfully synthesized from a stoichiometric mixture of the elements. The synthesis of pure-phase $Li_{4+x}Al_{2-x}Ge_2$ appeared to be very difficult: in almost all the syntheses a mixture of this phase and the tetragonal α-Li_5AlGe_2 was found. The synthesis of a sample rich of this compound was possible by heating a stoichiometric mixtures of the elements with small excess on Lithium (5% to compensate diffusion through the crucible) at 950°C (t_1 = 8 hours, r_1 = 200°C/h, r_e = 25°C/h). $Li_{4+x}Al_{2-x}Ge_2$ forms grey-silver crystals with a metallic lustre. It is brittle like $Li_{4+x}Al_{2-x}Si_2$ and also air and moisture sensitive. By contact with water it reacts leaving a yellow-orange powder, likely GeO_2. The decomposition products have a pungent smell.

4.6.2 Crystal Structure

Crystals were difficult to find in reaction products, moreover most of them were twins or intergrown. The existence of a superstructure like that observed in the silicon compound was confirmed by powder diffraction, however, in contrast with the silicon phase, the measurement of superstructure reflections was not possible in this case.

The crystal data were collected on a Siemens Platform diffractometer. All data were collected up to $2\theta = 70°$. Afterward the lattice parameters were redetermined on the four-circle diffractometer and taken for the structure refinement. The Laue symmetry of the main reflections is *6/mmm* and the extinctions are consistent with the space groups $P6_3mc$, $P\bar{6}2c$, and $P6_3/mmc$. The structure was solved in $P6_3/mmc$ using direct method. All atoms were anisotropically refined and the displacement parameters are all satisfactory, but also indicate split Li positions on the mixed occupied M position, as

indicated by the *U33* value of the this atom (Tab.4.36). Unfortunately the refinement of the structure using these split positions was impossible due to the high correlation between this new positions and the Al position. The occupancy factor of Al/Li for the mixed M position was also refined (Tab.4.37).

Table 4.34: Crystal data and parameters of the data collection for $Li_{4+x}Al_{2-x}Ge_2$

Empirical formula	Li5.13Al0.87Ge2
Formula weight [g/mol]	204.26
Crystal size [mm]	0.20 x 0.22 x 0.20
Colour	grey metallic lustre
Crystal system	hexagonal
Unit cell dimension [pm]	a = 441.0(1); c = 810.4(1)
Volume [pm^3]	$136.5(2)\cdot10^6$
Space group	*P6₃/mmc* (194)
Formula unit pro cell	1
ρ (calculated) [g/cm^3]	2.485
Absorption coefficient μ [mm^{-1}]	10.969
F (000)	91
Temperature [K]	298
Data collection	Siemens Platform CCD
Monochromator; Wavelength	graphite; λ(MoKα) = 0.71073 Å
Detector distance; Collection method	d = 30 mm; Hemisphere ω-Scan
Δω; Irradiation time	Δω = 0.20°; t = 30 sec
Theta range	2° < 2θ < 70°
h(min), h(max); k(min), k(max); l(min), l(max)	-7, 7; -7, 7 ; -12, 12
Reflections collected	4010
Independent reflections	142; R(int) = 0.0466
Independent reflections with $\|F\|^2 > 2\,\sigma(\|F\|^2)$	132
Absorption correction	empirical (SADABS)
Refinement	SHELXL-97 (full-matrix least-squares of F^2)
Parameters	10
Restraints	0
Extinction coefficient	0.16(2)
Maximal shift/esd	0.000
Mean shift/esd	0.000
Largest diff. peak and hole [electrons/$pm^3\cdot10^6$]	min = -0.957; max = 0.944
[a] wR for $\|F\|^2 > 2\,\sigma(\|F\|^2)$	0.0590
wR for all reflections	0.0602
[a] R for $\|F\|^2 > 2\,\sigma(\|F\|^2)$	0.0246
R for all reflections	0.0275
[a] Goodness of Fit (*GooF*) for all reflections	1.536

[a] the definitions are given in chapter 2.2, Table 2.3

Table 4.35: Wyckoff sites, atomic coordinates, and equivalent isotropic displacement parameters [pm^2] of $Li_{4+x}Al_{2-x}Ge_2$

Atoms	*Wyckoff site*	*x*	*y*	*z*	*U(iso)*
Ge	2*c*	1/3	2/3	1/4	139(3)
M	2*b*	0	0	1/4	310(9)
Li	4*f*	1/3	2/3	0.915(1)	290(20)

Table 4.36: Anisotropic displacement parameters [pm^2] for $Li_{4+x}Al_{2-x}Ge_2$

Atoms	*U11*	*U22*	*U33*	*U23*	*U13*	*U12*
Ge	140(3)	*U11*	138(3)	0	0	70(2)
M	178(10)	*U11*	570(30)	0	0	89(5)
Li	340(30)	*U11*	190(40)	0	0	168(16)

Table 4.37: Occupancy of the M position for $Li_{4+x}Al_{2-x}Ge_2$

Position	*Aluminum*	*Lithium*
M	0.435(9)	0.565(9)

Table 4.38: Selected interatomic distances [pm] for $Li_{4+x}Al_{2-x}Ge_2$

Li	–Li	268(2)	1x	Ge	–M	254.60(4)	3x	M	–Ge	254.60(4)	3x
	–Ge	271.2(9)	1x		–Li	271.2(9)	2x		–Li	287.7(5)	6x
	–M	287.7(5)	3x		–Li	287.7(5)	6x				
	–Ge	287.7(5)	3x								
	–Li	289.2(9)	3x								

$Li_{4+x}Al_{2-x}Ge_2$ (x ~ 1) crystallizes in the new structure type already found for the silicon compound (Fig.4.28).

The structure presents hexagonal layers of M-Ge atoms, these are staked along the c-axis in the same way as in hexagonal graphite: with an ABAB succession, where the M atoms are mapped on top of each other. In between the M-Ge layers there are two layers of trigonal arranged lithium atoms, these atoms build up a wurtzite network. With an occupancy of Li:Al ~ 1:1 of the M position, the composition of the phase is close to Li_5AlGe_2: the same found for the α- and β-Li_5AlGe_2. This means that this phase can be classified as the γ modification of the Li_5AlGe_2 compound.

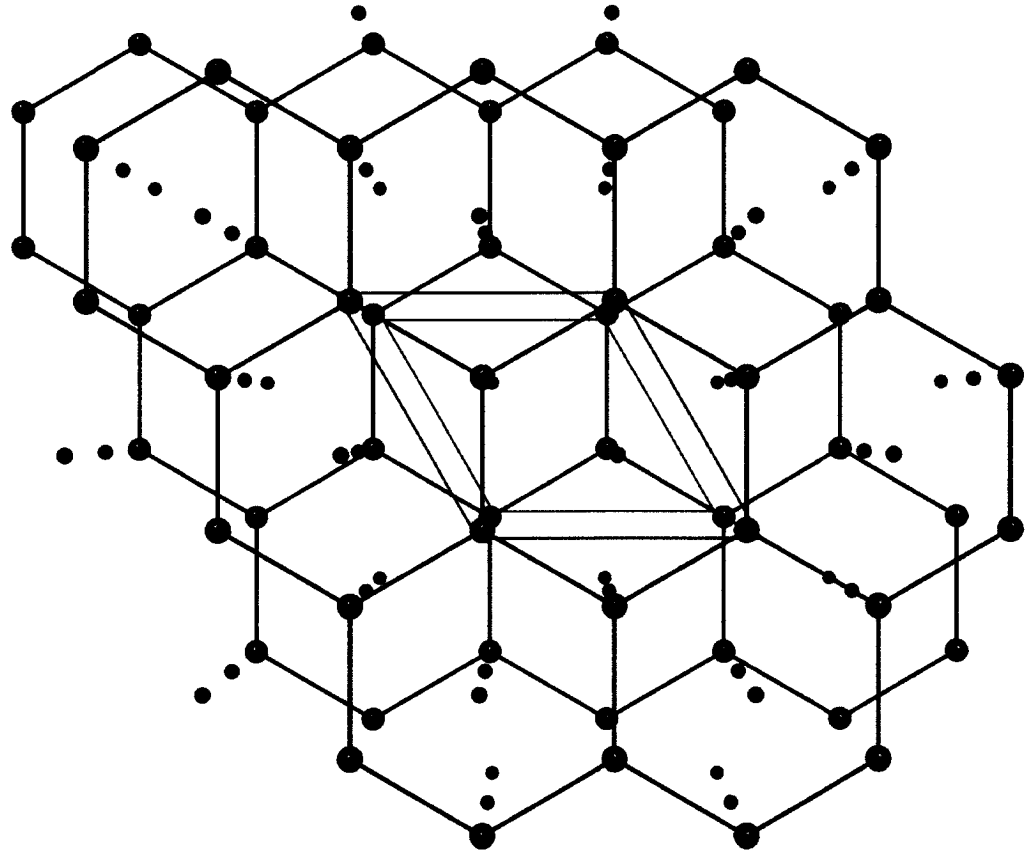

Figure 4.28: Structure of $Li_{4+x}Al_{2-x}Ge_2$ (Ge violet spheres, M turquoise, Li grey)

The Ge–M distance found in the small cell (254.6 pm) is in the range of covalent Ge–Al bonds but it is too short for Ge–Li distances, this is the explanation of the unusual *U33* value of the M position: in fact there exists a split position of lithium. Therefore, a deeper analysis of this position was carried out. The residual electron density on the

Fourier difference map around the M position clearly shows the existence of two split positions above and below it (Fig.4.29). These residual electron maxima lie on the special position 2*e* (0,0,0.19) and are likely under occupied by lithium, because the distance between them is only 0.97 Å. The resulting Ge–Li(split) distance is now 259 pm, which is still unusually short for lithium-germanium distances. In contrast to the silicon phase, here the maximum in the difference Fourier map is more elongated along the z direction. A small maximum is found on the special position 2*e* (0,0,0.1), which is however very close to the Li position in between the layers (254 pm).

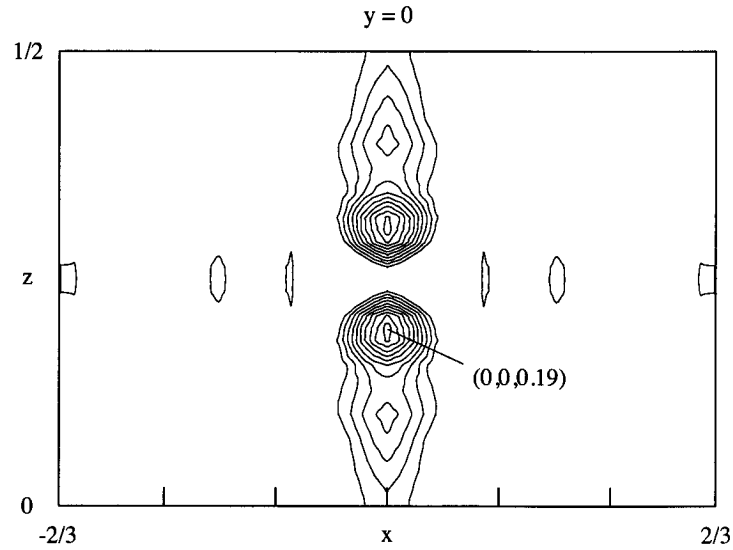

Figure 4.29: Difference Fourier map around the M position

In the Figure 4.30 the coordination of the different atoms in the $Li_{4+x}Al_{2-x}Ge_2$ structure are shown. The Ge atoms lie in the middle of a trigonal prism of lithium capped on the top by lithium atoms and on the side by the M atoms (top left).

The M atoms are also in the middle of a trigonal prism of lithium atoms capped on all faces by Ge atoms (top right). The Li atoms lie in the middle of two distorted tetrahedra: one built of lithium, the other of germanium atoms. The M atoms build a trigonal prism around the Li position, but the lithium does not lie in the middle of it.

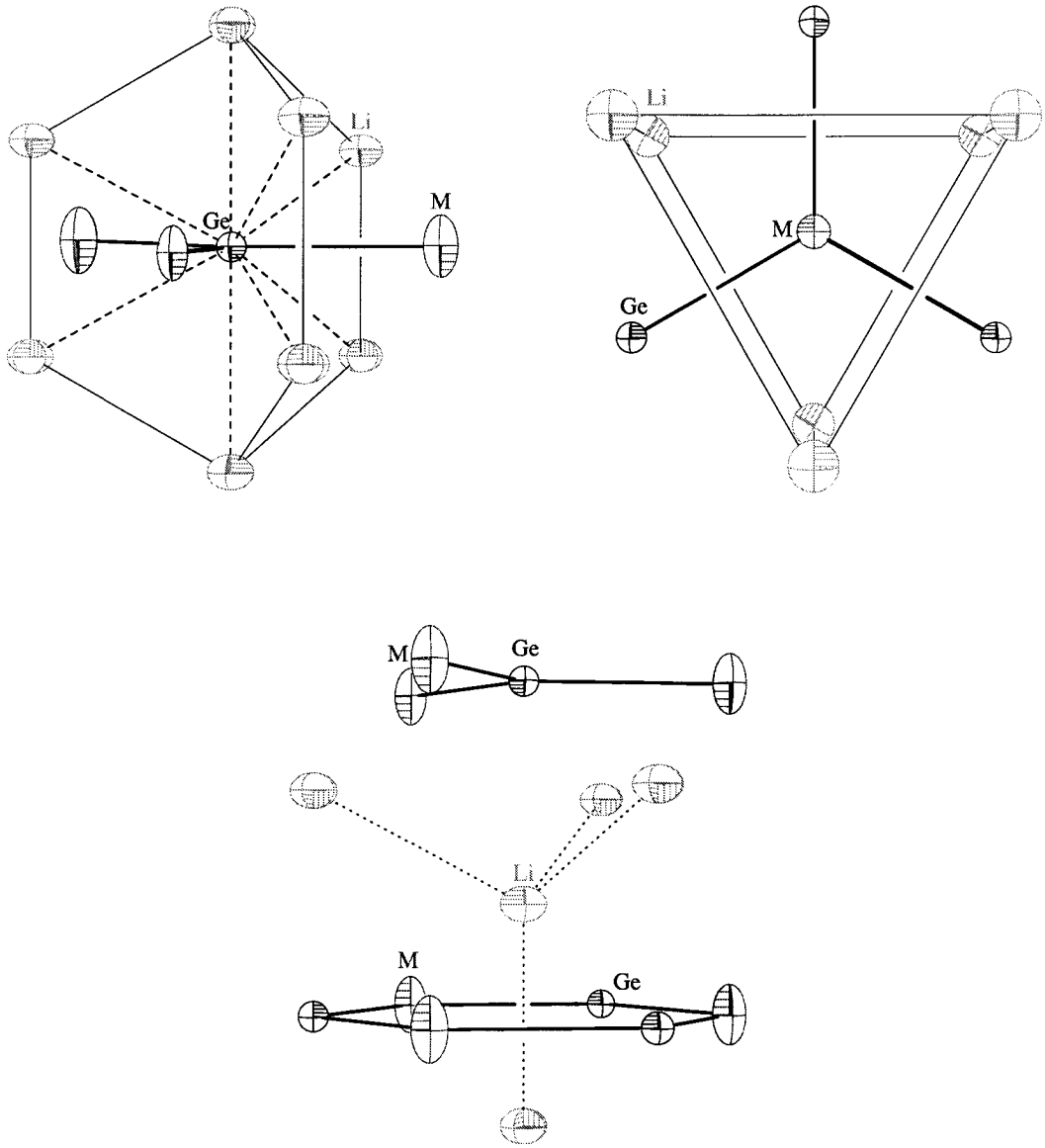

Figure 4.30: Coordination of the different atomic positions in the $Li_{4+x}Al_{2-x}Ge_2$ structure

4.6.3 Theoretical Investigations

The electronic properties of the $Li_{4+x}Al_{2-x}Ge_2$ compound were investigated on the basis of theoretical calculations performed using the LMTO method. Since the refined structure contains one mixed occupied M position of multiplicity two, an ordered model in a larger unit cell had to be found. The model already utilised for the silicon compound was used (Tab.4.39, Fig.4.18), with a super cell with $a' = 3a$. This model has the composition of Li_5AlGe_2 differing therefore significantly from the measured composition (where x is ~1.13)

Table 4.39: Atomic position in the $P\bar{6}$ (174) model used for LMTO calculations

Space group $P\bar{6}$ (174); a = 1323.0 pm, c = 810.4 pm				
Atoms	***Wyckoff site***	***x***	***y***	***z***
Ge1	3*j*	0.1111	0.2222	0
Ge2	3*j*	0.4444	0.2222	0
Ge 3	3*j*	0.1111	0.5556	0
Ge 4	3*k*	0.2222	0.1111	1/2
Ge 5	3*k*	0.2222	0.4444	1/2
Ge 6	3*k*	0.5556	0.4444	1/2
Al1	1*a*	0	0	0
Al2	1*d*	1/3	2/3	1/2
Al3	1*e*	2/3	1/3	0
Al4	3*j*	1/3	0	0
Al5	3*k*	1/3	1/3	1/2
Li1	1*b*	0	0	1/2
Li2	1*c*	1/3	2/3	0
Li3	1*f*	2/3	1/3	1/2
Li4	3*j*	1/3	1/3	0
Li5	3*k*	1/3	0	1/2
Li6	6*l*	0.1111	0.2222	0.3309
Li7	6*l*	0.4444	0.2222	0.3309
Li8	6*l*	0.1111	0.5556	0.3309
Li9	6*l*	0.2222	0.1111	0.8309
Li10	6*l*	0.2222	0.4444	0.8309
Li11	6*l*	0.5556	0.4444	0.8309

In the resulting structure there are two different types of germanium: one half of the germanium atoms are twice-bonded to aluminum, the other half has only one bond to the aluminum (Fig.4.18). As a prerequisite this model is valid in the frame of the Zintl-Klemm concept according to $(Li^+)_5[(3b)Al^-)((2b)Ge^-)((1b)Ge^{3-}]$ assuming π-contributions between the Al and the Si-2b. The occurance of π-bonds within the silicon-aluminum layers is highly probable for the same reasons given in chapter 4.3.4.
In the Figure 4.31 the calculated LMTO-DOS of the $Li_{4+x}Al_{2-x}Ge_2$ model is displayed. It shows metallic character for the compound. Again this has to be traced back to the incompletely filled π-system. The metallic character and consequently the adaptation to different electron counts may be an indication for the existence of a phasewidth of the compound.

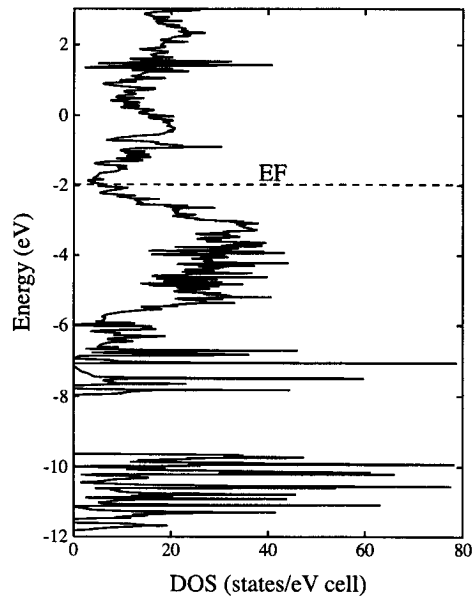

Figure 4.31: DOS of the $P\bar{6}$ model used for the $Li_{4+x}Al_{2-x}Ge_2$

4.7 The $Li_{4+x}Ga_{2-x}Si_2$ Phase

In the ternary system Li/Ga/Si no evidence of the existence neither of a tetragonal phase isostructural to the α-Li_5AlSi_2 nor to its high temperature modification β-Li_5AlSi_2 was found. However, the new phase $Li_{4+x}Ga_{2-x}Si_2$ (x ~ 1), isostructural to the $Li_{4+x}Al_{2-x}Si_2$ but with a new type of superstructure seem to dominate.

4.7.1 Synthesis

The compound was successfully synthezised from a stoichiometric mixture of the elements. The synthesis of pure-phase $Li_{4+x}Ga_{2-x}Si_2$ was not possible: in all the syntheses a mixture of this phase and other binary as well as unknown phase were obtained. The synthesis of a phase rich compound was possible by heating a stoichiometric mixture of the elements with small excess on lithium (5% to compensate diffusion through the crucible) at 800°C (t_1 = 6 hours, r_1 = 100°C/h, r_e = 20°C/h).

$Li_{4+x}Ga_{2-x}Si_2$ forms grey-silver crystals with a metallic lustre. It is brittle like $Li_{4+x}Al_{2-x}Si_2$ and also air and moisture sensitive. By contact with water it reacts explosively probably due to the formation of silanes SiH_x.

4.7.2 Crystal Structure

The quality of single crystals of $Li_{4+x}Ga_{2-x}Si_2$ was tested on a Bürger precession camera and then the crystal data were collected on a four-circle diffractometer (STADI STOE 4). The reflection data were collected up to 2θ = 60° (Tab.4.40). The crystal presents a new type of super structure with $c' = 3c$, and the same a-axis of the superstructure model of the aluminum-silicide phase. The Laue symmetry is $\bar{3}\,m1$ and the extinctions are consistent with the space groups $P3c1$, and $P\bar{3}\,c1$. The quality of the crystal, unfortunately, was not very good (cf. R(int), Tab.4.40) so that the refinement of the structure in the $P\bar{3}\,c1$ space group leads to unphysical temperature displacement parameters as well as severe correlation between the different M1-3, Ga1 and Li1 positions. The atomic positions as well as the occupancies of the M positions obtained by the refinement are displayed in the Tab.4.41-42, they are of interest because it seems

that there is a tendency to an ordering of the Ga/Li position along the *c*-direction, with the Ga1 as well as the Li1 positions within the layers fully occupied.

Table 4.40: Crystal data and parameters of the data collection for $Li_{4+x}Ga_{2-x}Si_2$

Empirical formula	Li4.98Ga1.02Si2
Formula weight [g/mol]	161.86
Crystal size [mm]	0.16 x 0.16 x 0.20
Colour	grey metallic lustre
Crystal system	trigonal
Unit cell dimension [pm]	a = 748.7(1); c = 2455.0(5)
Volume [pm^3]	$1191.9(3)\cdot10^6$
Space group	$P\bar{3}c1$ (165)
Formula unit pro cell	9
ρ (calculated) [g/cm^3]	2.029
Absorption coefficient μ [mm^{-1}]	5.56
F (000)	671
Temperature [K]	298
Data collection	four-circle diffractometer STOE STADI4
Monochromator; Wavelength	graphite; λ(MoKα) = 0.71073 Å
Scan parameters (steps; Δω; scan)	50; 0.03; ω-θ - Scan
Theta range	$2° < 2\theta < 60°$
h(min), h(max); k(min), k(max); l(min), l(max)	-8, 8; -8, 8; 0, 24
Reflections collected	4306
Independent reflections	828; R(int) = 0.2124
Independent reflections with $\|F\|^2 > 2\,\sigma(\|F\|^2)$	277
Absorption correction	Ψ-Scan
Refinement	SHELXL-97 (full-matrix least-squares of F^2)
Parameters	31
Restraints	0
Extinction coefficient	none
Maximal shift/esd	0.000
Mean shift/esd	0.000
Largest diff. peak and hole [electrons/$pm^3\cdot10^6$]	min = -1.73; max = 4.43
[a] wR for $\|F\|^2 > 2\,\sigma(\|F\|^2)$	0.1816
wR for all reflections	0.2489
[a] R for $\|F\|^2 > 2\,\sigma(\|F\|^2)$	0.0787
R for all reflections	0.2273
[a] Goodness of Fit (*GooF*) for all reflections	0.928

[a] the definitions are given in chapter 2.2, Table 2.3

Table 4.41: Wyckoff sites, atomic coordinates, and equivalent isotropic displacement parameters [pm^2] of $Li_{4+x}Ga_{2-x}Si_2$

Atoms	*Wyckoff site*	*x*	*y*	*z*	*Uiso*
Si1	6*f*	0.333(1)	0	1/4	110(30)
Si2	12*g*	0.327(1)	0.339(1)	0.083(1)	110(16)
Ga1	4*d*	1/3	2/3	0.082(2)	128(10)
M1	2*a*	0	0	1/4	210(40)
M2	4*c*	0	0	0.082(2)	140(30)
M3	4*d*	1/3	2/3	0.250(1)	130(30)
Li1	4*d*	1/3	2/3	0.914(3)	230(60)
Li2	12*g*	0.338(6)	0.992(5)	0.027(2)	170(80)
Li3	12*g*	0.357(7)	0.025(7)	0.138(2)	90(70)
Li4	12*g*	0.647(6)	0.982(6)	0.195(2)	220(80)

Table 4.42: Occupancies of the M positions

Position	*Gallium*	*Litihium*
M1	0.54(6)	0.46(6)
M2	0.51(2)	0.49(2)
M3	0.52(2)	0.48(2)

In the Figure 4.32 the superstructure of $Li_{4+x}Ga_{2-x}Si_2$ is shown. The layers with the fully occupied Ga1 and Li1 positions can be easily recognized. In the Tab.4.43 the distances of the Ga/Li positions within the layers are given for the refinement of the superstructure. It is interesting that Ga1 shows the shortest distance (243 pm) with silicon and Li1 the longest (257 pm), which is comparable to the Si–Li distances obtained for the split positions in the previously discussed compounds. The Si–M1 to M3 distances are all in the same range of about 249 pm. This is an indication that the Li atoms of these mixed occupied positions must also lie outside the plane, resulting in split positions since these distances are too short for a Si–Li contacts.

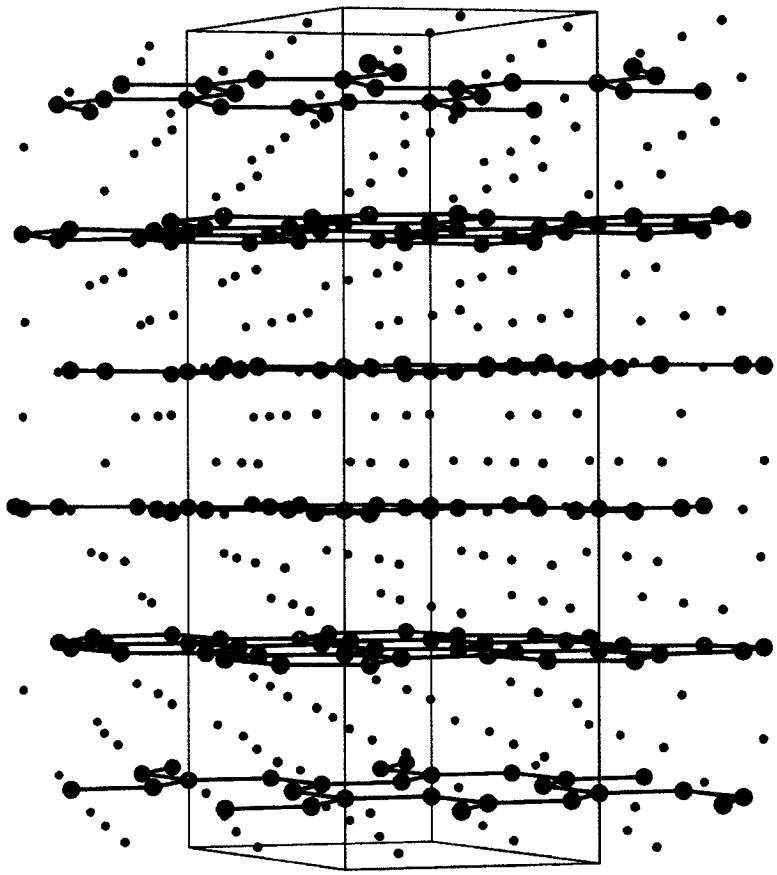

Figure 4.32: Superstructure of $Li_{4+x}Ga_{2-x}Si_2$ (Si red, Ga orange, M yellow, Li grey)

Table Error! No text of specified style in document..**1:** Selected distances of the Ga/Li positions within the layers

Ga1	–Si2	243.1(5)	3x	M2	–Si2	249.2(8)	3x	Li1	–Si2	256.7(6)	3x
	–Li2	276(3)	3x		–Li2	289(4)	3x		–Li3	264(5)	3x
	–Li3	294(5)	3x		–Li3	293(5)	3x		–Li2	289(5)	3x
M1	–Si1	249.2(9)	3x	M3	–Si1	249.8(5)	3x				
	–Li4	291(4)	6x		–Li4	272(3)	3x				
					–Li4	272(3)	3x				

Compared to the $Li_{4+x}Al_{2-x}Si_2$ phase, the superstructure found for the gallium compound shows an ordering of the triel/lithium positions along the z-direction, whereas the superstructure with $a' = 3a$ found for the aluminum compound was not observed.

The refinement of the structure was successful for using even only the main reflections. The Laue symmetry of the main reflections is *6/m* and the extinctions are consistent with the space groups $P6_3$, $P6_3/m$, and $P6_322$. The structure was refined in $P6_3/m$ (Tab.4.44). All atoms were anisotropically refined and the displacement parameters are all satisfactory, with the expected high value of *U33* for the M positions (Tab.4.46). The occupancy factors of Ga/Li for the mixed M1-3 positions were also refined (Tab.4.47).

Table 4.44: Crystal data and parameters of the data collection for the small cell of $Li_{4+x}Ga_{2-x}Si_2$ (the other parameters are the same as for the superstructure cf. Tab.4.40)

Empirical formula	Li4.98Ga1.02Si2
Formula weight [g/mol]	161.86
Crystal system	hexagonal
Unit cell dimension [pm]	a = 748.7(1); c = 818.4(2)
Volume [pm^3]	397.3(1)·10^6
Space group	$P6_3/m$ (176)
Formula unit pro cell	3
ρ (calculated) [g/cm^3]	2.029
Absorption coefficient μ [mm^{-1}]	5.56
F (000)	224
Temperature [K]	298
Theta range	2° < 2θ < 60°
h(min), h(max); k(min), k(max); l(min), l(max)	-8, 8; -8, 8; 0, 8
Reflections collected	1714
Independent reflections	301; R(int) = 0.1039
Independent reflections with $\|F\|^2 > 2\,\sigma(\|F\|^2)$	95
Refinement	SHELXL-97 (full-matrix least-squares of F^2)
Parameters	25
Restraints	0
Extinction coefficient	none
Maximal shift/esd	0.000
Mean shift/esd	0.000
Largest diff. peak and hole [electrons/pm^3·10^6]	min = -0.334; max = 0.233
[a] wR for $\|F\|^2 > 2\,\sigma(\|F\|^2)$	0.0726
wR for all reflections	0.0517
[a] R for $\|F\|^2 > 2\,\sigma(\|F\|^2)$	0.0277
R for all reflections	0.1152
[a] Goodness of Fit (*GooF*) for all reflections	0.938

[a] the definitions are given in chapter 2.2, Table 2.3

Table 4.45: Wyckoff sites, atomic coordinates, and equivalent isotropic displacement parameters [pm^2] of $Li_{4+x}Ga_{2-x}Si_2$, small cell

Atoms	*Wyckoff site*	*x*	*y*	*z*	*U(iso)*
Si	6*h*	0.000(1)	0.669(2)	1/4	120(5)
M1	2*d*	2/3	1/3	1/4	210(40)
M2	2*a*	0	0	1/4	90(30)
M3	2*c*	1/3	2/3	1/4	170(40)
Li	12*i*	0.018(5)	0.670(6)	0.918(1)	180(40)

Table 4.46: Anisotropic displacement parameters [pm^2] for $Li_{4+x}Ga_{2-x}Si_2$, small cell

Atoms	*U11*	*U22*	*U33*	*U23*	*U13*	*U12*
Si	110(30)	*U11*	142(7)	0	0	50(30)
M1	130(40)	*U11*	380(90)	0	0	60(20)
M2	70(30)	*U11*	140(30)	0	0	33(17)
M3	90(40)	*U11*	340(90)	0	0	50(20)
Li	150(80)	*U11*	230(40)	50(20)	0	70(50)

Table 4.47: Occupancies of the M positions

Position	*Gallium*	*Lithium*
M1	0.55(2)	0.45(2)
M2	0.50(2)	0.50(2)
M3	0.50(2)	0.50(2)

Table 4.48: Selected interatomic distances [pm] for $Li_{4+x}Ga_{2-x}Si_2$, small cell

Li	–Si	271.8(7)	1x	M1	–Si	250.4(4)	3x	Si	–M2	247.5(9)	1x
	–M1	274(3)	1x		–Li	274(3)	6x		–M1	250.4(9)	1x
	–Li	275.4(13)	1x						–M3	250.8(8)	1x
	–Si	277(3)	1x	M2	–Si	247.5(9)	3x		–Li	271.8(7)	2x
	–Li	277(7)	1x		–Li	289(3)	6x		–Li	277(3)	2x
	–Li	287(4)	2x						–Li	283(4)	2x
	–M2	289(3)	1x	M3	–Si	250.8(8)	3x		–Li	295(4)	2x
	–Si	283(4)	1x		–Li	292(3)	6x				
	–M3	292(3)	1x								
	–Si	295(4)	1x								

$Li_{4+x}Ga_{2-x}Si_2$ (x ~ 1) crystallizes in the same new structure type found for the $Li_{4+x}Al_{2-x}Si_2$ structure and therefore most of the structural considerations for $Li_{4+x}Al_{2-x}Si_2$ are also valid for the $Li_{4+x}Ga_{2-x}Si_2$ phase. The structure exhibits layers of fused sixrings of M-Si atoms (Fig.4.9, p.49 for the $Li_{4+x}Al_{2-x}Si_2$ structure). These are stacked along the *c*-axis in the same way as in hexagonal graphite: with an ABAB succession, with the M atoms lying on top of each other. The Li atoms build up a wurtzite network. The hexagonal layers are slightly distorted, resulting in different M–Si distances varying form 247.5 to 250.8 pm (Tab.4.48).

The anisotropic displacement parameters of the three different M positions found in the small cell (Tab.4.47) are of interest, because, as already shown for the other hexagonal compounds, this is an indication for split positions of lithium atoms (Fig.4.33).

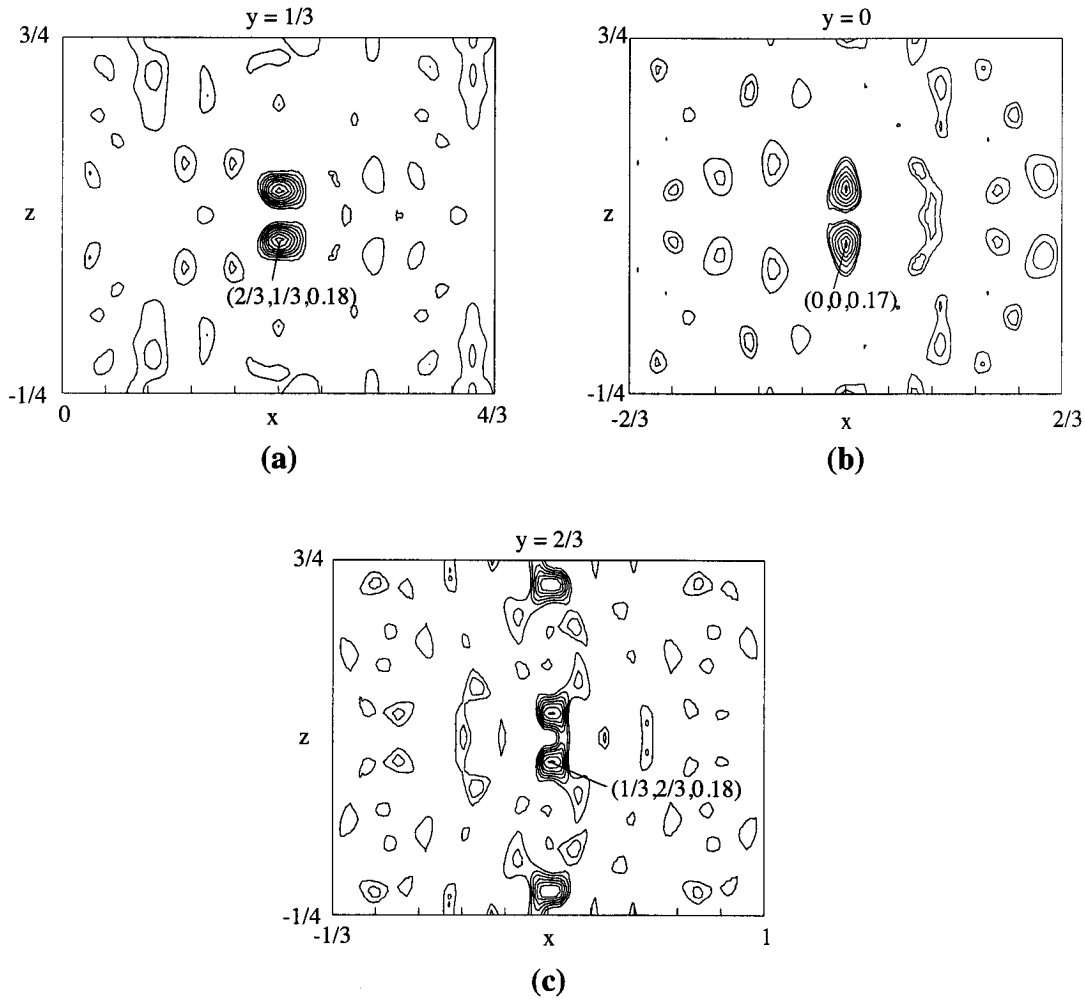

Figure 4.33: Difference Fourier maps around M1 (a), M2 (b), and M3 (c)

The difference Fourier map of a section where the lithium split positions around the different M positions are nicely displayed is shown in Figure 4.33. The resulting three positions lie on the special positions: 4*f* (1/3,2/3,0.68) for the M1, 4*e* (0,0,0.17) for the M2, and 4*f* (1/3,2/3,0.18) for the M3 position. As in the other similar cases the refinement of the structure using these split positions could not be carried out due to large correlation between the different split positions and the original M positions. The origin of these split positions is, as already explained for the other isostructural compounds, due to the too short silicon-lithium distances within the layers (248-250 pm). The resulting distances between the lithium split positions and silicon are around 258 pm.

4.7.3 Physical Properties

The existence of a phasewidth was also observed for this compound. Two different crystals were measured with a different Li:Ga ratio and different cell parameters (Tab.4.49). The observations done for the aluminum/silicon compound are also valid in this case (cf. Chapter 4.3.3).

Table 4.49: Cell parameters and Li content of the M position for the small cell

x value	*a* [pm]	*c* [pm]
0.97	432.3	818.4
1.04	433.0	817.4

4.7.4 Theoretical Investigations

The electronic properties of the $Li_{4+x}Ga_{2-x}Si_2$ compound were investigated on the basis of theoretical calculations performed using the LMTO method. The refined structure with the supercell with $c' = 3c$ (Tab.4.41-43) was used as starting model, because already eight of the eighteen M positions are ordered in that structure. Based on this, an expansion of the super cell was introduced with $a' = 2a$. The resulting 40 mixed occupied M positions were then arbitrary assigned to gallium and lithium. The model (Tab.4.50) has now the space group *Pma2* (28).

In the resulting structure there are two different types of silicon centers: one half of the silicon atoms are twobonded to gallium, the other half has only one bond with the gallium. Therefore the model is in accord with the Zintl-Klemm as described earlier.

Table 4.50: Atomic position in the ***Pma2*** (28) model used for LMTO calculations

Space group *Pma2* (28); a = 2455.0 pm, b = 748.7 pm, c = 1296.8 pm							
Atoms	***x***	***y***	***z***	***Atoms***	***x***	***y***	***z***
Si1	3/4	2/3	0	**Li4**	1/12	1/5	1/6
Si2	1/12	2/3	0	**Li5**	3/4	0	1/3
Si3	1/4	5/6	1/6	**Li6**	1/12	0	2/3
Si4	1/4	5/6	5/6	**Li7**	0.8061	1/3	0
Si5	11/12	5/6	5/6	**Li8**	0.1394	1/3	0
Si6	3/4	1/6	1/2	**Li9**	0.9728	2/3	0
Si7	11/12	5/6	1/6	**Li10**	0.3061	2/3	1/3
Si8	3/4	2/3	2/3	**Li11**	0.3061	2/3	2/3
Si9	3/4	2/3	1/3	**Li12**	0.8061	5/6	5/6
Si10	1/12	1/6	1/2	**Li13**	0.8606	2/3	2/3
Si11	1/12	2/3	1/3	**Li14**	0.8061	5/6	1/6
Si12	1/12	2/3	2/3	**Li15**	0.8606	2/3	1/3
Ga1	3/4	0	2/3	**Li16**	0.8061	5/6	1/2
Ga2	3/4	1/2	1/6	**Li17**	0.1394	5/6	1/6
Ga3	3/4	0	0	**Li18**	0.0272	5/6	1/6
Ga4	11/12	0	0	**Li19**	0.9728	2/3	1/3
Ga5	11/12	1/2	5/6	**Li20**	0.1394	5/6	5/6
Ga6	11/12	0	1/3	**Li21**	0.0272	5/6	5/6
Li1	3/4	1/2	1/2	**Li22**	0.9728	2/3	2/3
Li2	11/12	1/2	1/2	**Li23**	0.1394	5/6	1/2
Li3	3/4	1/2	5/6	**Li24**	0.9728	1/6	1/2

In the Figure 4.34 the calculated LMTO-DOS of the $Li_{4+x}Ga_{2-x}Si_2$ model is displayed. In the resulting DOS the metallic character of the compound becomes evident, due to underoccupied π-system.

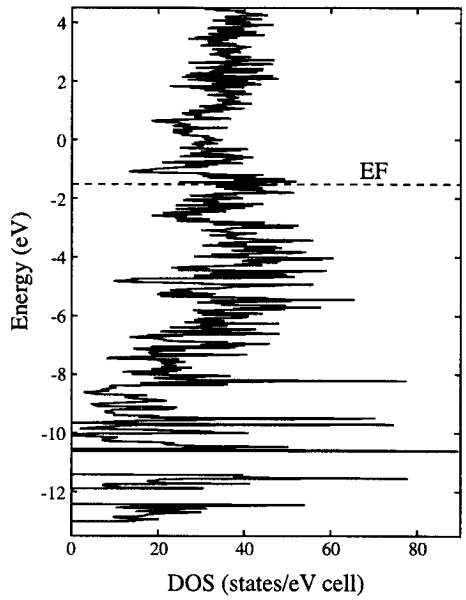

Figure 4.34: LMTO-DOS calculated for the model for the $Li_{4+x}Ga_{2-x}Si_2$ compound

4.8 The α-Li_5GaGe_2 Phase

4.8.1 Synthesis

The compound was successfully synthesized from the elements. The synthesis of pure-phase α-Li_5GaGe_2 appeared to be difficult: in almost all the synthesis the hexagonal $Li_{4+x}Ga_{2-x}Ge_2$ (x ~ 1) was a by product if not the only one. This is a sign either of a possible phase transition between these two new phases, or a peritectical decomposition of the tetragonal phase into the hexagonal.

Synthesis of phase pure product was achieved by heating a stoichiometric mixture of the elements with small excess on lithium (5% to compensate diffusion through the crucible) and on gallium (also 5%) at 700°C (t_1 = 24 hours, r_1 = 250°C/h, r_e = 20°C/h).

α-Li_5GaGe_2 forms grey-silver crystals with a light violet metallic lustre. It is brittle like α-Li_5AlSi_2 and also air and moisture sensitive. By contact with water reacts leaving a yellow-orange powder, according to the colour likely GeO_2. The decomposition products have a pungent smell.

4.8.2 Crystal Structure

Even if it was possible to obtain almost phase pure crystalline compound, the quality of the crystals found was very poor. Attempts to grow bigger crystals and more crystalline samples were unsuccessful. As intergrowth and twinning has no effect on the powder diffraction data a Rietveld analysis was carried out (Fig.4.35). For the refinement of the powder data the structure of α-Li_5AlSi_2 was taken as the starting model. The rest of the refinement was performed as in the other cases. However, the presence of two reflections, which could not be assigned to any known compound, increased the difficulties of the refinement. Problems arose also from the refinement of the atomic as well as the displacement parameters of all the lithium atoms, as the refinement was not very stable. Again the position of the Li3 atom had to be determined by difference Fourier analysis (Fig.4.36) like for the α-Li_5AlGe_2 phase, but could not be freely refined (Tab.4.52).

Table 4.51: Crystal data and parameters of the data collection for α-Li_5GaGe_2

Formula weight [g/mol]	249.61
Crystal system	tetragonal
Unit cell dimension [pm]	a = 617.8(3) pm; c = 1227.7(5) pm
Volume [pm^3]	$469(3)\cdot10^6$
Space group	$I\bar{4}2d$ (122)
Formula unit pro cell	4
ρ (calculated) [g/cm^3]	3.535
Absorption coefficient μ [mm^{-1}]	6.624
F (000)	224.0
Temperature [K]	298
Data collection	STOE STADI P2, PDS detector ($2\Theta_{eff}$ = 7°)
Monochromator; Wavelength	germanium; λ(CuKα) = 1.54056 Å
Scan parameters: step width; time/step	0.5°; 280 seconds
Theta range	14° < 2θ < 91°
Refinement	GSAS
Largest diff. peak and hole [electrons/$pm^3\cdot10^6$]	min = -0.69; max = 0.63
[a] wR_p	0.1216
[a] R_p	0.0825
[a] R_F	0.0667
[a] Goodness of Fit χ^2	2.00

[a] the definitions are given in chapter 2.2, Table 2.2

Table 4.52: Wyckoff sites, atomic coordinates, and equivalent isotropic displacement parameters [pm^2] for α-Li_5GaGe_2

Atom	*Wyckoff site*	*x*	*y*	*z*	*U(iso)*
Ge1	*8d*	0.252(2)	1/4	1/8	170(20)
Ga1	*4b*	0	0	1/2	290(30)
Li1	*4a*	0	0	0	130(30)
Li2	*8c*	0	0	0.251(4)	230(40)
Li3	*8d*	0.752	1/4	1/8	610(50)

Table 4.53: Selected interatomic distances [pm] for α-Li_5GaGe_2

Ga1	–Ge1	266(1)	4x	Li1	–Li3	266	4x	Li3	–Li1	266 2x
	–Li3	268	4x		–Ge1	268(2)	4x		–Li2	267 4x
	–Li2	306(2)	2x		–Li2	308(3)	2x		–Ga1	268 2x
	–Li2	309(4)	4x		–Li2	309(4)	4x		–Ge1	307 2x
									–Ge1	308 1x
Ge1	–Li2	265(2)	2x	Li2	–Ge1	265(2)	2x		–Ge1	309 3x
	–Ga1	266(1)	2x		–Li3	267	4x			
	–Li1	268(2)	2x		–Ge1	269(2)	2x			
	–Li2	269(2)	2x		–Ga1	306(2)	1x			
	–Li3	307	2x		–Li1	308(3)	1x			
	–Li3	308	1x		–Li1	309(4)	2x			
	–Li3	309	3x		–Ga1	309(4)	2x			

The good quality of the Rietveld refinement is seen in Figure 4.35: the pink curve at the bottom represents the difference between the calculated curve (blue line in the figure) and the measured reflection pattern (represented by red crosses in the figure).

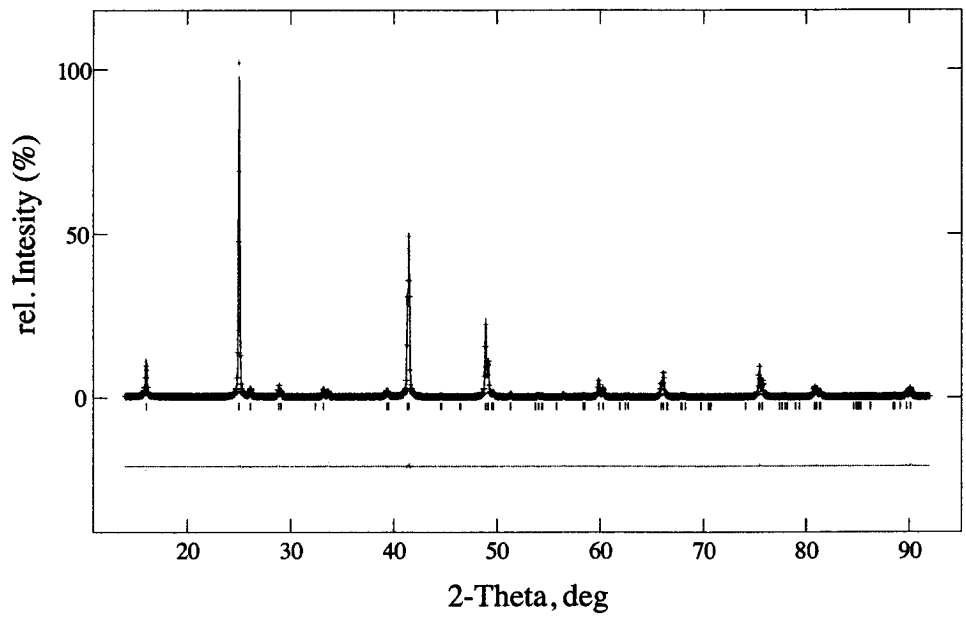

Figure 4.35: Rietveld Analysis of the α-Li_5GaGe_2 structure

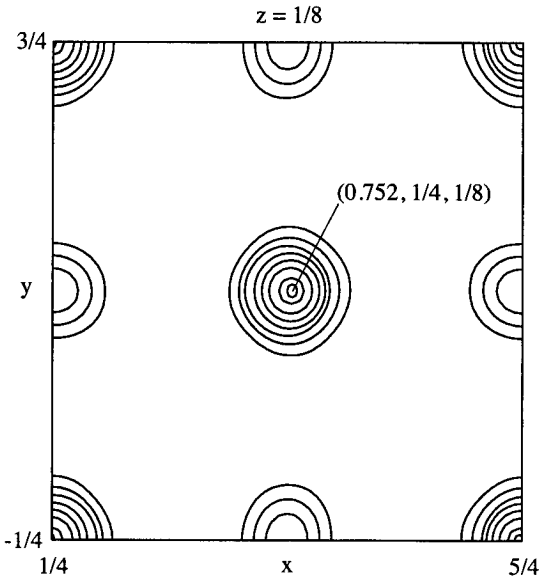

Figure 4.36: Difference Fourier Map around the Li3 position

α-Li_5GaGe_2 crystallizes in the new structure type already found for α-Li_5AlSi_2 and α-Li_5AlGe_2. The Ge–Ga distance of 266 pm (Tab.4.53) in the anionic framework is slightly longer than those observed in the LiGaGe structure (254 and 258 pm) but still in the range of Ge–Ga covalent bonds (254-268 pm).

Compared to the α-Li_5AlSi_2 phase the basic cell of the α-Li_5GaGe_2 compound is, as expected, larger. The *a*-axis is slightly longer (0.1%), whereas the *c*-axis is 0.7% longer, this results in an increase in the volume of about 1.1%. As expected from known distances in aluminides and in gallides, the cell is slightly smaller than that of the α-Li_5AlGe_2 (1.2%).

4.8.3 Physical Properties

The tetragonal phase α-Li_5GaGe_2, like its other analogue undergoes a phase transition around the temperature of 200°C to the cubic high temperature modification β-Li_5GaGe_2. This phase transition was investigated by high temperature X-ray experiments (Fig.4.37). Unfortunately, in contrast to the two previously discussed phases, the refinement of the structure was not possible since neither pure phase samples nor single crystals were obtained during this work.

For the X-ray powder diffraction experiments the grounded sample was transferred to a

glass capillary (0.3 mm), this was sealed and then inserted into one quartz capillary (0.5 mm), which was closed using wax in the glove box to avoid any contact with oxygen and moisture.

The measurements were carried out at different temperatures (starting temperature 100°C, end temperature 300°C, step 25°C, heat/cooling rate 50-100°C/h, holding time before the measurement 3-10 minutes, measurement time 5 minutes).

In Figure 4.37 the resulting powder diffractions from 150°C to 250°C and back to 175°C are shown. The phase transition from the low temperature phase (tetragonal, the calculated position of the reflections is given in the figure) to the high temperature (cubic with $c' \sim c/2$) is evident between 200 and 250°C. The super-structure reflections belonging only to the tetragonal phase are marked by red arrows.

However, in contrast to the other previous discussed tetragonal compounds, the phase transition is much slower and thus exhibits a more pronounced hysteresis. In fact, during the heating procedure, the phase transition starts at around 225°C and ends at 250°C, where only the reflections belonging to the β-Li_5GaGe_2 are present. On cooling from 225°C only the cubic phase is present, then the low temperature α-Li_5GaGe_2 phase starts to occur slowly at 200°C and at 175°C it is completely reformed.

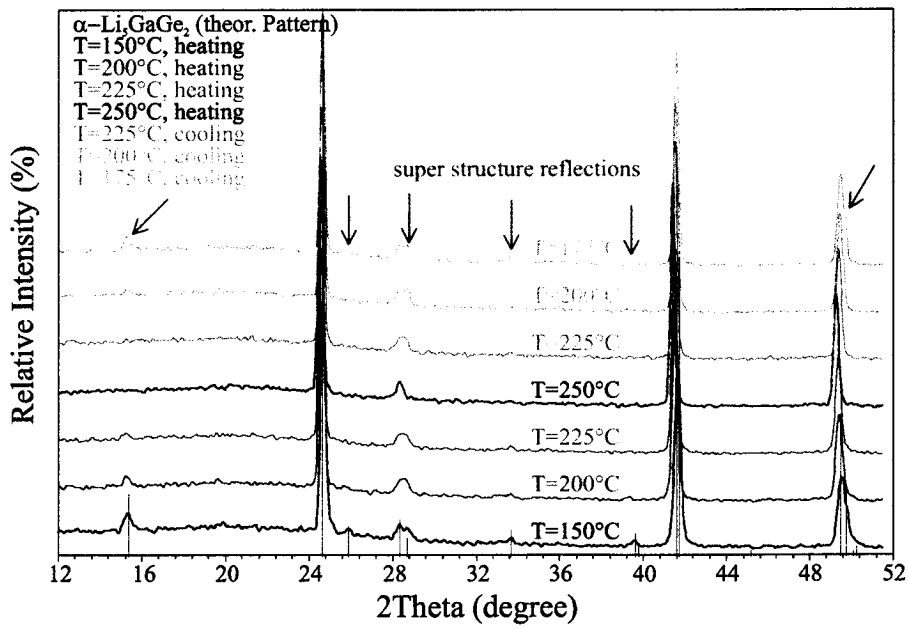

Figure 4.37: High temperature powder diagrams of the Li_5GaGe_2

4.8.4 Theoretical Investigations

In order to investigate the electronic properties and bonding structure of α-Li_5GaGe_2 we performed theoretical calculations using LMTO-methods. The band structure as well as the DOS are similar to the other already discussed isostructural compounds. As expected the DOS calculated by the LMTO-method shows a band gap though very tiny. Therefore, α-Li_5GaGe_2 is a semimetal (Fig.4.38).

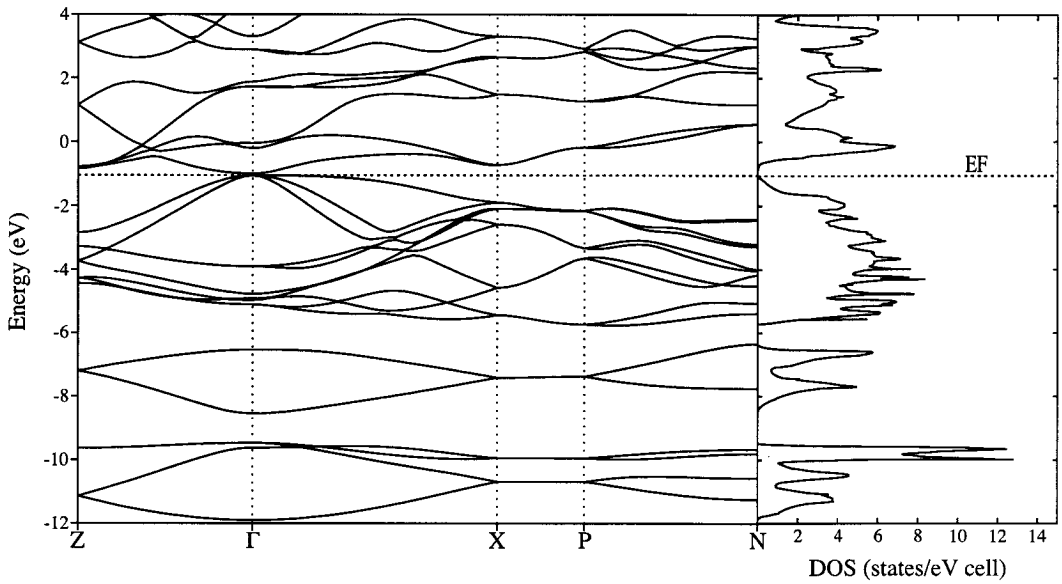

Figure 4.38: Band structure and DOS calculated using LMTO method for α-Li_5GaGe_2

4.9 The $Li_{4+x}Ga_{2-x}Ge_2$ Phase

4.9.1 Synthesis

The compound was successfully synthezised from a stoichiometric mixture of the elements. The synthesis of pure-phase $Li_{4+x}Ga_{2-x}Ge_2$ was not possible: in all the syntheses a mixture of this phase and of the tetragonal α-Li_5GaGe_2 was obtained.

The synthesis of a phase rich compound was performed by heating a stoichiometric mixture of the elements with small excess on lithium (5% to compensate diffusion through the crucible) at 900°C (t_1 = 6 hours, r_1 = 300°C/h, r_2 = 5°C/h, T_2 = 620°C, t_2 = 5 min, r_e = 100°C/h).

$Li_{4+x}Ga_{2-x}Ge_2$ forms grey-silver crystals with a metallic lustre. At contact with water reacts leaving a yellow-orange powder, according to the colour likely GeO_2. The decomposition products have a pungent smell.

4.9.2 Crystal Structure

Crystals were difficult to find in reaction products, moreover most of them were twins or intergrowth. In contrast to the $Li_{4+x}Al_{2-x}Si_2$ compound no crystal of good quality presenting super structure reflections were detected. The crystal data were collected on a Siemens Platform diffractometer. Either again the quality of the crystal was not very good (cf. *R*(int), Tab.4.54). All data were collected up to $2\theta = 60°$ (Tab.4.54-58). Afterwards the lattice parameters were redetermined on the four-circle diffractometer and taken for the structure refinement.

The Laue symmetry of the main reflections is *6/mmm* and the extinctions are consistent with the space groups $P6_3mc$, $P\bar{6}2c$, and $P6_3/mmc$. The structure was solved in $P6_3/mmc$ using direct methods. All atoms were anisotropically refined and the displacement parameters are all satisfactory, but also indicate the presence of split Li positions on the mixed occupied M position, as indicated by the *U33* value of this atom (Tab.4.56). During the refinement of the split positions a high correlation between these and the Ga position made it impossible to yield reasonable parameters. The occupancy factor of Ga/Li for the mixed M position was refined (Tab.4.57).

Table 4.54: Crystal data and parameters of the data collection for $Li_{4+x}Ga_{2-x}Ge_2$

Empirical formula	Li4.99Ga1.01Ge2
Formula weight [g/mol]	250.23
Crystal size [mm]	0.08 x 0.08 x 0.24
Colour	grey metallic lustre
Crystal system	hexagonal
Unit cell dimension [pm]	a = 437.2(1); c = 822.0(1)
Volume [pm^3]	$136.1(1)\cdot10^6$
Space group	*P6₃/mmc* (194)
Formula unit pro cell	1
ρ (calculated) [g/cm^3]	3.054
Absorption coefficient μ [mm^{-1}]	15.76
F (000)	110
Temperature [K]	298
Data collection	Siemens Platform CCD
Monochromator; Wavelength	graphite; λ(MoKα) = 0.71073 Å
Detector distance; Collection method	d = 30 mm; Hemisphere ω-Scan
Δω; Irradiation time	Δω = 0.20°; t = 15 sec
Theta range	$2° < 2\theta < 70°$
h(min), h(max); k(min), k(max); l(min), l(max)	-6, 6; -6, 6; -12, 12
Reflections collected	1931
Independent reflections	136 ; R(int) = 0.1083
Independent reflections with $\|F\|^2 > 2\,\sigma(\|F\|^2)$	84
Absorption correction	empirical (SADABS)
Refinement	SHELXL-97 (full-matrix least-squares of F^2)
Parameters	10
Restraints	0
Extinction coefficient	0.025(3)
Maximal shift/esd	0.000
Mean shift/esd	0.000
Largest diff. peak and hole [electrons/$pm^3\cdot10^6$]	min = -1.048; max = 1.558
[a] wR for $\|F\|^2 > 2\,\sigma(\|F\|^2)$	0.0778
wR for all reflections	0.0900
[a] R for $\|F\|^2 > 2\,\sigma(\|F\|^2)$	0.0380
R for all reflections	0.0852
[a] Goodness of Fit (*GooF*) for all reflections	1.256

[a] the definitions are given in chapter 2.2, Table 2.3

Table 4.55: Wyckoff sites, atomic coordinates, and equivalent isotropic displacement parameters [pm^2] of $Li_{4+x}Ga_{2-x}Ge_2$

Atoms	*Wyckoff site*	*x*	*y*	*z*	*U(iso)*
Ge	2*d*	1/3	2/3	3/4	140(5)
M	2*b*	0	0	1/4	181(11)
Li	4*f*	1/3	2/3	0.081(2)	260(40)

Table 4.56: Anisotropic displacement parameters [pm^2] for $Li_{4+x}Ga_{2-x}Ge_2$

Atoms	*U11*	*U22*	*U33*	*U13*	*U23*	*U12*
Ge	123(5)	*U11*	174(7)	0	0	62(3)
M	115(13)	*U11*	310(20)	0	0	58(6)
Li	270(50)	*U11*	240(70)	0	0	130(30)

Table 4.57: Occupancy of the M position

Position	*Gallium*	*Litihium*
M	0.508(8)	0.492(8)

Table 4.58: Selected interatomic distances [pm] for $Li_{4+x}Ga_{2-x}Ge_2$

Li	–Ge	271.7(2)	1x	Ge	–M	252.39(3)	3x	M	–Ge	252.39(3)	3x
	–Li	279(3)	1x		–Li	271.7(2)	2x		–Li	288.3(8)	6x
	–Li	285.0(16)	3x		–Li	288.3(8)	6x				
	–Ge	288.3(8)	3x								
	–M	288.3(8)	3x								

$Li_{4+x}Ga_{2-x}Ge_2$ (x ~ 1) crystallizes with the $Li_{4+x}Al_{2-x}Si_2$ structure type and therefore most of the structural considerations for $Li_{4+x}Al_{2-x}Si_2$ are also valid for this phase. With an occupancy of Li:Ga = 1:1 of the M position, the composition of the phase is Li_5GaGe_2: the same found for the α- and β-Li_5GaGe_2. Therefore, like for the previously discussed ternary systems, this phase can be described as the high temperature γ-modification of the Li_5GaGe_2 phase.

The Ge–M distance of 252.4 pm is in the range of covalent Ge–Ga bonds but it is too short for Ge–Li distances. Consequently a split position of lithium is found. The residual electron density on the Fourier difference map around the M position is shown in Figure 4.39. These residual electron density maxima lie on the special position 2*e* (0,0,0.20) and the resulting Ge-Li distance is 257 pm, which is still unusually short for lithium germanium distances.

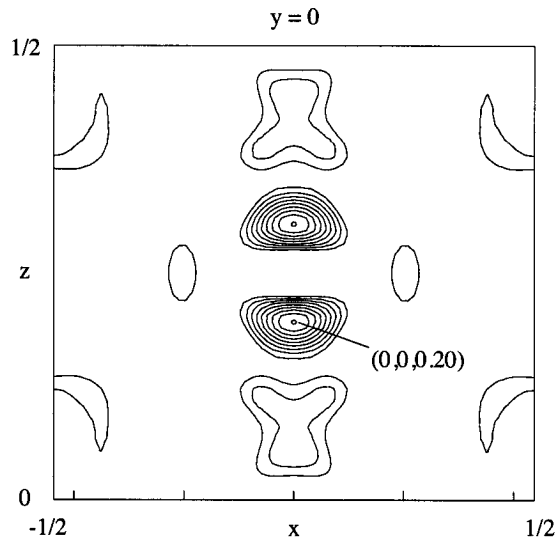

Figure 4.39: Difference Fourier map around the M position

4.9.3 Theoretical Investigations

The electronic properties of the $Li_{4+x}Ga_{2-x}Ge_2$ compound were investigated on the basis of theoretical calculations performed using the LMTO method. The model already used for the aluminum-silicon compound was applied (Tab.4.59, Fig.4.18 p. 64), with a super cell with $a' = 3a$, and the space group $P\bar{6}$.

Table 4.59: Atomic position in the $P\bar{6}$ (174) model used for LMTO calculations

Space group $P\bar{6}$ (174); a = 1311.6 pm, c = 822.0 pm				
Atoms	***Wyckoff site***	***x***	***y***	***z***
Ge1	3*j*	0.1111	0.2222	0
Ge2	3*j*	0.4444	0.2222	0
Ge 3	3*j*	0.1111	0.5556	0
Ge 4	3*k*	0.2222	0.1111	1/2
Ge 5	3*k*	0.2222	0.4444	1/2
Ge 6	3*k*	0.5556	0.4444	1/2
Ga1	1*a*	0	0	0
Ga2	1*d*	1/3	2/3	1/2
Ga3	1*e*	2/3	1/3	0
Ga4	3*j*	1/3	0	0
Ga5	3*k*	1/3	1/3	1/2
Li1	1*b*	0	0	1/2
Li2	1*c*	1/3	2/3	0
Li3	1*f*	2/3	1/3	1/2
Li4	3*j*	1/3	1/3	0
Li5	3*k*	1/3	0	1/2
Li6	6*l*	0.1111	0.2222	0.3309
Li7	6*l*	0.4444	0.2222	0.3309
Li8	6*l*	0.1111	0.5556	0.3309
Li9	6*l*	0.2222	0.1111	0.8309
Li10	6*l*	0.2222	0.4444	0.8309
Li11	6*l*	0.5556	0.4444	0.8309

In the Figure 4.40 the calculated LMTO-DOS of the $Li_{4+x}Ga_{2-x}Ge_2$ model is displayed. It does not show additional features compared to the other isotypic phases.

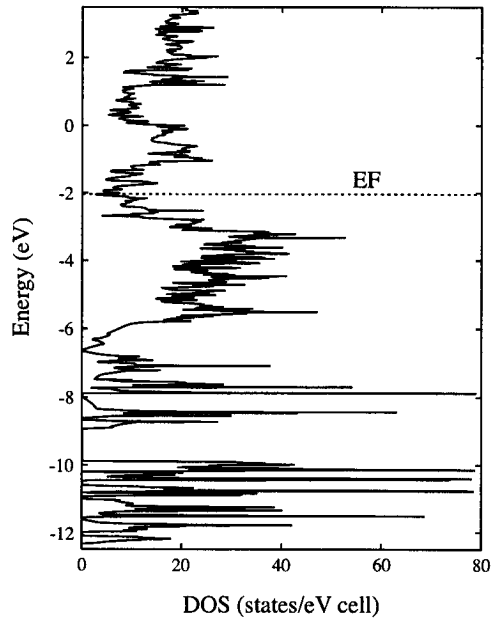

Figure 4.40: LMTO-DOS of the $P\bar{6}$ model used for the $Li_{4+x}Ga_{2-x}Ge_2$

4.10 The Li_5AlSn_2 Phase

Here, synthesis and characterization of the α-Li_5AlSn_2 phase, which is isotypic to α-Li_5AlSi_2 is reported.

In this ternary system Li/Al/Sn no evidence was found for the existence of a hexagonal phase isostructural to $Li_{4+x}Al_{2-x}Si_2$.

4.10.1 Synthesis

The compound was successfully synthesized from the elements. The synthesis of pure-phase Li_5AlSn_2 was difficult. Synthesis of almost phase pure product was achieved by heating a stoichiometric mixture of the elements with small excess on lithium (5% to compensate diffusion through the crucible) and on aluminum (also 5%) at 700°C (t_1 = 12 hours, r_1 = 200°C/h, r_e = 10°C/h).

Li_5AlSn_2 forms grey-silvery crystals with a light violet metallic lustre. It is brittle like α-Li_5AlSi_2 and also air and moisture sensitive. By contact with water reacts leaving a black powder.

4.10.2 Crystal Structure

Crystals were difficult to find in reaction products, moreover most of them were twins or intergrown. However, it was possible to isolate a single crystal, the diffraction data of which were collected on a 4-circle diffractometer. During a first measurement the superstructure reflections ($c' = 2c$) were not detected, but since the refinement did not lead to a good solution, a second measurement was carried out, which gave clear evidence for a larger cell. All data were collected up to $2\theta = 60°$ (Tab.4.60-64). The Laue symmetry is *4/mmm* and the extinctions are consistent with the space group $I4_1/amd$, but, like for the aluminum-silicon compound, no reasonable refinement could be done in this space group. The symmetry was reduced and structure solutions were tried. The actual space group is in fact $I\bar{4}2d$: the *a*-glide plane extinctions arise from a *a*/2 pseudo translation in [100] direction. After finishing the structure refinement it became clear that the *a* glide plane is fulfilled by only three of the five atomic sites. The structure was then refined in $I\bar{4}2d$. Unfortunately the refinement of the anisotropic

displacement parameters of the lithium atoms was not possible since it leaded to unphysical values, probably because of the strong influence of only one heavy scatterer, the Sn atom.

Table 4.60: Crystal data and parameters of the data collection for Li_5AlSn_2

Empirical formula	Li5Al1Sn2
Formula weight [g/mol]	299.06
Crystal size [mm]	0.08 x 0.08 x 0.10
Colour	grey metallic lustre
Crystal system	tetragonal
Unit cell dimension [pm]	a = 660.1(1); c = 1304.2(3)
Volume [pm^3]	$568.3(2)\cdot10^6$
Space group	$I\bar{4}2d$ (122)
Formula unit pro cell	4
ρ (calculated) [g/cm^3]	3.495
Absorption coefficient μ [mm^{-1}]	8.77
F (000)	512.0
Temperature [K]	298
Data collection	four-circle diffractometer STOE STADI4
Monochromator; Wavelength	graphite; λ(MoKα) = 0.71073 Å
Scan parameters (steps; Δω; scan)	59; 0.03; ω-θ - Scan
Theta range	$2° < 2\theta < 65°$
h(min), h(max); k(min), k(max); l(min), l(max)	-9, 7; -7, 9; -18, 18
Reflections collected	1167
Independent reflections	281; R(int) = 0.0434
Independent reflections with $\|F\|^2 > 2\,\sigma(\|F\|^2)$	179
Absorption correction	Ψ-Scan
Refinement	SHELXL-97 (full-matrix least-squares of F^2)
Parameters	11
Restraints	0
Extinction coefficient	none
Maximal shift/esd	0.000
Mean shift/esd	0.000
Largest diff. peak and hole [electrons/$pm^3\cdot10^6$]	min = -0.984; max = 1.599
[a] wR for $\|F\|^2 > 2\,\sigma(\|F\|^2)$	0.0466
wR for all reflections	0.0517
[a] R for $\|F\|^2 > 2\,\sigma(\|F\|^2)$	0.0206
R for all reflections	0.0450
[a] Goodness of Fit (*GooF*) for all reflections	1.104

[a] the definitions are given in chapter 2.2, Table 2.3

Table 4.61: Wyckoff sites, atomic coordinates, and equivalent isotropic displacement parameters [pm^2] for Li_5AlSn_2

Atoms	*Wyckoff site*	*x*	*y*	*z*	*U(iso)*
Sn1	*8d*	0.2558(1)	1/4	1/8	157(1)
Al1	*4b*	0	0	1/2	115(7)
Li1	*4a*	0	0	0	180(50)
Li2	*8c*	0	0	0.250(2)	120(50)
Li3	*8d*	0.770(4)	1/4	1/8	470(50)

Table 4.62: Anisotropic displacement parameters [pm^2] for Li_5AlSn_2

Atoms	*U11*	*U22*	*U33*	*U23*	*U13*	*U12*
Sn1	154(14)	141(14)	177(2)	0	0	0
Al1	101(11)	*U11*	147(17)	0	0	0

Table 4.63: Selected interatomic distances [pm] for Li_5AlSn_2

Al1	–Sn1	282.48(6)	4x	Li1	–Li3	277.4(9)	4x	Li3	–Li1	277.4(9)	2x
	–Li3	292.4(9)	4x		–Sn1	286.93(6)	4x		–Li2	277.6(9)	2x
	–Li2	326(2)	2x		–Li2	326(2)	2x		–Li2	292.2(9)	2x
	–Li2	330.06(3)	4x		–Li2	330.06(3)	4x		–Al1	292.4(9)	2x
									–Sn1	321(2)	1x
Sn1	–Li2	282.3(9)	2x	Li2	–Li3	277.6(9)	2x		–Sn1	326.3(1)	2x
	–Al1	282.48(6)	2x		–Sn1	282.3(9)	2x		–Sn1	330.5(1)	2x
	–Li1	286.92(6)	2x		–Sn1	287.1(9)	2x		–Sn1	339(2)	1x
	–Li2	287.1(9)	2x		–Li3	292.2(9)	2x				
	–Li3	321(2)	1x		–Al1	326(2)	1x				
	–Li3	326.3(1)	2x		–Li1	326(2)	1x				
	–Li3	330.5(1)	2x		–Al1	330.06(3)	2x				
	–Li3	339(2)	1x		–Li1	330.06(3)	2x				

The Li_5AlSn_2 compound crystallizes in the new structure type found for α-Li_5AlSi_2. The resulting Sn–Al distance of 282.5 pm (Tab.4.63) in the anionic framework is quite long, and since very few Al-Sn compounds are known hitherto, difficult to interpret, because there are not very many reference distances available. The difference compared to the other isostructural compounds becomes clearer by the inspection of the sum of the covalent radii of the two elements (265 pm vs. 240-250 pm for the other triel-tetrel combinations investigated during this work).

Compared to the silicon phase the basic cell of the tin compound is, as expected, much larger. The *a*- as well as the *c*-axis are about 6.9% longer, leading to an increase in the volume of about 22%. This dramatic increase in the volume was already observed for the other known aluminun-tin compound $Sr_3Al_2Sn_2$ vs. $Sr_3Al_2Si_2$ (cf. Chapter 3.3.1), where an increase of the volume of ~17% is found for the same number of Si/Sn sites in the reference cells.

4.10.3 Theoretical Investigations

The bonding structure of Li_5AlSn_2 accords with the Zintl-Klemm concept. In order to investigate the electronic properties and bonding structure of Li_5AlSn_2 theoretical calculations using LMTO-methods were performed.

In contrast to the silicide the tin compound is a metal according to the calculated DOS and band structure. The metallic character of the phase is due to the crossing of the Fermi level by one band going from the Z- to the Γ-point (Fig.4.41). However, the density of states at the Fermi level is still very small.

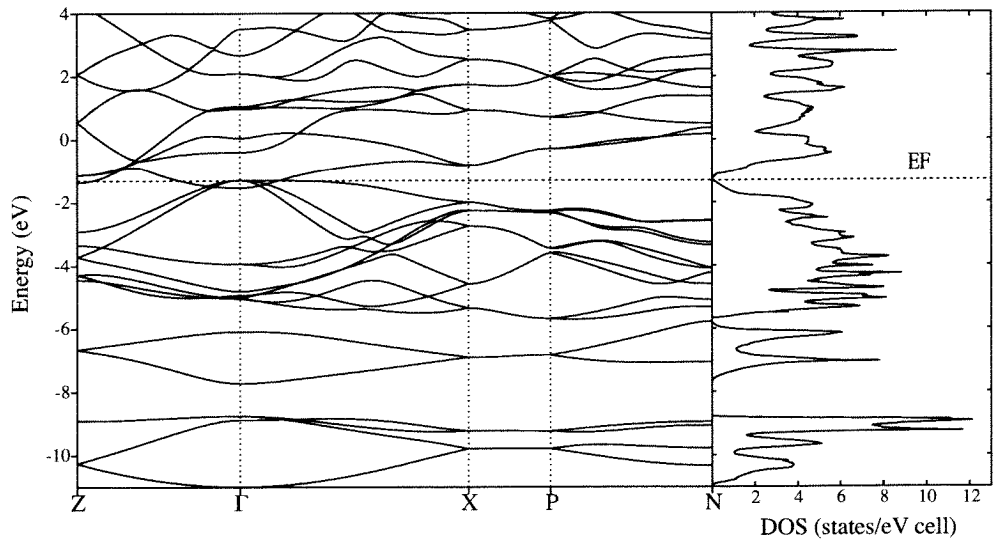

Figure 4.41: Band structure and DOS calculated with the LMTO method for Li_5AlSn_2

In the Figure 4.42 the LMTO-ELF section of the Li_5AlSn_2 structure is shown. The ELF confirms the prevalent covalent character of the aluminum-tin network, this is nicely shown by the high electron localisation between the two elements. Also the lone pair region is found at tin pointing towards the lithium atoms, and is nice displayed on the Figure 4.42 (bottom left and right), whereas the very low electron localisation between the lithium atoms and the two others elements is typical for ionic interactions. All these remarks underline the typical Zintl phase character of the Li_5AlSn_2 structure.

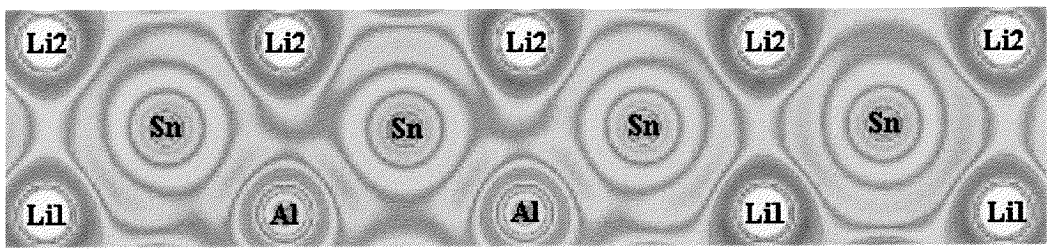

Figure 4.42: ELF-section along one part of the Al-Sn network ($\bar{2}01$ plane)

4.11 Conclusions

Structures

The ternary systems Li/Tr/Tt show a fairly uniform behaviour. For most of them there is a compound Li_5TrTt_2 which can occur in at least two modifications. The new phases α-Li_5TrTt_2 (Tr = Al, Ga; Tt = Si, Ge, and Sn), β-Li_5TrTt_2 (Tr = Al, Ga; Tt = Si, Ge), and $Li_{4+x}Tr_{2-x}Tt_2$ (Tr = Al, Ga; Tt = Si, Ge) were synthesized and their structures were determined.

The α-Li_5AlSi_2 as well as the α-Li_5AlSn_2 structures were determined by single crystal measurements, whereas the α-Li_5AlGe_2 as well as the α-Li_5GaGe_2 structures were refined from powder diffraction data. All these phase can be described according to the Zintl-Klemm concept by the formulation $(Li^+)_5\,{}^3_\infty[((4b)Tr^-)((2b)Tt^{2-})_{4/2}]$. Characteristic feature of these phases is the cristobalite-like anionic network built of the triel and tetrel elements.

Excluding the tin compound, for all other phases a structural transition at higher temperatures is observed. The high temperature modification exhibits mixed occupied triel/lithium positions, the resulting structure is characterised by a diamond network built of tetrel elements and the M atoms. The structure of the high temperature phase β-Li_5AlGe_2 was determined by single crystal measurement, the structure of the β-Li_5AlSi_2 was determined from powder diffraction data, whereas the structure of the β-Li_5GaGe_2 could not be refined since there was no sufficiently good set of data.

The occurence of a high temperature phase of the tin compound could not be proved, because no phase pure sample for the high temperature powder diffraction experiment was gained.

For the system Li/Ga/Si the existence of the tetragonal phase could not be proved, even if weak reflections which could belong to this phase were seen in powder diffraction patterns near the strong reflections of the $Li_{4+x}Ga_{2-x}Si_2$ phase. However, it was not yet possible to isolate single crystals.

The hexagonal structure $Li_{4+x}Tr_{2-x}Tt_2$ was characterised for the triel elements Al and Ga and for the tetrel elements Si and Ge, x could not be determined to high accuracy, since, in all compounds mixed occupation on the triel/lithium positions is observed. These

new phases crystallize with the Li_2ZnSi structure type. In all these hexagonal compounds one mixed occupied position was found with a Tr:Li ratio of about one. The existence of a phasewidth is quite probable, since for the Al-Si compound three different crystals were characterised with different Li:Al ratios as well as cell parameters. The existence of a phasewidth in these compounds does not exclude the description of these phases as high temperature modification of the α- and β-Li_5TrTt_2 compounds. However, in the case of the Li/Ga/Si system the hexagonal compound seems to be the room temperature phase.

Comparisons

In the table 4.64 the bond distances between the triel and the tetrel elements in the different structures are summarized. Interesting is the expected contraction of bond length changing the triel element from aluminum to gallium. The π character of the bond in the hexagonal structures is nicely shown by the shorter distances compared to the α- and β-Li_5TrTt_2 phases. In the table 4.65 the densities of the different phases are shown. Interesting is here the contraction of the densities down the columns as expected for high temperature phases.

Table 4.64: Triel – Tetrel bond distances [pm] in the different structures

Structure\Bond	Al – Si	Al – Ge	Al – Sn	Ga – Si	Ga – Ge
α-Li_5TrTt_2	261.19(9)	265.8(1)	282.48(6)	–	266(1)
β-Li_5TrTt_2	266.5(3)	268.7(1)	–	–	–
[a]$Li_{4+x}Tr_{2-x}Tt_2$	250.75(3)	254.60(4)	–	249.58(3)	252.39(3)

[a] The distances here are those between the Tt and the M position in the substructure

Table 4.65: Densities [g/cm^3] of the different ternary phases

Structure\El.	Al / Si	Al / Ge	Al / Sn	Ga / Si	Ga / Ge
α-Li_5TrTt_2	1.687	2.893	3.495	–	3.535
β-Li_5TrTt_2	1.678	2.869	–	–	–
$Li_{4+x}Tr_{2-x}Tt_2$	1.490	2.515	–	2.031	3.062

The border nature (metal/semimetal) of the electronegative elements is nicely shown by the physical properties of the different structures: semiconductors most of the α-Li_5TrTt_3 phases (with the exception of the tin compound discussed later), metals all the hexagonal $Li_{4+x}Tr_{2-x}Tt_2$ phases. Unfortunately the physical properties of the β phases could not be investigated.

In the figure 4.43 the band structure as well as the DOS of the α-Li_5TrTt_3 phases are shown. For the aluminum compounds the band gap decreases, as expected, going from silicon to tin, where the band gap disappears and the phase is a metal, reflecting the properties of the tetrel elements.

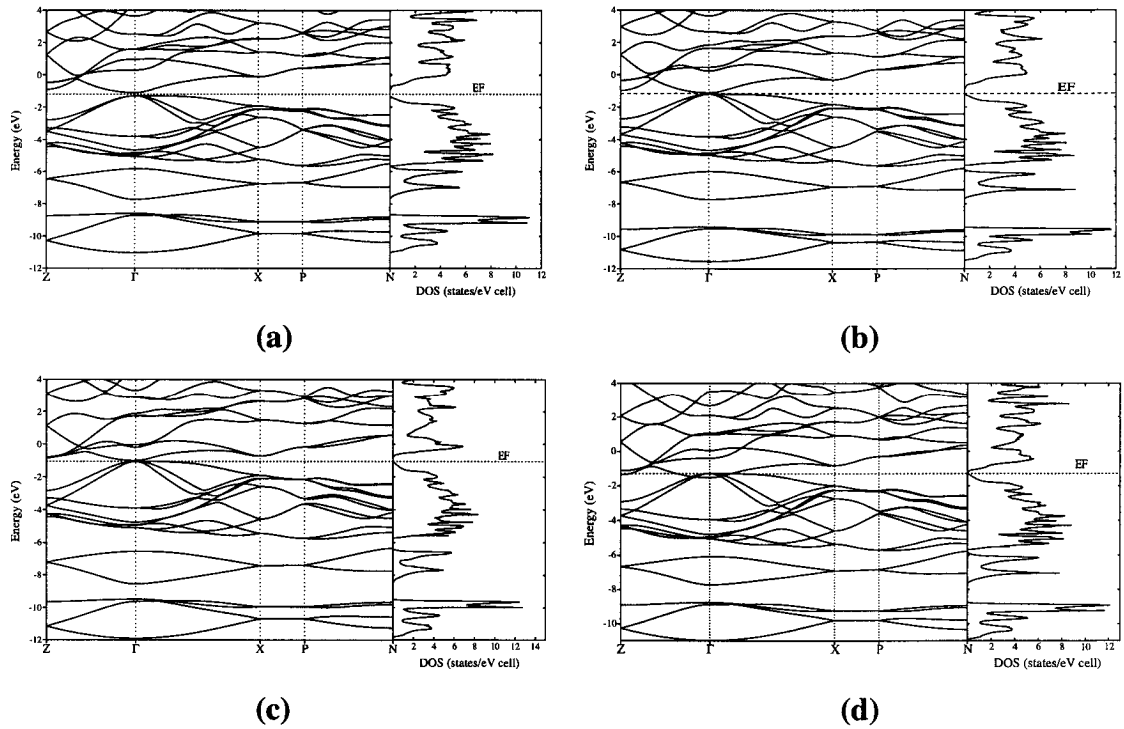

Figure 4.43: LMTO-Band structures and DOS calculated for the α-Li_5TrTt_2; (a) α-Li_5AlSi_2, (b) α-Li_5AlGe_2, (c) α-Li_5GaGe_2, (d) Li_5AlSn_2,

In the Figure 4.44 the ELF section along the triel-tetrel network of the tetragonal α-Li_5TrTt_2 phases are shown. The ELF-pictures confirm the prevalent covalent character of the triel-tetrel network. This is nicely shown by the high electron pair localisation between the two elements. Also the lone pair localised on the tetrel pointing towards the lithium atoms are nicely displayed in Figure 4.44, whereas the very low

electron localisation between the lithium atoms and the two others centers is typical for ionic interactions. Furthermore it is clear that the tetrel element is the electron sink in these compounds. The ELF pictures confirm also the decreasing electron localization the by changing the tetrel elements, leading to the metallicity of the tin compound.

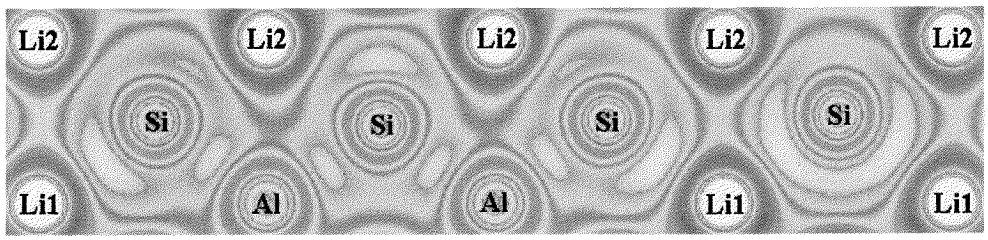

(a)

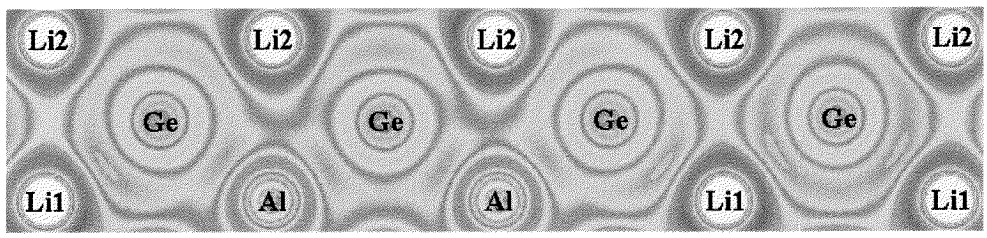

(b)

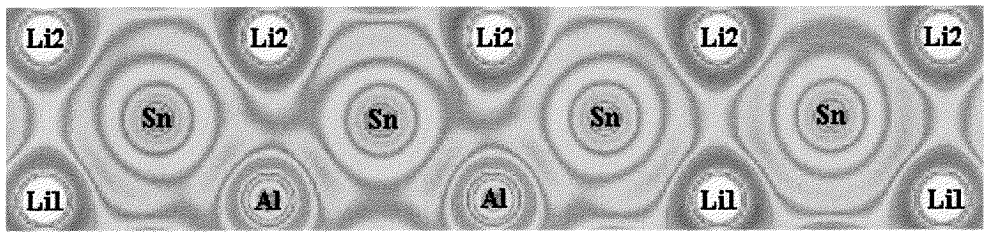

(c)

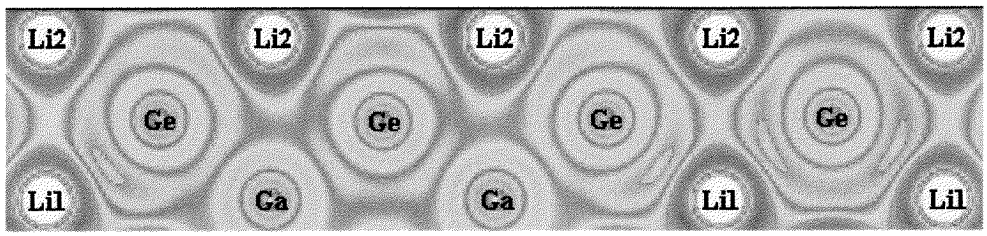

(d)

Figure 4.44: ELF-sections of the α-Li_5TrTt_2 phases; (a) α-Li_5AlSi_2, (b) α-Li_5AlGe_2, (c) Li_5AlSn_2, (d) α-Li_5GaGe_2,

Phase relations

The three new structure type found in this system have almost the same composition. The second class of compounds, the cubic β-Li_5TrTt_2, is the high temperature modification of the tetragonal α-Li_5TrTt_2 with transition temperatures around 300°C.
The hexagonal $Li_{4+x}Tr_{2-x}Tt_2$ (x ~ 1) phases have almost the same composition as the two other compounds. As there is a certain phasewidth one may assume that these compounds set up another form, namely the γ-high temperature modification of the Li_5TrTt_2 phases which survives up to the melting points. For all these phases phasewidth is very probable but could not precisely be determined, yet. Thus a peritectical decomposition of the β-Li_5TrTt_2 modification into the hexagonal phase and a small amount of other by-products is also a possible, but improbable, scenario.
For the Li/Al/Si ternary the phase diagram in the region of the Li_5AlSi_2 compound can be drawn as in the figure 4.45, for the other investigated system the temperatures are slightly different.

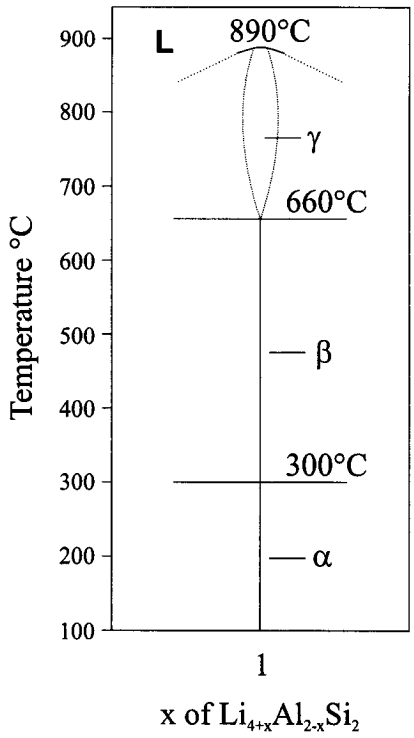

Figure 4.45: Proposed phase diagram for the Li/Al/Si system

Superstructures of the $Li_{4+x}Tr_{2-x}Tt_2$

All structures of the different $Li_{4+x}Tr_{2-x}Tt_2$ compounds were determined based on single crystal diffraction data.

In some cases superstructure reflections were observed. For the Al/Si compound two types of superstructure have been observed: (A) has a hexagonal lattice constant $a_x' = a_x - a_y$, $a_y' = a_x + 2a_y$ (Fig.4.13, p. 52), that leads to a threefold superstructure, and the other one (B) shows $a'' = 3a$, leading to a ninefold superstructure. Whereas in the first structure the Al/Li positions are still mixed, in the second structure some of these positions show ordered occupation and are fully occupied by aluminum resp. lithium.

For the gallium/silicon compound, near the (A) type of superstructure, another new superstructure is observed with $c' = 3c$, resulting in a ninefold cell expansion compared to the small substructure. This superstructure contains also fully occupied Li resp. Ga positions near still mixed occupied Ga/Li positions.

Surprisingly, for the corresponding germanium compounds, no indications for superstructures were observed in single crystal diffraction experiments, but still observed in powder diagrams.

The presence of this collection of different types of superstructures indicates a fairly high ordering tendency compared to typical intermetallics and a lower one compared to typical Zintl phases.

5. The Quaternary Li/Sr/Al/Tetrel System

In this quaternary system there were no phases known. The ability of aluminum and silicon to form covalent networks is already known and it was our interest to evaluate whether and how different cations may influence structure and characteristics of such compounds.

During this work it was possible to synthesize four new phases: $Li_xSrAl_{1-x}Tt$ (x = 0.5; Tt = Si, Ge, NaAlSi-structure type), $Li_{2+x}Sr_2Al_{6-x}Si_6$ (x ~ 2.8) and $Li_{3+x}Sr_5Al_{16-x}Si_{12}$ (x ~ 6.2),. The later two crystallise with new structure types.

5.1 The Li_xSrAl_{1-x}Tetrel Phases

In order to investigate the quartenary system, a series of syntheses was performed with the compositions leading to an $[AlSi_{4/2}]^{5-}$ network already found in the tetragonal ternary phase Li_5AlSi_2. The chosen stoichiometry was Li : Sr : Al : Si = 1 : 2 : 1 : 2 because the intention was to synthesize another, cristobalite-related, network with one lithium occupying the Li1 position of the tetragonal Li_5AlSi_2 structure and one strontium occupying one of the two other lithium positions.

We succeeded in the preparation and characterisation of two new isostructural phases with the composition $Li_xSrAl_{1-x}Tt$ (Tt = Si, Ge), where x, according to our investigations, has a value of 0.5. These compounds are isostructural with the NaAlSi ternary phase (anti-PbFCl type) [92], the same structure is also found for the ternary compounds BaMgTt (Tt = Si, Ge, Sn, Pb) [93,94].

5.1.1 $Li_xSrAl_{1-x}Si$

Experiments were carried out with variation of the Al:Li ratio from 7:3 to 3:7. They did not show any significant variation of the lattice parameters. This is a sign that the phase has no, or an only very narrow phasewidth. The phase, therefore, tends to be "electron precise" with the formula $LiSr_2AlSi_2$, resulting not only isostructural but also isoelectronic to the NaAlSi phase.

5.1.1.1 Synthesis

Phase pure $Li_xSrAl_{1-x}Si$ (x = 0.5) was prepared by tempering a stoichiometric mixture of the elements at 1050°C (t_1 = 4 hours, r_e = 25°C/h). $Li_xSrAl_{1-x}Si$ (x = 0.5) forms brittle grey, irregular crystals with metallic lustre. The compound is very air and moisture sensitive and by contact with water reacts explosively probably due to the formation of SiH_n giving a black powder as product.

5.1.1.2 Crystal Structure

A single crystal of $Li_xSrAl_{1-x}Si$ (x = 0.5) was measured on a four-circle diffractometer. All data were collected up to 2θ = 65°. The Laue symmetry is *4/mmm* and the extinctions are consistent with the space groups *P4/n* and *P4/nmm*. The structure was solved in *P4/nmm* using direct methods (Tab.5.1). All atoms were anisotropically refined and the displacement parameters are all in the usual range (Tab.5.2-3). The metal position M exhibits mixed occupation by aluminum and lithium. The corresponding occupancy factor was also refined (Tab.5.4).

Some reflections, which may or may not belong to the crystal structure, were seen on long time exposition pictures but could not be indexed and measured properly. Thus, there may be a superstructure.

The refinement of the structure in the space group $P\bar{4}$ was carried out in addition. In this space group the M position is splitted in two different crystallographically independent positions. The refinement did not lead to any significant change in the structure as the R values and the anisotropic displacement parameters are considerably worse, and the occupancies of the two M positions differ only slightly (Tab.5.6).

In conclusion, being the extinction conditions consistent with the higher symmetric space group and the changes in the Li/Al ratio of the two independent M positions in $P\bar{4}$ not very significant, the higher symmetric space group was chosen for the structure refinement.

Table 5.1: Crystal data and parameters of the data collection for $Li_xSrAl_{1-x}Si$ (x = 0.5) (the first given reliability parameters refer to a free refinement of the Al to Li ratio, the second ones to an occupancy of 1:1)

Empirical formula	Li1Sr2Al1Si2	
Formula weight [g/mol]	265.14	
Crystal size [mm]	0.16 x 0.12 x 0.12	
Colour	grey with metallic lustre	
Crystal system	tetragonal	
Unit cell dimension [pm]	a = 443.8(1); c = 724.2(1)	
Volume [pm^3]	142.6(1)·10^6	
Space group	*P*4/*nmm* (129)	
Formula unit pro cell	1	
ρ (calculated) [g/cm^3]	3.087	
Absorption coefficient μ [mm^{-1}]	19.11	
F (000)	119.9	
Temperature [K]	298	
Data collection	four-circle diffractometer STOE STADI4	
Monochromator; Wavelength	graphite; λ(MoKα) = 0.71073 Å	
Detector distance; Collection method	48; 0.03; ω-θ - Scan	
Theta range	2° < 2θ < 65°	
h(min), h(max); k(min), k(max); l(min), l(max)	-6, 6; -6, 6; 0, 10	
Reflections collected	1030	
Independent reflections	181; R(int) = 0.0529	
Independent reflections with $\|F\|^2 > 2\,\sigma(\|F\|^2)$	158	
Absorption correction	Ψ-Scan	
Refinement	SHELXL-97 (full-matrix least-squares of F^2)	
Parameters	10	
Restraints	0	
Extinction coefficient	none	
Maximal shift/esd	0.000	
Mean shift/esd	0.000	
Largest diff. peak and hole [electrons/pm^3·10^6]	min = -0.647; max = 0.400	
[a] wR for $\|F\|^2 > 2\,\sigma(\|F\|^2)$	0.0364	0.0366
wR for all reflections	0.0380	0.0381
[a] R for $\|F\|^2 > 2\,\sigma(\|F\|^2)$	0.0175	0.0177
R for all reflections	0.0266	0.0267
[a] Goodness of Fit (*GooF*) for all reflections	1.104	1.109

[a] the definitions are given in chapter 2.2, Table 2.3

Table 5.2: Wyckoff sites, atomic coordinates, and equivalent isotropic displacement parameters [pm^2] for $Li_xSrAl_{1-x}Si$ (x = 0.5)

Atoms	*Wyckoff site*	*x*	*y*	*z*	*U(iso)*
Sr	2*c*	1/4	1/4	0.82869(5)	158(2)
Si	2*c*	1/4	1/4	0.2941(2)	166(3)
M	2*b*	3/4	1/4	1/2	123(6)

Table 5.3: Anisotropic displacement parameters [pm^2] for $Li_xSrAl_{1-x}Si$ (x = 0.5)

Atoms	*U11*	*U22*	*U33*	*U23*	*U13*	*U12*
Sr	170(2)	*U11*	133(2)	0	0	0
Si	188(4)	*U11*	121(5)	0	0	0
M	127(8)	*U11*	115(9)	0	0	0

Table 5.4: Occupancy of the M-position for $Li_xSrAl_{1-x}Si$ (x = 0.5)

Position	*Aluminum*	*Lithium*
M	0.49(1)	0.51(1)

Table 5.5: Selected interatomic distances [pm] for $Li_xSrAl_{1-x}Si$ (x = 0.5)

Sr	–M	325.41(5)	4x	Si	–M	267.32(7)	4x	M	–Si	267.32(7)	4x
	–Si	326.18(6)	4x		–Sr	326.18(6)	4x		–M	313.81(4)	4x
	–Si	337.05(6)	1x		–Sr	337.05(6)	1x		–Sr	325.41(5)	4x
	–Sr	400.04(7)	4x								

Table 5.6: Selected parameters of refinement in $P\bar{4}$

R(int) for 1100 indedent reflections = 0.0406	
R for all refl. = 0.0416	wR for all refl. = 0.0643
R for $\|F\|^2 > 2\,\sigma(\|F\|^2)$ = 0.0276	wR for $\|F\|^2 > 2\,\sigma(\|F\|^2)$ = 0.0611

Position	*Aluminum*	*Lithium*
M1	0.55(6)	0.45(6)
M2	0.44(6)	0.54(6)

The inspection of the occupancy factors reveals that the Li to Al ratio is 1:1 in the range of the standard deviations. A constraint refinement of the structure with an occupancy of 1:1 leads to almost unchanged R-values (Tab.5.1). As the model with 50% occupancy is more reasonable (cf. Chapter 5.1.1.4), anyhow we assume that this is correct, the composition is then $LiSr_2AlSi_2$.

This compound is isostructural with the NaAlSi ternary phase (anti-PbFCl type) and has a comparable VEC of about 8. The exchange of the Na- by the Sr-atoms increases the VEC by one, which is compensated by substitution of 50% of aluminum with lithium. It is interesting to note that despite the typical intermetallic character the structure clearly seems to be "electron precise".

The substitution of the basal aluminum by lithium has been already found in the $SrLi_xAl_{4-x}$ (x = 0.34) compound ($BaAl_4$ structure type) [89]. In the cited work the bonds between the apical silicon and the four basal atoms were described as 6e-5c bonds. The apical silicon atoms carry, then, a non bonding electron pair. The mixed occupancy of the basal positions leads to a significant change of the Si–M distances (Tab.5.5): they are significantly longer compared to the Al–Si distances in the NaAlSi structure (267.3 pm compared to 256.5 pm) [92].

The structure shows similarities with the $BaAl_4$ type (Figure 5.2) but here the bond between the apical atoms is removed and the Si-M-layers are shifted by (1/2,1/2,z), the number of earth alkaline metals between the square pyramid layers is now doubled.

These structural changes are well explained by the presence of non bonding electron pairs on the silicon atoms.

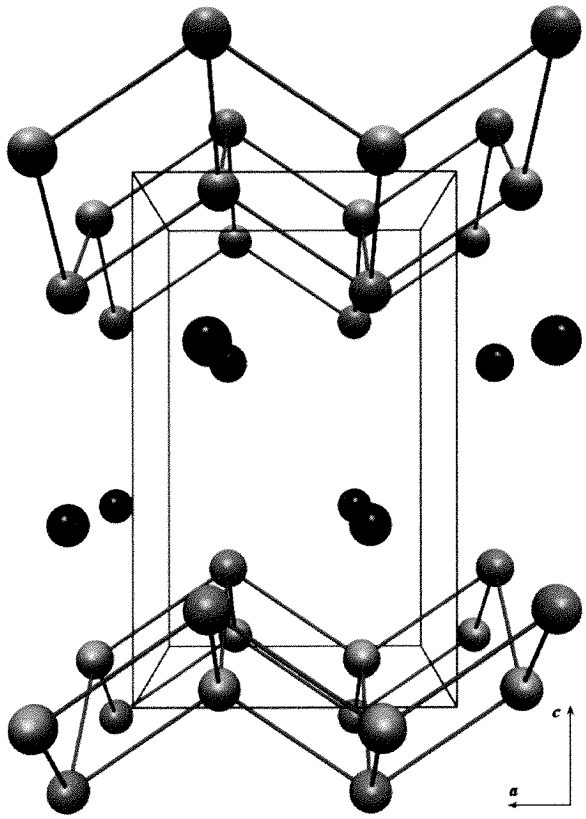

Figure 5.1: Structure of $LiSr_2AlSi_2$ (Si red spheres; M turquoise; Sr black)

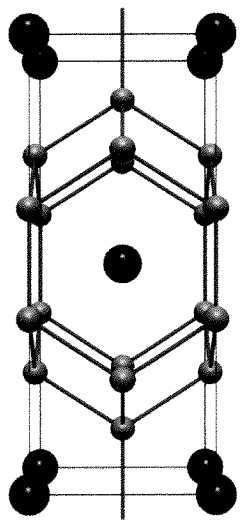

Figure 5.2: The Structure of $BaAl_4$ (Ba black spheres, Al green)

The structure (Fig. 5.1) contains layers of squares pyramids of [SiM_4], connected on the edge, with Si at the apical position and alternately above and below the layer of the M atoms. In between the Si/M layers lie two layers of squared arranged strontium atoms, so that the Sr are coordinated from one side by four M and four Si atoms and from the other side by one Si atom and four Sr atoms (Figure 5.3, top left).

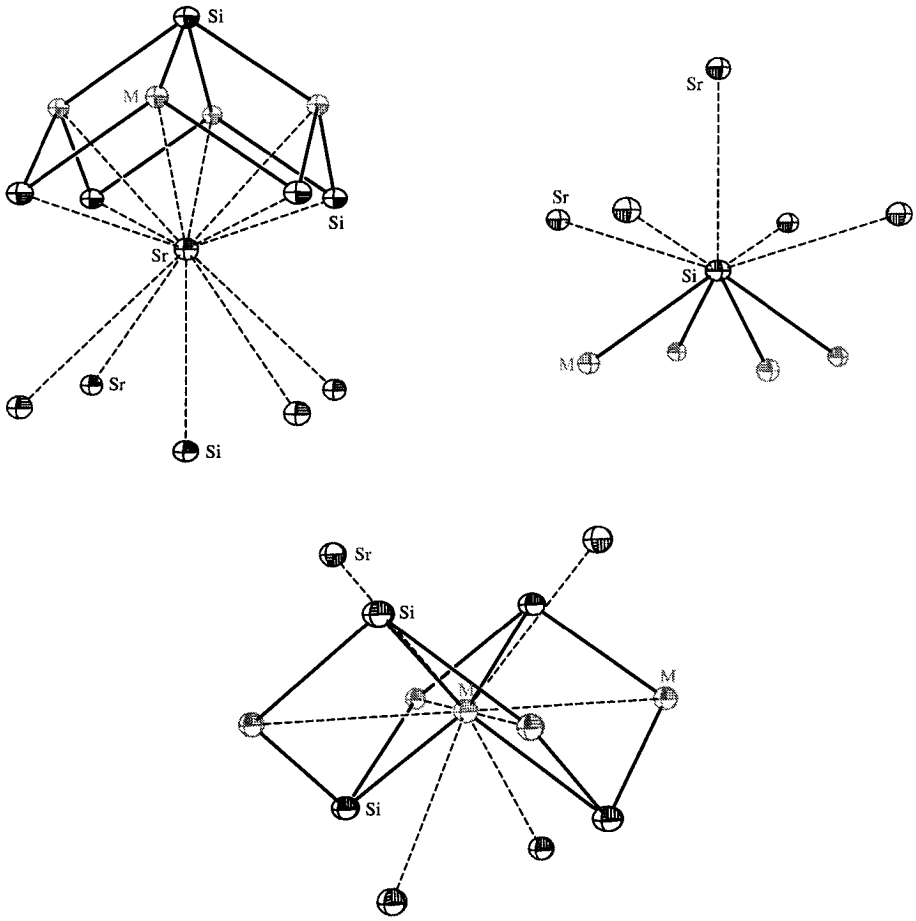

Figure 5.3: Coordination of Sr (top left), Si (top right), and M (bottom)

The silicon atoms lie in the middle of strongly distorted antiprisms formed on one side by strontium on the other side by M positions, perpendicular to the Sr face there is another strontium atom that coordinate silicon (Fig.5.3, top right).

The M atoms lie in the middle of one tetrahedron of Sr atoms and one tetrahedron of silicon atoms. The M positions form layers of squares of atoms with a short M–M distance of 313.8 pm (Fig.5.3, bottom).

5.1.1.3 Physical Properties

A DTA of the compound $LiSr_2AlSi_2$ was performed (Fig.5.4) between room temperature and 1100°C. The pure compound was prepared by tempering at 1050°C (t_1 = 4 hours, r_e = 25°C/h) a stoichiometric mixture of the elements. The composition of the compound refers to the starting mixture and not to a single crystal measurement. The product was pure-phase and the lattice parameters were in the same range of the measured single crystal.

According to this measurement, $LiSr_2AlSi_2$ melts congruently at 920°C as confirmed by powder diffraction pattern taken after the DTA measurement, which showed phase pure compound. No other thermal effects were observed.

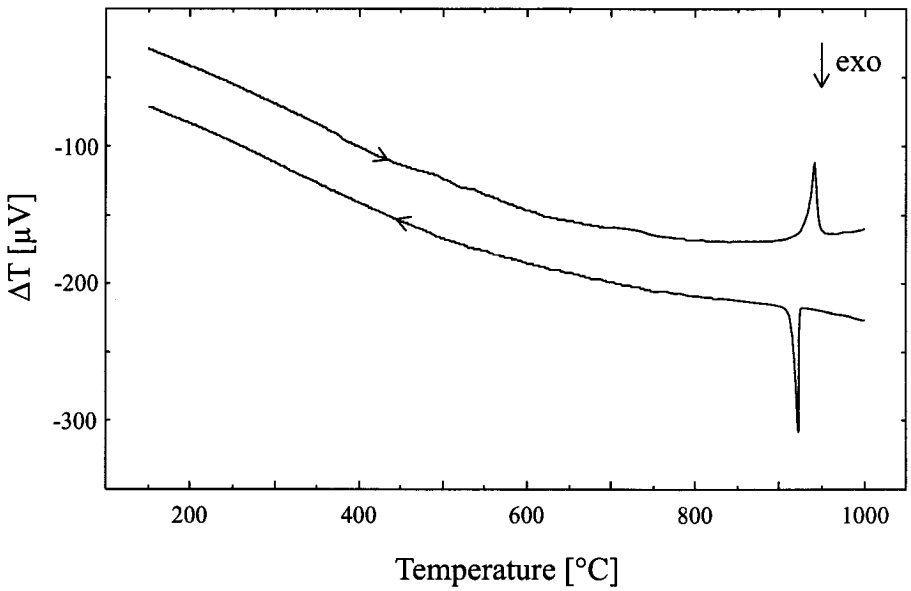

Figure 5.4: DTA of $LiSr_2AlSi_2$

The measurement of the electric conductivity was performed on a pellet (diameter = 6 mm; thickness = 0.75 mm), which was heated during two days at 800°C to avoid the grain boundary effects. According to the conductivity measurement (Fig.5.5), $LiSr_2AlSi_2$ is a metal with a specific resistance of $\rho_{0K} = 1.406 \cdot 10^{-3}$ Ω·cm.

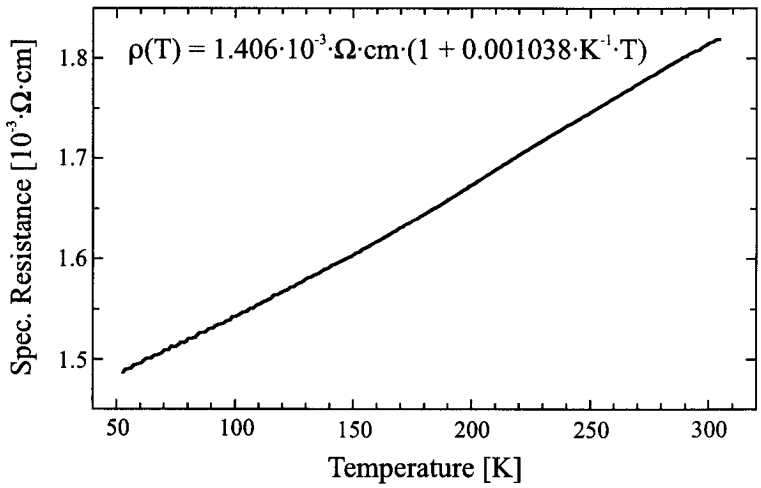

Figure 5.5: Conductivity of $LiSr_2AlSi_2$

5.1.1.4 Theoretical Investigations

In order to investigate the electronic properties and bonding structure of $LiSr_2AlSi_2$ theoretical calculations were performed using the LMTO method. Since there is one mixed occupied M position of multiplicity two, calculations of DOS were performed using one model with ordered aluminum lithium positions. An orthorhombic *C*-centred superstructure was developed (Fig.5.6) with O' = (3/4,1/4,0), $a' = a - b$, $b' = 3a + 3b$. In this model there are two independent crystallographic positions for each element, and the composition is $Li_6Sr_{12}Al_6Si_{12}$, resulting in a sixfold superstructure.

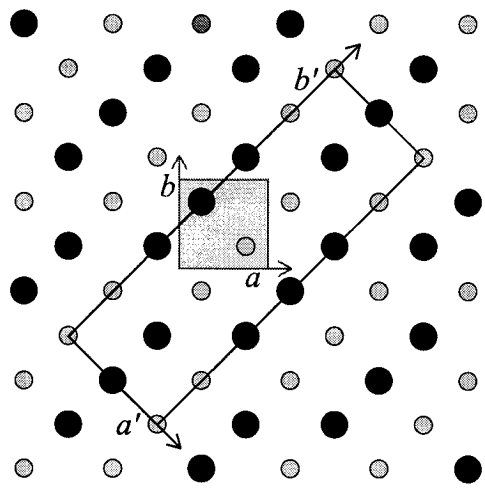

Figure 5.6: Model for the LMTO calculations. Basic cell: shadowed square; *C222* model: open rectangle; aluminum: large circles; lithium: small circles

The cell parameters as well as the atom positions of the resulting structure are given in Tab.5.7.

Table 5.7: Atomic positions in the *C222* model for LMTO calculations

Space group *C222* (21); a = 627.6 pm, b = 1882.9 pm, c = 724.2 pm				
Atoms	***Wyckoff site***	***x***	***y***	***z***
Sr1	4*k*	1/4	1/4	0.1713
Sr2	8*l*	1/4	0.9167	0.1713
Si1	4*k*	1/4	1/4	0.7059
Si2	8*l*	1/4	0.9167	0.7059
Al1	2*c*	1/2	0	1/2
Al2	4*h*	0	0.3333	1/2
Li1	2*d*	0	0	1/2
Li2	4*h*	0	0.8333	1/2

The resulting structure shows an interesting 2D-network of Si-Al atoms, where each silicon atom forms two bonds with aluminum, which itself is tetrahedrally bonded to silicon. Along the *b'* axis there are then spiro[3,3]-like Al-Si heterocycles interconnected by silicon atoms (Fig.5.7). This arrangement can be then very well described by the Zintl-Klemm concept as $(Li^{+})(Sr^{2+})_2\,{}^{3}_{\infty}[((4b)Al^{-})((2b)Si^{2-})_2]$ and the compound is isoelectronic to the Li_5AlSi_2 compound but the electronegative network has a different form.

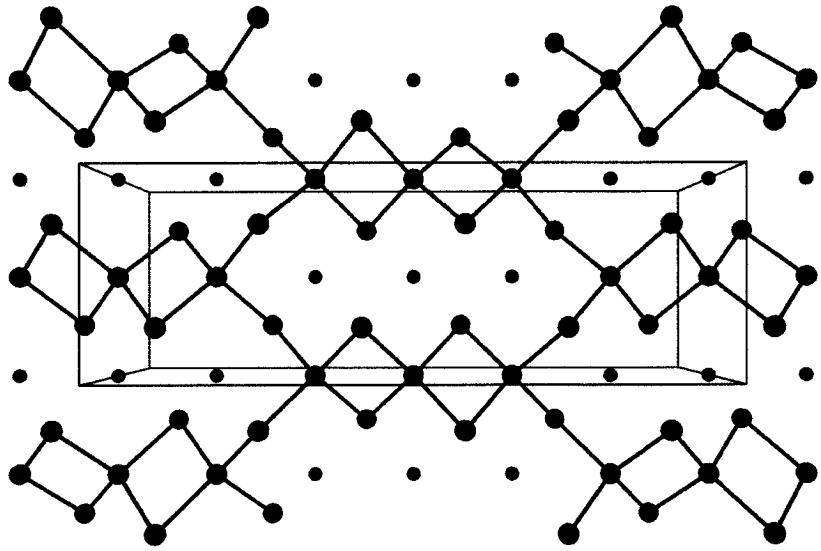

Figure 5.7: Structure of the model used for the LMTO calculations of the $LiSr_2AlSi_2$ (silicon red, aluminum green, lithium grey)

The structure model is of great interest because the simulated diffraction data are very similar to the measured data set and the superstructure reflections are very weak (Tab.5.8). This may be an indication that this is the real structure or, at least, the real structure may not be very different. Maybe because of the crystal size or because of incomplete ordering it is possible that the superstructure reflections were not seen although present.

Table 5.8: Simulated intensities ($I > 0.09\%$ of the I_{max}) of the superstructure reflections for the model in *C222*

hkl	*I*	*hkl*	*I*	*hkl*	*I*	*hkl*	*I*
$\frac{2}{3}\frac{1}{3}1$	1.48%	$\frac{2}{3}\frac{1}{3}0$	1.39%	$\frac{2}{3}\frac{1}{3}2$	0.51%	$\frac{4}{3}\frac{1}{3}1$	0.45%
$\frac{4}{3}\frac{1}{3}0$	0.29%	$\frac{4}{3}\frac{1}{3}2$	0.25%	$\frac{5}{3}\frac{2}{3}1$	0.23%	$\frac{2}{3}\frac{1}{3}3$	0.20%
$\frac{5}{3}\frac{2}{3}2$	0.15%	$\frac{5}{3}\frac{4}{3}1$	0.14%	$\frac{5}{3}\frac{2}{3}0$	0.13%	$\frac{4}{3}\frac{1}{3}3$	0.13%
$\frac{5}{3}\frac{4}{3}2$	0.10%	$\frac{7}{3}\frac{2}{3}1$	0.10%	$\frac{2}{3}\frac{1}{3}4$	0.09%	$\frac{5}{3}\frac{2}{3}3$	0.09%

In the Figure 5.8 the calculated DOS of the $LiSr_2AlSi_2$ model is displayed. According to this DOS the compound should be a metal. This result is consistent with the conductivity measurements that clearly show metallic conductivity (Chapter 5.1.1.3). The metallic character may allow for a phasewidth of the compound with different Li/Al ratios. However, the existence of a phasewidth for this compound was not observed.

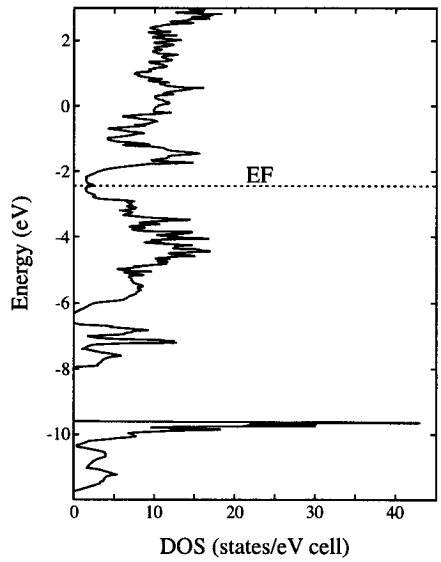

Figure 5.8: LMTO-DOS of the *C222* model of the $LiSr_2AlSi_2$

In order to investigate accurately the bonding structure ELF calculations were carried out in the framework of the LMTO method on the model in *C222* already used for DOS calculations. In all the different ELF pictures the prevalent covalent character of the Si–Al bond is quite clearly confirmed by the high electron localisation between the two elements (Fig.5.9). Also the lone pair localised on the silicon pointing towards the lithium atoms are nicely displayed in Figure 5.9, whereas the very low electron localisation between the lithium and the silicon atoms is typical for interactions of predominant ionic character. In Figure 5.10 the 3D-ELF of the two different types of SiM_4 pyramids present in the structure are displayed: the lone pair on the silicon pointing towards the strontium, and the lithium atoms can be seen very nicely. All these remarks underline a typical Zintl phase character of $LiSr_2AlSi_2$ based on the superstructure model.

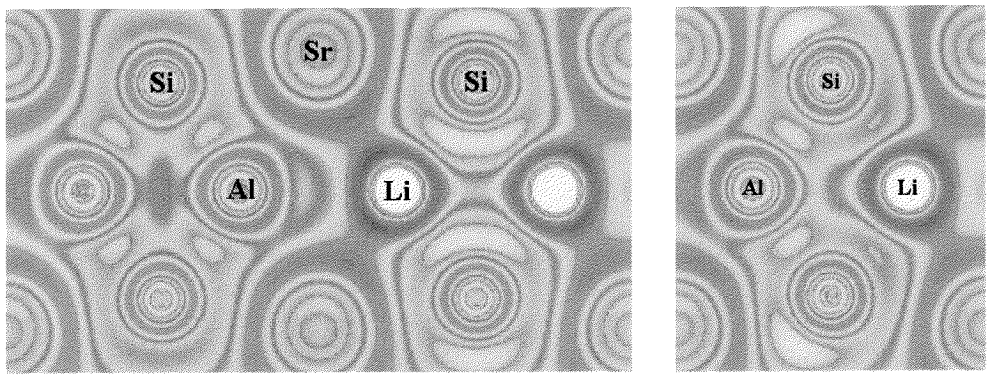

(a) (b)

Figure 5.9: Section of the Si-M four rings: **(a)** left Si_2Al_2 and right Si_2Li_2 **(b)** Si_2AlLi

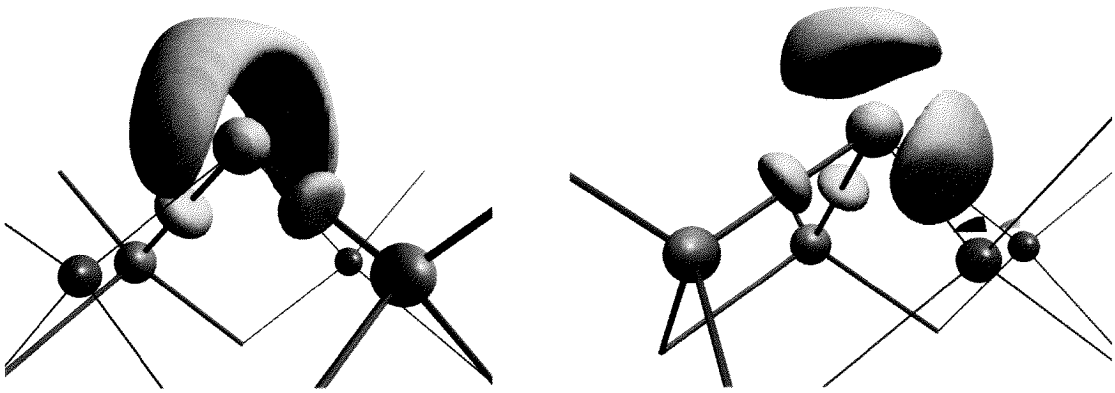

Figure 5.10: ELF of the two different $Si[M]_4$ pyramids in the structure (ELF = 0.8)

The differentiation between bonding and lone electron pairs, though not precisely possible, correlates reasonably well with the spatial extension of such electron spaces. This is clearly seen in Figure 5.10. A quantitative evaluation of electron spaces was performed by Häussermann some years ago [95]. For $CaAl_2Si_2$ the same lone pair behaviour in the neighbourhood of Al–Si bonds was found and quantized by Bader's orthogonal trajectory method [96,97].

5.1.2 $Li_xSrAl_{1-x}Ge$

After the discovery of the new phase $LiSr_2AlSi_2$, experiments were carried out in the quaternary systems Li/Sr/Triel/Tetrel by substituting either the Triel or the Tetrel elements or both, with the aim of finding new compounds which are isoelectronic and isostructural to the $LiSr_2AlSi_2$ phase. We succeeded in the preparation and characterisation of the corresponding germanium compound with the composition $Li_xSrAl_{1-x}Ge$ ($x \sim 0.5$).

5.1.2.1 Synthesis

Phase pure $Li_xSrAl_{1-x}Ge$ was prepared by tempering a stoichiometric mixture of the elements at 1050°C (t_1 = 4 hours, r_e = 25°C/h). $Li_xSrAl_{1-x}Ge$ forms brittle grey crystals with metallic lustre. Exposed to air $Li_xSrAl_{1-x}Ge$ decomposes within a short time to a yellow-orange powder, probably GeO_2. By contact with water it reacts explosively under release of gas, and the decomposition products have then a very pungent smell.

5.1.2.2 Crystal Structure

A single crystal of $Li_xSrAl_{1-x}Ge$ was measured on a four-circle diffractometer. All data were collected up to $2\theta = 60°$. The Laue symmetry is *4/mmm* and the extinctions are consistent with the space groups *P4/n* and *P4/nmm*. Using the silicon analogous compound as starting model the structure was refined in *P4/nmm*. All atoms were anisotropically described and the displacement parameters are all satisfactory (Tab.5.9-11). The metal position M exhibits mixed occupation of aluminum and lithium (Tab.5.12). Again indications for superstructure reflection were found but could not be measured. Although, in the free refinement the ratio Li:Al differs significantly from one, a constraint refinement with an occupancy of 1:1 on M leads to better reliability parameters and especially better displacement parameters for M (cf. Tab.5.9-11). As the 50% occupancy model is more reasonable anyhow we assume that this is correct, the composition of the compound is then $LiSr_2AlGe_2$.

Table 5.9: Crystal data and parameters of the data collection for $Li_xSrAl_{1-x}Ge$ (the first parameters refer to a free refinement of the Al:Li ratio, the second ones to an occupancy of 1:1).

Empirical formula	Li1.18Sr2Al0.82Ge2	Li1Sr2Al1Ge2
Formula weight [g/mol]	350.74	354.34
Crystal size [mm]	0.12 x 0.16 x 0.18	
Colour	grey metallic lustre	
Crystal system	tetragonal	
Unit cell dimension [pm]	a = 446.4(2); c = 730.3(4)	
Volume [pm^3]	$145.6(3)\cdot10^6$	
Space group	$P4/nmm$ (129)	
Formula unit pro cell	2	
ρ (calculated) [g/cm^3]	4.001	4.004
Absorption coefficient μ [mm^{-1}]	28.41	28.438
F (000)	154.2	156
Temperature [K]	298	
Data collection	four-circle diffractometer STOE STADI4	
Monochromator; Wavelength	Graphite; λ(MoKα) = 0.71073 Å	
Scan parameters (steps; Δω; scan)	50; 0.03; ω-θ - Scan	
Theta range	$2° < 2\theta < 60°$	
h(min), h(max); k(min), k(max); l(min), l(max)	-4, 4; -6, 6; -10, 10	
Reflections collected	1014; R(int) = 0.0787	
Independent reflections	156	
Independent reflections with $\|F\|^2 > 2\,\sigma(\|F\|^2)$	140	
Absorption correction	Ψ-Scan	
Refinement	SHELXL-97 (full-matrix least-squares of F^2)	
Parameters	11	
Restraints	0	
Extinction coefficient	0.068(5)	0.059(5)
Maximal shift/esd	0.000	
Mean shift/esd	0.000	
Largest diff. peak and hole [electrons/$pm^3\cdot10^6$]	min = -0.92 – -0.877	max = 0.43 – 0.345
[a] wR for $\|F\|^2 > 2\,\sigma(\|F\|^2)$	0.0388	0.0451
wR for all reflections	0.0397	0.0461
[a] R for $\|F\|^2 > 2\,\sigma(\|F\|^2)$	0.0188	0.0171
R for all reflections	0.0215	0.0208
[a] Goodness of Fit (*GooF*) for all reflections	1.335	1.326

[a] the definitions are given in chapter 2.2, Table 2.3

The refinement of the structure in the space group $P\bar{4}$ was also carried out like for the silicon compound trying to split the M position into two different crystallographic independent positions for Al and Li. The refinement did not lead to any significant change in the structure as the *R* values, the anisotropic displacement parameters were clearly worse because of correlation effects, and the occupancies of the two M positions differed only slightly in the range of realistic standard deviations.

Table 5.10: Wyckoff sites, atomic coordinates, and equivalent isotropic displacement parameters [pm^2] for $Li_xSrAl_{1-x}Ge$ (the first U(iso)s refer to a free refinement of the Al to Li ratio, the second refer to a 1:1 ratio)

Atoms	*Wyckoff site*	*x*	*y*	*z*	*U(iso)*
Sr	2*c*	1/4	1/4	0.3287(1)	195(2) 189(3)
Ge	2*c*	1/4	1/4	0.7908(1)	185(3) 180(3)
M	2*b*	3/4	1/4	0	107(9) 162(8)

Table 5.11: Anisotropic displacement parameters [pm^2] for $Li_xSrAl_{1-x}Ge$ (the first *Us* refer to a free refinement of the Al to Li ratio, the second refer to a 1:1 ratio)

Atoms	*U11*	*U22*	*U33*	*U23*	*U13*	*U12*
Sr	211(3) 206(3)	*U11*	163(3) 157(3)	0	0	0
Ge	203(3) 198(4)	*U11*	148(3) 144(4)	0	0	0
M	114(11) 165(12)	*U11*	95(12) 156(12)	0	0	0

Table 5.12: Refined occupancy of the M-position for $Li_xSrAl_{1-x}Ge$

Position	*Aluminum*	*Lithium*
M	0.41(1)	0.59(1)

Table 5.13: Selected interatomic distances [pm] for $Li_xSrAl_{1-x}Ge$

Sr	–Ge	327.51(5)	4x	Ge	–M	270.51(4)	4x	M	–Ge	270.51(4)	4x
	–M	327.81(6)	4x		–Sr	327.51(5)	4x		–M	315.67(4)	4x
	–Ge	337.42(6)	1x		–Sr	337.42(6)	1x		–Sr	327.81(6)	4x

This compound is isostructural with the NaAlSi phase as well as with its silicon analogous $LiSr_2AlSi_2$ (for the structure see Figure 5.1). Compared to the silicon compound the germanium compound shows an increase of the a-axis of about 0.6%, of the c-axis of about 0.8%, and of the volume of about 2.1%.

The germanium aluminum distance is, just like for the Si–Al distance observed in the silicon compound, slightly longer than in most other germanium aluminides: 270.5 pm against the usual 255-265 pm.

5.1.2.3 Physical Properties

The DTA of the compound $LiSr_2AlGe_2$ was performed (Figure 5.11). The pure compound was prepared by tempering a stoichiometric mixture of the elements at 1050°C (t_1 = 4 hours, r_e = 25°C/h). The composition of the compound refers to the starting mixture and not to a single crystal measurement. According to powder XRD the product was pure-phase and the lattice parameters were in the same range of the measured crystal.

According to the thermal analysis $LiSr_2AlGe_2$ melts congruently at 960°C and no other thermal effects were observed in the temperature range investigated.

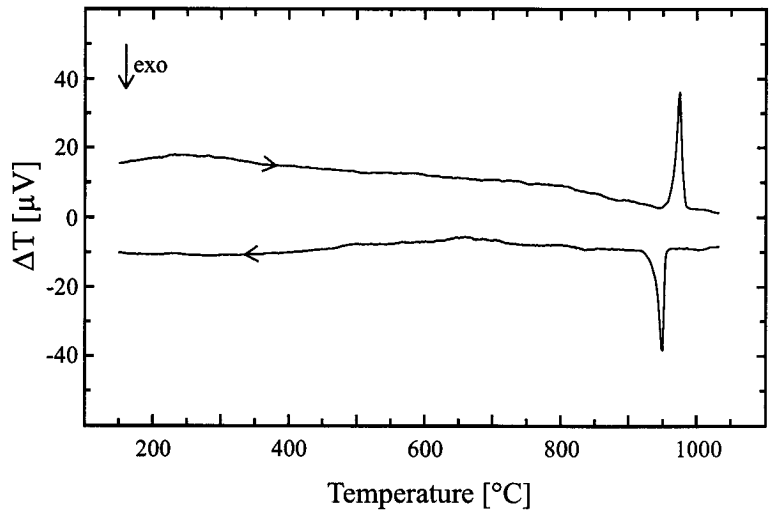

Figure 5.11: DTA of $LiSr_2AlGe_2$

The measurement of the conductivity was not performed due to occurence of minor impurities in the samples.

5.1.2.4 Theoretical Investigations

In order to investigate the electronic properties and bonding structure of the $LiSr_2AlGe_2$ compound, theoretical calculations were performed using the LMTO method. The same model used for the silicon compound was applied (Fig.5.6-7, Tab.5.14).

Table 5.14: Atomic positions in the *C222* model for LMTO calculations

Space group *C222* (21); a = 631.3 pm, b = 1893.9 pm, c = 730.3 pm				
Atoms	***Wyckoff site***	***x***	***y***	***z***
Sr1	4*k*	1/4	1/4	0.1787
Sr2	8*l*	1/4	0.9167	0.1787
Ge1	4*k*	1/4	1/4	0.7092
Ge2	8*l*	1/4	0.9167	0.7092
Al1	2*c*	1/2	0	1/2
Al2	4*h*	0	0.3333	1/2
Li1	2*d*	0	0	1/2
Li2	4*h*	0	0.8333	1/2

The structure model is of great interest because the simulated diffraction data are very close to the measured data set and the superstructure reflections are very weak (Tab.5.15), even weaker than in the silicon compound. This could be a sign that this is the real structure or, at least, the real structure is not very different where superstructure reflections were not so strong that they could be measured.

In analogy to the Si compound this structure model can be expressed in terms of the Zintl-Klemm concept as $(Li^+)(Sr^{2+})_2\,{}^3_\infty[((4b)Al^-)((2b)Ge^{2-})_2]$ and the compound is isoelectronic to Li_5AlGe_2 but the electronegative network has a different form to adapt to the different cation substructure.

Table 5.15: Simulated intensities (I > 0.07% of the I_{max}) of the super structure reflections for the model in *C222*

hkl	*I*	*hkl*	*I*	*hkl*	*I*	*hkl*	*I*
$\frac{2}{3}\frac{1}{3}1$	0.56%	$\frac{2}{3}\frac{1}{3}0$	0.52%	$\frac{2}{3}\frac{1}{3}2$	0.20%	$\frac{4}{3}\frac{1}{3}1$	0.17%
$\frac{1}{3}\frac{1}{3}0$	0.15%	$\frac{4}{3}\frac{1}{3}0$	0.11%	$\frac{1}{3}00$	0.10%	$\frac{1}{3}\frac{1}{3}1$	0.10%
$\frac{4}{3}\frac{1}{3}2$	0.10%	$\frac{5}{3}\frac{2}{3}1$	0.09%	$\frac{2}{3}\frac{1}{3}3$	0.08%	$\frac{2}{3}00$	0.07%

In Figure 5.12 the calculated DOS of the $LiSr_2AlGe_2$ model is displayed. According to this DOS the compound should be a weak metal. Based on the metallic character phasewidth is possible, however, was not observed.

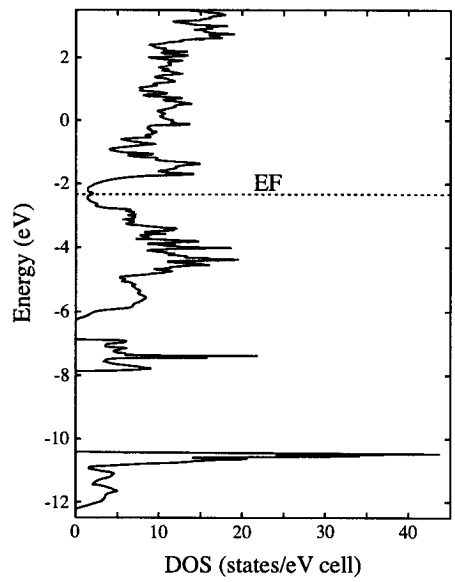

Figure 5.12: LMTO-DOS of the *C222* model of $LiSr_2AlGe_2$

5.2 $Li_{2+x}Sr_2Al_{6-x}Si_6$

Syntheses with different stoichiometric ratio in the quaternary system Li/Sr/Al/Si were carried out with the aim to find new intermetallic compounds with more new Al/Si networks. After syntheses at the atomic ratio close to Li:Sr:Al:Si = 3:1:1:2 the presence of new compounds became evident.

We succeeded in the preparation and characterisation of the new, tetragonal, phase with the composition $Li_{2+x}Sr_2Al_{6-x}Si_6$ where x has a value around 2.8. During our experiments however the synthesis of phase pure product turned out to be very difficult and therefore the determination of the existence of a phasewidth could not be carried out. This compound crystallizes in a new structure type, which can be described as an intermediate between the, well known, $BaAl_4$ structure and the NaAlSi structure already found for the $LiSr_2AlSi_2$ (see chapter 5.1.1). In this respect, the goal of this work, to use subtle changes of stoichiometry and components to tune the structural characteristic between Zintl phases and metals was successfully approached.

5.2.1 Synthesis

Crystals of good quality were found in mixtures tempered at 1050°C (r_1 = 100°C/h, t_1 = 12 h, r_2 = 15°C/h, T_2 = 600°C, r_e = 50°C/h), with stoichiometric ratios of Li:Sr:Al:Si = 4:1:2:4. $Li_{2+x}Sr_2Al_{6-x}Si_6$ forms brittle grey, irregular crystals with a metallic lustre. It is sensitive to air and, especially, to moisture. At contact with water it reacts explosively probably due to the formation of SiH_n resulting in black powdered products.

5.2.2 Crystal Structure

A single crystal of $Li_{2+x}Sr_2Al_{6-x}Si_6$ (x ~ 2.8) was measured on a four-circle diffractometer and all data were collected up to 2Θ = 60°. The Laue symmetry is *4/mmm* and the extintions are consistent with the space groups *P4/n* and *P4/nmm*. The structure was solved in *P4/nmm* using direct methods. All atoms were anisotropically refined and the displacements parameters are all in a reasonable range (Tab.5.16-18).

The metal positions M1 and M2 show mixed occupation by aluminum and lithium. The corresponding occupancy factors were also refined (Tab.5.19). The inspection of the occupancy factors for the M positions reveals that the Li to Al ratio is almost 1:1. A

constraint refinement of the structure with an occupancy of 1:1 leads to almost unchanged *R*-values (Tab.5.16). As the 50% occupancy model is more reasonable anyhow we assume that this is correct

Table 5.16: Crystal data and parameters of the data collection for $Li_{2+x}Sr_2Al_{6-x}Si_6$ (the first given reliability parameters refer to a free refinement of the Al to Li ratio for the M positions, the second ones to an occupancy of 1:1, the third to a 50% occupation of Li1)

Empirical formula	Li4.82Sr2Al3.18Si6	Li5Sr2Al3Si6	Li4Sr2Al3Si6
Formula weight [g/mol]	462.83	459.42	452.48
Crystal size [mm]	0.15 x 0.15 x 0.15		
Colour	dark grey		
Crystal system	Tetragonal		
Unit cell dimension [pm]	a = 434.4(3); c = 1666.3(6)		
Volume [pm^3]	$314.5(1)\cdot10^6$		
Space group	*P4/nmm* (129)		
Formula unit pro cell	1		
ρ (calculated) [g/cm^3]	2.444	2.426	2.389
Absorption coefficient μ [mm^{-1}]	9.22	9.21	9.21
F (000)	216	214	211
Temperature [K]	298		
Data collection	four-circle diffractometer STOE STADI4		
Monochromator; Wavelength	Graphite; λ(MoKα) = 0.71073 Å		
Scan parameters (steps; Δω; scan)	40; 0.03; ω-θ - Scan		
Theta range	$2° < 2\theta < 60°$		
h(min), *h*(max); *k*(min), *k*(max); *l*(min), *l*(max)	-4, 4; -6, 6; -23, 23		
Reflections collected	1883		
Independent reflections	336; *R*(int) = 0.0442		
Independent reflections with $\|F\|^2 > 2\,\sigma(\|F\|^2)$	290		
Absorption correction	Ψ-Scan		
Refinement	SHELXL-97 (full-matrix least-squares of F^2)		
Parameters	24		
Restraints	0		
Extinction coefficient	0.0125(9)	0.012(3)	0.015(3)
Maximal shift/esd	0.000		
Mean shift/esd	0.000		
Largest diff. peak and hole [electrons/$pm^3\cdot10^6$]	min = -0.57 |-0.57 |-0.45; max = 0.72|0.75|0.78		
[a] w*R* for $\|F\|^2 > 2\,\sigma(\|F\|^2)$	0.0489	0.0514	0.0533
w*R* for all reflections	0.0508	0.0536	0.0512
[a] *R* for $\|F\|^2 > 2\,\sigma(\|F\|^2)$	0.0226	0.0237	0.0234
R for all reflections	0.0301	0.0315	0.0310
[a] Goodness of Fit (*GooF*) for all reflections	1.065	1.074	1.070

[a] the definitions are given in chapter 2.2, Table 2.3

Table 5.17: Wyckoff sites, atomic coordinates, and equivalent isotropic displacement parameters [pm^2] for $Li_{2+x}Sr_2Al_{6-x}Si_6$ (the first *U(iso)* for the Li1 position refers to a full occupation, the second to a 50%)

Atoms	*Wyckoff site*	*x*	*y*	*z*	*U(iso)*
Sr1	2*c*	1/4	1/4	0.6636(1)	150(2)
Si1	2*c*	1/4	1/4	0.4146(1)	163(3)
Si2	2*c*	1/4	1/4	0.2709(1)	149(3)
Si3	2*c*	1/4	1/4	0.9003(1)	253(4)
M1	2*b*	3/4	1/4	1/2	167(8)
M2	4*f*	3/4	1/4	0.1822(1)	184(6)
Li1	2*a*	3/4	1/4	0	820(60) 260(40)

Table 5.18: Anisotropic displacement parameters [pm^2] for $Li_{2+x}Sr_2Al_{6-x}Si_6$ (the first *Us* for the Li1 position refers to a full occupation, the second to a 50%)

Atoms	*U11*	*U22*	*U33*	*U23*	*U13*	*U12*
Sr1	144(2)	*U11*	161(2)	0	0	0
Si1	179(4)	*U11*	132(6)	0	0	0
Si2	163(4)	*U11*	121(6)	0	0	0
Si3	294(5)	*U11*	171(7)	0	0	0
M1	183(9)	*U11*	136(13)	0	0	0
M2	183(10)	212(10)	158(10)	0	0	0
Li1	770(70) 310(60)	*U11*	940(130) 170(80)	0	0	0

Table 5.19: Occupancy of the M-positions for $Li_{2+x}Sr_2Al_{6-x}Si_6$

Position	*Aluminum*	*Lithium*
M1	0.51(1)	0.49(1)
M2	0.54(2)	0.46(1)

Table 5.20: Selected interatomic distances [pm] for $Li_{2+x}Sr_2Al_{6-x}Si_6$

Sr1	–Si2	325.98(7)	4x	Si2	–Si1	239.4(2)	1x	M2	–Si3	257.0(1)	2x
	–Si1	333.68(7)	4x		–M2	262.8(1)	4x		–Si2	262.8(1)	2x
	–M2	336.4(2)	4x		–Sr1	325.98(7)	4x		–Li1	303.6(2)	1x
	–M1	348.61(6)	4x						–M2	307.19(4)	4x
				Si3	–M2	257.0(1)	4x		–Sr1	336.4(2)	2x
Si1	–Si2	239.4(2)	1x		–Li1	273.5(1)	4x				
	–M1	259.70(9)	4x					Li1	–Si3	273.5(1)	4x
	–Sr1	333.68(7)	4x	M1	–Si1	259.70(9)	4x		–M2	303.6(2)	2x
					–M1	307.19(4)	4x		–Li1	307.19(4)	4x
					–Sr1	348.61(6)	4x				

The large displacement factors of the Li1 need further analysis. A constraint refinement with a 50% occupation of this site leads to more reliable displacements parameters (Tab.5.17-18) and leaves the *R*-values almost unchanged (Tab.5.16, third refinement). If we assume that the large U_{iso} for the free refinement of Li1 is due to under occupancy of this site, the constraint refinement III becomes more reliable. The composition of the compound is then $Li_{1+x}Sr_2Al_{6-x}Si_6$ (x = 3).

This compound crystallises in a new structure type (Fig.5.13 left), which can be seen as an intermediate between the $BaAl_4$ structure type (Fig.5.13 right) and the NaAlSi structure type found already for the $LiSr_2AlSi_2$ phase (see. Fig.5.2 left and, resp., Fig.5.1).

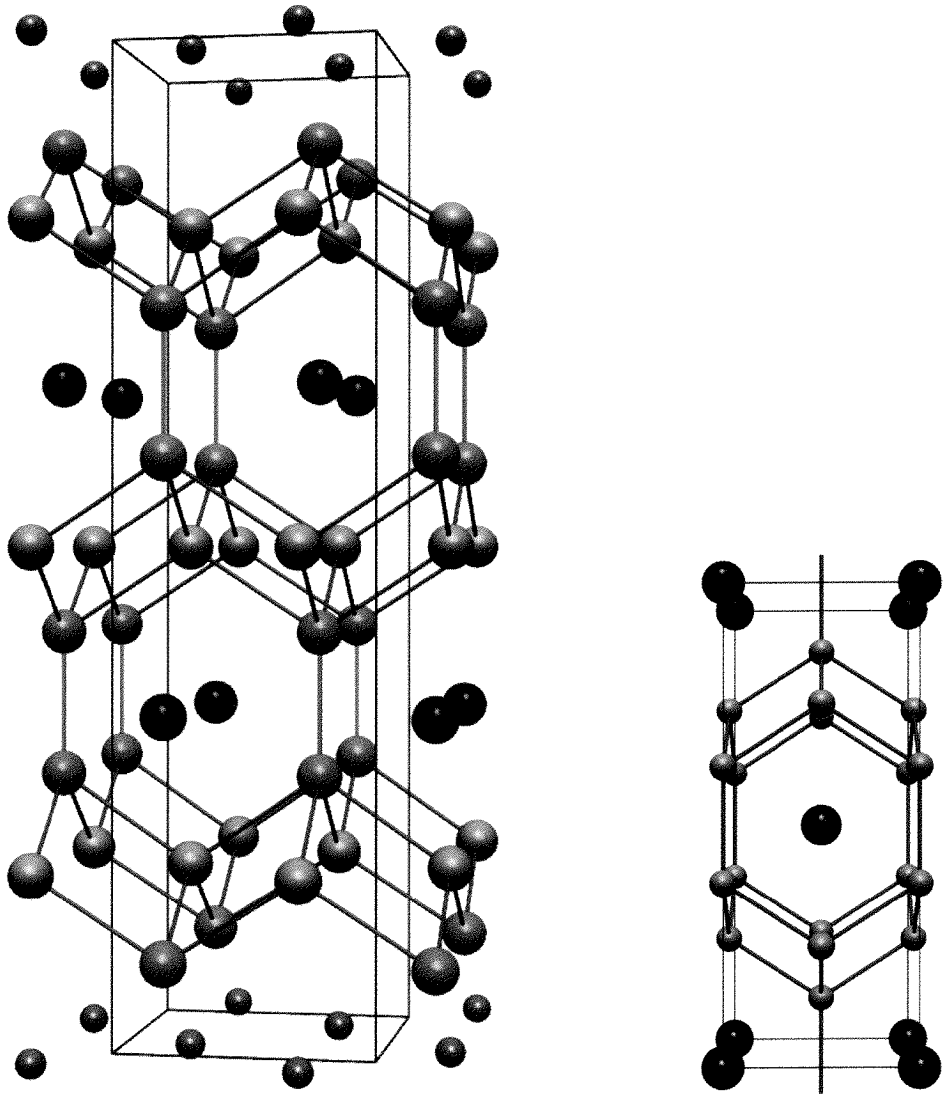

Figure 5.13: The structures of the $Li_{2+x}Sr_2Al_{6-x}Si_6$ phase (left; Sr black, Li grey, Si red, M turquoise) and of $BaAl_4$ (right; Ba black, Al green)

The structure (Fig.5.13) contains layers of squares pyramids of $[SiM_4]$, connected via the edges, with Si at the apical position and alternately above and below the layers of the M atoms. Three of these layers are connected via silicon-silicon bonds between the apical positions (orange in Figure 5.13). One half of the apical silicon atoms of the first and of the third layer carry then lone pairs like in the $LiSr_2AlSi_2$ phase.

This network is separated along the c-axis by a squared layer of lithium atoms, which are not very ordered since the Li1 has very big anisotropic displacement parameters.

The strontium atoms exhibit the same coordination as in the $BaAl_4$ structure with the apical position occupied by silicon.

In contrast to the previous structure, here, silicon-silicon bonds are present linking the pyramidal layers. The Si–Si distance of 239.4 pm (Tab.5.20) is comparable to the Si–Si single bond distance but it should be mentioned that this is fairly variable in the Zintl phases. The Si–M distances (257-263 pm, Tab.5.20) are in the range of normal Si–Al distances found in covalent networks like in LiAlSi (257 pm), thus sensibly shorter than the Si–M distances in the $LiSr_2AlSi_2$ phase (267 pm) as well as those in the $Li_xCaAl_{1-x}Si$ phase (263-276 pm).

In the Figure 5.14 the different coordinations in the $Li_{2+x}Sr_2Al_{6-x}Si_6$ structure are shown. The Si–Si bonds exhibit the typical coordination of silicon dumb-bells by earth-alkaline metals: the centre of the Si–Si bond is coordinated by a square of strontium atoms. Together with the four M atoms at the end a distorted square antiprism is formed around the Si1 as well as the Si2 (Fig.5.14 top left). This coordination motive is most frequent in Zintl phases of the tetralides. The apical Si3 atom is found in the middle of a distorted cube of four M2 atoms on one side and four Li1 atoms on the opposite side (Fig.5.14 middle). The M1 atoms have the same coordination found for the M positions in the $Li_xSrAl_{1-x}Si$ phase: they are situated in the middle of one tetrahedron of Sr1 atoms and another, tetrahedron of Si1 atoms orthogonally oriented to the first. This M1 positions form layers of squared arranged atoms with a short M1–M1 distance of 307 pm (Fig.5.14, top left).

The coordination of the M2 atoms differs from the M1 for the cations: the M2 atoms are coordinated by two Sr1 on one side and one Li1 on the opposite side; and for the M2 silicon distances: the two with the Si3 are shorter (257 pm) than the two with the Si2 (263 pm). Like for the M1 the M2-atoms form layers of squared arranged atoms with a short M2-M2 distance of 307 pm (Fig.5.14, top left).

The Sr1 atoms lie almost in the middle of a tetragonal prism of silicon atoms, they are shifted towards the Si2 square, and coordinate in this way the Si1–Si2 bonds (Fig.5.14, bottom left).

The Li1 then is found in the middle of a tetrahedron of Si3, and two M2 atoms. Like for the M positions the Li1 builds a square layer of Li atoms with Li–Li distances of 307 pm.

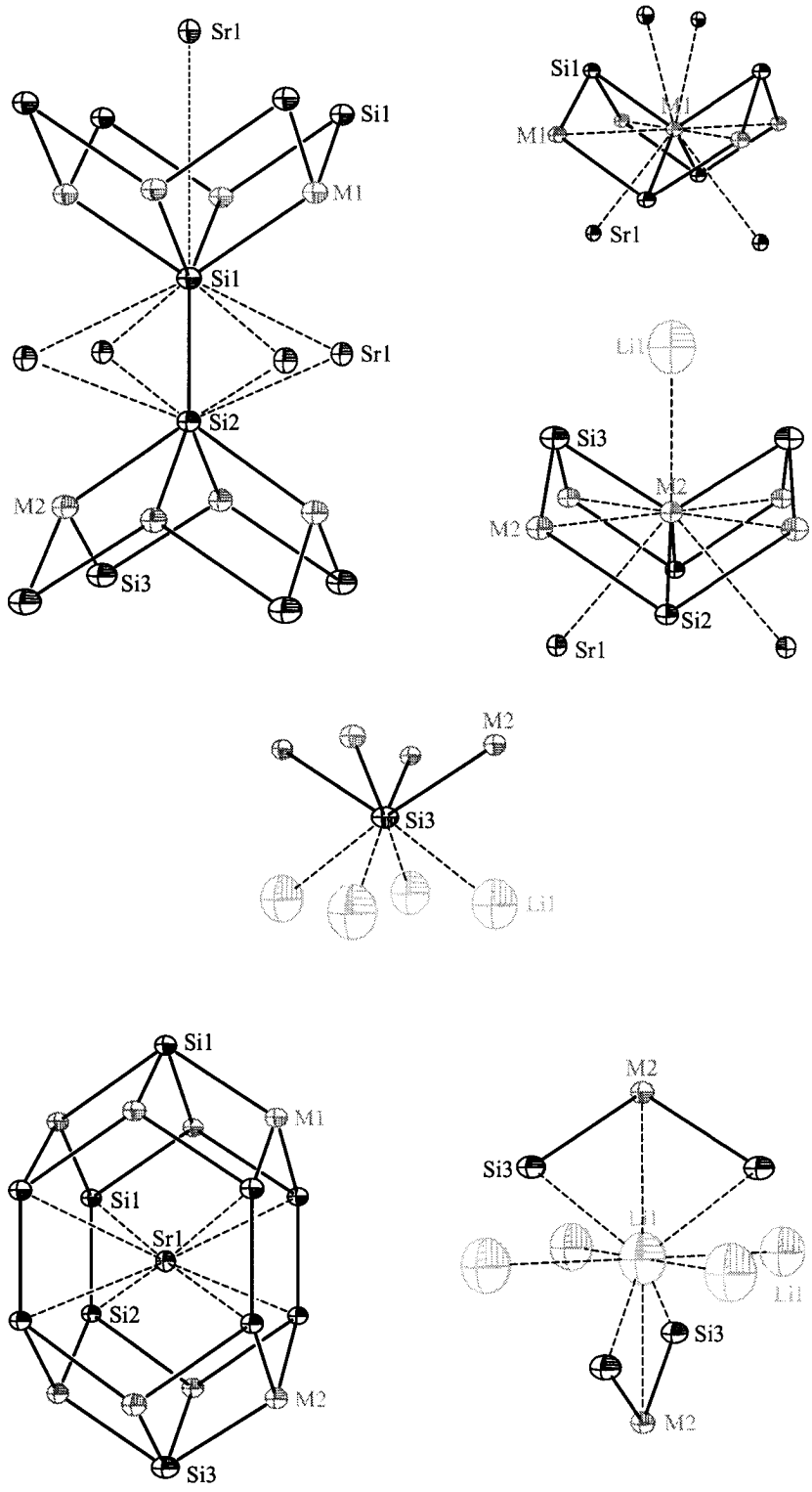

Figure 5.14: Coordination of the Si1-Si2-bond (top left), M1 and M2 (top right), Si3 (middle), Sr1 (bottom left), and Li1 (bottom right)

5.2.3 Theoretical Investigations

In order to investigate the electronic properties and bonding structure of the $Li_{4.8}Sr_2Al_{3.2}Si_6$ compound, theoretical calculations were performed using the LMTO method. Because of the two mixed occupied M positions, calculations of DOS were performed using two models with differently ordered aluminum lithium positions. The ordering reduces the symmetry to the space group $P\bar{4}m2$ (n° 115, Tab.5.21).

In both models (Fig.5.15) the Si1 have two bonds to Al2 whereas Si2 and Si3 exhibit three such bonds. According the Zintl Klemm concept this leads to the following valence description $(Li^+)_5(Sr^{2+})_2[((4b)Al^-)_3((2b)Si^{2-})_2((3b)Si^-)_4]$, however this formulation leads to an excess of a negative charge of 2-.

However, model2 (Fig.5.15 right) contains already a possible solution: the resulting $(Al1)_2Si2\text{-}Si3(Al2)_2$-unit forms a plane, so that, assuming π-contributions between the Al and the Si-3b, the compound is electron precise by an occupation of one electron per π^*-state.

Table 5.21: Atomic position in the two models in $P\bar{4}m2$ for LMTO calculations

Model1	Model2	*Wyckoff*	*x*	*y*	*z*
Sr1	**Sr1**	2*g*	1/2	0	0.3364
Si1	**Si1**	2*g*	1/2	0	0.0997
Si2	**Si2**	2*g*	1/2	0	0.5854
Si3	**Si3**	2*g*	1/2	0	0.7291
Al1	**Li1**	1*c*	1/2	1/2	1/2
Al2	**Al1**	2*e*	0	0	0.8178
Li1	**Al2**	1*d*	0	0	1/2
Li2	**Li2**	2*f*	1/2	1/2	0.8178
Li3	**Li3**	1*a*	0	0	0
Li4	**Li4**	1*b*	1/2	1/2	0

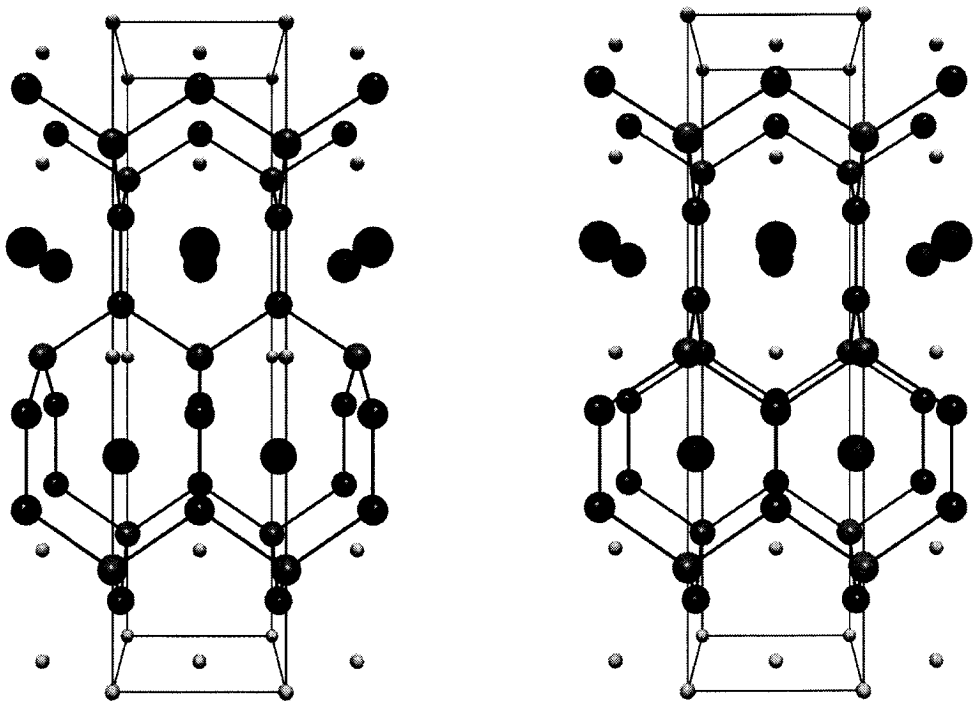

Figure 5.15: Models for LMTO calculations (model1 left, model2 right) (Si small black spheres, Al large grey spheres, Sr large black spheres, Li small grey spheres)

The resulting DOS from the two different models are shown in Figure 5.16. Both of them clearly show metallic character. Based on the LMTO method DOS calculations of other models with different Li/Al occupations were also performed. All of them lead to a metallic characteristic

At least both model 1 and 2 exhibits a filling level close to a local minimum in the DOS assuming 50% occupancy of the Li1 (dotted lines in Figure 5.16). The composition of the compound is, therefore, more likely $Li_{1+x}Sr_2Al_{6-x}Si_6$ (x ~ 3) than $Li_{2+x}Sr_2Al_{6-x}Si_6$ (x ~ 3).

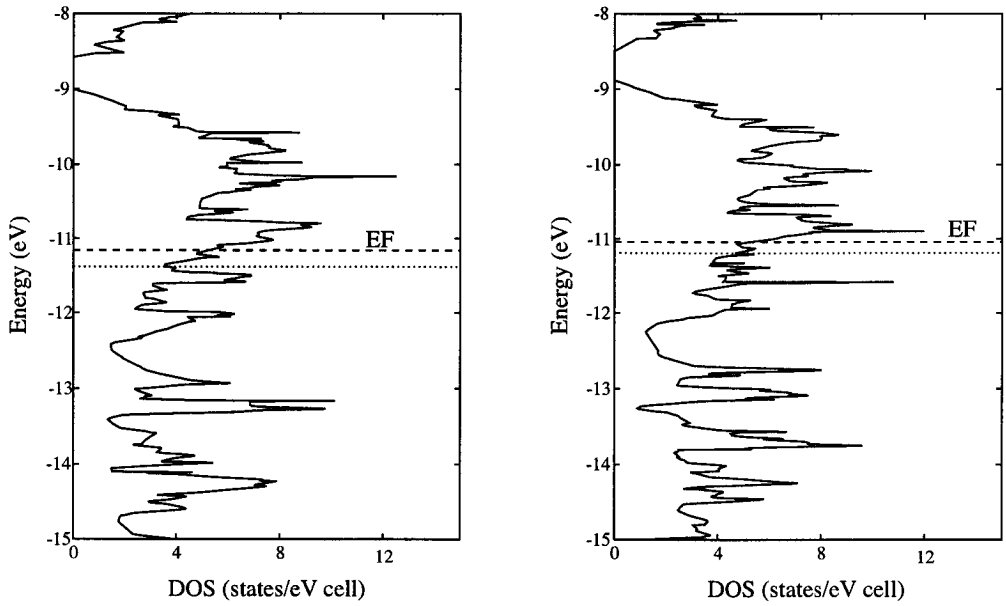

Figure 5.16: LMTO-DOS section in the region of the Fermi level of the two models in $P\bar{4}m2$ of $Li_{2+x}Sr_2Al_{6-x}Si_6$ (model1 left, model2 right). The Fermi level is given by the dashed line for the 100% occupancy of Li1, and by the dotted line for the 50% occupancy of Li1.

5.3 $Li_{3+x}Sr_5Al_{16-x}Si_{12}$

Syntheses with different stoichiometric ratios in the quaternary system Li/Sr/Al/Si were carried out. At the atomic ratio Li:Sr:Al:Si = 2:1:2:4 the presence of new compounds became evident. We succeeded in the preparation and characterisation of the new, hexagonal, phase with the composition $Li_{3+x}Sr_5Al_{16-x}Si_{12}$ (x ~ 6.2). During our experiments however the synthesis of phase pure product turned out to be very difficult and therefore the determination of the existence of a phasewidth could not be carried out. The new compound crystallises in a new structure type, which has a zeolite-related morphology with channels filled up by cations.

5.3.1 Synthesis

Crystals of good quality were found in a mixture of the composition Li:Sr:Al:Si = 2:1:2:4. tempered at 1050°C (r_1 = 100°C/h, t_1 = 12 h, r_2 = 15°C/h, T_2 = 600°C, r_e = 50°C/h). $Li_{3+x}Sr_5Al_{16-x}Si_{12}$ (x ~ 6.2) forms brittle grey long needle's shaped crystals (ranging from 0.1 to 1 mm of length), however most of them are twinned. Surprisingly and very different from the other compounds presented in this chapter, $Li_{3+x}Sr_5Al_{16-x}Si_{12}$ is stable against water: crystals treated with water did not show any change in colour and any gas evolution under the microscope. One of these crystals was also measured after such a treatment and did not exhibit any changes compared to the structure of the untreated phase. Thus, no water was found in the cavities.

5.3.2 Crystal Structure

A single crystal of $Li_{3+x}Sr_5Al_{16-x}Si_{12}$ (x ~ 6.2) was measured on a four-circle diffractometer. All data were collected up to $2\Theta = 60°$. The Laue symmetry is *6/mmm* and the extintions are consistent with the space groups *P6*, $P\bar{6}$, *P6/m*, *P622*, *P6mm*, $P\bar{6}2m$, $P\bar{6}m2$, and *P6/mmm*. The structure was solved in $P\bar{6}2m$ using direct methods. All atoms were anisotropically refined and the displacements parameters are all satisfactory (Tab.5.22-24). The metal position M1, M2 and M3 are mixed occupied by aluminum and lithium. The corresponding occupancy factors were also refined (Tab.5.25).

Table 5.22: Crystal data and parameters of the data collection for $Li_{3+x}Sr_5Al_{16-x}Si_{12}$

Empirical formula	Li9.16Sr5Al9.84Si12
Formula weight [g/mol]	1104.23
Crystal size [mm]	0.04 x 0.04 x 0.24
Colour	grey-black with metallic lustre
Crystal system	hexagonal
Unit cell dimension [pm]	a = 1383.3(6); c = 420.7(2)
Volume [pm^3]	697.1(2)·10^6
Space group	$P\bar{6}2m$ (189)
Formula unit pro cell	1
ρ (calculated) [g/cm^3]	2.630
Absorption coefficient μ [mm^{-1}]	10.33
F (000)	513
Temperature [K]	298
Data collection	four-circle diffractometer STOE STADI4
Monochromator; Wavelength	Graphite; λ(MoKα) = 0.71073 Å
Scan parameters (steps; Δω; scan)	40; 0.03; ω-θ - Scan
Theta range	2° < 2θ < 60°
h(min), h(max); k(min), k(max); l(min), l(max)	-15, 15; -15, 15; 0, 5
Reflections collected	4001
Independent reflections	809; R(int) = 0.0578
Independent reflections with $\|F\|^2 > 2\,\sigma(\|F\|^2)$	660
Absorption correction	Ψ-Scan
Refinement	SHELXL-97 (full-matrix least-squares of F^2)
Parameters	47
Restraints	0
Extinction coefficient	none
Maximal shift/esd	0.000
Mean shift/esd	0.000
Largest diff. peak and hole [electrons/pm^3·10^6]	min = -0.69 ; max = 0.44
[a] wR for $\|F\|^2 > 2\,\sigma(\|F\|^2)$	0.0498
wR for all reflections	0.0505
[a] R for $\|F\|^2 > 2\,\sigma(\|F\|^2)$	0.0221
R for all reflections	0.0255
[a] Goodness of Fit (*GooF*) for all reflections	1.296

[a] the definitions are given in chapter 2.2, Table 2.3

Table 5.23: Wyckoff sites, atomic coordinates, and equivalent isotropic displacement parameters [pm^2] for $Li_{3+x}Sr_5Al_{16-x}Si_{12}$

Atoms	*Wyckoff site*	*x*	*y*	*z*	*U(iso)*
Sr1	2*d*	1/3	2/3	1/2	100(5)
Sr2	3*f*	0.18767(9)	0	0	106(5)
Si1	3*g*	0.8213(4)	0	1/2	113(14)
Si2	3*g*	0.3670(4)	0	1/2	179(14)
Si3	6*j*	0.4762(3)	0.3042(4)	0	162(9)
Al1	3*f*	0.7123(4)	0	0	128(12)
M1	1*b*	0	0	1/2	530(60)
M2	6*k*	0.8108(6)	0.1886(5)	1/2	167(19)
M3	6*j*	0.1209(6)	0.4819(6)	0	130(30)
Li1	3*g*	0.561(2)	0	1/2	220(30)

Table 5.24: Anisotropic displacement parameters [pm^2] for $Li_{3+x}Sr_5Al_{16-x}Si_{12}$

Atoms	*U11*	*U22*	*U33*	*U23*	*U13*	*U12*
Sr1	82(7)	*U11*	137(9)	0	0	41(3)
Sr2	121(7)	130(9)	69(9)	0	0	65(5)
Si1	90(29)	*U11*	130(29)	0	0	30(20)
Si2	140(20)	380(20)	90(30)	0	0	190(20)
Si3	130(20)	210(18)	180(20)	0	0	113(19)
Al1	130(20)	*U11*	120(20)	0	0	67(14)
M1	70(30)	*U11*	1460(150)	0	0	30(30)
M2	260(40)	200(30)	140(3)	0	0	190(30)
M3	90(40)	70(50)	190(40)	0	0	20(10)
Li1	90(9)	90(9)	220(40)	0	0	-15(10)

Table 5.25: Occupancy of the M-positions for $Li_{3+x}Sr_5Al_{16-x}Si_{12}$

Position	*Aluminum*	*Lithium*
M1	0.75(3)	0.25(3)
M2	0.60(1)	0.40(1)
M3	0.41(1)	0.59(1)

It is interesting to note that there is a mutual inverse relation of the occupancy factors of M2 and M3. By inspection of the local coordinations and the bonding argumentation given later in this chapter it turns out to be very reasonable that M2 is not occupied by Al when M3 is.

This compound crystallises in a new structure type (Fig.5.17), which contains channels along the *c*-axis filled up by either strontium or lithium atoms. The network is built up by silicon and aluminum atoms, however, the majority of the Al position are mixed occupied by aluminum and lithium.

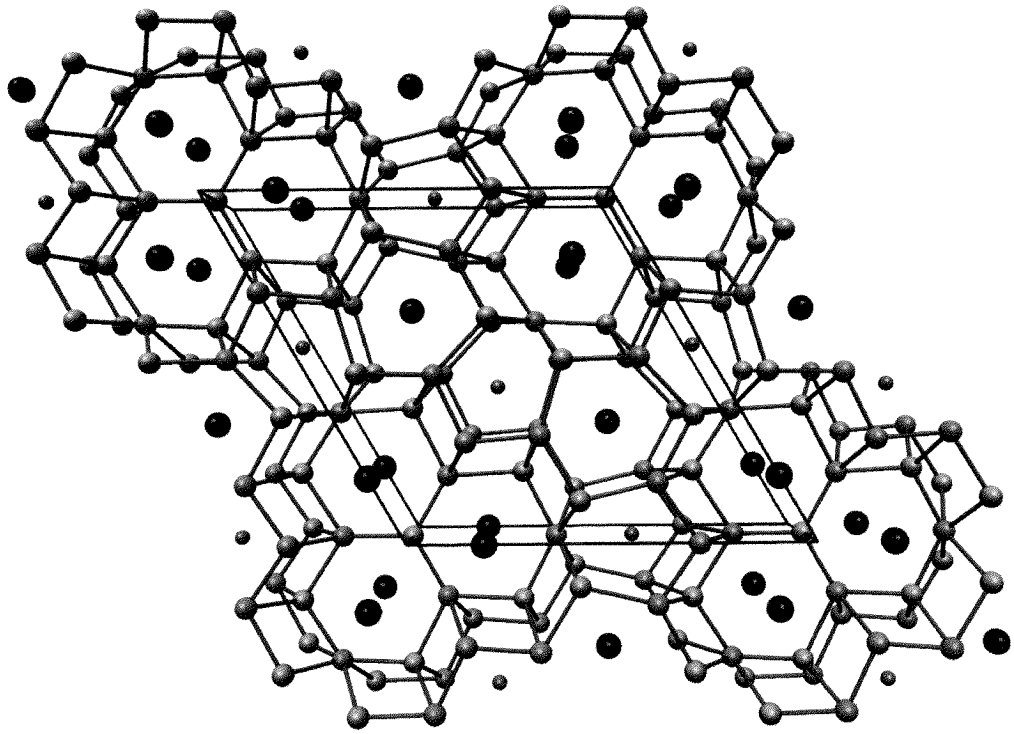

Figure 5.17: Structure of $Li_{3+x}Sr_5Al_{16-x}Si_{12}$ (Sr black spheres, Si red, Li grey, Al green, M turquoise)

The structure still contains the pyramids of [SiM_4] already presents in the previous structures (chap.5.1-2), but here there are no layers formed by the pyramids but just short layer-like pieces which are mutually connected by the sixfoldly coordinated Si2 atoms. Three of these [SiM_4]-layer patches are connected through the M1 positions. This connection contains channels along the z-direction which are filled by the Sr2 atoms. These layers are interconnected by the Si3–M3 bonds resulting in the formation of two additional channel types: a smaller one filled by a chain of Li1 atoms and a larger one centered by Sr1. The present structure thus contains a lot of building elements of the original $BaAl_4$ aristotype but only in form of small local patches which are linked in a completely novel way.

This arrangement becomes clear by analyzing Figure 5.18 in which all Si3–M3 bonds have been removed.

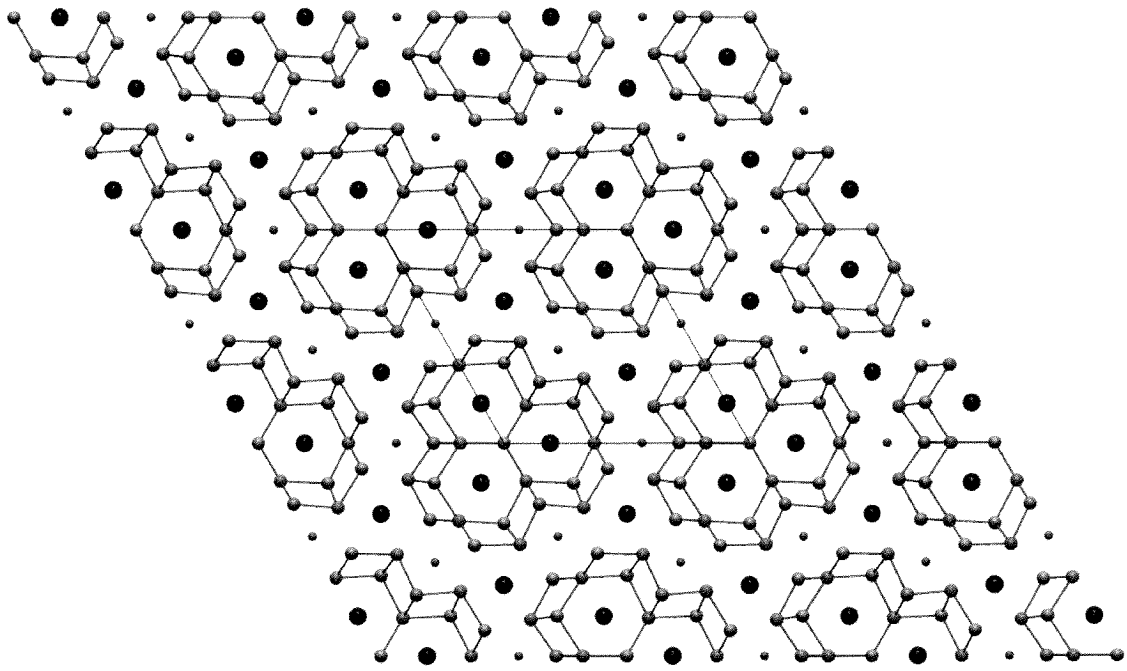

Figure 5.18: [SiM_4]-pyramids layer in the $Li_{3+x}Sr_5Al_{16-x}Si_{12}$

The coordination of the different positions in the $Li_{3+x}Sr_5Al_{16-x}Si_{12}$ structure are shown in the Figure 5.19, and the discussed interatomic distances are given in the Tab.5.26.

Table 5.26: Selected interatomic distances [pm] for $Li_{9.2}Sr_5Al_{9.8}Si_{12}$

Sr1	–Si3	323.5(3)	6x	Si1	–M1	247.2(5)	1x	M1	–Si1	247.2(5)	3x
	–M2	346.0(6)	3x		–Al1	258.8(4)	2x		–Sr2	334.12(9)	6x
	–M3	347.6(6)	6x		–M2	268.5(6)	2x				
					–Sr2	329.5(2)	4x	M2	–Si2	254.5(8)	1x
Sr2	–Si2	325.2(4)	2x		–Li1	360.0(6)	1x		–Si3	257.8(5)	2x
	–Si1	329.5(2)	4x						–Si1	268.5(6)	1x
	–M1	334.12(9)	2x	Si2	–M2	254.5(8)	2x		–M3	295.8(7)	2x
	–M2	336.3(6)	4x		–M3	266.3(5)	4x		–Al1	308.8(4)	2x
	–Al1	350.0(4)	2x		–Li1	268(3)	1x		–Li1	311.9(2)	1x
	–M3	354.4(6)	2x		–Sr2	325.2(4)	2x		–Sr2	336.3(6)	2x
									–Sr1	346.0(6)	1x
Li1	–Si2	268(3)	1x	Si3	–Al1	2.501(5)	1x				
	–Al1	296.7(2)	2x		–M3	257.6(8)	1x	M3	–Si3	257.6(8)	1x
	–Si3	302.1(7)	4x		–M2	257.8(5)	2x		–Si2	266.3(5)	2x
	–M2	311.9(2)	2x		–M3	267.6(9)	1x		–Si3	267.6(9)	1x
	–M3	320.2(1)	4x		–Li1	302.1(7)	2x		–M3	289.7(9)	1x
	–Si1	360.0(6)	1x		–Sr1	323.5(3)	2x		–M2	295.8(7)	2x
									–Li1	320.2(1)	2x
				Al1	–Si3	2.501(5)	2x		–Sr1	347.6(6)	2x
					–Si1	258.8(4)	2x		–Sr2	354.4(6)	1x
					–Li1	296.7(2)	2x				
					–M2	308.8(4)	4x				
					–Sr2	350.0(4)	2x				

The Si1 atom is situated in the middle of a distorted square antiprism of Sr2 atoms, on one side, and Al1 and M2 on the other (Fig.5.19, first row left). These two square faces are capped by one M1, on the face set up by Sr2, and one Li1 atom on the Al1-M2 face. The Si1–M1 distance of 247 pm is quite short, whereas the Si1-Al1 distance of 259 pm is fairly long for covalent Al–Si bonds (245-258 pm) but still in the range of accepted covalent single bonds. The Si1–M2 distance is even larger with 269 pm, but comparable

to the Si–M distances found in the previously described compounds. If one applies the observed Al occupancies Si1 is just fourbonded (n=3.95).

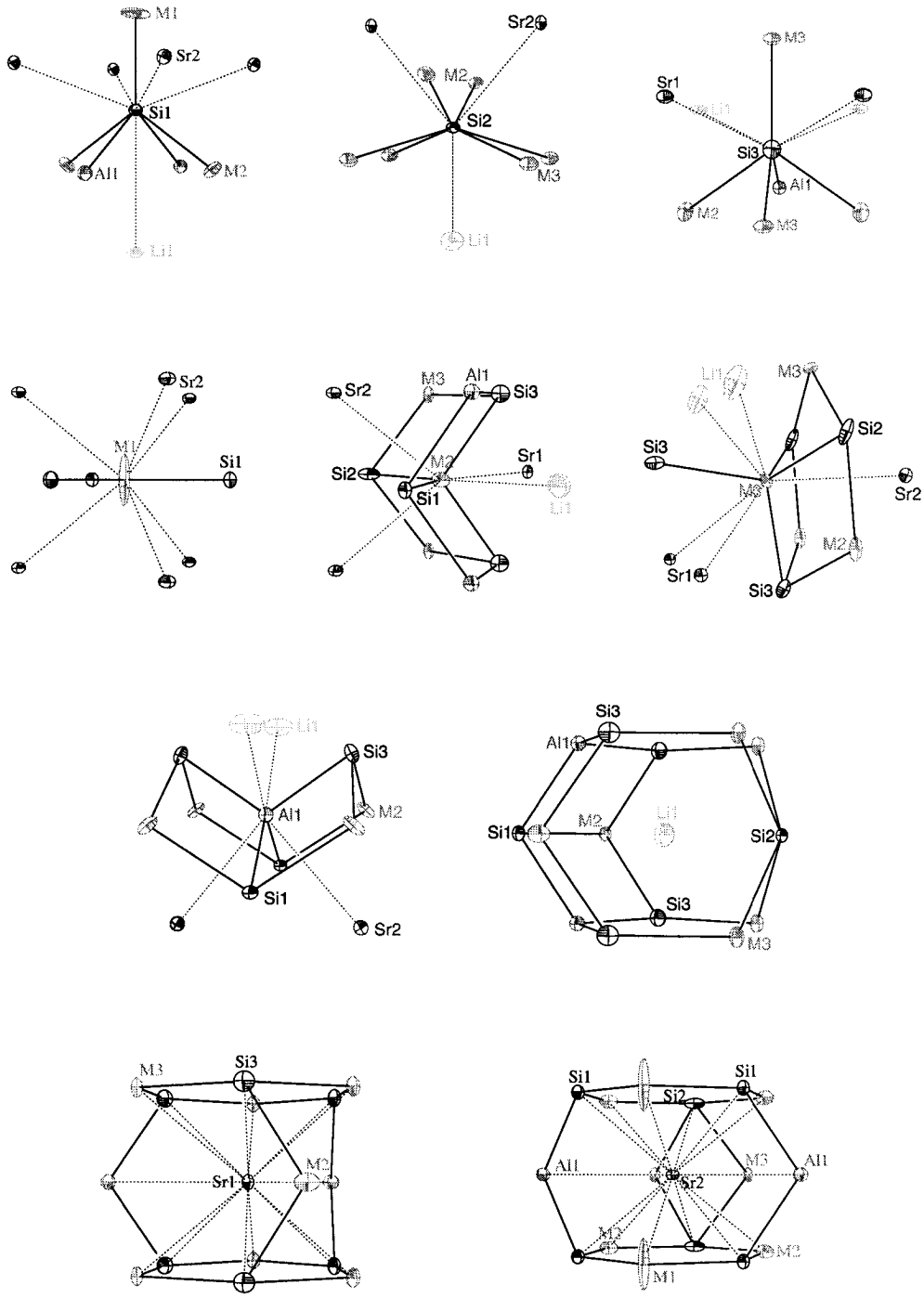

Figure 5.19: Coordination of Si1-3 (first row); M1-3 (second row); Al1 and Li1 (third row, left resp. right); and Sr1-2 (fourth row)

The Si2 atom has the unusual coordination of six M atoms (Fig.5.19, first row middle), but since these are mixed occupied positions the real number of Si–Al bonds is smaller, on the average it is n=2.8 and may thus be equals three due to local ordering. The Si2–M2 distance (254 pm) is in the range of covalent Si–Al bonds, whereas the Si2–M3 distance of 268 pm is comparable to the longer Si–M distances already encountered.
The Si3 position is also found in the middle of a distorted square antiprism of Sr1 and Li1 atoms, on one side, and Al1, M2 and M3 on the other side (Fig.5.19, first row right). The Sr1-Li1 face is capped by an M3 atom. The Si3–Al1, Si3–M3, and the Si3–M2 distances (250, 257, and resp. 258 pm) are in the range of covalent Si–Al bonds. The other Si3–M3 distance (268 pm) is in the range of all the other, already observed, Si–M distances. The average bond order of Si3 is n=3 (3.02). The M1 position needs further explications (see later): it lies in the middle of a trigonal prism of Sr2 atoms with the rectangular faces capped by Si1 atoms (Fig.5.19, second row left), the resulting $M1(Si1)_3$-unit lies on a plane. The M1–Si1 distance (247 pm) is in the range of short Si–Al covalent bonds. The M2 position shows the same coordination of the M position found in the $LiSr_2AlSi_2$ compound (Chapter 5.1.1): together with the Al1 and the M3 position they build a layer of square arranged atoms, capped by silicon atoms alternatively above and below it (Fig.5.19, second row middle). The M2 atom lies in the middle of a distorted tetrahedron of Si1, Si2, and Si3 as well as of Sr2, Sr1 and Li1. The latter four form a distorted heterocubane together with the four silicon neighbours. The resulting M2–M3 and M2–Al1 distances are too short for being non-bonding and too long for normal single bonds (296 pm resp. 309 pm). The clue to this problem seems to be the mutual distribution of Si and Al around M2, which is just what the Al atoms in the square layer in $BaAl_4$ experience. The inplane contacts (of just this length) are nonbonding because all the orbitals at the center atom have to be used for the stronger bonds in the silicon tetrahedron. The same holds for M3: it is in the middle of a trigonal prism of Sr1, Sr2 and Li1 atoms, and also of a tetrahedron of silicon atoms (Fig.5.19, second row right). The M3 site has also one short distance to another M3 atom of 290 pm, which is the shortest observed in the compounds discussed in this work, and two M3–M2 distances of 296 pm. According to the above mentioned reasoning, these contacts should be nonbonding. The coordination of Al1 is almost the same of the M2

and M3 sites (Fig.5.19, third row left), here the tetrahedron is built of Sr2 and Li1 atoms. The Al1–Si3 distance is typical for covalent Al–Si bonds, the Al1–Si1 distance (259 pm) is longer but still well in the range of covalent bonds and the four silicon neighbours form a distorted tetrahedron. The Li1 atoms fill the smaller channels of the structure (Fig.5.17), they show a ferrocene like coordination of Si3, Al1 and M3 atoms (Fig.5.19, third row right). The two five rings are inter connected by Si1, Si2 and M2 atoms, which lie on the same plane as Li1. The Sr atoms fill the largest channels in the structure (Fig.5.17 and 18). Both lie in the middle of a sandwich of six rings built of silicon and M atoms. In the Sr1 coordination the six ring is built of M3 and Si3, the two rings are connected by three Si3-M2-Si3 connections, so that Sr1 and M2 are planar (Fig.5.19, fourth row left). The Sr2 lies also in the middle of a hexagonal prism built of Si1, Si2, M2 and M1 atoms, but here the two six rings are connected through four atoms: two Al1 and two M3. All these atoms lie on the same plane as Sr2 (Fig.5.19, fourth row right).

As already pointed out the M1 position needs a deeper analysis, the *U33* displacement factor is unusually large. This could be a sign for split positions, since this position shows a mixed occupation of aluminum and lithium. The residual electron density on the Fourier difference map around the M1 position clearly shows the existence of two split positions above and below it (Fig.5.20). These residual electron maxima lie on the special position 2*e* (0,0,0.338). Thus the unusual *U33* displacement factor is the resulting of an aluminum underoccupied 1*b* position and another lithium underoccupied 2*e* position, with the sum of the occupancy of these two positions being one since only one atom can exist in this region at the same time. The existence of this split positions of lithium can be explained by the Si1–M1 distance of 247 pm, which is clearly too short for Si–Li distances. Based on the split model the resulting distance Si1–Li(2*e*) is enlarged to 257 pm, which is still short but in the range of other already observed Si–Li distances in Zintl phases.

However, the refinement of the structure with this new atomic arrangement turned out to be impossible since the new lithium position was too correlated to the resulting Al position (old M1 position). The consequence of this observation is that the real ratio of aluminum vs. lithium of this position remains uncertain.

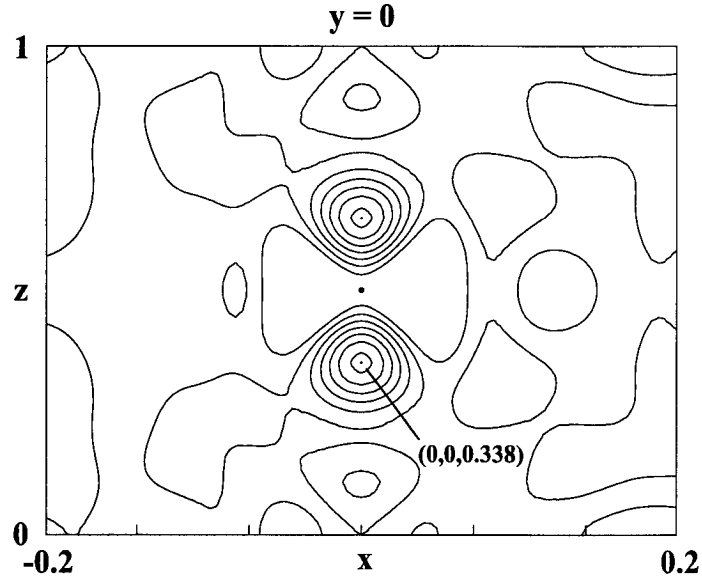

Figure 5.20: Difference Fourier Map around the M1 position

5.3.3 Theoretical Investigation

In order to investigate the electronic properties and bonding structure of $Li_{3+x}Sr_5Al_{16-x}Si_{12}$ (x ~ 6.2), theoretical calculations were performed using the LMTO method. Since there are three mixed occupied M positions, calculations of DOS were performed on two ordered models with different aluminium and lithium positions. In both models the M1 position is fully occupied by Al. In order to split the other two M special positions of multiplicity six, the symmetry was reduced to the space group $P\bar{6}$, where these two positions are split into four different special sites of multiplicity three (Tab.5.27).

Table 5.27: Occupation of the M positions in the models used for LMTO calculations

Position	*x*	*y*	*z*	Model1	Model2
M2	0.8108	0.1886	1/2	Al	Li
	0.1892	0.3778	1/2	Li	Li
M3	0.1209	0.4819	0	Al	Al
	0.8791	0.3610	0	Li	Al

The resulting chemical composition in both of the two models is $Li_9Sr_5Al_{10}Si_{12}$which is close to the experimentally determined composition $Li_{9.19}Sr_5Al_{9.81}Si_{12}$.

According to the Zintl-Klemm concept both models can be described as $(Li^+)_9(Sr^{2+})_5[((3b)Al^{2-})((4b)Al^-)_9((4b)Si)_3((3b)Si^-)_9]$, this description leads to an excess of one negative charge. In case of a 2:1 occupation of M1, which is the site occupied by the $(3b)Al^-$, the compound is electron precise. On the other hand a change of the occupation factors of the other M positions could easily result in the necessary increase of the Li per formula unit to change the stoichiometry to $Li_{9.5}Sr_5Al_{9.5}Si_{12}$, which again is electron precise. The resulting DOS of the two different models are shown in Figure 5.21. These clearly show metallic character. However, model 2 comes close to an ideal electronic situation for a metal with the Fermi energy in a minimum of the DOS. Thus an electron count off the Zintl-Klemm concept is tolerable. According to the DOS of model2 one would not expect a reduction of the Al content for an increase of the number of Li because that would shift the Fermi level off the favourable minimum.

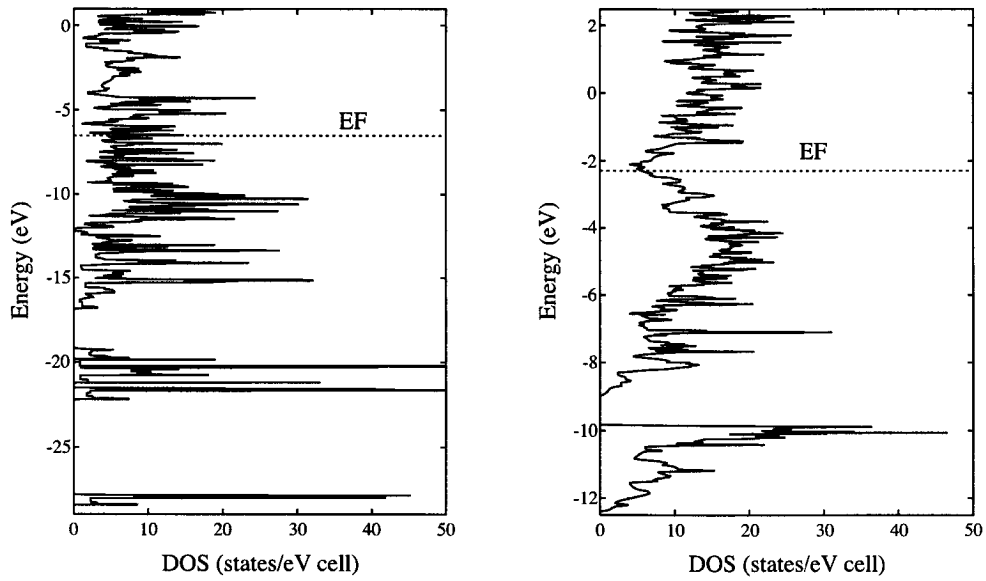

Figure 5.21: LMTO-DOS of $Li_{3+x}Sr_5Al_{16-x}Si_{12}$ (model1 left, model2 right)

5.4 Overview

The comparison of the quaternary structure types presented in this chapter reveals very strongly the valence concept or the Zintl-Klemm rules in a compound series just in between metals and semiconductors. In terms of electrical properties, they all belong to the intermetallic side but still tend strongly to preserve the local bonding strategy. In Figure 5.22 a comparative overview over these structures is given.

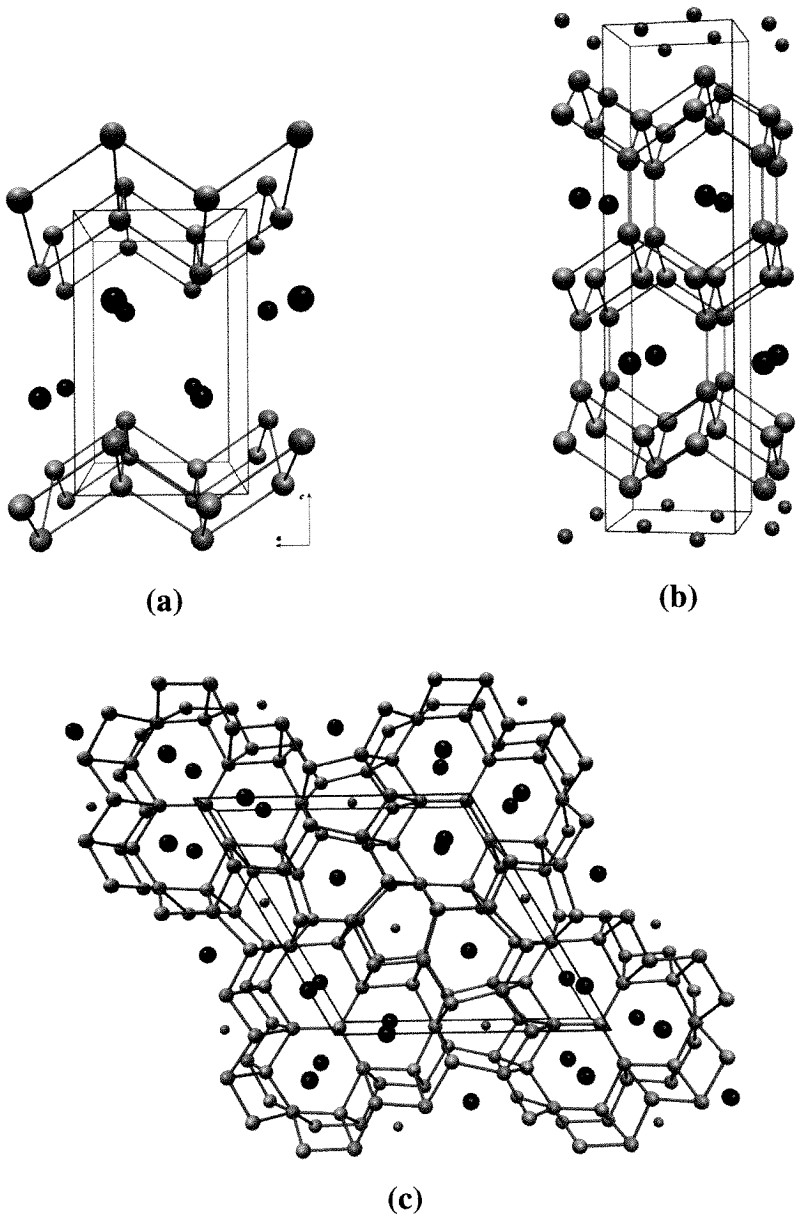

Figure 5.22: Structure found in the Li/Sr/Al/Si system; **(a)** $LiSr_2AlTt_2$, **(b)** $Li_{3+x}Sr_2Al_{6-x}Si_6$; **(c)** $Li_{3+x}Sr_5Al_{16-x}Si_{12}$

6. The Quaternary Li/Ca/Al/Tetrel System

In this quaternary system no known phases were found in the relevant literature. During this work, it was possible to synthesize the new Li_xCaAl_{1-x}Tetrel phases ($0.4 < x < 0.6$; Tetrel = Si, Ge). These two new phases crystallize with the NaAuSn structure type.

6.1 $Li_xCaAl_{1-x}Si$

In order to investigate this system, a series of syntheses was performed with stoichiometry selections which should lead to an $[AlSi_{4/2}]^{5-}$ network already found in the ternary system Li/Al/Si. Thus the goal was compositions which had already been found in the quaternary system Li/Sr/Al/Si.

We succeeded in the preparation and characterisation of a new phase with the composition $Li_xCaAl_{1-x}Si$, where x can assume a range of different values between 0.4 and 0.6. For x=0.5 the composition $LiCa_2AlSi_2$ results and the compound is isoelectronic to the Li_5AlSi_2 phase and to the $Li_xSrAl_{1-x}Si$ (x = 0.5) (NaAlSi structure type), but crystallizes in a different structure type.

6.1.1 Synthesis

Phase pure $Li_xCaAl_{1-x}Si$ ($0.4 < x < 0.6$) was prepared by tempering stoichiometric mixtures of the elements at 1050°C (t_1 = 8 hours, r_e = 50°C/h). All phases $Li_xCaAl_{1-x}Si$ form brittle grey crystals with metallic lustre. The compound is air and moisture sensitive and it decomposes on contact with water into a black powder by releasing gaseous silanes.

6.1.2 Crystal Structure

A single crystal of $Li_xCaAl_{1-x}Si$ was measured on a CCD system diffractometer. All data were collected up to $2\theta = 60°$. The Laue symmetry is *mmm* and the extinctions are consistent with the space groups $Pna2_1$ and *Pnma*. The structure was solved in *Pnma* using direct methods. All atoms were anisotropically refined and the displacement

parameters are altogether in the normal range (Tab.6.1-5). One metal position M exhibits mixed occupation by aluminum and lithium as given in Table 6.4.

Table 6.1: Crystal data and parameters of the data collection for $Li_xCaAl_{1-x}Si$

Empirical formula	Li0.96Ca2Al1.04Si2
Formula weight [g/mol]	171.06
Crystal size [mm]	0.14 x 0.16 x 0.18
Colour	grey metallic lustre
Crystal system	orthorhombic
Unit cell dimension [pm]	a = 729.4(1); b = 433.1(1); c = 795.4(1)
Volume [pm^3]	251.3(3)·10^6
Space group	*Pnma* (62)
Formula unit pro cell	2
ρ (calculated) [g/cm^3]	2.261
Absorption coefficient μ [mm^{-1}]	2.74
F (000)	169
Temperature [K]	298
Data collection	Siemens Platform CCD
Monochromator; Wavelength	Graphite; λ(MoKα) = 0.71073 Å
Detector distance; Collection method	d = 30 mm; Hemisphere ω-Scan
Δω; Irradiation time	Δω = 0.20°; t = 20 sec
Theta range	2° < 2θ < 70°
h(min), h(max); k(min), k(max); l(min), l(max)	-11, 11; -6, 6; -12, 12
Reflections collected	7688
Independent reflections	590 ; R(int) = 0.0332
Independent reflections with $\|F\|^2 > 2\,\sigma(\|F\|^2)$	501
Absorption correction	empirical (SADABS)
Refinement	SHELXL-97 (full-matrix least-squares of F^2)
Parameters	21
Restraints	0
Extinction coefficient	0.043(4)
Maximal shift/esd	0.000
Mean shift/esd	0.000
Largest diff. peak and hole [electrons/pm^3·10^6]	min = -0.344; max = 0.316
[a] wR for $\|F\|^2 > 2\,\sigma(\|F\|^2)$	0.0392
wR for all reflections	0.0404
[a] R for $\|F\|^2 > 2\,\sigma(\|F\|^2)$	0.0178
R for all reflections	0.0251
[a] Goodness of Fit (*GooF*) for all reflections	0.960

[a] the definitions are given in chapter 2.2, Table 2.3

Table 6.2: Wyckoff sites, atomic coordinates, and equivalent isotropic displacement parameters [pm^2] for $Li_xCaAl_{1-x}Si$

Atoms	*Wyckoff site*	*x*	*y*	*z*	*U(iso)*
Ca	4*c*	0.51085(4)	1/4	0.68936(3)	149(1)
Si	4*c*	0.78015(5)	1/4	0.39547(5)	160(1)
M	4*c*	0.14809(9)	1/4	0.42970(8)	120(2)

Table 6.3: Anisotropic displacement parameters [pm^2] for $Li_xCaAl_{1-x}Si$

Atoms	*U11*	*U22*	*U33*	*U23*	*U13*	*U12*
Ca	122(1)	176(1)	148(1)	0	-16(1)	0
Si	119(2)	134(2)	228(2)	0	-18(1)	0
M	126(3)	112(3)	123(3)	0	-1(2)	0

Table 6.4: Occupancy of the M-position for $Li_xCaAl_{1-x}Si$

Position	*Aluminum*	*Litihium*
M	0.480(3)	0.520(3)

Table 6.5: Selected interatomic distances [pm] for $Li_xCaAl_{1-x}Si$

Ca	–Si	305.33(6)	1x	Si	–M	262.61(5)	2x	M	–Si	262.61(5)	2x
	–Si	310.64(4)	2x		–M	269.75(8)	1x		–Si	269.75(8)	1x
	–M	311.25(5)	2x		–M	276.01(8)	1x		–Si	276.01(8)	1x
	–Si	311.46(4)	2x		–Ca	305.33(6)	1x		–Ca	311.25(5)	2x
	–M	319.10(8)	1x		–Ca	310.64(4)	2x		–Ca	319.10(8)	1x
	–M	335.66(8)	1x		–Ca	311.46(4)	2x		–M	326.3(7)	2x
	–M	343.13(6)	2x		–Ca	370.6(1)	1x		–Ca	335.66(8)	1x
	–Si	370.6(1)	1x						–Ca	343.13(6)	2x

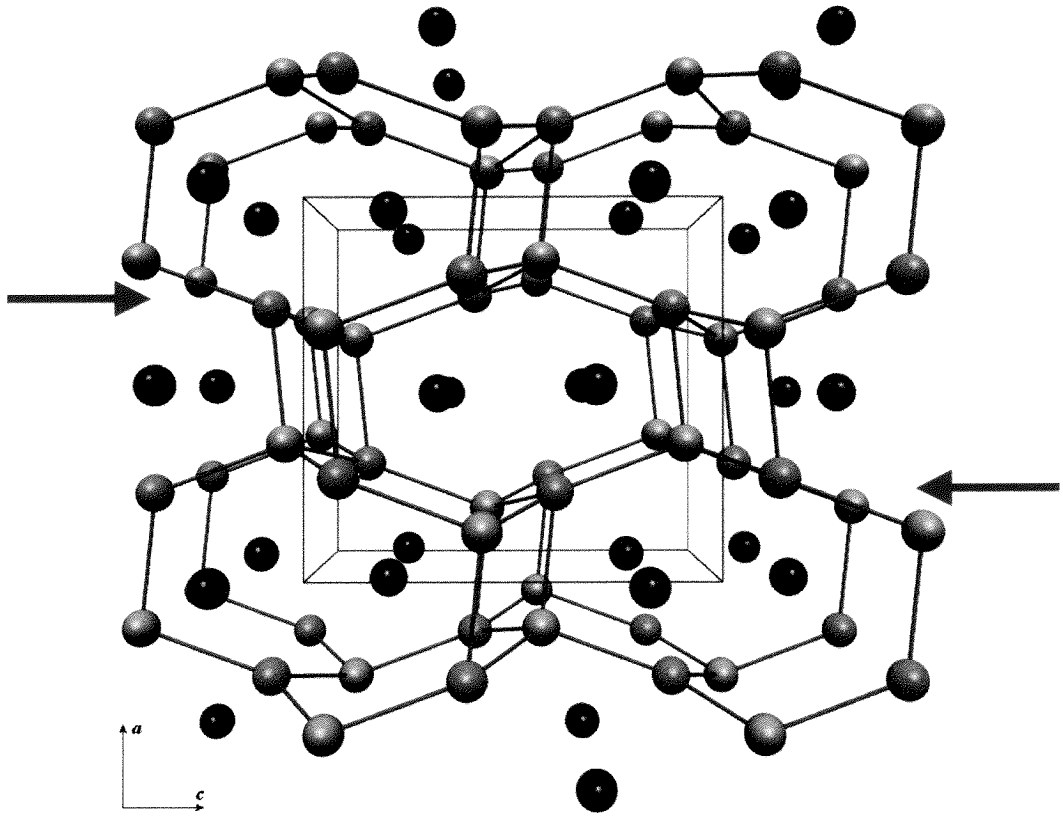

Figure 6.1: Structure of $Li_xCaAl_{1-x}Si$ (basic cell; Si red spheres, M turquoise, Ca black; hexagonal layers marked by blue arrows)

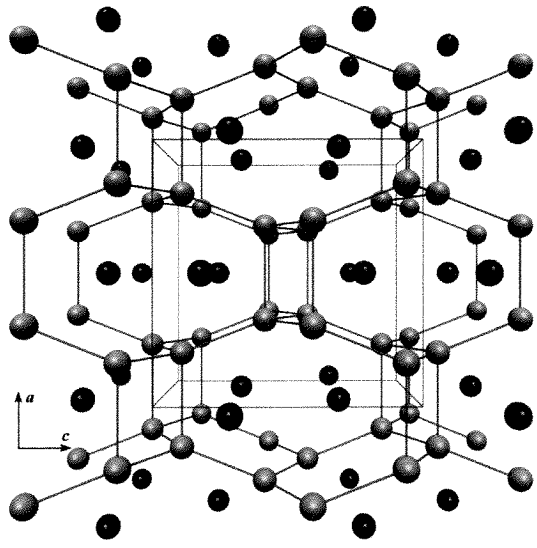

Figure 6.2: Structure of $SrAl_2$ (Al green spheres, Sr black)

The $Li_xCaAl_{1-x}Si$ phases crystallize in the NaAuSn structure type (Fig. 6.1), which can be described as a distorted $SrAl_2$ structure type (*Imma*; Fig. 6.2), the only difference being the four rings: in this structure they build a rhombus whereas in the $SrAl_2$ structure they form rectangles (allowing for a centring of the unit cell). By this distortion the structure can adopt for the smaller calcium species.

The structure consists of puckered layers of sixrings which are set up by silicon and by mixed occupied aluminum/lithium sites. These layers are then connected to each other by Si-M four rings. The calcium atoms lie in the middle of two Si-M six rings belonging to two different Si-M layers (Fig. 6.1).

The silicon atoms are coordinated by four M atoms building a strongly distorted tetrahedron, where three M atoms and the silicon are coplanar. Therefore the angles within the rhombus shrink from the ideal 109.5° to 75.4° (Fig.6.4, top left). This coordination of silicon is similar to that observed in the $CaAl_2Si_2$ structure (Fig.6.3), where the silicon shows an "umbrella" coordination with bond angles of 73.4°. The sixring layers are interconnected through four rings and two layers of six rings are then separated by layers of calcium atoms with a long separation of 457 pm.

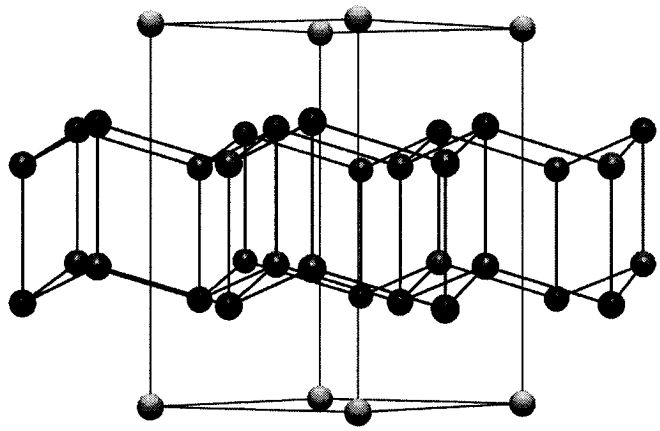

Figure 6.3: Structure of $CaAl_2Si_2$, showing the "umbrella" coordination of silicon (Si black, Al small grey spheres, Ca large grey spheres)

In contrast to the silicon coordination, the M atoms lie in the middle of an only slightly distorted tetrahedron of Si atoms (Fig.6.4, top right). The silicon, as well as the M atoms, lie in the middle of a strongly distorted trigonal prism of calcium atoms (Fig.6.4 top).

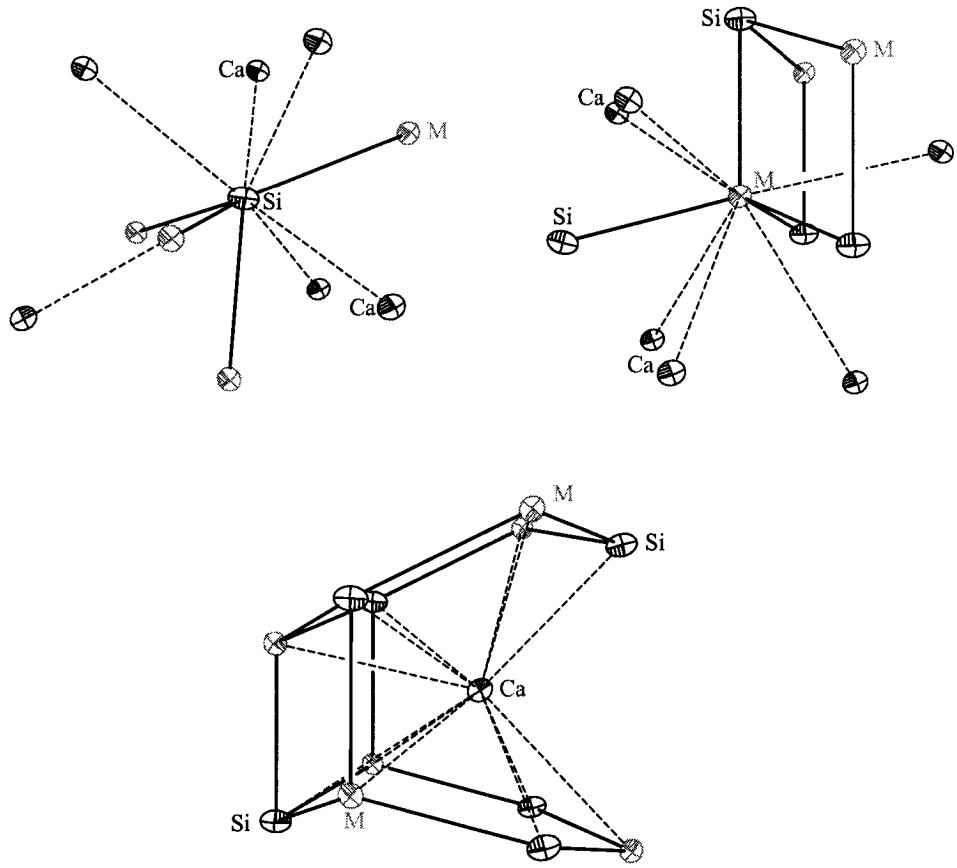

Figure 6.4: Coordination of Si (top left), M (top right), and Ca (bottom)

In addition to these 10 coordinating atoms there are additionally two other M atoms (the shortest diagonal of the rhombus) around the M position. The calcium atom is situated in the middle of two six rings connected each other via the four rings (Fig.6.4 bottom) and it has a coordination number of 12.

The Si–M distances are not equivalent (Tab.6.5): the four rings are built of two short Si–M bonds of 262.6 pm, which belong also to the six ring layer, and of the two bonds of 269.7 pm, which mutually connect to form the sixring layers. The longest Si–M distance of 276.0 pm is then the bond which belongs only to the sixrings.

Compared to Al–Si bonds normally found in similar compounds (255-262 pm) the two longest slightly surpass this range. However, it should be considered that the presence of lithium atoms influences the average Si–M distance.

There is also a short M–M distance, the short diagonal of the rhombus, of 326.3 pm as already observed in the $Li_xSrAl_{1-x}Si$ phase as well as in the $CaAl_2Si_2$ phase but here are slightly longer (326.3 pm vs. 313.8 pm resp. 302.3 pm).

6.1.3 Crystal Structure of the Super Cell

The presence of mixed occupied crystallographic positions is an invitation to check for a superstructure. Although nature does not know mixed atoms, the question is how large the ordered domains must be to achieve a Bragg scattering response. To answer this question a very accurate investigation of the reciprocal space must be carried out aiming to find superstructure reflections, which are usually much weaker than the main reflections.

Therefore the crystal of the $Li_xCaAl_{1-x}Si$ phase was remeasured on the four circle diffractometer. During this measurement, axial photographs of the reciprocal lattice were taken with very long exposition time. The picture parallel to the reciprocal axis b^* clearly shows weak fourfold superstructure reflections (Fig. 6.5), whereas no superstructure reflections were observed in the pictures parallel to the other two reciprocal axis.

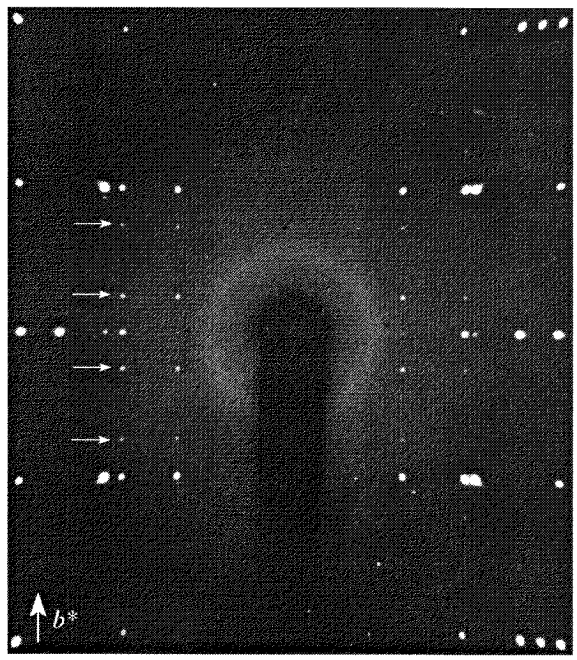

Figure 6.5: Diffraction picture (rotation photograph) parallel to the b^*-axis showing series of hkl reflections with k=0, ±1 and ±2 as well as k= ±1/4, ±3/4 (white arrows)

An expanded set of data for $b' = 4b$ was then collected on the four-circle diffractometer up to $2\Theta = 60°$ (Tab.6.5). The Laue symmetry is *mm2* and the extinctions are consistent with the space groups $Pmc2_1$, *P2cm*, *Pmcm*.

However, the structure refinement turned out to be very difficult because of the large number of parameters and too large correlations between them. This correlation arises from the fact that the three independent atom positions of the basic cell are now splitted into twelve different independent positions in the space group $Pmc2_1$ and this splitting is only described by few and very weak superstructure reflections. The refinement therefore was unstable and did not lead to a reliable solution.

The superspace description (see chapter 2.2.1.3) turned out to be useful in our case as the superspace group, $Pbnm(00\gamma)$ in this case, has a higher symmetry than the superstructure space group. In this approach, the superstructure reflections are treated as satellite reflections. These are due to a periodic distortion of the basic cell. Therefore, the parameters necessary to describe this structural ordering are less than the ones needed for the superstructure space group, namely 40 against 69.

It is interesting to note that the second order satellite reflections are not observed as can be seen in the Figure 6.5. The parameters of the structure refinement and of the periodic functions are summarised in the Tables 6.6-7.

Table 6.6: Crystal data and parameters of the data collection for $Li_xCaAl_{1-x}Si$

Empirical formula	Li7.84Ca16Al8.16Si16
Formula weight [g/mol]	1363.36
Crystal size [mm]	0.16 x 0.18 x 0.14
Colour	grey metallic lustre
Crystal system	orthorhombic
Unit cell dimension [pm]	a = 795.4(3); b = 729.4(3); c = 433.1(2);
Superstructure axis [a)]	$\gamma = 0.25$[a)]; c' = 1732.4(8)
Volume [pm^3]	$1005.0(4)\cdot10^6$
Super space group [a)]	*Pbnm*(00γ) (62.3)[a)]
Formula unit pro cell	1
ρ (calculated) [g/cm^3]	2.256
Absorption coefficient μ [mm^{-1}]	2.73
F (000)	673.6
Temperature [K]	298
Data collection	four-circle diffractometer STOE STADI4
Monochromator; Wavelength	graphite; λ(MoKα) = 0.71073 Å
Scan parameters (steps; $\Delta\omega$; scan)	40; 0.03; ω-θ-Scan
Theta range	$2° < 2\theta < 60°$
h_{min}, h_{max}; k_{min}, k_{max}; l_{min}, l_{max}; m_{min}, m_{max} [a)]	-8, 8; 0, 8; -3, 3; -1, 1
Reflections collected	2246
Independent reflections	1177; R(int) = 0.0299 (orthorhombic)
Independent reflections with $\|F\|^2 > 2\,\sigma(\|F\|^2)$	607 (orthorhombic)
Absorption correction	Ψ-Scan
Refinement	JANA2000
Parameters	40
Phase shift parameters t[a)]	0.105
Overall R factor	0.0408 for $\|F\|^2 > 2\,\sigma(\|F\|^2)$; 0.1173 for all
Overall wR factor	0.1104 for $\|F\|^2 > 2\,\sigma(\|F\|^2)$; 0.1128 for all
R for main reflections	0.0404 for $\|F\|^2 > 2\,\sigma(\|F\|^2)$; 0.0481 for all
wR for main reflections	0.1117 for $\|F\|^2 > 2\,\sigma(\|F\|^2)$; 0.1119 for all
R for satellite reflections of order 1 [a)]	0.0427 for $\|F\|^2 > 2\,\sigma(\|F\|^2)$; 0.1927 for all
wR for satellite reflections of order 1 [a)]	0.0894 for $\|F\|^2 > 2\,\sigma(\|F\|^2)$; 0.1105 for all

[a)] for the definitions see Chapter 2.2.1.3

Table 6.7: Components of the position modulation functions

Atoms (μ)	$A_{\mu,x}$	$A_{\mu,y}$	$A_{\mu,z}$	$B_{\mu,x}$	$B_{\mu,y}$	$B_{\mu,z}$
Ca	0.0052	0.0047	-0.0001	0.0001	0.0001	0.0199
Si	0.0142	0.0051	-0.0004	-0.0001	-0.0001	-0.0175
M	-0.0034	0.0023	0.0001	-0.0001	0.0001	-0.0051

Table 6.8: Components of the occupation modulation function

Atoms (μ)	A_μ	B_μ
M	0.4970	-0.0024

The different components refer to the following modulation functions (for a better explanation cf. Chapter 2.2.1.3). For the positions (Tab.6.7):

$$x_{\mu,i} = \bar{x}_{\mu,i} + u_{\mu,i}(\bar{x}_{\mu,4}) \;,\; \bar{x}_{\mu,4} = \mathrm{q}\cdot\bar{\mathrm{r}}_\mu + t$$

$$\bar{\mathrm{r}}_\mu = \left(\bar{x}_{\mu,1}, \bar{x}_{\mu,2}, \bar{x}_{\mu,3}\right)$$

$$u_{\mu,i} = A_{\mu,i}\cdot\sin\left(2\pi\bar{x}_{\mu,4}\right) + B_{\mu,i}\cdot\cos\left(2\pi\bar{x}_{\mu,4}\right),$$

and for the occupations (Tab.6.8):

$$P_\mu = \overline{P}_\mu + p_\mu\left(\bar{x}_{\mu,4}\right)$$

$$p_\mu = A_\mu\cdot\sin\left(2\pi\bar{x}_{\mu,4}\right) + B_\mu\cdot\cos\left(2\pi\bar{x}_{\mu,4}\right)$$

Table 6.9: Wyckoff sites, atomic coordinates, and equivalent isotropic displacement parameters [pm^2] for the basic cell in the space group *Pbnm*.

Atoms	*Wyckoff site*	*x*	*y*	*z*	*U(iso)*
Ca	4*c*	0.8108(1)	0.0110(1)	1/4	149(1)
Si	4*c*	0.1045(1)	0.2799(1)	1/4	160(1)
M	4*c*	0.4313(1)	0.1460(1)	1/4	120(2)

Table 6.10: Occupancy of the M-position for the basic cell

Position	*Aluminum*	*Litihium*
M	0.51(1)	0.49(1)

The atomic positions as well as the occupancy of this basic cell were then modulated with the given (Tab. 6.7-8) parameters to obtain the new atomic positions and the different occupancies for the super cell (Tab.6.12). The space group of this new set of atoms is then only *P1*. We decided not to modulate the displacement factors with the aim to reduce the number of parameters to be refined.

Another step in the solution of the structure was to refine the structural model with different values of t (see above, and Chapter 2.2.1.3). The best R-values were then obtained from the refinement with $t = 0.105$ (Tab. 6.11). This parameter, as well as the others given in Table 6.7-8, was used to calculate the atomic parameters given in Table 6.12.

Table 6.11: R-values (%) of satellite reflections by applying different t parameters

t	*R(obs)*	*wR(obs)*	*R(all)*	*wR(all)*
0.0	4.34	9.00	19.35	11.11
0.05	4.31	8.96	19.32	11.07
0.1	4.27	8.94	19.28	11.05
0.105	**4.27**	**8.94**	**19.27**	**11.05**
0.15	4.27	8.95	19.28	11.06
0.20	4.30	8.96	19.32	11.07

Table 6.12: Atomic coordinates, and occupancies of the M positions in the super cell

Atoms	*x*	*y*	*z*	*Occupancy*	
				Al	Li
Ca1	0.8153	0.0151	0.0650		
Ca2	0.6937	0.5151	0.0650		
Ca3	0.3158	0.4934	0.1862		
Ca4	0.1942	0.9934	0.1862		
Ca5	0.8134	0.0133	0.3082		
Ca6	0.6918	0.5133	0.3082		
Ca7	0.3094	0.4877	0.4327		
Ca8	0.1878	0.9877	0.4327		
Ca9	0.8063	0.0070	0.5601		
Ca10	0.6847	0.5070	0.5601		
Ca11	0.3058	0.4845	0.6888		
Ca12	0.1842	0.9845	0.6888		
Ca13	0.8083	0.0088	0.8168		
Ca14	0.6866	0.5088	0.8168		
Ca15	0.3122	0.4903	0.9423		
Ca16	0.1906	0.9903	0.9423		
Si1	0.4078	0.7843	0.0602		
Si2	0.1168	0.2843	0.0602		
Si3	0.9092	0.7250	0.1886		
Si4	0.6182	0.2250	0.1886		
Si5	0.4026	0.7825	0.3163		
Si6	0.1116	0.2825	0.3163		
Si7	0.8918	0.7188	0.4418		
Si8	0.6008	0.2188	0.4418		
Si9	0.3832	0.7755	0.5648		
Si10	0.0922	0.2755	0.5648		
Si11	0.8818	0.7152	0.6864		
Si12	0.5908	0.2152	0.6864		
Si13	0.3884	0.7773	0.8087		
Si14	0.0974	0.2773	0.8087		
Si15	0.8992	0.7214	0.9333		
Si16	0.6082	0.2214	0.9333		
M1	0.4283	0.1480	0.0619	0.94	0.06
M2	0.0657	0.6480	0.0619	0.94	0.06
M3	0.9280	0.3562	0.1879	0.99	0.01
M4	0.5654	0.8562	0.1879	0.99	0.01
M5	0.4296	0.1470	0.3136	0.76	0.24
M6	0.0671	0.6470	0.3136	0.76	0.24
M7	0.9322	0.3533	0.4387	0.38	0.62
M8	0.5697	0.8533	0.4387	0.38	0.62
M9	0.4343	0.1439	0.5631	0.08	0.92
M10	0.0718	0.6439	0.5631	0.08	0.92
M11	0.9346	0.3519	0.6872	0.03	0.97
M12	0.5721	0.8519	0.6872	0.03	0.97
M13	0.4329	0.1449	0.8114	0.26	0.74
M14	0.0704	0.6449	0.8114	0.26	0.74
M15	0.9303	0.3548	0.9363	0.64	0.36
M16	0.5678	0.8548	0.9363	0.64	0.36

Analysis of the occupancies for the **M** positions shows that it is possible to divide the structure in four different blocks: the first is almost fully occupied by aluminum atoms, the second and the fourth blocks exhibit nearly statistical mixing of Li and Al, whereas the third block is almost fully occupied by lithium (Fig. 6.6). This may be termed a stoichiometrically frozen in charge density wave.

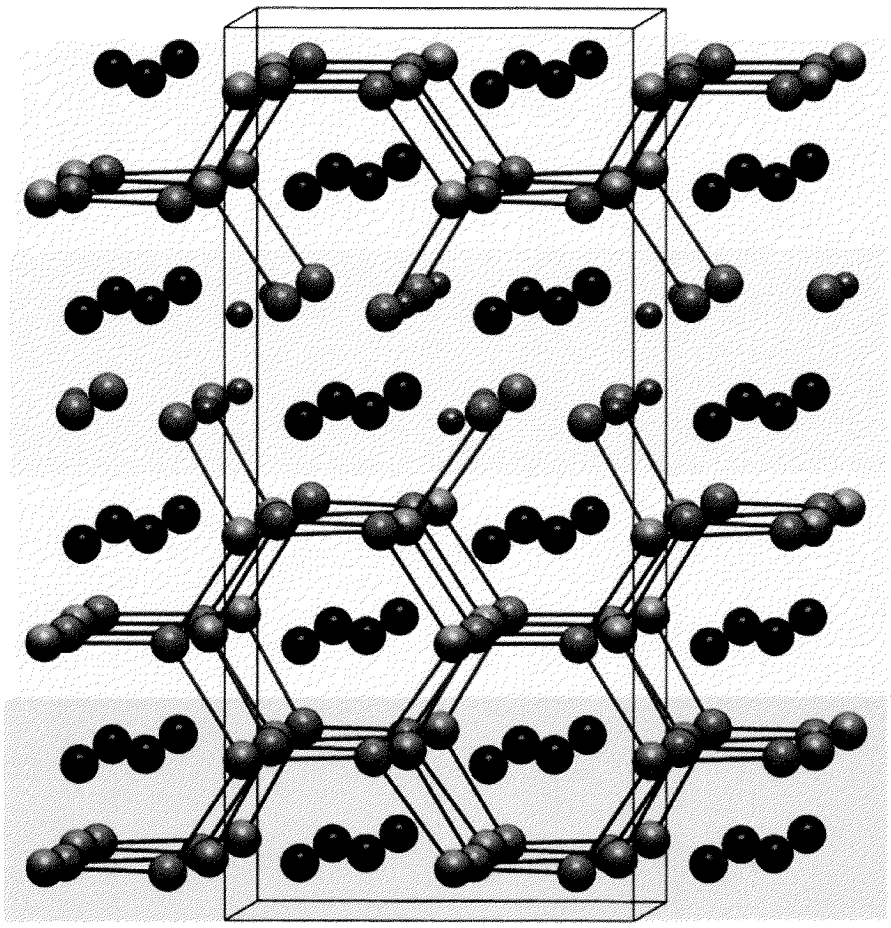

Figure 6.6: Structure of the supercell, green block: Al rich part, grey block: Li rich part

It is interesting to note, that this supercell is still not the fully ordered cell of the compound: mixed occupied M positions still exist in the turquoise blocks of the structure. The superstructure reflections are due to sequence of blocks with different Li : Al ratios. Therefore, a larger basic cell with then ordered M position must exist, however was not observed.

In Table 6.13 the M–Si distances are listed. Interesting is that there is no big difference in the bond distances between the Al rich M positions and the Li rich M positions.
The shortest Si–M distances are still those within the four rings, which belong also to the six ring layer, and the longest Si–M distances are still the bonds which belong only to the six rings.

Table 6.13: Selected interatomic distances [pm] for the M positions in the super cell

M1	–Si1	265.8	M2	–Si3	258.5	M3	–Si4	264.3	M4	–Si1	259.5
	–Si2	267.0		–Si15	264.7		–Si3	269.4		–Si5	263.0
	–Si16	270.0		–Si2	268.4		–Si6	271.5		–Si4	272.3
	–Si4	272.3		–Si1	289.7		–Si2	272.4		–Si3	289.7
M5	–Si8	265.7	M6	–Si3	256.8	M7	–Si10	259.0	M8	–Si5	255.6
	–Si5	266.7		–Si7	267.3		–Si6	260.8		–Si8	267.8
	–Si4	269.6		–Si6	268.2		–Si7	268.6		–Si9	270.0
	–Si6	271.6		–Si5	284.6		–Si8	281.3		–Si7	274.4
M9	–Si12	252.7	M10	–Si7	260.1	M11	–Si10	252.6	M12	–Si13	262.0
	–Si8	254.4		–Si9	265.7		–Si14	253.2		–Si12	265.4
	–Si9	271.8		–Si11	266.8		–Si11	268.3		–Si9	265.8
	–Si10	288.5		–Si10	269.2		–Si12	291.1		–Si11	265.8
M13	–Si12	255.4	M14	–Si15	257.3	M15	–Si14	264.0	M16	–Si1	254.9
	–Si16	259.0		–Si11	268.3		–Si2	266.0		–Si13	269.0
	–Si13	270.5		–Si14	269.0		–Si15	268.6		–Si16	269.4
	–Si14	283.8		–Si13	270.8		–Si16	274.1		–Si15	281.0

6.1.4 Physical Properties

The DTA of the compound $Li_xCaAl_{1-x}Si$ (x ~ 0.5) was performed (Fig. 6.7). The pure compound was prepared by heating at 1050°C (t_1 = 8 hours, r_e = 50°C/h) a stoichiometric mixture of the elements. The composition of the compound refers to the starting mixture and not to a single crystal determination. According powder XRD a single phase product was formed and the lattice parameters were very similar to those of the single crystal.

According to this measurement, $Li_xCaAl_{1-x}Si$ (x ~ 0.5) melts congruently at about 1030°C. No other thermal effects were observed in the temperature range applied.

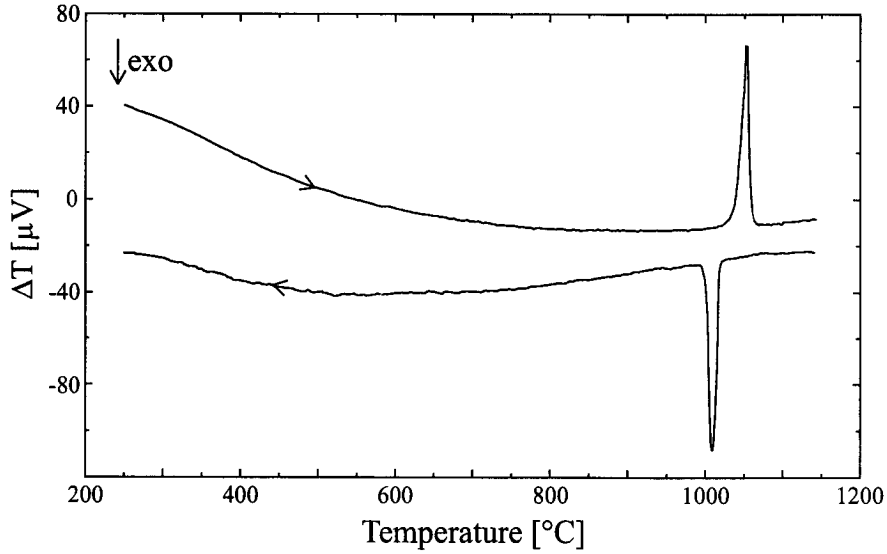

Figure 6.7: DTA of $Li_xCaAl_{1-x}Si$ (x ~ 0.5)

Measurements of the electric conductivity were also performed on a pellet (diameter = 6 mm; thickness = 0.75 mm), which was tempered during two days at 800°C.

However, the measurements turned out to be difficult cause grain boundary effects and contacts problems between pellets and electrodes. Therefore no quantitative results could be obtained, but qualitatively it is possible to classify the compound as a metal, as, in almost all measurements a clear metallic tendency was observed, i.e. raising resistance with increasing temperature.

6.1.5 Theoretical Investigations

In order to investigate the electronic properties and bonding structure of the $Li_xCaAl_{1-x}Si$ compound, theoretical calculations were performed in the framework of the LMTO method. As even in the super cell (16 positions) mixed occupancies were found, calculations of DOS were performed on simplified models. The model development was based on the supercell model. There is a pseudo symmetry which allows to couple pairs of atoms of the same type and leads to *Pc* instead of *P1* (Tab.6.14). In this space group the 16 independent M positions are reduced to 8 different independent crystallographic positions, the same for the 16 calcium and the 16 silicon positions. All atoms lie on the general crystallographic position *2a* in *Pc*. The higher symmetry was achieved by changing the cell axis (*a'* = *c*, *b'* = *a*, and *c'* = *b*); by shifting the origin (0,-1/4,0); and by averaging the y' coordinates of the two different positions. This averaging was necessary in order to follow the site symmetry relationship: x,y,z and x,$\bar{y}$,z+1/2. This coordinate shift was always in the order of ±0.004(1), resulting in a shift of about 0.03 Å, which is in the range of the standard deviations and therefore *Pc* is the space group of the refined superstructure model. Starting from this model the LMTO calculations were then performed on three different fully ordered models (Tab.6.15). These models differ in the occupation of the M positions: the still existing 8 M positions were reduced to four different M positions as two can be already considered as fully occupied by Al (M1 and M2 have occupations of 99% and 94% of Al, cf. Table 6.12 and 6.14) and two fully occupied Li sites (M5 and M6 have occupations of 97% resp. 92% of Li, cf. Table 6.12 and 6.14). The three models differ then in the occupation of the remaining four M positions. Two extreme models were used: one with another four Li positions, the other with four Al positions, and a mixed model with two Li and two Al on these sites.

Table 6.14: Atomic coordinates of the model in *Pc* for LMTO calculations (occupations are taken from the superstructure refinement)

Atoms	*x*	*y*	*z*	
Ca1	0.0650	0.5608	0.0151	
Ca2	0.1862	0.0608	0.4934	
Ca3	0.3082	0.5608	0.0133	
Ca4	0.4327	0.0608	0.4877	
Ca5	0.5601	0.5608	0.0070	
Ca6	0.6888	0.0608	0.4845	
Ca7	0.8168	0.5608	0.0088	
Ca8	0.9423	0.0608	0.4903	
Si1	0.0602	0.1455	0.7843	
Si2	0.1886	0.6455	0.7250	
Si3	0.3163	0.1455	0.7825	
Si4	0.4418	0.6455	0.7188	
Si5	0.5648	0.1455	0.7755	
Si6	0.6864	0.6455	0.7152	
Si7	0.8087	0.1455	0.7773	
Si8	0.9333	0.6455	0.7214	**Occ. Al**
M1	0.0619	0.1813	0.1480	0.941
M2	0.1879	0.6813	0.3562	0.990
M3	0.3136	0.1813	0.1450	0.759
M4	0.4387	0.6813	0.3533	0.381
M5	0.5631	0.1813	0.1439	0.080
M6	0.6872	0.6813	0.3519	0.030
M7	0.8114	0.1813	0.1449	0.262
M8	0.9363	0.6813	0.3548	0.639

Table 6.15: Occupation of the M positions for the three different models used for the LMTO calculations

Position	model1	model2	model3
M1	Al	Al	Al
M2	Al	Al	Al
M3	Al	Li	Al
M4	Li	Li	Al
M5	Li	Li	Li
M6	Li	Li	Li
M7	Li	Li	Al
M8	Al	Li	Al
Li : Al	4 : 4	6 : 2	2 : 6

The model2 and model3 yield the compositions $Li_3Ca_4AlSi_4$ and $LiCa_4Al_3Si_4$, respectively. Model1 then yields the composition $LiCa_2AlSi_2$ which is very close to the measured composition in the single crystal.

According to the Zintl-Klemm concept model 1 can be described as $(Li^+)_2(Ca^{2+})_4((4b)Al^-)_2((4b)Si)((3b)Si^-)((1b)Si^{3-})(Si^{4-})$ and is electron precise, model 2 as $(Li^+)_3(Ca^{2+})_4(Al(4b)^-)(Si(3b)^-)(Si(1b)^{3-})(Si^{4-})_2$ and presents an excess of two negative charges, and model 3 as $(Li^+)(Ca^{2+})_4(Al(4b)^-)_3(Si(4b))_2(Si(3b)^-)(Si(1b)^{3-})$ with an excess of two positive charge.

In Figure 6.8 the three calculated DOS are then displayed. Despite the complexity of the DOS it is possible to recognize in all three calculated DOS the metallic character of the $Li_xCaAl_{1-x}Si$ compound. This result is consistent with the observation of a phasewidth with the Li : Al ratio assuming values varying from 0.4 to 0.6, as well as with the conductivity measurements.

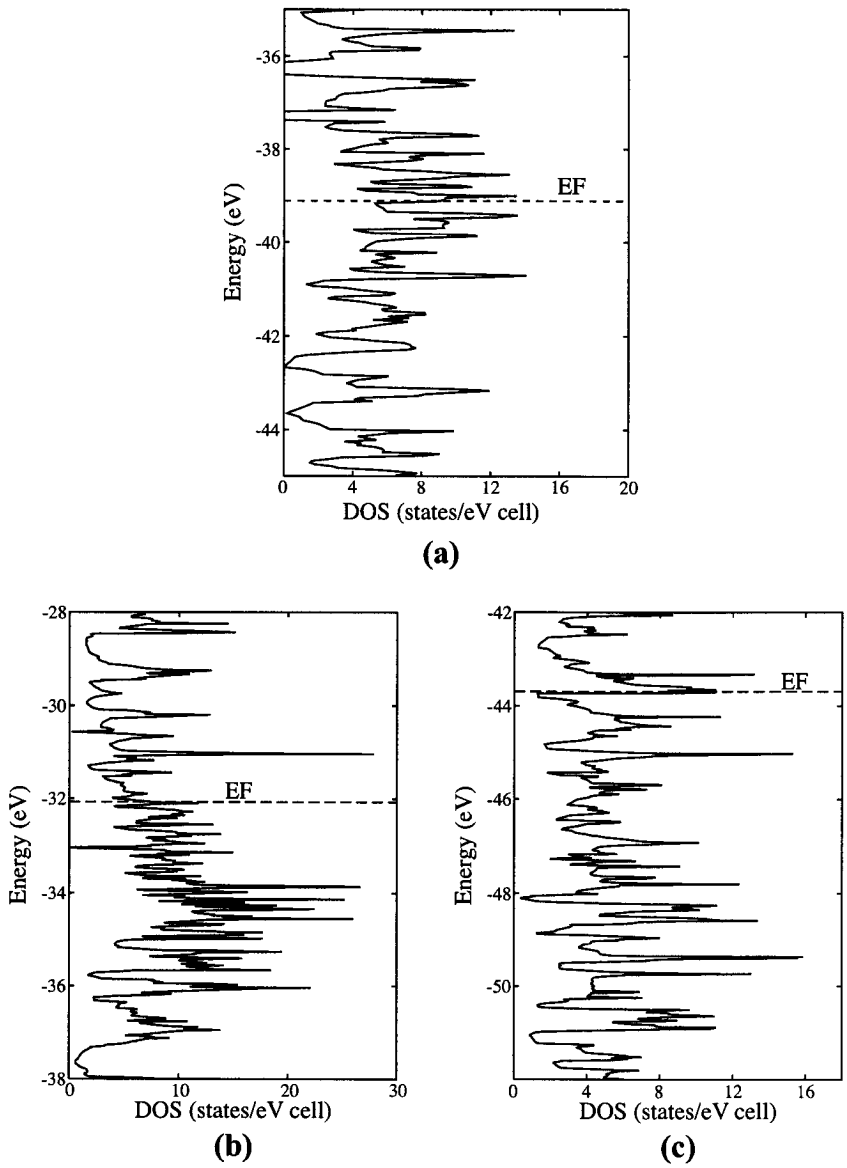

Figure 6.8: LMTO-DOS of the three models of $Li_xCaAl_{1-x}Si$: (a) model1 with Li:Al = 4:4; (b) model2 with Li:Al = 6:2; (c) model3 with Li:Al = 2:6

Although model 1 seems to fit best in terms of the Zintl-Klemm concept, models 2 and 3 may energetically be more favourable because their Fermi levels fall into regions of low DOS. This would be a reasonable cause for a charge density wave by which many domains could restrict to a favourable band structure while only few would have to suffer from a high DOS for the energetically least favourable electrons at E_F.

6.2 $Li_xCaAl_{1-x}Ge$

After the discovery of the new phase $Li_xCaAl_{1-x}Si$, experiments were carried out in the quaternary systems Li/Ca/Triel/Tetrel by substituting either the Triel or the Tetrel elements or both, with the aim of finding new compounds isoelectronic and isostructural to the $Li_xCaAl_{1-x}Si$ phase. We succeeded in the preparation and characterisation of the new phase $Li_xCaAl_{1-x}Ge$, with x varying between about 0.4 and 0.6. This phase is isoelectronic to $Li_xCaAl_{1-x}Si$ ($0.4 < x < 0.6$) and consequently exhibits a phasewidth too.

6.2.1 Synthesis

Almost single phase samples of $Li_xCaAl_{1-x}Ge$ ($0.4 < x < 0.6$) were prepared by tempering stoichiometric mixtures of the elements at 1050°C (t_1 = 8 hours, r_e = 50°C/h). $Li_xCaAl_{1-x}Ge$ forms brittle grey crystals with a metallic lustre. $Li_xCaAl_{1-x}Ge$ is air and moisture sensitive. The compound decomposes on contact with water into a yellow-orange powder by releasing gaseous species. According to the colour the solid residue is very likely GeO_2. The decomposition products have a pungent smell.

6.2.2 Crystal Structure

It was possible to find single crystals but of relatively poor quality (cf *R*(int) in Table 6.16) in the products. A single crystal of $Li_xCaAl_{1-x}Ge$ (x ~0.5) was measured on a CCD diffractometer. All data were collected up to $2\theta = 60°$. In contrast to the $Li_xCaAl_{1-x}Si$ (x ~ 0.5) phase, here no superstructure reflections were observed. This is maybe a consequence of the poor quality of the crystals or, on the other hand, this may as well be a sign that the ordering of the M positions is worse than for the silicide, a finding which is in line with the observations on ternary silicides and germanides (cf. Chap. 4).

The Laue symmetry is *mmm* and lower symmetric Laue classes do not show better *R*(int). The extinctions are consistent with the space groups $Pna2_1$ and *Pnma*. The structure was solved in *Pnma* applying direct methods. All atoms were anisotropically refined (Tab. 6.17-18). The metal position M is occupied by aluminum and lithium as given by the corresponding occupancy factors (Tab.6.19).

Table 6.16: Crystal data and parameters of the data collection for $Li_xCaAl_{1-x}Ge$

Empirical formula	Li1.02Ca2Al0.98Ge2
Formula weight [g/mol]	258.86
Crystal size [mm]	0.06 x 0.10 x 0.12
Colour	grey metallic lustre
Crystal system	orthorhombic
Unit cell dimension [pm]	a = 732.5(6); b = 435.0(4); c = 805.0(6)
Volume [pm^3]	$256.5(5)\cdot10^6$
Space group	*Pnma* (62)
Formula unit pro cell	4
ρ (calculated) [g/cm^3]	3.352
Absorption coefficient μ [mm^{-1}]	13.70
F (000)	240
Temperature [K]	298
Data collection	Siemens Platform CCD
Monochromator; Wavelength	graphite; λ(MoKα) = 0.71073 Å
Detector distance; Collection method	d = 30 mm; Hemisphere ω-Scan
Δω; Irradiation time	Δω = 0.15°; t = 30 sec
Theta range	$2° < 2\theta < 70°$
h(min), h(max); k(min), k(max); l(min), l(max)	-11, 11; -7, 7; -12, 12
Reflections collected	3769
Independent reflections	582; R(int) = 0.1938
Independent reflections with $\|F\|^2 > 2\,\sigma(\|F\|^2)$	355
Absorption correction	empirical (SADABS)
Refinement	SHELXL-97 (full-matrix least-squares of F^2)
Parameters	21
Restraints	0
Extinction coefficient	0.018(6)
Maximal shift/esd	0.000
Mean shift/esd	0.000
Largest diff. peak and hole [electrons/$pm^3\cdot10^6$]	min = -2.071; max = 2.050
[a] wR for $\|F\|^2 > 2\,\sigma(\|F\|^2)$	0.1354
wR for all reflections	0.1542
[a] R for $\|F\|^2 > 2\,\sigma(\|F\|^2)$	0.0633
R for all reflections	0.1178
[a] Goodness of Fit (*GooF*) for all reflections	0.949

[a] the definitions are given in chapter 2.2, Table 2.3

Table 6.17: Wyckoff sites, atomic coordinates, and equivalent isotropic displacement parameters [pm^2] for $Li_xCaAl_{1-x}Ge$

Atoms	*Wyckoff site*	*x*	*y*	*z*	*U(iso)*
Ca	4*c*	0.5119(3)	1/4	0.6891(2)	145(5)
Ge	4*c*	0.7775(1)	1/4	0.3946(1)	153(4)
M	4*c*	0.1470(7)	1/4	0.4297(6)	107(15)

Table 6.18: Anisotropic displacement parameters [pm^2] for $Li_xCaAl_{1-x}Ge$

Atoms	*U11*	*U22*	*U33*	*U23*	*U13*	*U12*
Ca	102(9)	176(9)	158(9)	0	-30(4)	0
Ge	105(6)	153(5)	203(6)	0	-21(7)	0
M	110(30)	120(30)	90(20)	0	0	0

Table 6.19: Occupancy of the M-position for $Li_xCaAl_{1-x}Ge$

Position	*Aluminum*	*Litihium*
M	0.49(2)	0.51(2)

Table 6.20: Selected interatomic distances [pm] for $Li_xCaAl_{1-x}Ge$

Ca	–Ge	306.8(2)	1x	Ge	–M	265.3(3)	2x	M	–Ge	265.3(3)	2x
	–Ge	311.1(2)	2x		–M	272.1(5)	1x		–Ge	272.1(5)	1x
	–M	313.6(4)	2x		–M	278.0(5)	1x		–Ge	278.0(5)	1x
	–Ge	313.8(2)	2x		–Ca	306.8(2)	1x		–Ca	313.6(4)	2x
	–M	322.4(5)	1x		–Ca	311.1(2)	2x		–Ca	322.4(5)	1x
	–M	339.1(6)	1x		–Ca	313.8(2)	2x		–M	326.3(7)	2x
	–M	344.8(4)	2x		–Ca	376.6(2)	1x		–Ca	339.1(6)	1x
	–Ge	376.6(2)	1x						–Ca	344.8(4)	2x

The $Li_xCaAl_{1-x}Ge$ ($0.4 < x < 0.6$) phase is isotypic to the silicon compound (cf. Fig.6.1) and crystallizes with the NaAuSn structure type.

The angle in the rhombus of germanium and M atoms is 74.8°, compared to 75.4° for the silicon analogue. Like for the silicides there is a related ternary compound $CaAl_2Ge_2$ where the germanium exhibits an "umbrella" coordination. The fourring interconnections of the six ring layers exhibit an angle of 73.3°, which again is practically identical to that in the isostructural $CaAl_2Si_2$ (73.4°).

The Ge–M distances are listed in Table 6.20). The four rings consist of two short Ge–M bonds of 265.3 pm (which belong also to the six ring layer) and of two bonds of 272.1 pm. The longest Ge–M separation of 278.0 pm belongs only to the six rings. Compared to the Si–M distances in the silicon analogue the Ge–M distances are, as expected, slightly longer.

There is also a relatively short M–M distance, namely the short diagonal of the rhombus, of 326.3 pm. This distance is practically as long as in the corresponding silicide due to the greater distortion of the M-Ge-M angle (74.8° vs 75.4°).

6.2.3 Physical Properties

The DTA of $Li_xCaAl_{1-x}Ge$ (x ~ 0.5) was performed (Fig.6.9) on an almost pure compound which was prepared at 1050°C (t_1 = 8 hours, r_e = 50°C/h) from a stoichiometric mixture of the elements. The almost single phase product exhibits lattice parameters very close to those found for the single crystal. According to this measurement, $Li_xCaAl_{1-x}Ge$ (x ~ 0.5) melts congruently at about 1045°C. No other thermal effects were observed.

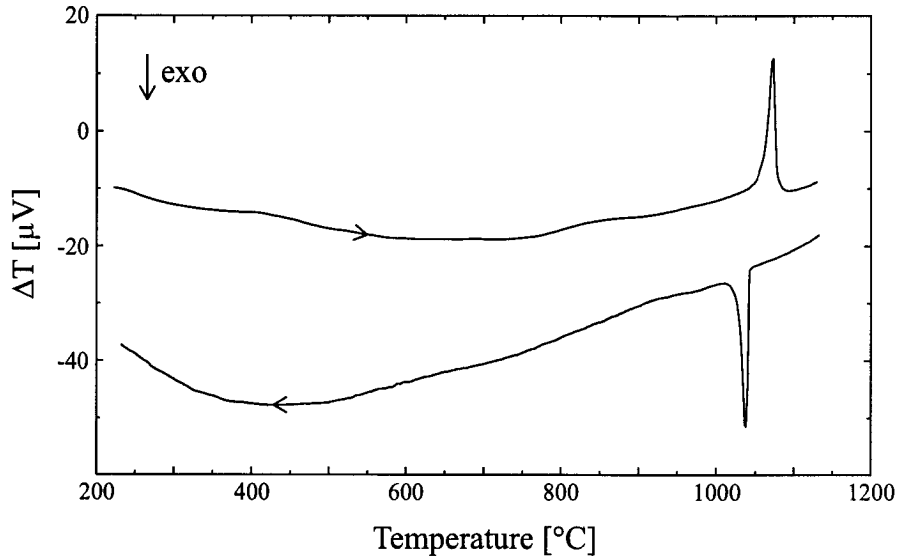

Figure 6.9: DTA of $Li_xCaAl_{1-x}Ge$ (x ~ 0.5)

A measurement of the conductivity was not performed as it was very difficult to get rid of the impurities in the samples of $Li_xCaAl_{1-x}Ge$.

6.2.4 Theoretical Investigations

Two simple models starting from the small unit cell were developed at first: one with all M positions occupied by lithium atoms and a chemical composition of $Li_4Ca_4Ge_4$, the other with all M positions occupied by aluminum atoms and therefore a composition of $Ca_4Al_4Ge_4$. In addition to these two models a DOS calculation was also performed using model2 (see 6.1.5) already utilised in the silicon analogue.

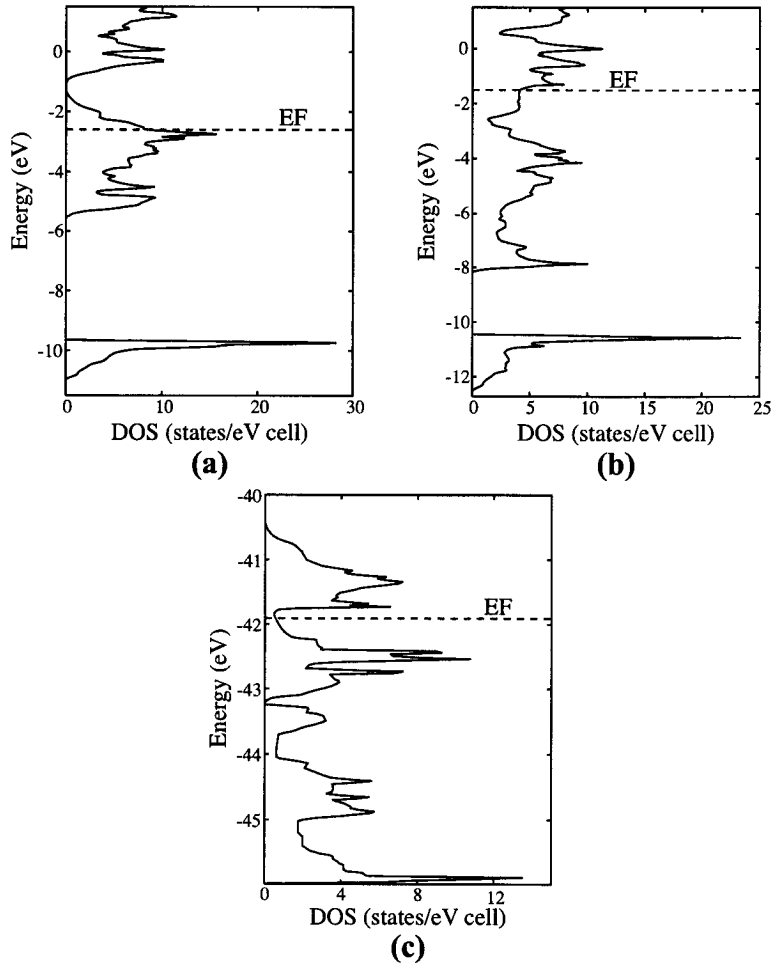

Figure 6.10: LMTO-DOS of the three models of $Li_xCaAl_{1-x}Ge$: (a) small cell $Li_4Ca_4Ge_4$; (b) small cell $Ca_4Al_4Ge_4$; (c) model1 of the supercell with the composition $Li_4Ca_{16}Al_4Ge_{16}$

In Figure 6.10 the three calculated DOS are displayed. Although the complexity of the DOS it is possible to recognize in all three calculated DOS the metallic character of the $Li_xCaAl_{1-x}Ge$ ($0.4 < x < 0.6$) compound. This result is consistent with the observation of a phase width with the Li : Al ratio assuming values varying from 0.4 to 0.6, as well as with results from the isoelectronic and isostructural silicon compound (see 6.1). Clearly the mixed situation (model 3) shows the most favourable DOS and thus one would not expect superstructure formation.

Seite Leer /
Blank leaf

7. The SrGaSi Phase

In the ternary system Sr/Ga/Si only the clathrate phase $Sr_8Ga_{16}Si_{30}$ was already known. However, for the isoelectronic Ca/Ga/Tt- (Tt = Si, Ge, Sn), Sr/Ga/Tt- (Tt = Ge, Sn, Ba/Ga/Ge [84] and Sr/Al/Si-systems [85] the equiatomic compounds with VEC = 9 had been reported. They exhibit AlB_2-related structures like $CaIn_2$. Attempting to synthesize Li/Sr/Ga/Si compounds, we were able to isolate a crystal of this new ternary phase.

7.1 Synthesis

Crystals of this new compound were isolated first from a sample of the composition Li:Sr:Ga:Si = 1:2:1:2 tempered at 1050°C. However, it was not possible to synthesize a pure phase as traces of $SrGa_2$, $SrGa_4$ and other compounds were always present. Also the question whether there is a phasewidth could not be carried out reliably because of different amounts of neighbouring phases. Due to the electronic properties (see 7.3) this is quite likely and would relate to the already known isostructural $SrGa_x$ ($1.85 < x < 2.37$) [98].

7.2 Crystal Structure

A single crystal of SrGaSi was examined on a four-circle diffractometer. All data were collected up to $2\theta = 65°$ (Tab.7.1). The Laue symmetry is *6/mmm* and there are no systematic extinctions consistent with the space groups *P6*, $P\bar{6}$, *P6/m*, *P622*, *P6mm*, $P\bar{6}2m$, $P\bar{6}m2$, and *P6/mmm*. The structure was solved in the highest space group using direct methods. The *2c* position is clearly statistically occupied by gallium and silicon (almost 50%). Attempts to solve the structure in lower symmetric space group as $P\bar{6}m2$, where the Ga/Si position is separated into two independent sites resulted in correlations and bad anisotropic displacement parameters. All atoms were anisotropically refined in *P6/mmm* and the displacement parameters are all satisfactory, but also indicate a light tendency of the Ga/Si-layer not to be planar, as indicated by the *U33* value (Tab.7.3). Nevertheless, this parameter is clearly smaller than in the CaGaSi

compound which also exhibit on the average a planar layer arrangement. The occupancy factor of the mixed semimetal position Ga/Si was refined (Tab.7.4).

Table 7.1: Crystal data and parameters of the data collection for SrGaSi

Empirical formula	Sr1Ga0.98Si1.02
Formula weight [g/mol]	184.6
Crystal size [mm]	0.12 x 0.14 x 0.20
Colour	grey metallic lustre
Crystal system	hexagonal
Unit cell dimension [pm]	a = 420.9(3); c = 471.5(3)
Volume [pm^3]	72.31(3)·10^6
Space group	*P6/mmm* (191)
Formula unit pro cell	1
ρ (calculated) [g/cm^3]	4.239
Absorption coefficient μ [mm^{-1}]	27.65
F (000)	83
Temperature [K]	298
Data collection	four-circle diffractometer STOE STADI4
Monochromator; Wavelength	graphite; λ(MoKα) = 0.71073 Å
Scan parameters (steps; Δω; scan)	44; 0.03; ω-θ - Scan
Theta range	2° < 2θ < 65°
h(min), h(max); k(min), k(max); l(min),	-6, 6; -6, 6; -7, 7
Reflections collected	998
Independent reflections	87 ; R(int) = 0.0544
Independent reflections with $\|F\|^2 > 2\,\sigma(\|F\|^2)$	84
Absorption correction	Ψ - Scan
Refinement	SHELXL-97 (full-matrix least-squares of F^2)
Parameters	7
Restraints	0
Extinction coefficient	0.98(6)
Maximal shift/esd	0.000
Mean shift/esd	0.000
Largest diff. peak and hole	min = -0.993; max = 0.776
[a] wR for $\|F\|^2 > 2\,\sigma(\|F\|^2)$	0.0436
wR for all reflections	0.0438
[a] R for $\|F\|^2 > 2\,\sigma(\|F\|^2)$	0.0185
R for all reflections	0.0198
[a] Goodness of Fit (*GooF*) for all reflections	1.197

[a] the definitions are given in chapter 2.2, Table 2.3

Table 7.2: Wyckoff sites, atomic coordinates, occupancy for SrGaSi

Atoms	*Wyckoff site*	*x*	*y*	*z*	*U(iso)*
Sr	1*b*	0	0	1/2	148(2)
X	2*c*	2/3	1/3	0	200(3)

Table 7.3: Anisotropic displacement parameters [pm^2] for SrGaSi

Atoms	*U11*	*U22*	*U33*	*U23*	*U13*	*U12*
Sr	140(3)	*U11*	164(3)	0	0	70(14)
X	120(3)	*U11*	359(4)	0	0	60(16)

Table 7.4: Occupancy of the Ga/Si-position for the SrGaSi

Position	*Gallium*	*Silicon*
X	0.492(3)	0.508(3)

Table 7.5: Selected interatomic distances [pm] for SrGaSi

Sr	–X	338.54(4)	12x	X	–X	242.84(3)	3x
	–Sr	420.9(3)	6x		–Sr	338.54(4)	6x
	–Sr	471.5(3)	2x		–X	471.5(3)	2x

The SrGaSi compound is isotypic to CaGaSi- as well as to the SrAlSi-phase. It crystallizes as a coloured derivative of the well known AlB_2 structure type (Fig.7.1). The positions in the hexagonal layer are statistically occupied by gallium and silicon atoms. Like in the isostructural CaGaSi, but unlikely all other EA/Ga/Tt, superstructure reflections were not observed, even on long time exposition pictures taken on the four circle diffractometer, and a lowering of the space group symmetry to the space group

$P\bar{6}m2$ by splitting the metal positions in two independent positions leads to unreliable anisotropic displacement parameters.

In contrast to the CaGaSi structure, where a torsion angle of 13° of the layer was evaluated [84], the U_{33} parameter of the gallium/silicon position is not as large (359 pm^2 vs. 820 pm^2). This indicates that possible distortions of the gallium/silicon layer are much smaller than for CaGaSi. The square roots of the displacement parameters U_{33} are 19pm and 29pm, for Sr and Ca compounds, respectively.

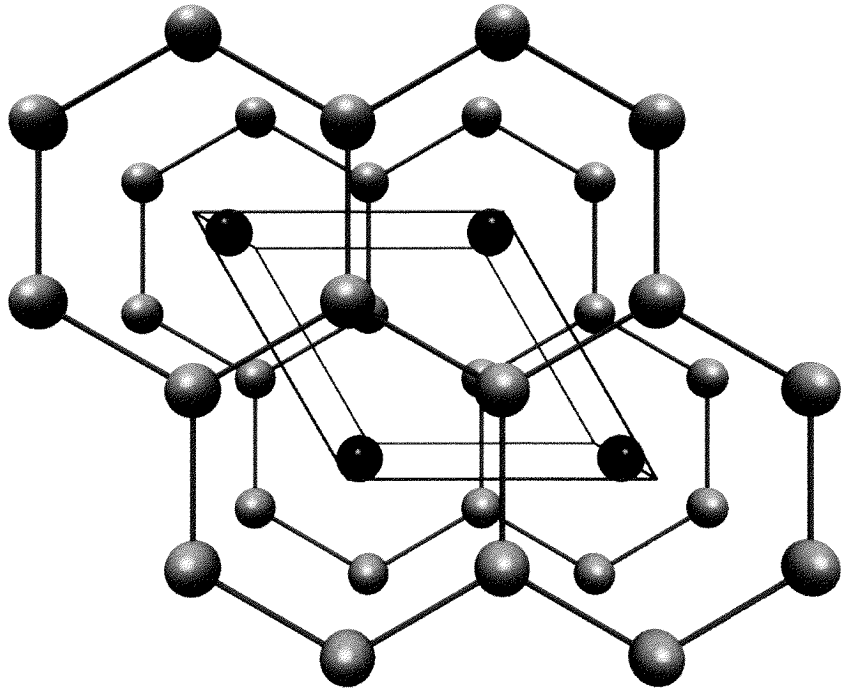

Figure 7.1: SrGaSi structure (Sr black, Ga/Si yellow)

The AlB_2-type shows close packed layers of the metal atoms Al, while the B atoms center the trigonal prisms of Al atoms and build up a planar six ring layers.

In SrGaSi the aluminum position is occupied by the earth alkali metal Sr, whereas the B site is statistically occupied by silicon and gallium (Fig.7.2 left). The Sr atoms are in the center of hexagonal prisms of Ga/Si atoms (Fig.7.2 right).

The Ga–Si distance within the sixring layer (243 pm) is comparable to the reported Ga–Si covalent bond distances but slightly longer than that observed in CaGaSi (238 pm). This is due to the larger alkaline-earth cations.

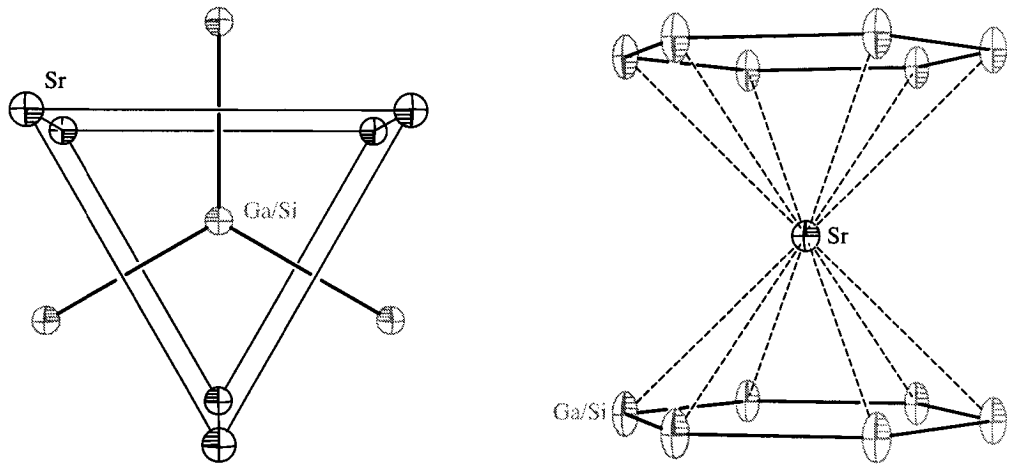

Figure 7.2: Coordination of Ga/Si (left) and Sr (right)

7.3 Physical Properties

Only recently, superconductivity of MgB_2 was discovered [99]. Since this compound crystallizes with the AlB_2 type just like the SrGaSi, the magnetic behaviour of SrGaSi was investigated to check for a superconducting phase transition. The main problem are the impurities contained in the product, because all attempts to synthesize a pure compound failed. The main byproduct was $SrGa_2$, which also crystallizes in the AlB_2 structure type. The measurement of the magnetic properties of the later compound was also performed based on the synthesis of a pure phase sample. $SrGa_2$ shows no superconducting transition down to 2K.

The magnetic measurements were performed on a SQUID magnetometer (MPMS 5S, Quantum Design) between 2 and 100 K in a constant magnetic field (12.2 G). The samples were finely ground and then transferred into a small quarz tube.

SrGaSi exhibits a superconducting behaviour below the critical temperature of about 4.5 K (Fig.7.3). As the sample still contains some impurities like $SrGa_4$ and eventually other compounds, the superconductivity of SrGaSi is not ultimately sure.

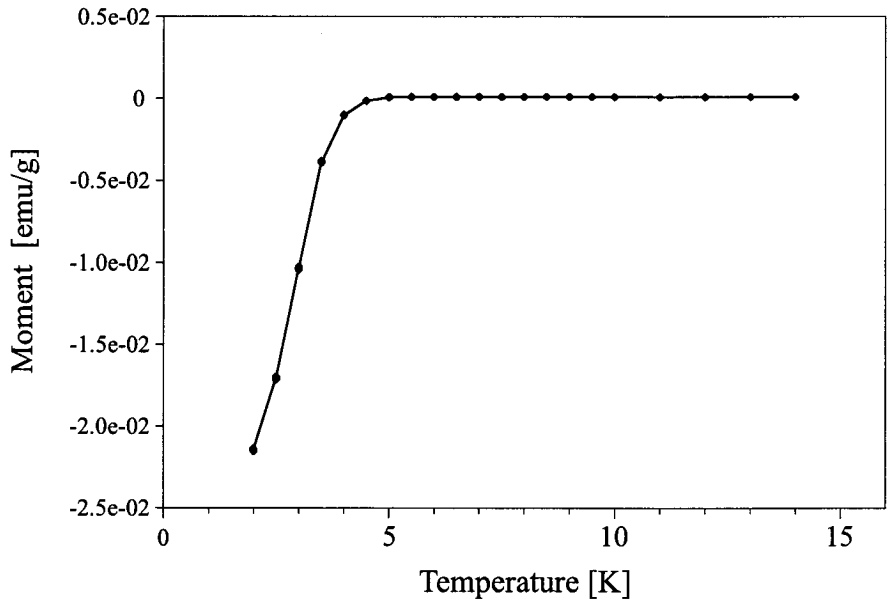

Figure 7.3: Magnetic moment of SrGaSi (low field)

7.4 Theoretical Investigations

In order to investigate the electronic properties and bonding structure of SrGaSi theoretical calculations in the EHMO framework (parameters: cf. Tab.A1) as well as by the LMTO method were performed. The first method was used for band structure and DOS calculations, the second for the development of ELF maps.

Since there is a mixed position occupied by silicon and by gallium in the ratio close to 1.1 and because there is no further information about an ordering of the two atoms types, calculations of band structure and DOS were performed on the three different models (Fig.7.4-6): full occupation with silicon, full occupation with gallium, and one model isostructural to the LiBC structure ($P6_3/mmc$ (194), c' = 943 pm) where the Si occupies the 2*c*, the Ga the 2*d* sites. The Fermi level was then shifted to the right number of valence electrons: 9. The three different calculations do not show large differences (Fig.7.4-6). The resulting DOS does not exhibit a band gap at the Fermi level (Fig.7.4-6). This was expected since the electronic structure of SrGaSi does not

follow the simple Zintl-Klemm concept: with VEC = 9 it is expected an average number of bonds of 3.5 per metametals (assuming a complete electron transfer from Sr to these elements). The Ga/Si layers seem to be planar and therefore it is convenient to compare these layers with those of graphite: the exceeding electron will be placed in the π^*-states. This is confirmed by the DOS (Fig.7.4-6) where the largest contribution to the states at the Fermi level is due to the p_z-orbitals of the Ga/Si atoms (black filled on the figures).

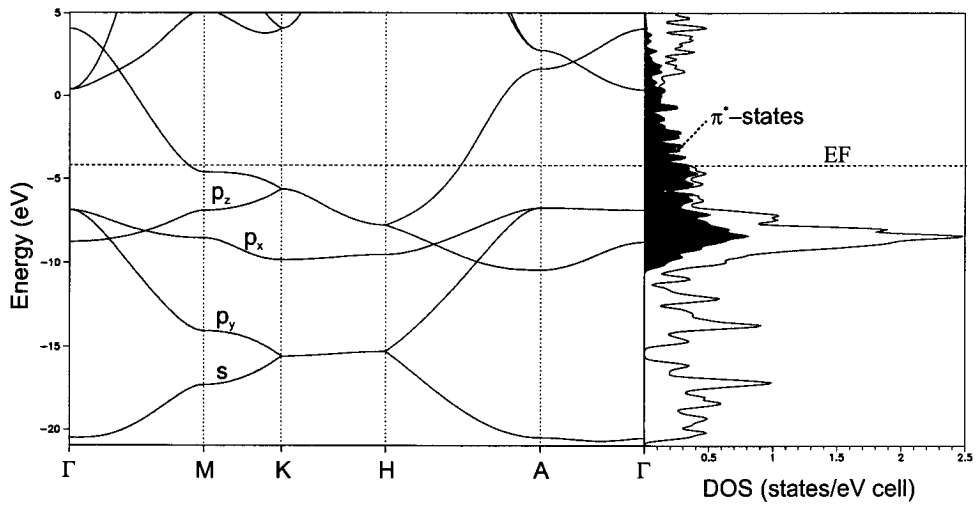

Figure 7.4: calculated EHMO-DOS: Ga/Si position occupied only by Ga. The black partial DOS is due to the p_z states and thus to π and π^* states

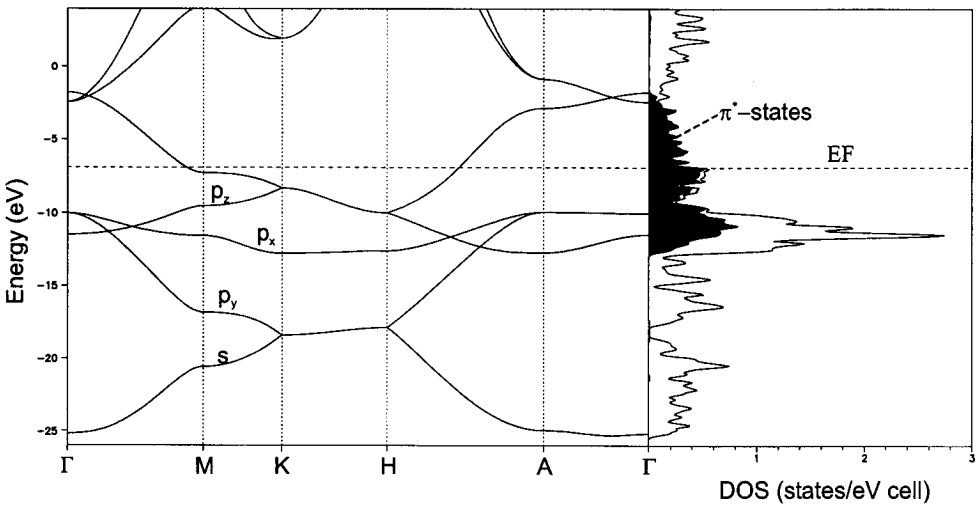

Figure 7.5: calculated EHMO-DOS: Ga/Si position occupied only by Si. The black partial DOS is due to the p_z states and thus to π and π^* states.

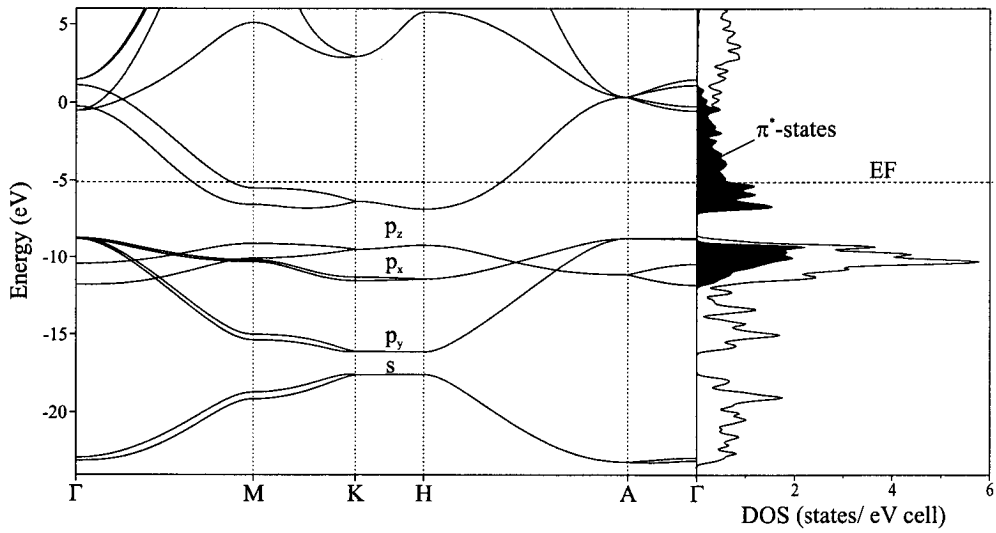

Figure 7.6: calculated EHMO-DOS for the model isotructural to LiBC. The black partial DOS is due to the p_z states and thus to π and π^* states

The metallicity is, like in graphite, 2 dimensional. This is nicely shown by the band structure (Fig.7.4-6): the p_z-orbitals undergo large dispersion (cutting the Fermi Level) from the Γ point to M, from M to K, and as well from H to A. This means that they interact strong within the Si/Ga layers. In contrast going from K to H and from A to Γ, investigating the interaction perpendicular to the layers, the p_z-orbitals do only show small dispersions, especially in the to LiBC isostructural model (Fig. 7.6). This means that, despite the relatively short distance between the different layers (471.5 pm), the electrons in the π^*-states are only slightly stabilised by interlayer interactions. This is not the case in other ecliptically stacked planar systems of Zintl anions with comparable anion-anion distances. For many Tetrel anions large interactions between adjacent π^*-systems were found [30,100,101].

In contrast to the article of Czybulka et al. [84] where the isostructural CaGaSi phase was described as covalent Ga/Si layer with sp^2 hybrid orbitals embedded in a metallic matrix of alkaline earth metals, our calculations does not show significant contributions of strontium sites to the states at the Fermi level.

In figure7.6 the COOP of the three cases are displayed: the occupancy of π^*-states is nicely shown as the Fermi level lies above the transition from bonding to antibonding interactions, and the states at the Fermi level are mainly π*-states as already shown in the DOS.

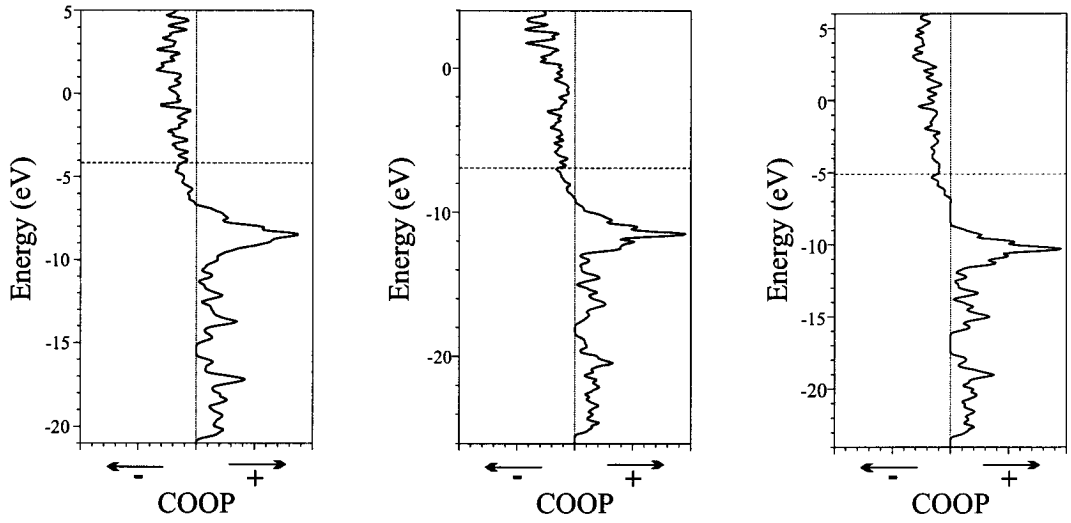

Figure 7.6: COOP of the three different models used for SrGaSi (left only Ga, middel only Si in the sixring layers, right model with LiBC structure type)

In order to investigate the bonding structure in more detail ELF calculations were carried out using LMTO methods. To overcome the problem of the mixed occupied Ga/Si position the space group $P\bar{6}\,m2$ was used instead of *P6/mmm*. In this space group the mixed occupied crystallographic position *2c* is divided into two independent crystallographic positions: *1c* and *1e*. As there is no difference between the two sites, the silicon placed on the *1c* position, whereas the gallium on 1e.

The bonding structure derived from EHMO calculations is confirmed by the ELF calculations which is quite nicely displayed by the ELF pictures (Fig.7.7a-c). The section of the Si-Ga bond is not rotationally symmetric, but rather has an oval shape, which is a clear indication of a π-bond character (Fig.7.7a). On the other hand the strong localisation on the silicon and on the gallium atoms can be interpreted as the partially filled π^*-states (Fig.7.7b). Moreover the very low electron localisation between the strontium on the one hand and the Ga and Si on the other is typical for interactions of

ionic character (Fig.7.7b). The ELF picture of the hexagonal layer shows a relatively high electron localisation as usual for covalent bonds (Fig.7.7c).

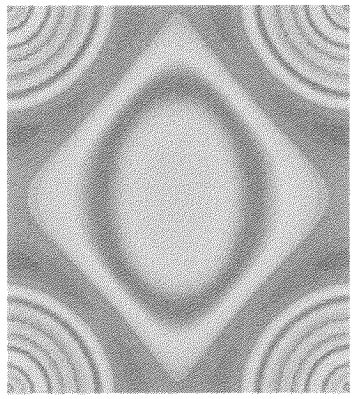

(a)

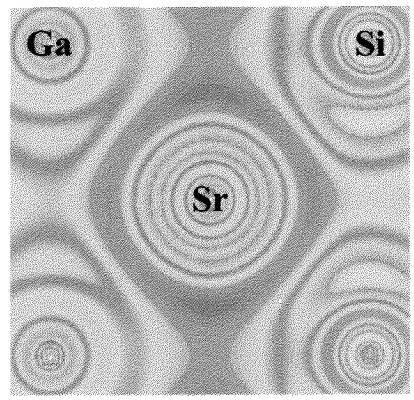

(b)

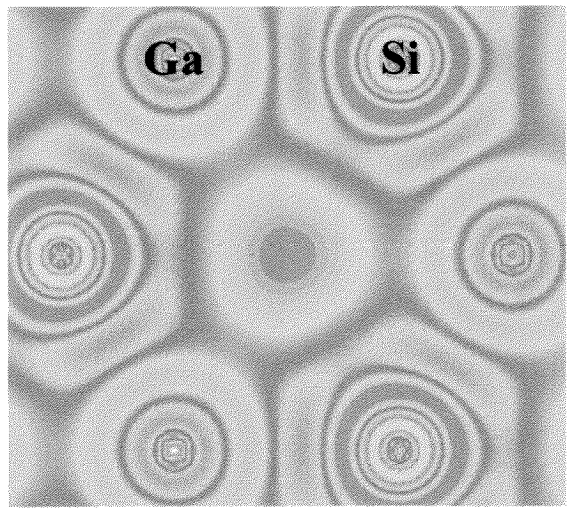

(c)

Figure 7.7a-c: LMTO-ELF Sections: **(a)** Perpendicular to the Ga-Si bond; **(b)** *100* plane through Sr; **(c)** part of the Ga-Si layer.

8. Overview

Finally, we will compare the new structures against each other and mark the important trends.

For the composition Li_5TrTt_2 (Tr = Al, Ga; Tt = Si, Ge, Sn) three different structural arrangements have been found which transform into each other at different transition temperatures. While the α–form (I) is an ordered tetrahedral framework, the β–phase (closely related to I, but with mixed occupied Tr/Li positions) is a disordered variant, and the γ-modification (II) exhibits a planar sixring layer structure. The formal charge per network atom is –1.67 and the VEC is 5.33.

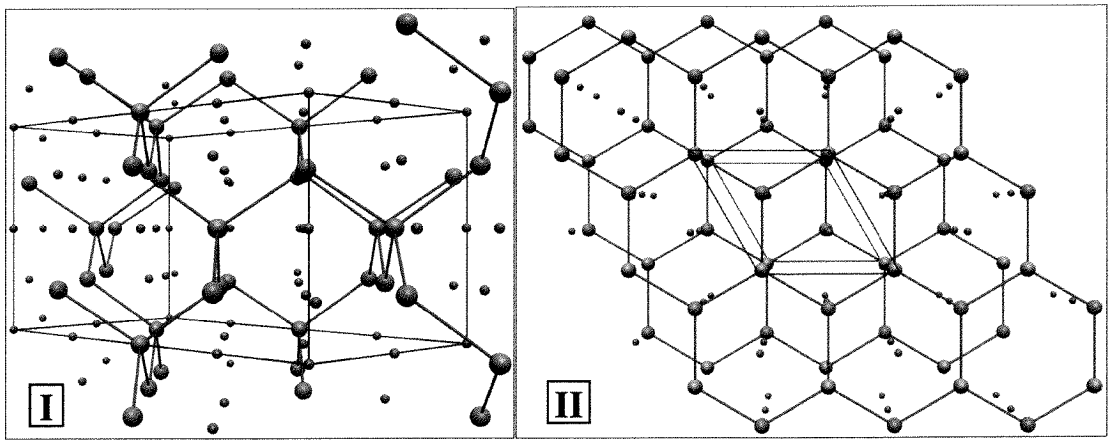

Because of a ratio Al : Si = 1 : 2 an alternating distribution as it is found for LiBC for example is not possible. Only for Tt = Si partially ordered variants of γ–form (III, for Tr = Ga) were detected and investigated. In the case of Ga, this seems to be somehow more stable and thus appears to be the only modification of this three-component composition, i.e. α– and β–forms have not been observed.

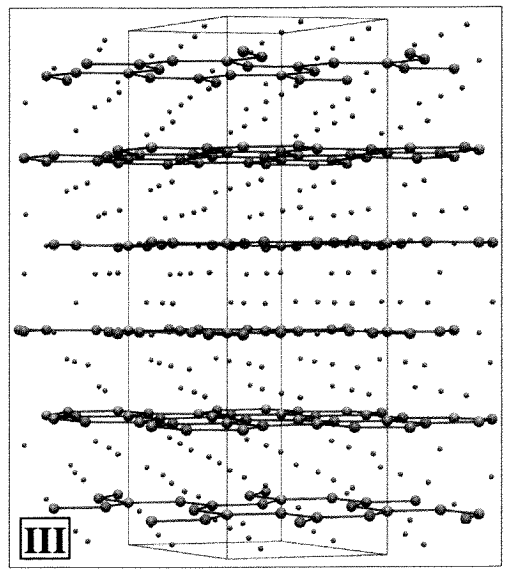

While these three forms can easily be derived from the classical Zintl phases the isoelectronic compounds $LiSr_2AlTt_2$ (Tt = Si, Ge) (IV) clearly belong to the intermetallic family. These show that neither the charge transfer (q = -1.67) nor VEC (5.33) nor the Al : Tt ratio (also 1 : 2) can be relevant for the structural change.
It is obviously due to a packing effect, i.e. the different requirements of two large cations instead of four small one per formula unit which have to be properly placed in space. On the other hand, it becomes very clear that an $[AlSi_2]$ framework with 5.33 electron per atom can survive in quite different structural arrangements.

In addition, the size of the divalent cation is very important and even such seemingly small differences of radii as found for Ca^{2+} and Sr^{2+} make the game. So comparing $LiSr_2AlTt_2$ and $LiCa_2AlTt_2$ (V) one finds intermetallic character for both of them, but the latter has a 3D framework structure instead of a layered arrangement.

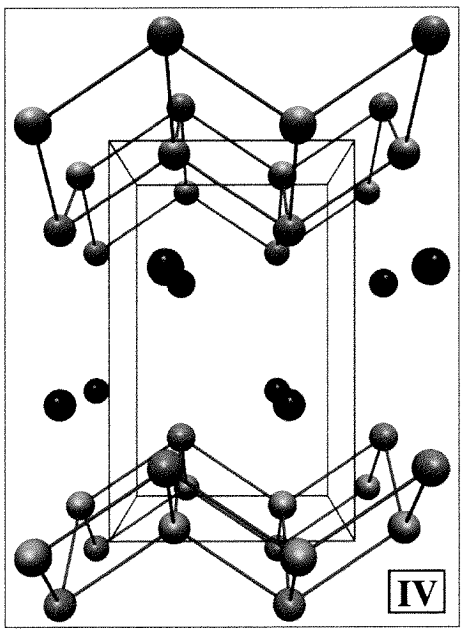

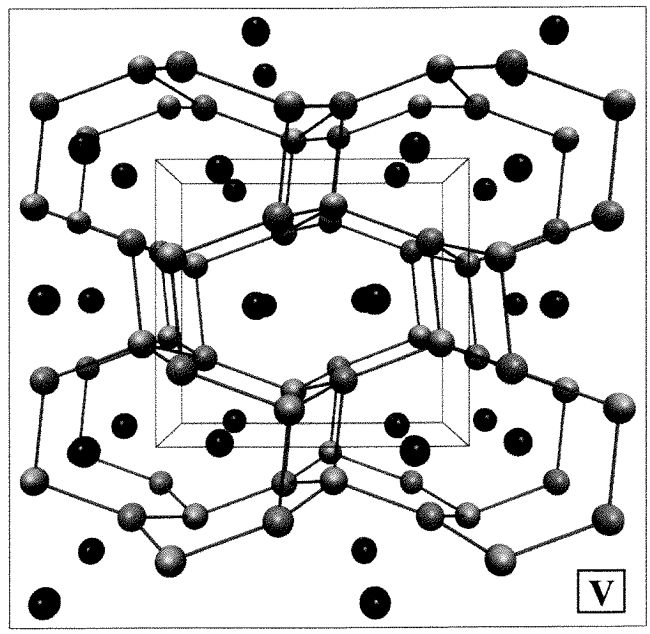

The latter structure is very much related to $SrAl_2$ and thus does not really change by introducing a large amount of Tetrel element.

$Li_{3.9}Sr_2Al_{3.1}Si_6$ has an average charge of q = -0.89 and a VEC = 4.56, the first of which is slightly smaller and the latter slightly larger than the corresponding value of SrGaSi (q = -1, VEC = 4.5). However, the structure belongs clearly to the intermetallic side (VI) and it is like (IV) a variant of the $BaAl_4$ parent type.

$Li_{9.2}Sr_5Al_{9.8}Si_{12}$ with q = -0.88 and VEC = 4.35 (VII) again shows an intermetallic structure characteristic and is a very interesting new, zeolite-like, intermetallic phase which derives in a novel way from $BaAl_4$ motives. This is another beautiful example for the enormous variability of such intermetallic bond systems.

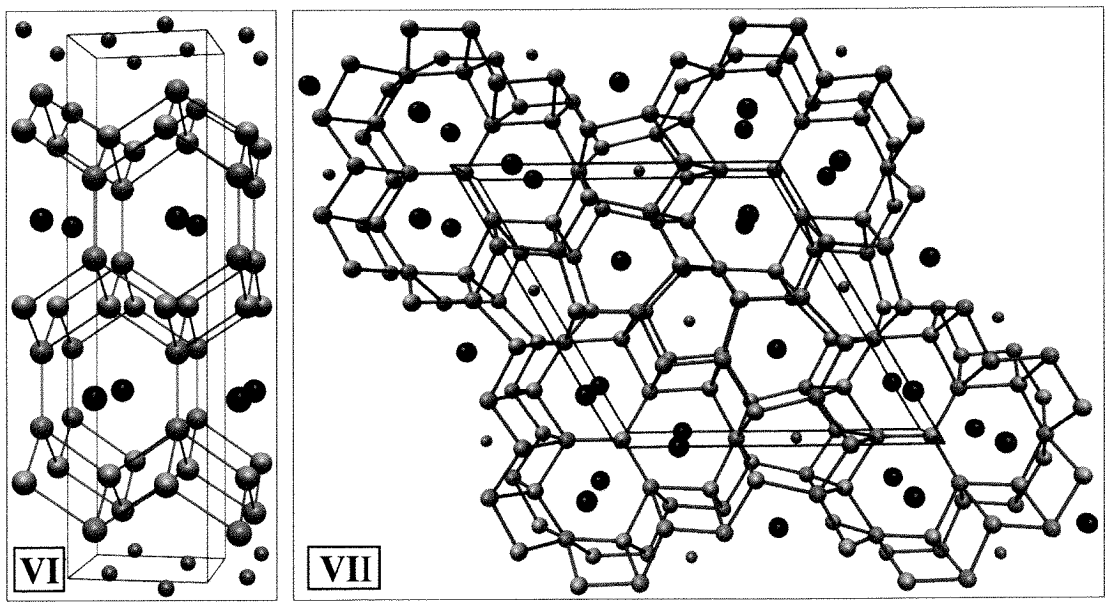

One even gets the impression that intermetallic structures and consequently a large variety of bonding schemes offers much better possibilities for rearrangements than Zintl phases or insulator compounds with their clearcut structural solutions which, in most cases, can only be changed against large kinetic hindrance and only to structures very distinct from the original one. The variety belongs to the metals! This is well observed in the healing properties of many metals which makes up for their fracture resistance.

Seite Leer /
Blank leaf

Appendix

A.1 Abbreviation

CCD	Charge Coupled Device
CN	Coordination Number
COOP	Crystal Orbital Overlap Population
DOS	Density of States
DTA	Differential Thermal Analysis
EA	Alkaline-earth metal
E_f	Energy at the Fermi level
EHMO	Extended-Hückel Molecule Orbital
ELF	Electron Localisation Function
LMTO	Linear Muffin Tin Orbital
PDS	Position Sensitive Detector
XRD	X-ray Diffraction
Tr	Triel (group number 13) element
Tt	Tetrel (group number 14) element
VEC	Valence Electron Count

A.2 ELF Scale

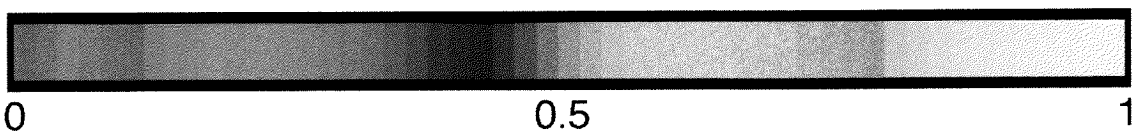

Figure A.1: The ELF scale for the 2D-ELF pictures

A.3 EHMO Parameters

Tab.A.1: Standard parameters used for the EHMO calculations

Element	H_{ii} [eV]	α	Element	H_{ii} [eV]	α
Li-2s	-5.4	0.65	**Ga-4s**	-14.58	1.77
Li-2p	-3.5	0.65	**Ga-4p**	-6.75	1.55
Ca-4s	-7.0	1.2	**Si-3s**	-17.3	1.383
Ca-4p	-4.0	1.2	**Si-3p**	-9.2	1.383
Sr-5s	-6.62	1.214	**Ge-4s**	-16.0	2.16
Sr-5p	-3.92	1.214	**Ge-4p**	-9.0	1.85
Al-3s	-12.3	1.167	**Sn-5s**	-16.16	2.12
Al-3p	-6.5	1.167	**Sn-5p**	-8.32	1.82

H_{ii}: diagonal element of the Hamilton matrix; α: Slater exponent

A.4 Brillouin Zones

The Brillouin zones of the Bravais lattices used in the band structure calculations are represented here with the corresponding special k-points (Fig. A2-5), according to [102]. The coordinates of the special k-points are given in units of reciprocal lattice vectors. The orientation of the Brillouin zones in Cartesian coordinates can be extrapolated from the definition of the real lattice vectors in Table A.2.

Tab.A.2: Lattice vectors of the Bravais lattices

Bravais lattice	Real lattice vectors
orthorhombic *P*	(0,-*b*,0); (*a*,0,0); (0,0,*c*)
tetragonal *P*	(*a*,0,0); (0,*a*,0); (0,0,*c*)
tetragonal *I*	$\frac{1}{2}$(-*a*,*a*,*c*); $\frac{1}{2}$(*a*,-*a*,*c*); $\frac{1}{2}$(*a*,*a*,-*c*)
hexagonal *P*	(0,-*a*,0); $\frac{1}{2}$ ($a\sqrt{3}$,*a*, 0); (0,0,*c*)
cubic *P*	(*a*,0,0); (0,*a*,0); (0,0,*a*)

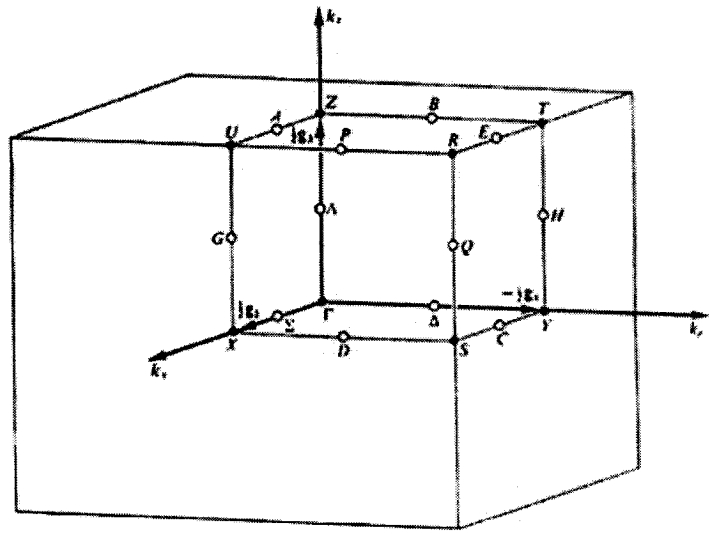

Figure A.2: The Brillouin zone for orthorhombic *P*. Γ = (000); $Y = (\bar{\frac{1}{2}}00)$; $X = (0\frac{1}{2}0)$; $Z = (00\frac{1}{2})$; $U = (0\frac{1}{2}\frac{1}{2})$; $T = (\bar{\frac{1}{2}}0\frac{1}{2})$; $S = (\bar{\frac{1}{2}}\frac{1}{2}0)$; $R = (\bar{\frac{1}{2}}\frac{1}{2}\frac{1}{2})$.

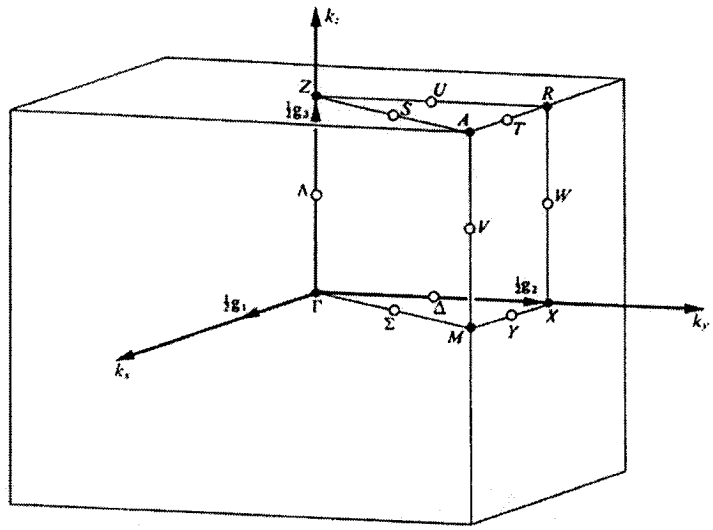

Figure A.3: The Brillouin zone for tetragonal *P*. Γ = (000); $M = (\frac{1}{2}\,\frac{1}{2}0)$; $Z = (00\frac{1}{2})$; $A = (\frac{1}{2}\,\frac{1}{2}\,\frac{1}{2})$; $R = (0\,\frac{1}{2}\,\frac{1}{2})$; $X = (0\,\frac{1}{2}0)$.

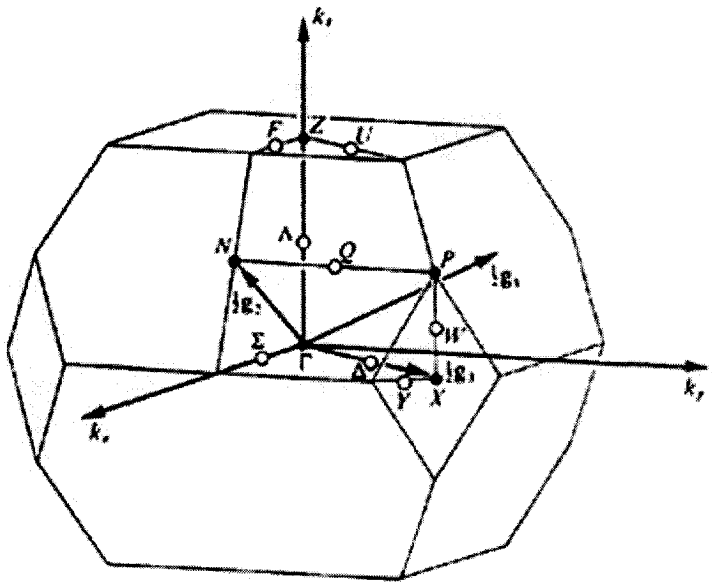

Figure A.4: The Brillouin zone for tetragonal *I*. For $c > a$, Γ = (000); $N = (0\,\frac{1}{2}0)$; $X = (00\frac{1}{2})$; $Z = (\frac{1}{2}\,\frac{1}{2}\,\bar{\frac{1}{2}})$; $P = (\frac{1}{4}\,\frac{1}{4}\,\frac{1}{4})$.

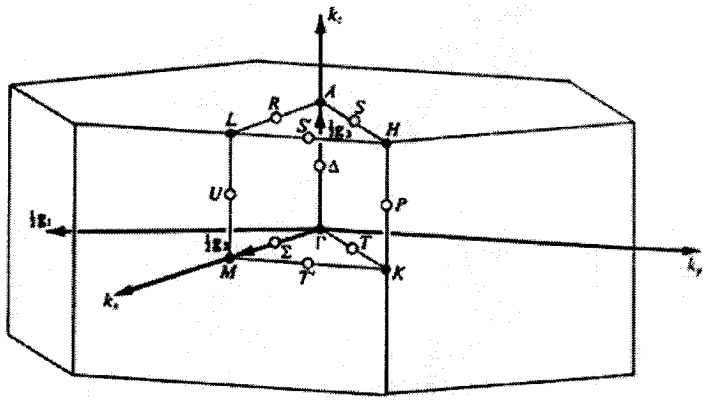

Figure A.5: The Brillouin zone for hexagonal P. $\Gamma = (000)$; $M = (0\frac{1}{2}0)$; $A = (00\frac{1}{2})$; $L = (0\frac{1}{2}\frac{1}{2})$; $K = (\frac{\bar{1}}{3}\frac{2}{3}0)$; $H = (\frac{\bar{1}}{3}\frac{2}{3}\frac{1}{2})$

Seite Leer /
Blank leaf

Literature

[1] R. Ramirez, R. Nesper, H. G. v. Schnering, M. C. Böhm, *J. Phys. Chem. Solids* **48**, 51 (1987)

[2] R. Hoffmann, *Solids and Surfaces. A Chemist's View of Bonding in Extended Structures,* VCH Publishers Inc., New York (1989)

[3] J. Hafner, *From Hamilton to Phase Diagrams,* Springer, Berlin (1987)

[4] W. B. Pearson, *J. Less-Common Met.* **109**, L3 (1985)

[5] J. Burdett, *J. Am. Chem. Soc.* **102**, 450 (1980)

[6] T. Albright, J. Burdett, M.-H. Wangbo, *Orbital Interactions in Chemistry,* Wiley, New York (1985)

[7] J. Burdett, S. Lee, *J. Am. Chem. Soc.* **107**, 3050 (1985)

[8] J. Burdett, S. Lee, *J. Am. Chem. Soc.* **107**, 3063 (1985)

[9] J. Burdett, S. Lee, T. McLarnan, *J. Am. Chem. Soc.* **107**, 3083 (1985)

[10] J. Burdett, G. Miller, *J. Am. Chem. Soc.* **109**, 4081 (1987)

[11] J. Burdett, B. Coddens, *Inorg. Chem.* **27**, 418 (1988)

[12] J. Burdett, G. Miller, *Chem. Mater.* **2**, 12 (1990)

[13] J. Burdett, E. Canadell, *J. Am. Chem. Soc.* **112**, 7207 (1990)

[14] J. Burdett, E. Canadell, *Inorg. Chem.* **30**, 1991 (1991)

[15] C. Zheng, R. Hoffmann, *Z. Naturforsch.* **41b**, 292 (1986)

[16] C. Zheng, R. Hoffmann, R. Nesper, H. G. v. Schnering, *J. Am. Chem. Soc.* **108**, 1876 (1986)

[17] C. Zheng, R. Hoffmann, *J. Solid State Chem.* **72**, 58 (1988)

[18] C. Zheng, R. Hoffmann, *Inorg. Chem.* **28**, 1074 (1989)

[19] U. Häussermann, S. Wengert, R. Nesper, *Angew. Chem. Int. Ed. Engl.* **33**, 2073 (1994)

[20] W. Klemm, *Angew. Chem.* **62**, 133 (1950)

[21] W. Klemm, *Proc. Chem. Soc. London*, 329 (1959)

[22] E. Zintl, *Z. Phys. Chem.* **A154**, 1 (1931)

[23] E. Zintl, *Z. Phys. Chem.* **A154**, 47 (1931)

[24] E. Zintl, *Z. Phys. Chem.* **B16**, 195 (1932)

[25] E. Zintl, *Z. Elektrochem.* **41**, 876 (1935)

[26] Zintl, *Angew. Chem.* **52**, 1 (1939)

[27] S. M. Kauzlarich, *Chemistry, Structure, and Bonding of Zintl Phases and Ions,* VCH Publishers Inc., New York (1996)

[28] A. Savin, R. Nesper, S. Wengert, T. Fässler, *Angew. Chem.* **109**, 1892 (1997)

[29] R. Nesper, S. Wengert, *Chem. Eur. J.* **3**, 985 (1997)

[30] S. Wengert, *Dissertation ETH Nr. 12070*, ETH Zürich (1997)

[31] E. Mooser, W. B. Pearson, *Phys. Rev.* **101**, 1608 (1956)

[32] E. Parthé, *Cristallochemie des Structures Tetraédriques,* Gordon and Breach, Paris (1972)

[33] H. Schäfer, B. Eisenmann, W. Müller, *Angew. Chem.* **85**, 742 (1973)

[34] R. Nesper, H. G. v. Schnering, *Tschermarks Miner. Petr. Mitt.* **32**, 195 (1983)

[35] R. Nesper, *Prog. Solid St. Chem.* **20**, 1 (1990)

[36] R. Ramirez, *Chemische Bindung an Zintl-Phasen. Theoretische Untersuchungen an ausgewählten Beispielen.*, Universität Stuttgart (1986)

[37] R. Ramirez, R. Nesper, H. G. v. Schnering, M. C. Böhm, *Z. Naturforsch.* **41a**, 1267 (1986)

[38] E. Mooser, W. B. Pearson, *Progress in Semiconductors,* Ed. Gibson, Kröger and Burgess, Wiley & Sons Inc., New York (1960)

[39] W. Klemm, *Festkörperprobleme,* Vierweg, Braunschweig (1963)

[40] E. Busmann, *Z. Anorg. Allg. Chem.* **313**, 90 (1961)

[41] W. Klemm, E. Busmann, *Z. Anorg. Allg. Chem.* **319**, 297 (1963)

[42] H. G. v. Schnering, *Angew. Chem.* **93**, 44 (1981)

[43] R. Nesper, *Habilitationsschrift*, Univesity Stuttgart (1988)

[44] R. Nesper, H. G. v. Schnering, J. Curda, *Chem. Ber.* **119**, 3576 (1986)

[45] P. Villars, L. D. Calvert, *Pearson's Handbook of Crystallographic Data for Intermetallic Phases,* Second Edition, ASM International, (1991)

[46] T. B. Massalski, *Binary Alloy Phase Diagrams,* Second Edition, ASM International, (1992)

[47] A. Larson, R. V. Dreele, *GSAS General Structure Analysis System*, Los Alamos National Laboratory, San Francisco (1985)

[48] Siemens Analytical X-Ray Systems Inc., Madison, USA,

[49] G. M. Sheldrick, University of Göttingen, Germany

[50] Siemens Analytical X-Ray Instruments Inc., *SHELXTL PLUS*, Release 5.0, Madison, USA (1995)

[51] G. M. Sheldrick, *SHELXS-97 Program for the Solution of Crystal Structures*, University of Göttingen, Germany (1997)

[52] G. M. Sheldrick, *SHELXL-97 Program for the Refinement of Crystal Structures*, University of Göttingen, Germany (1997)

[53] W. Furrey, *PHASES Program for the Electron Density Calculations*, Version September 1994, University of Pittsburgh, Dep. of Crystallography,

[54] Y. L. Page, *MISSYM Computer Program for Recognizing and Correcting Space Group Errors*, NRC of Canada, Ottawa, Canada (1990)

[55] R. Nesper, *STRUKTUR*, ETH Zürich (1995)

[56] W. R. Busing, K. O. Martin, H. A. Levy, *ORFFE Crystallographic Function and Error Program*, Report ORNL-TM-306, Oak Ridge National Laboratory, Oak Ridge, USA (1971)

[57] C. K. Johnson, *ORTEPII*, Report ORNL-5138, Oak Ridge National Laboratory, Oak Ridge, USA (1976)

[58] A. C. Larson, F. L. Lee, Y. L. Page, M. Webster, J.-P. Charland, E. J. Gabe, *NRCVAX Crystal Structure System with Interactive Version of ORTEPII*, NRC of Canada, Ottawa, Canada (1986)

[59] P. Hofmann, R. Nesper, *COLTURE 3-D Color Graphics Program*, Laboratorium für Anorganische Chemie, ETH Zürich (1995)

[60] MSI, *Cerius*^{2}, 4.2, Molecular Simulations, San Diego (2000)

[61] V. Petricek, M. Dusek, *JANA'2000*, Institute of Physics, Academy of Sciences of the Czech Republic, Prag (2000)

[62] O. K. Andersen, *Phys. Rev.* **B 12**, 3060 (1975)

[63] O. K. Andersen, O. Jepsen, D. Glötzel, *Highlights of Condensed Matter Theory,* North-Holland, Amsterdam (1985)

[64] H. L. Skriver, *The LMTO Method, Muffin-Tin Orbitals and Electronic Structure,* Springer Verlag, Berlin (1984)

[65] A. D. Becke, K. E. Edgecombe, *J. Chem. Phys.* **92**, 5397 (1990)

[66] A. Savin, A. D. Becke, J. Flad, R. Nesper, H. Preuss, H. G. v. Schnering, *Angew. Chem.* **103**, 421 (1991)

[67] B. Silvi, A. Savin, *Nature* **371**, 683 (1994)

[68] T. Fässler, A. Savin, *Chemie in unsere Zeit* **3**, 110 (1997)

[69] G. Krier, O. Jepsen, A. Burckhardt, O. K. Andersen, *TB-LMTO-ASA Program,* Version 45, MPI Stuttgart, Germany (1994)

[70] M.-H. Wangbo, M. Evain, T. Hughbanks, M. Kertesz, S. Wijezesekera, C. Wilker, C. Zheng, R. Hoffmann, *Program EHMACC: Extended Hückel Molecular and Crystal Calculations; Program EHPC: Extended Hückel Property Calculations,*

[71] J. Flad, F.-X. Fraschio, B. Miehlich, *Program GRAPA*, Institut für Theoretische Chemie der Universität Stuttgart, Germany

[72] H. Nowotny, F. Holub, *Mh. Chem.* **91**, 877 (1960)

[73] H.-U. Schuster, H.-W. Hinterkeuser, W. Schäfer, G. Will, *Z. Naturforsch.* **31b**, 1540 (1976)

[74] V. Pavlyuk, O. Bodak, *Izv. Ak. Nauk SSSR, Neorg. Mat.* **28**, 988 (1992)

[75] W. Bockelmann, H.-U. Schuster, *Z. Anorg. Allg. Chem.* **410**, 241 (1974)

[76] W. Bockelmann, H. Jacobs, H.-U. Schuster, *Z. Naturforsch.* **25b**, 1305 (1970)

[77] W. Bockelmann, H.-U. Schuster, *Z. Anorg. Allg. Chem.* **410**, 233 (1974)

[78] W. Blase, G. Cordier, R. Kniep, *Z. Anorg. Allg. Chem.* **619**, 1161 (1993)

[79] H.-U. Schuster, W. Bockelmann, *Z. Naturforsch.* **24b**, 1189 (1969)

[80] E. Gladyshevskii, P. Kipyakevich, O. Bodak, *Ukr. Physics J.* **12**, 447 (1967)

[81] A. Widera, H. Schäfer, *Z. Naturforsch.* **32b**, 1349 (1977)

[82] A. Widera, B. Eisenmann, H. Schäfer, K. Turban, *Z. Naturforsch.* **31b**, 1592 (1976)

[83] G. Cordier, H. Schäfer, *Z. Anorg. Allg. Chem.* **490**, 136 (1982)

[84] A. Czybulka, B. Pinger, H.-U. Schuster, *Z. Anorg. Allg. Chem.* **579**, 151 (1989)

[85] I. Ganiev, A. Vakhobov, T. Dzhurayev, *Russ. Metall. Engl. Transl.* **4**, 175 (1977)

[86] B. Eisenmann, H. Schäfer, R. Zagler, *J. Less-Common Met.* **118**, 43 (1986)

[87] A. Widera, H. Schäfer, *Z. Naturforsch.* **33b**, 1769 (1979)

[88] N. E. Christensen, *Phys. Rev.* **B 32**, 6490 (1985)

[89] U. Häussermann, *Dissertation ETH Nr. 10990*, ETH Zürich (1995)

[90] S. Leoni, *Dissertation ETH Nr. 12783*, ETH Zürich (1998)

[91] A. Grüttner, *Über das System Lithium - Germanium und die Bildung metastabiler Germanium-Modifikationen aus Li - Germaniden*, Stuttgart (1982)

[92] W. Westerhaus, H.-U. Schuster, *Z. Naturforsch.* **34b**, 352 (1979)

[93] B. Eisenmann, H. Schäfer, A. Weiss, *Z. Naturforsch.* **25b**, 651 (1970)

[94] B. Eisenmann, H. Schäfer, A. Weiss, *Z. Anorg. Allg. Chem.* **391**, 241 (1972)

[95] U. Häussermann, S. Wengert, R. Nesper, *Angew. Chem.* **106**, 2151 (1994)

[96] R. W. F. Bader, *Atoms in Molecules, A Quantum Theory,* Oxford University Press, Oxford (1990)

[97] R. W. F. Bader, P. Popelier, T. Keith, *Angew. Chem.* **106**, 647 (1994)

[98] G. Bruzzone, *Boll. Sc. Fac. Chim. Ind. Bologna* **24**, 113 (1966)

[99] J. Nagamatsu, N. Nakagawa, T. Muranaka, Y. Zenitani, J. Akimitsu, *Nature* **410**, 63 (2001)

[100] A. Currao, *Dissertation ETH Nr. 11747*, ETH Zürich (1996)

[101] F. Zürcher, *Dissertation ETH Nr. 12546*, ETH Zürich (1998)

[102] C. J. Bradley, A. P. Cracknell, *The Mathematical Theory of Symmetry in Solids,* Clarendon Press, Oxford (1972)

Acknowledgements

I would like to express my heartfelt gratitude to Prof. Dr. Reinhard Nesper for giving me the opportunity to join his group, for his essential scientific support, for the freedom he granted me in the realization of this work, and for his participation in the preparation of this thesis.

I would also like to thanks Prof. Dr. Hansjörg Grützmacher for taking on the task of co-examiner.

My best and special thanks to:

Dr. Michael Wörle, for introducing me in the world of crystallography, and for the kind support he gave me every time I encountered problems in this domain;

Dr. Steffen Wengert, for teaching me the basics of theoretical calculations and for the patience he showed in helping me to solve my endless problems with computers;

my brother Dr. Fabio Zürcher, for the patience he showed in introducing me in the world of solid state chemistry;

Christian Mensing and Dieter von Arx, for the conductivity measurements and, respectively, for the magnetic susceptibility measurements;

all the members of the Nesper group for the exceptionally good working atmosphere;

i miei amici della pausa pranzo Diego, Enrico, Fabio, Lino, Marcello, Riccardo, Roberto e Walter; della squadra dei Bödri Luca e Daniel; e tutti gli altri amici conosciuti a Zurigo per aver reso eccezionale questo periodo;

i miei genitori, i miei fratelli e Elisabetta per il loro sostegno in questi anni

Curriculum Vitae

Simone Alessandro Zürcher

Place and date of birth:	Sorengo (Switzerland); 6th November, 1972
Citizen of:	Thalwil (ZH), Switzerland
Title:	Dipl. Chem. ETH

Education

1978-1983	Primary school in Viganello (TI)
1983-1987	Secondary school in Viganello (TI)
1987-1991	Scientific high school/college in Lugano (TI)
1991-1996	Graduate studies in chemistry at the Swiss Federal Institute of Technology (ETH) in Zürich (Switzerland)
	Graduate thesis at the Institute of Inorganic Chemistry of the ETH Zürich, under the supervision of Prof. Dr. R. Nesper *"Untersuchungen zu den Reaktionen von Kalium-Fulleriden mit* $[Mo_6Cl_8]Cl_4$*"* (*"Study on the Reactions of Potassium Fullerenes with* $[Mo_6Cl_8]Cl_4$*")*
1996-2001	Ph.D. studies at the Institute of Inorganic Chemistry of the ETH Zürich, under the supervision of Prof. Dr. R. Nesper (this work)